X-ray phase imaging based on Hartmann Wavefront Sensor for applications on the study of neurodegenerative diseases

Ginevra Begani Provinciali

INSTITUT POLYTECHNIQUE DE PARIS

NNT : 2022IPPAE004

Thèse de doctorat

X-ray phase imaging based on Hartmann Wavefront Sensor for applications on the study of neurodegenerative diseases

Thèse de doctorat de l'Institut Polytechnique de Paris
préparée à Laboratoire d'Optique Appliqueé (LOA), ENSTA Paris, CNRS, Institut Polytechnique de Paris

École doctorale n°626 de l'Institut Polytechnique de Paris (EDIPP)
Spécialité de doctorat : Physique

Thèse présentée et soutenue à Palaiseau, le 21/03/2022, par

GINEVRA BEGANI PROVINCIALI

Composition du Jury :

Lucie Sancey Directeur de recherche, Institute for Advanced Biosciences, France	Président
Fulvia Arfelli Full professor Dip. di Fisica, Università di Trieste and INFN, Italy	Rapporteur
David Ros Maître de conférences,Enseignant-Chercheur Physique, France	Rapporteur
Jean-Claude Kieffer Full professor, INRS, Canada	Examinateur
Alessia Cedola Directrice de recherche CNR-Institute of Nanotechnology c/o Physics Department 'Sapienza' University, Italy	Examinateur
Philippe Zeitoun Directeur de recherche, LOA, France	Directeur de thèse

Résumé en français

L'objectif de cette thèse consiste en le développement d'une technique d'imagerie X de phase basée sur l'utilisation d'un senseur de front d'onde de type Hartmann pour être exploité sur différentes applications et de comparer ce nouveau système avec des techniques bien connues d'imagerie en contraste de phase. L'imagerie de phase sera principalement réalisée en 3D par tomographie. L'application principale inclue l'étude d'altérations du système nerveux central induites par des maladies neurodégénératives.
La première section d'introduction décrit les aspects de base de l'interaction rayons X-matière et de la théorie de la cohérence avec des application spécifiques à la conception de senseur de front d'onde de Hartmann. Dans le deuxième chapitre, une introduction à l'imagerie par contraste de phase est donnée, avec une attention particulière sur la technique en propagation libre. Le troisième chapitre examine les principes de la tomographie et des logiciels de reconstruction disponibles.
Un chapitre séparé, numéroté 4, est dédié à la théorie des senseurs de front d'onde de Hartmann. Un modèle de propagation en 3D basé sur le propagateur de Fresnel a été développé pour optimiser l'architecture du senseur complet incluant la plaque de Hartmann, les distances entre les différents éléments du montage et enfin les propriétés de la source X. Le modèle peut gérer n'importe quel degré de cohérence spatiale, permettant de réaliser des modélisation précises d'une grande variété de source X. Différentes simulations de situation expérimentales sont décrites pour valider le programme. Puis, les programmes principaux de reconstruction du front d'onde ont été analysés. Premièrement, nous avons considéré les caractéristiques connectées avec la propagation d'un élément du montage à un autre : énergie de la source, forme des ouvertures et espacement du masque de Hartmann et distances. En deuxième, différents paramètres connectés avec la détection des barycentres des spots ont été analysés. Les capacités des algorithmes classiques ont été étudiées pour des spots théoriques (forme gaussienne) avec une attention particulière sur l'effet du seuillage sur les images binarisées.
Afin d'améliorer les performances de détection, des algorithmes plus avancés (gaussienne pondérée itératif et interpolation gaussienne en 2D) ont été testés. Per la suite les résultats de ces deux sections ont été combinés pour analyser les résultats de plusieurs algorithmes de détection appliqués à des faisceau propagés (fonction Bessel et sinus cardinal). Finalement, cette analyse a été appliquée à des spots réels.
Dans le chapitre 5, nous allons présenter des résultats expérimentaux obtenus avec le senseur de font d'onde X en géométries de faisceau parallèle (synchrotron) ou conique (mesure en laboratoire). Différentes plaques de Hartmann ont été utilisé sur le montage de laboratoire pour visualiser une série d'échantillons tes et biologiques. De plus, sur synchrotron, nous avons testé le senseur de Hartmann pour retrouver la composition chimique d'objets composés de matériaux connus. La composition chimique peut être estimée à partir de mesures directes et indépendantes de la partie réelle (proportionnelle à la phase) et la partie imaginaire (proportionnelle à l'absorption) de l'indice de réfraction de l'échantillon.
Dans le chapitre 6, les résultats expérimentaux obtenus en tomographie X par contraste de phase en propagation libre seront discutés. Nous avons exploité la capacité de l'imagerie X par contraste de phase pour étudier les effets des maladies neurodégénératives du système nerveux central. Les résultats de deux expériences sont présentés. La première expérience a été réalisée avec des cerveaux de souris affectées par le modèle animal de la maladie d'Alzheimer et la deuxième a été faite sur des échantillons de moelle épinière de souris affectées par le modèle animal de la sclérose latérale amyotrophique.

Contents

Acknowledgement

My deep gratitude goes first to Philippe Zeitoun who guided me during the PhD, he has been offering advice and encouragement with a perfect blend of insight and humor.He provided invaluable feedback on my analysis, at times responding to emails late at night and early in the morning. I'm proud of, and grateful for, my time working with Philippe.
I especially want to thank the members of my thesis jury: the president Lucie Sancey, the referees Fulvia Arfelli and David Ros, the examiners Alessia Cedola and Jean Claude Kieffer.
Countless people supported my effort at LOA, expecially the directors Stéphane Sebban and Antoine Rousse and the head of SIIM group Alessandro Flacco. My thesis would not be possible without the administrative and technical support of all the secretaries and of the Atelier that made the impossible always possible.
Thank you to my research group : Philippe Zeitoun, Ying Li, Ghada Mahmoud, Thi Xiu Le and Daniel Adjei.
I was delighted to meet Ombeline de La Rochefoucauld that was always bringing happiness during the long experimental shifts and provided helpful comments and suggestions during all my PhD.
I would also like to thank Alessia Cedola that provided me with the financial means to complete this project, and the Tomalab group in Rome that have always supported me through every challenge.
Last but not the least I would also like to thank Eduardo Oliva Gonzalo and Manuel Cotelo Ferreiro of Universidad Politécnica de Madrid for the patience they had with my terrible programming skills.
I also express my deepest gratitude to my family and friends for their unfailing support and continuous encouragement.

Chapter 1

Introduction

Neurodegeneration is a process by which a progressive loss of neuronal structure and function occurs in many central nervous system (CNS) pathologies and it is generally associated with neuroinflammation. Neurodegenerative diseases are presently incurable and current therapies have minimal or no significant effect in reversing the CNS damage. New efforts are necessary for the comprehension of disease mechanisms and monitoring of therapeutic approaches. In particular, the research in neurodegenerative diseases requires tools enabling the visualization of disease-relevant networks, such as the vascular and neuronal networks.
The techniques currently used to investigate tissue damage at cellular level suffer from several limitations. In particular, 2D imaging (immuno-histochemistry and electron microscopy) present a limited spatial coverage, involves a destructive sample preparation and is only applicable at the ex vivo level. Although jumping from 2D to 3D represented an outstanding breakthrough in the general quality of imaging and information obtained, magnetic resonance imaging (MRI), positron emission tomography (PET), and X-ray computed tomography fail to provide a satisfactory answer to the current imaging needs. Thus, MRI and PET are limited in terms of spatial resolution, while X-ray computed tomography is a non-destructive, high-resolution technique that provides a tridimensional reconstruction of the object.
These severe limitations in 3D imaging can be overcome by the more advanced X-ray phase contrast tomography (XPCT), which provides much higher resolution and contrast at cellular level also in soft tissues. Many techniques have been implemented to perform XPCT like free-space propagation set-ups, coded aperture, Talbot and Talbot-Laue, and interferometry. The majority of phase contrast methods provide a qualitative analysis of the sample. The principal limitation concerning free-space phase contrast imaging is that is mainly qualitative, and it does not allow to separate the contribution of phase and absorption of the object. Losing this information prevents the calculation of the exact density of the material or retrieving its chemical composition. An imaging techniques that allows quantitative data analysis might be of great interest, we thus developed a new X-ray imaging system to overcome these limitations.

In this thesis, we implement a non-classical use of X-ray Hartmann wavefront sensor for phase imaging an alternative to X-ray phase-contrast imaging. This technique can in fact be implemented to characterize biological samples, to retrieve information about the components of the index of refraction and to infer the chemical properties and the density of a given material.
The Hartmann wavefront sensor can be used to retrieve quantitative information about the object density, in 2D or in 3D when combined with tomography. The system provides absorption, deflection and phase images with a single acquisition.

Such capacity of Hartmann-based X-ray phase imaging would open new opportunities in non-destructive testing.

In chapter 1, we analyzed how X-ray photons are produced and their connection with different atomic processes. We then introduced the main types of X-rays sources, such as X-ray tubes or synchrotron facilities.
The next section was focus on X-rays interaction with matter. We first considered a general description of the fundamental interaction mechanisms of X-rays, then we applied it to extract important parameters connected with X-ray propagation in the medium using an atomic physics description. Finally, to relate this analysis with imaging, we also consider a wave optic model.
In the last section, we reviewed the elements of the classical coherence theory since this parameter may possibly impact the performance of the wavefront sensor. Starting from the effects of spatial and temporal coherence, we considered the aspects of the theory of partial coherence that are related to the design of optical instruments.

In chapter 2, we introduced the main principles of X-ray phase-contrast and phase imaging. Respect to the classical absorption-based imaging, this group of techniques retrieves the phase changes introduced by the refraction of X-rays while propagating through an object. Then, an overview of the main X-ray phase-contrast imaging methods is provided.
A separate section is dedicated to free space propagation, where the image contrast is due to the interference between the beam diffracted by the object and the reference beam. Wave optic theory was used for a general description of free space propagation. In free space propagation the phase cannot be measured directly, it has to be recovered numerically with phase retrieval algorithms. The multiple distance and single distance (Paganin) phase retrieval algorithms are discussed.

In chapter 3, we introduced the main characteristics of X-ray tomography. In particular, from a mathematical point of view the reconstruction of tomographic data is connected with the Radon Transform that maps a function in the real space into the set of its linear integrals. A separate section is dedicated to the Backprojection algorithm that is used to obtain the volumetric reconstruction, both the parallel and cone beam geometries are described.
Finally, a brief explanation of iterative reconstruction methods for tomographic data sets is given.

In chapter 4, we defined the concept of wavefront using the Huygens-Fresnel principle and then the implementation of an Hartmann wavefront sensor for phase contrast images is described.
Basic data treatment to detect the incident wavefront are discussed, with particular attention given to centroiding methods.
The general design of the Hartman wavefront sensor was simulated thanks to the implementation of a 3D wave propagation model based on Fresnel propagator. The different components of the simulation tool, implemented in Python, are described and validated with standard experimental situations.
A separate modellization is reported to determine the Hartmann sensor accuracy.
The simulation tool previously described was used to investigate many parameters related with the Hartmann sensor design. In the first section features connected with the propagation process were considered: source energy, aperture shape, pitch and set-up distances. In the second section several parameters connected with the detection process have been analyzed : first, the capabilities of classical detection algorithms (First Moment, Weighted First moment, Gaussian Three-Point Fitting) will

be studied for a theoretical spot (gaussian shape). To improve the detection performance, more advanced algorithms (Iterative Gaussian Weighted and 2D Gaussian Fit) were also described.
Later, the results of these two sections were combined together to analyze the outcome of several detection algorithms to a propagated spot (Bessel and Sinc functions). Finally, the same analysis will be applied to a real experimental spot.

In chapter 5, experimental results with the X-ray Hartmann wavefront sensor are shown both for the laboratory set-up and for the synchrotron measurements.
Three different Hartmann plates were tested: a compact X-ray Hartmann wavefront sensor and two prototypes with larger field of view.
Results using laboratory sources on edge detection and propagation effects are presented for the compact X-ray Hartmann wavefront sensor. These experimental results were the first examples of the advantages of deflection and, consequently, phase image to improve the quantitative separation between different materials.
Images acquired with the second Hartmann wavefront sensor prototype with a larger field of view are then presented. The results from tomographic scans of biological samples (mouse brain and rat spine) showed the capabilities of the Hartmann wavefront sensor to perform biomedical imaging.

In chapter 6 the compact Hartmann sensor was used with synchrotron light to differentiate the chemical composition and the density of test objects composed of known material. A direct and independent measurements of the real part (δ proportional to the phase) and the imaginary part (β proportional to the absorption) of the sample refractive index (n) is shown. The comparison of the trend of δ and β respect to the incident energy with the tabulated curves can give information on the chemical composition of unknown material. The same samples were analyzed with polychromatic and monochromatic beams.

In chapter 7, we focused on the capabilities of X-ray phase-contrast imaging for the investigation of the effects of neurodegenerative diseases on the central nervous system. The X-ray phase-contrast tomography images were obtained with the free space propagation technique with synchrotron light .
The results from two experiments are presented: the first one was carried out on mouse brain samples affected by an animal model of Alzheimer and the second one was performed on mouse spinal cord samples affected by an animal model of Amyotrophic Lateral Sclerosis.
For the brain samples affected by Alzheimer, a quantitative analysis was performed on brain fibers and on the volume of plaques deposits both in the brain cortex and hippocampus.
For the study of mouse spinal cord affected by Amyotrophic Lateral sclerosis, we quantified a specific kind of neurons, called motor neurons and also the alterations in the vasculature architecture.

Chapter 2

Fundamentals of X-ray imaging

X-rays have been used for imaging, especially for medical diagnostics, since their interactions with matter are so small that internal structures can be observed in a non-destructive way. In this chapter we will concentrate on a general description of X-ray imaging, with particular interest on biological tissues imaging.

2.1 X-rays

X-rays have been discovered by the German physicist Wilhelm Conrad Roentgen in 1895 who received the Nobel Prize for Physics in 1901. He was experimenting with a new apparatus composed by a partially evacuated cathode ray tube with a fluorescent screen placed some distance away.
The glass tubing housed a negatively charged cathode, a heated filament, which spewed electrons toward the anode, a positively charged metallic target.
Upon contact with the anode, electrons were rapidly decelerated, transferring a proportion of their kinetic energy into an electromagnetic radiation that were called X-rays (X for unknown).
This radiation, called *Bremsstrahlung* radiation, has an energy range of $0 < E < E_{electron}$, where $E_{electron}$ is the kinetic energy of the electrons (Michette and Pfauntsch, 1996).
The discovery marked a milestone in scientific progress and found its first relevance in the field of medicine.
The many applications of X-rays immediately generated enormous interest, allowing the development of a multitude of different techniques, not only in medicine but also in biology, material science, industry and cultural heritage.
The X-ray regime includes photons of higher energy than visible and ultraviolet light, but lower than gamma rays. Their wavelengths are comparable with the atomic radius and are thus typically measured in Angstroms, $\dot{A} = 10^{-10}m$ (fig.2.1).
Since X-rays span a very wide range of wavelengths, it is often simpler to differentiate them in terms of their energies, which range from about 100 electron volts (eV) at the low end, to an upper limit of several hundreds of keV.
X-rays with high photon energies above 5–10 keV (below 0.2–0.1 nm wavelength) are called hard X-rays, while those with lower energy (and longer wavelength) are called soft X-rays.
The wavelength λ is related to the energy E, measured in eV, by the equation:

$$E = \frac{hc}{1.602 \cdot 10^{-19}\lambda} \tag{2.1}$$

where h =6.626 x 10^{-34} m^2 kg/s is the Planck constant, and c = 3 x 10^8 m/s is the speed of light in vacuum.

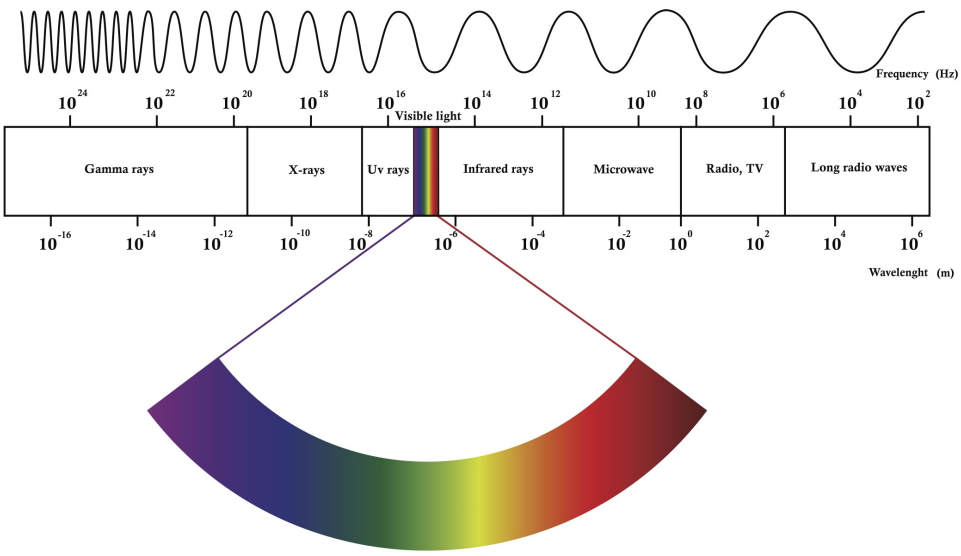

FIGURE 2.1: X-rays are part of the electromagnetic spectrum, with wavelengths shorter than UV light. Their wavelengths are comparable to the atomic radius and are thus typically measured in Angstroms ($\dot{A}$).

2.1.1 Production of X-rays

X-ray photons are produced by high-speed electrons interacting with matter and thus connected with different atomic processes.
The first case we will investigate is the bremsstrahlung radiation.
In general, bremsstrahlung refers to any production of electromagnetic radiation connected with the deceleration of a charged particle. It occurs when electrons enter the anode and start interacting with atoms. The electric field of each atom modify the electrons trajectory and thus decelerate them.
The total intensity of the bremsstrahlung radiation, resulting from an electron of mass m, electric charge e, incident on a target nucleus of charge Ze, is proportional to:

$$I \propto \frac{Z^2 e^2}{m^2} \tag{2.2}$$

It follows immediately from eq.2.2 that the production of bremsstrahlung radiation is the more effective the higher is the atomic number Z of the target.
Also, the anode normally is a metal plate with high atomic number and high melting point (e.g. tungsten, molybdenum, copper), and is the source of X-rays.
In addition to bremsstrahlung radiation, which describes a continuous spread of photon energies up to the maximum electron energy, X-rays are also generated through characteristic emission lines. In this case, an incident electron interacts with, and causes the ejection of, one of an atom's inner shell electrons.
The atom will be in a highly excited state, due to the lack of one of its electrons with highly negative binding energy; an outer shell electron will tend to fill the hole in the inner shell and a characteristic radiation is emitted.
From the nucleus moving outwards, the orbitals are labelled as K, L, M, N (etc.) shells, with specific quantized energy levels.
Therefore, the energy of the characteristic X-ray is equal to the difference between

the binding energies of the two shells involved. Each element in the periodic table has its own unique binding energies for each shell, so the energies of characteristic X-rays are different for each atom.

2.1.2 X-rays sources

In the following, we will look at some of the X-rays sources that have found wide applications in various fields, such as X-ray tubes or Synchrotron facilities. In an X-ray tube the target (anode) is kept very close (typically 1-3 cm) to the source of electrons (cathode). A high electric potential between cathode and anode accelerates the electrons to high velocities (Ahmed, 2015). The maximum kinetic energy in electron volts attained by these electrons is equal to the electric potential (in volts) applied between the two electrodes (fig.2.2).
For example, an X-ray machine working at a potential of 30 kV can accelerate electrons up to a kinetic energy of 30 keV. X-ray machines are poorly efficient in the sense that 99% of their energy is converted into heat and only 1% is used to generate X-rays. This results in the production of two types of X-rays: Bremsstrahlung and characteristic X-ray lines (already described in section 2.1).

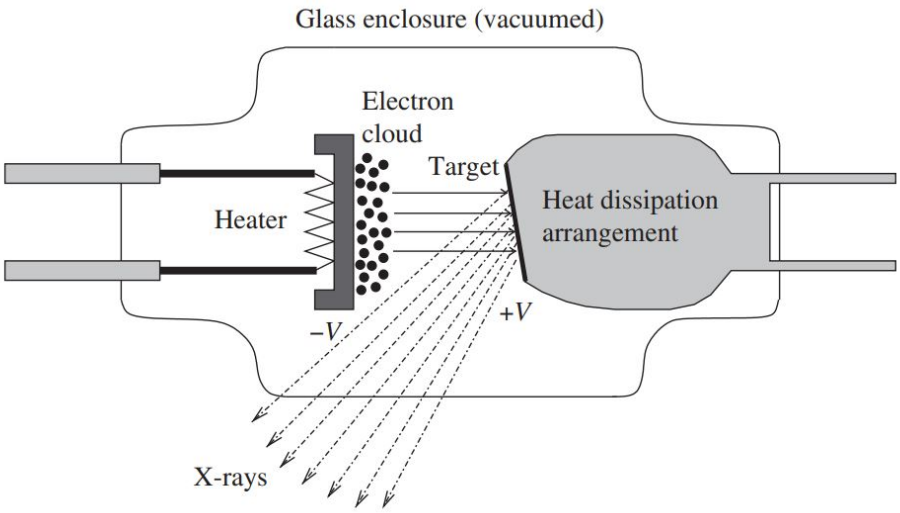

FIGURE 2.2: Sketch of a typical X-ray tube. Image from (Ahmed, 2015).

X-ray tubes are not the only means of producing X-rays. In high-energy particle physics facilities, where particles are accelerated in curved paths at relativistic velocities using magnetic fields, highly intense beams of photons, called synchrotron radiation, are produced. The production of radiation in these facilities, can be distinguished from X-ray tubes by noting that Bremsstrahlung is a product of tangential acceleration, while synchrotron radiation is produced by centripetal acceleration of charged particles. The spectrum of synchrotron radiation is continuous and extends over a broad energy range, from infrared to hard X-rays. The X-rays produced as synchrotron radiation are extremely intense, highly collimated, and polarized in contrast to conventional X-rays, which have very low intensities, very difficult to collimate and completely unpolarized.

However, the production of synchrotron radiation needs dedicated facilities, developed around the world, where beam time is made available to researchers. A synchrotron machine consists of a combination of different structures. As shown in fig.2.3, the principal ones are storage ring, Linac (linear accelerator), booster and beamlines. Before being injected in the storage ring, the electrons that will produce synchrotron radiation are firstly accelerated in the Linac and then in the booster, up to the desired energy. Only at this point they enter into the storage ring, where they circulate for hours or days at a speed close to the one of light. The synchrotron radiation produced by the insertion devices, a periodic series of magnets, is collected by the beamlines, constructed tangentially to the storage ring.

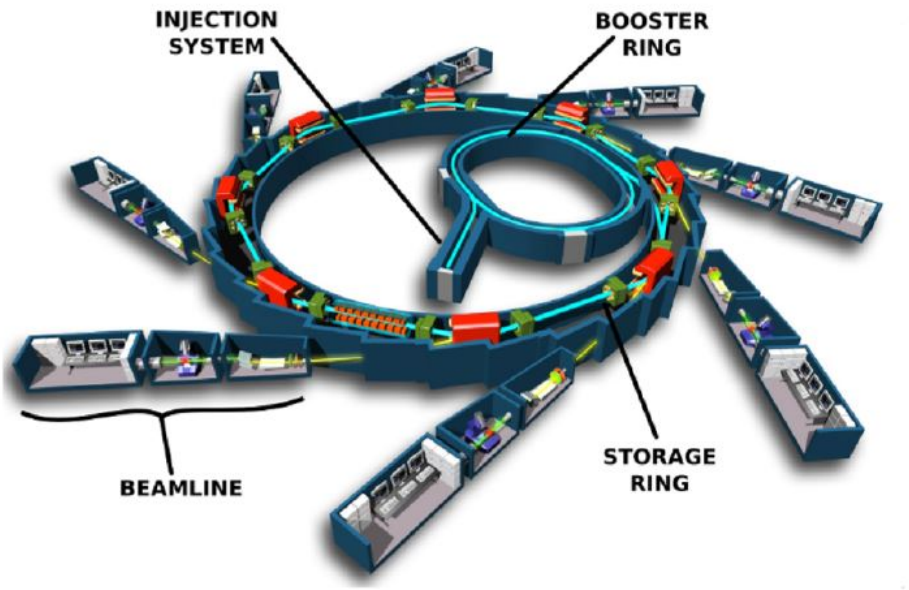

FIGURE 2.3: The principal structures of a synchrotron: injection system (Linac), booster ring, storage ring, beamlines. Image credit: "Schéma de principe du synchrotron.jpg", EPSIM 3D/JF Santarelli, Synchrotron Soleil.

X-rays can also be produced through Laser (Light Amplification by Stimulated Emission of Radiation) (Duguay and Rentzepis, 1967,Rohringer and London, 2009). This X-ray emission is generated by exploiting a quantum mechanical phenomenon called stimulated emission. Stimulated emission is an optical amplification process in which the photon population is increased by the interaction of the incident photons to interact with atoms or molecules in excited states. For simplicity, we will refer just to atoms while the physical processes are the same for ions and molecules. The initial photon is not destroyed in the process but if its energy is resonant with an atomic transition it forces the atom to emit a photon that is the twin of the incident photon (same phase, polarization, energy, direction). Laser always start with spontaneous emission that is a stochastic process. In general, amplification barely modify the stochasticity. Several solutions have been set to produce collimated, polarized and coherent beams, the most efficient being the used of cavity. Most X-ray mirrors have low reflectivity preventing the use of cavity. In that case, elongated amplification media (Benware et al., 1997) or injection of coherent external X-ray beam (Zeitoun

et al., 2004) allows the production of high quality laser beams. Lasers can be produced either as continuous waves or in the form of pulses by a variety of materials in different states.
Also, another kind of sources has been developed rapidly over the past 50 years, called Free-electron lasers (FELs). The radiation results from the interaction of an optical wave and a relativistic electron bunch, leading to an energy exchange between the light pulses and the relativistic electrons (Couprie et al., 2004, Yoneda et al., 2015, Emma et al., 2010, Schreiber et al., 2010). Like in synchrotrons, electrons are submitted to external magnetic fields that force them to oscillate and then to emit X-rays. For FEL, the period of oscillation is resonant with the wavelength of the emitted X-rays producing a strong monochromatic, low divergence emission comparable to a laser. FEL produces coherent electromagnetic laser waves with continuous tunability and short-pulse duration.

2.2 X-rays interaction with matter

We will now consider in details the X-rays interaction with matter. Since in the following we will focus on imaging techniques, it is crucial to understand the fundamental interaction mechanisms related with image formation. In this section we will first consider a general description, then in section 2.2.1 we will apply it to extract important parameters connected with X-ray propagation in the medium using an atomic physics description. . Finally, in section 2.2.2, to relate this analysis with imaging, we will consider the beam using a wave optic model.
When an X-rays beam passes through a medium, it undergoes attenuation. This attenuation can be connected to either absorption or scattering of photons by the medium. In absorption, the energy of the photon is completely transferred to the atoms, whereas in scattering, the X-ray beam undergoes a change in direction that may be accompanied by a change in its energy.
In the energy domain related to medical physics (30-150 keV) the main three mechanisms by which X-rays can interact with matter are: **Coherent (or Rayleigh) Scattering**, **Auger effect**, **Photoelectric Effect** and **Compton Scattering**. Which interaction process will dominate for the photons in the beam, depends on the photons' energy (E_γ) and on the type (atomic number, Z) of the attenuating material.

Coherent scattering refers to the elastic scattering of a photon beam with atomic electrons, in which no energy transfer to medium takes place.
The photon's electromagnetic field let the electrons in the medium oscillate, they will emit a photon with the same energy as the incident photon in order to come back to their original state. After the interaction, the angle between the incident photon and the scattered photon is small and the scattered photon has the same energy of the incident photon. The probability of coherent scattering is higher when the photon energy is very small and the medium atomic number Z is very large.

In the **photoelectric effect**, the incident photon interacts with an atom and ejects one of the bound electrons (from K, L, M, or N shells). All the photon energy is transfer to the atom in the medium. Some of the photon energy is used to overcome the binding energy of the electron, and the rest is converted into kinetic energy of the electron:

$$E_K = h\nu - E_b \tag{2.3}$$

where E_K is the kinetic energy of the electron, hv is the incident photon energy and E_b is the binding energy of the electron.
For the photoelectric effect to take place, the energy of the incident photon must be larger than the binding energy of the bound electron.
In the **Compton effect** a photon interacting with an electron from an outer shell will transfer some of its initial energy to the electron. The energy loss can be calculated by considering the conservation of both energy and momentum during the interaction.
As a result, the electron is ejected, and the photon is scattered with a reduced energy. Since only a small portion of the photon energy is absorbed, the energy absorbed is considerably less than the photoelectric effect.
In both absorption and scattering, the net result is the transfer of energy to the medium. Therefore, X-ray radiation is attenuated when it passes through a material. The attenuation can be expressed by the relationship for a monochromatic incident X-ray beam and a material of uniform density and atomic number:

$$I = I_0 e^{-\eta(\sigma_{ph}+\sigma_C+\sigma_R)} \tag{2.4}$$

where I and I_0 are the transmitted and the incident beam intensities, η is the thickness of the material multiplied by the linear attenuation coefficients of photoelectric effect (σ_{ph}), Compton effect (σ_C) and Rayleigh scattering (σ_R) of the material.
The coherent scattering is significant for very low-energy photons (<10 keV). The photoelectric interaction is most common at intermediate photon energies (about 25 keV) and the Compton effect dominates at higher energies (from 25 keV to 5 MeV).

2.2.1 X-ray interaction considering atomic processes

From Maxwell equations the expression for a wave that propagates in a dissipative medium is described by the following expression:

$$\Delta^2 E = \frac{\epsilon}{c^2}\frac{\partial^2 E}{\partial t^2} + \frac{4\pi\sigma}{c^2}\frac{\partial E}{\partial t} \tag{2.5}$$

Considering only one frequency ω, a solution is the following electric field (Attwood, 1999):

$$E = E_0 e^{(i(k\cdot r-\omega t))} \tag{2.6}$$

where the propagation constant k is equal to:

$$k = \frac{\omega}{c}(\epsilon + \frac{i4\pi\sigma}{\omega})^{\frac{1}{2}} \tag{2.7}$$

If the propagation happens in vacuum, the expression for k is simplified:

$$k = \frac{\omega}{c} \tag{2.8}$$

and satisfies the following dispersion relation inside the medium and is used to introduce the index of refraction:

$$k = \frac{\omega^2 n^2}{c^2} \tag{2.9}$$

Each material can be described through its refraction index, for X-rays is defined as the ratio between the speed of the light in vacuum and its speed in the medium:

$$n(\omega) = 1 - \delta(\omega) + i\beta(\omega) \tag{2.10}$$

The refraction index defined in eq.2.10, can be rewritten in the X-ray region as:

$$n(\omega) = 1 - \frac{n_a r_e \lambda^2}{2\pi}(f_1^0(\omega) + if_2^0(\omega)) \tag{2.11}$$

where f_1^0 and f_2^0 are the real and imaginary part of the total linear scattering factor $f^0 = (f_1^0(\omega) + if_2^0(\omega))$. The wavelength in vacuum is defined by λ, n_a is the atomic density and r_e is the classical electron radius. The real and imaginary parts of the total linear scattering factor f^0 can be expressed as:

$$\begin{aligned} f_1^0(\omega) &= \sum_s g_s \frac{\omega(\omega^2 - \omega_s^2)}{(\omega^2 - \omega_s^2)^2 + \gamma^2\omega^2} \\ f_2^0(\omega) &= \sum_s g_s \frac{\gamma\omega^2}{(\omega^2 - \omega_s^2)^2 + \gamma^2\omega^2} \end{aligned} \tag{2.12}$$

where ω_s is the atomic resonance frequency of the electrons, γ is a dissipative term and g_s are the oscillator strengths, such that the sum of the oscillator strengths is equal to the atomic number Z. The two optical constants, $f_1^0(\omega)$ and $f_2^0(\omega)$, describe the phase shifts and the absorption of X-rays inside a medium.
For $\omega >> \omega_s$, f_1^0 and f_2^0 tend asymptotically to:

$$\begin{aligned} f_1^0 &\to Z \\ f_2^0 &\to 0 \end{aligned} \tag{2.13}$$

where Z is the atomic number.
Considering eq.2.11, δ and β can be rewritten as:

$$\begin{aligned} \delta &= \frac{n_a r_e \lambda^2}{2\pi} f_1^0(\omega) \\ \beta &= \frac{n_a r_e \lambda^2}{2\pi} f_2^0(\omega) \end{aligned} \tag{2.14}$$

From eqs.2.14, δ and β are proportional to the real and imaginary parts of of the total scattering factor.

We can now concentrate on how δ and β are related to the propagation of X-rays inside a medium.
To answer this question let us consider a monochromatic plane wave of the form:

$$E(r,t) = E_0 e^{i(\omega t - \mathbf{k}\cdot\mathbf{r})} \tag{2.15}$$

where $\mathbf{k}$ and $\mathbf{r}$ are vectors with the same direction so that $\mathbf{k}\cdot\mathbf{r} = kr$. And we assume the dispersion relation:

$$E(r,t) = E_0 e^{i(\omega t - k_0 r)} e^{i(k_0 \delta r)} e^{i(-k_0 \beta r)} \tag{2.16}$$

where $k_0 = \frac{\omega}{c}$ is the wave vector in vacuum. We can distinguish three terms in equation 2.16:

- The first term represents the wave propagating in vacuum,
- The second term, which contains δ, describes the phase shift due to the interaction between the radiation and the medium.
  The phase shift $\Delta\phi(x,y)$ between a wave passing through an object of a given thickness η and the same wave free-propagating in vacuum can be written as:

$$\Delta\phi(x,y) = -\frac{2\pi}{\lambda}\int_0^{\eta}\delta(x,y,z)dz \tag{2.17}$$

  where z is the propagation direction over the object.
- The third term represents the decay of the wave amplitude in the medium due to photo-absorption and Compton effect.
  The decrease in amplitude can be expressed through the parameter:

$$\mu_z(x,y) = \frac{1}{2}\int \mu(x,y,z)dz = \frac{2\pi}{\lambda}\int \beta(x,y,z)dz \tag{2.18}$$

where μ_z is the attenuation coefficient, a constant that describes the fraction of attenuated incident photons in a mono-energetic beam per unit thickness of a material for an homogeneous object::

$$\mu = \frac{4\pi\beta}{\lambda} \tag{2.19}$$

The interaction of an electromagnetic wave with matter affects both the wave amplitude and phase. A visual representation is shown in fig.2.4, where two monochromatic plane waves travelling in the vacuum (upper image) and in a material with refractive index $n < 1$ (lower image) are compared. After the interaction with matter, the latter is longitudinally shifted (phase shift, $\Delta\phi$) and its amplitude decreases (attenuation). Considering again eq.2.14, for low Z elements and high energies, $f_1^0(\omega)$ is constant and $f_2^0(\omega)$ tends to $\frac{1}{E^2}$. For this reason, in the hard X-ray region (E $\geq$ 10 keV), δ is several orders of magnitude larger than the imaginary part of the refraction index β. Thus, when considering biological samples at high energy (hard X-rays), phase imaging will be predominant over amplitude imaging.

Since in the following sections we will image brain tissue of small animals, we study the trend of δ and β respect to the incident energy for this particular sample. For the chemical composition and density of the brain tissue we used here the data published in (ICRU Report 44, Griffiths, 1989) that is available on the National Institute of Standards and Technology (NIST) website (Hubbell and Seltzer, 2004). We used the Center for X-ray Optics website for calculating δ and β.
In fig.2.5 we can see the plot of δ and β respect to the incident energy for brain tissue. In the hard X-ray region (yellow inset) the contribution of δ is $10^3 - 10^4$ times larger than β. Phase imaging of the biological tissue in this energy range will provide higher accuracy respect to absorption imaging.

2.2.2 The Transmission Function

This section will focus on propagation related problems using wave optics theory. The first step to solve the interaction problem is to calculate the field emerging from the object just downstream of the object plane.
Since finding the exact solution for this problem is not always straightforward, some approximations will be presented in the text.

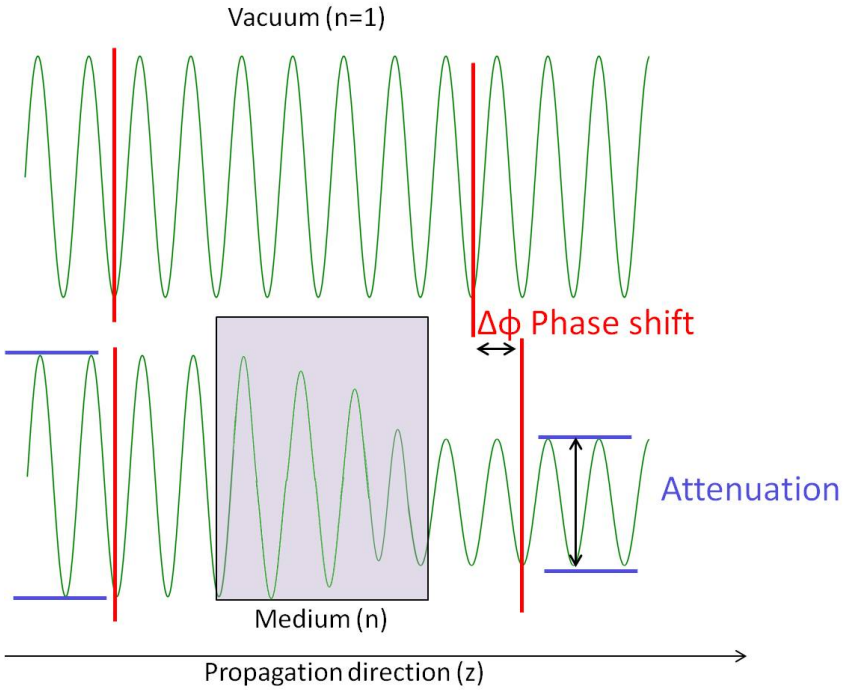

FIGURE 2.4: Schematic representation of the interaction of a wave with a medium: amplitude and phase are modified respect to the incident wave.

The transmission function defines how the wave is modified by the interaction with the object. Let us start from the following linear relation (Born and Wolf, 1980):

$$E_0(x,y) = T(x,y)E_{incident}(x,y) \tag{2.20}$$

The transmission function T(x,y) is defined as the ratio between the emerging field after the object $E_0(x,y)$ and the incident field $E_{incident}(x,y)$. In principle the transmission function should depend on both the sample and the incident wavelength. In practice, T(x,y) is often estimated a priori and considered a function depending exclusively on the object. The dependence of T(x,y) from the incident field can be ignored under the projection approximation or thin objects approximation. In this approximation the object is considered optically thin so that the beam does not significantly change along the whole thickness of the sample. Also, the scattering effects inside the object can be neglected. We use the Born approximation ignoring multiple scattering events. This second condition is satisfied when considering biological samples imaged in the hard X-ray region. The object is assumed to be sufficiently thin so that we can neglect any deviation from the straight line propagation through the sample.
Since in the X-ray region the real part of the complex refraction index n (see eq.2.10) is always smaller than 1, the shifts within the matter respect to the incident direction of the X-rays are negligible. The equation that describes an electric field inside a material is :

$$\left(\frac{n^2}{c^2}\frac{\partial^2}{\partial t^2} - \Delta^2\right)E(x,y,z,t) = 0 \tag{2.21}$$

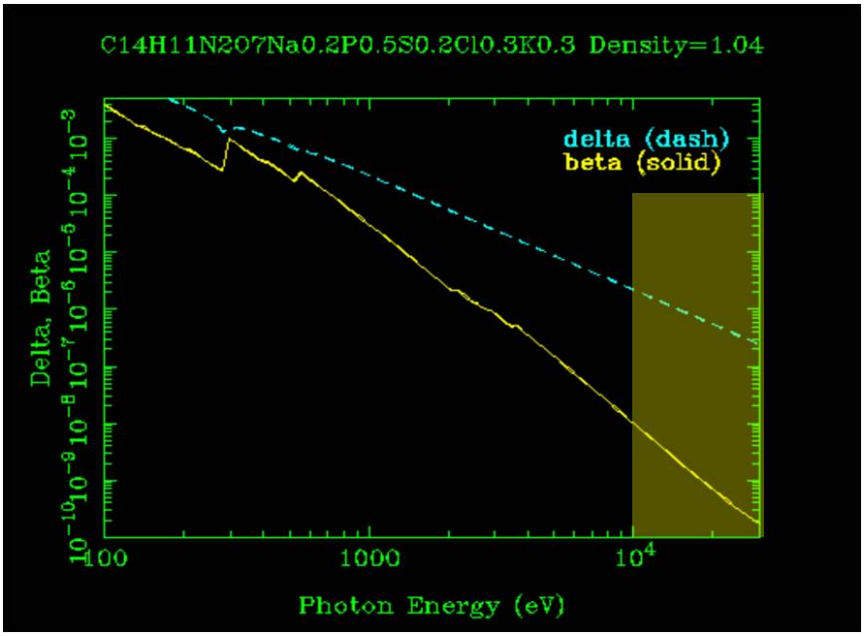

FIGURE 2.5: Plot of δ and β respect to the incident energy for brain tissue. The chemical composition and density of the tissue were obtained by the ICRU Report 44 (Griffiths, 1989). The yellow inset is in the hard X-rays region, where the contribution of δ is is several orders of magnitude larger than β.

The solution of eq.2.21 satisfies the Helmholtz equation :

$$(\Delta^2 + k^2 n^2) E_\omega(x, y, z) = 0 \tag{2.22}$$

and in the paraxial approximation can be written as:

$$E_\omega(x, y, z) = E_0(x, y, z) e^{ikz} \tag{2.23}$$

where z represents the wave propagation direction, $k = 2\pi/\lambda$ and $E_0(x, y, z)$ is the electric field at z=0. Substituting eq.2.23 into the Helmholtz equation (eq.2.22) we obtain:

$$\Delta_\perp E_0 + 2ik \frac{\partial E_0}{\partial z} + (n^2 - 1) k^2 E_0 = 0 \tag{2.24}$$

where the second derivative where neglected since the amplitude is weakly variable in the propagation direction and $\Delta_\perp$ is the Laplacian in the (x,y) plane.
Eq.2.24 can be solved applying the thin object approximation, mentioned above, which states that every element inside the specimen interacts only with the incident wave and not with the scattered one. In this approximation the effect of the transverse Laplacian (in x and y) will be much smaller than the axial derivative (in z), so we can rewrite eq. 2.24 as:

$$2ik \frac{\partial E_0}{\partial z} + (n^2 - 1) k^2 E_0 = 0 \tag{2.25}$$

whose solution corresponds to the linear relation that describes the transmission function T(x,y) (eq.2.20). The transmission function is described by (Thibault, 2007):

$$T(x,y) = exp(ik \int \frac{n^2-1}{2} dz) \tag{2.26}$$

with the integral evaluated simply along the optical axis z. Concentrating on the term $\frac{n^2-1}{2}$ and using eq.2.10 for n, we can neglect the second-order terms, since δ and β are extremely small in the hard X-rays range (fig.2.5).
We can rewrite the transmission function as:

$$T(x,y) = exp[-k \int \beta(x,y,z)dz - ik \int \delta(x,y,z)dz] \tag{2.27}$$

Combining eq.2.27 with the expressions given before for $\phi(x,y)$ (eq.2.17) and μ_z (eq.2.18), the transmission function can be rewritten in a new form:

$$T(x,y) = e^{-\mu_z(x,y)} e^{i\phi(x,y)} \tag{2.28}$$

In eq.2.28 we find again a similar expression for the transmission function, already shown in eq.2.16. If the interactions (absorption and phase shift imparted by the object) are assumed to be sufficiently weak, the terms $\mu_z(x,y)$ and $\phi(x,y)$ in eq.2.28 can be considered smaller than 1, we can use the Taylor series expansion up to the first order for the expression of T(x,y) :

$$T(x,y) \approx 1 - \mu_z(x,y) + i\phi(x,y) \tag{2.29}$$

In order to the verify the weak object approximation assumed in eq.2.29, the lateral displacement of the rays inside the object has to be small compared to the spatial resolution r:

$$\sqrt{2\delta}\eta < r \tag{2.30}$$

where $\sqrt{2\delta}$ is the maximum angular deviation for total external deflection and η is the object thickness.

2.2.3 Impact of Absorption on X-ray Imaging

In classical X-ray imaging, the image formation is usually due to the attenuation of the beam passing through the matter, where the contrast is given by absorption and scattering processes. The intensity of the beam, defined as the energy transported by the radiation per unit area and per unit of time, decreases with an exponential law known as the Bouger-Lambert-Beer attenuation law (Sólyom, 2010):

$$I = I_{incident} e^{-\mu\eta} \tag{2.31}$$

where I is the field intensity after the object and $I_{incident}$ is the incident field intensities, η is the material thickness, and μ is the linear absorption coefficient.
According to equation 2.31, the intensity decreases with increasing propagation distance within homogeneous matter and proportionally to the attenuation coefficient of the material. Thus the X-ray beam will be more attenuated as the energy decreases and the thickness η increases. The coefficient μ (eq.2.18) is proportional to the photon energy, to the chemical composition and to material density. From eq.2.18 we can say that if the object is homogeneous μ is constant. To better understand the mechanisms underneath the absorption process, we consider again the expression

given for β in eq.2.14.
The attenuation of the beam for a given energy increases with the electron density of the material and with the atomic number of its constituting elements. The image contrast increases when a great difference in the atomic numbers of two materials occurs. Absorption contrast is in fact ideal for medical imaging of high-density bone surrounded by low density tissues, such as muscle and skin.
For an inhomogeneous object, eq.2.31 will be modified considering the attenuation coefficient $\mu(x,y)$ as a function of x and y, and the intensity has to be calculated with a line integral along the beam direction r:

$$I = I_{incident} e^{-\int \mu(x,y) d\eta} \tag{2.32}$$

To reconstruct the attenuation coefficient values, the measured intensity data (I) have to be first linearized.
The attenuation coefficient A_0 is defined by:

$$A_0 = -ln\left(\frac{I}{I_{incident}}\right) = \int \mu(x,y) d\eta \tag{2.33}$$

Therefore, absorption imaging provides a 2D map of $\mu(x,y)$, while the information about the phase is lost. Figure 2.6, sums up how the incident beam attenuation depends on the properties of the material (atomic number and the mass density), the object thickness and the radiation wavelength. To retrieve the other parameters

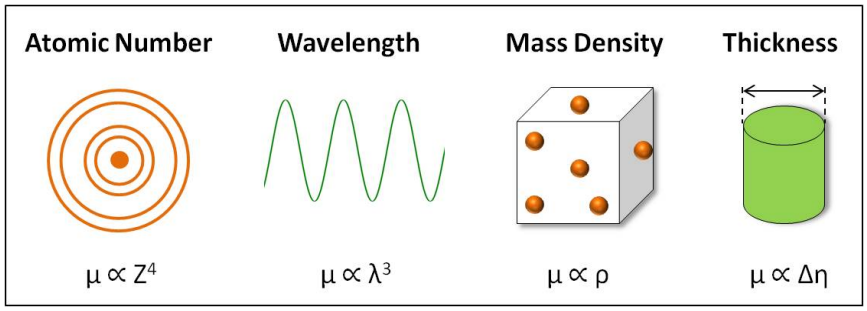

FIGURE 2.6: The absorption coefficient is a function of the atomic number Z, of the wavelength λ, density mass ρ and object thickness $\Delta\eta$.

, we can write the total linear attenuation coefficient μ as:

$$\mu = \frac{\rho}{N_A A}\sigma_a \tag{2.34}$$

where σ_a denotes the total attenuation cross section of a single atom (indexed with a), ρ is the mass density, N_A is Avogadro's constant, and A is the atomic mass number. Databases typically contain the mass attenuation coefficient μ/ρ.
At photon energies E where photoelectric absorption is the dominant interaction process (up to about 25 keV), it is possible to substitute σ_a with the total photoelectric cross-section, which can be approximate as:

$$\sigma_a \propto \frac{Z^n}{E^3} \tag{2.35}$$

with $n \approx 4.5$ for light elements and $n \approx 4$ for heavy elements.
The linear attenuation coefficient, therefore, varies approximately as:

$$\mu \propto \rho \frac{Z^{n-1}}{E^3} \tag{2.36}$$

2.3 Propagation in Vacuum

In the previous section (section 2.2.3) to calculate the solution of the interaction problem, we calculated the field E_0 emerging from the object, once the incident field E_i and the object properties are known. After the interaction with the sample, the wavefront undergoes further modifications during the propagation in free space. We will describe the propagation of the field by calculating the expression of the field E_z at any finite distance z from the object. Diffraction arises when a wave encounters an obstacle in its path and its associated with the deviation of the wave from its previous propagation trajectory. Diffraction effects are described by the Huygens-Fresnel principle, which states that the wave propagation can be predicted by assuming that each point of a wavefront acts as the source of a spherical secondary wavelet with the same frequency as the primary wave. These secondary waves will define the new wavefront after propagation.

Let us translate Huygens-Fresnel principle in a precise mathematical form known as Fresnel-Kirchhoff formula. Let consider a single plane wave of the following form:

$$E(x,y) = E_0(x,y)e^{-i(k_x x + k_y y)} \tag{2.37}$$

at the plane z= 0 (where the object is located). Considering the propagation of the wave from z=0 to $z = D$ a factor $e^{-ik_z D}$ will be added.
Thus, the expression of the field E_D at a distance D will be:

$$E_D(x,y) = E_0(x,y)e^{-i(k_x x + k_y y)}e^{-ik_z D} \tag{2.38}$$

The plane wave E_0 can be decomposed through a Fourier expansion and thanks to the linearity of this decomposition, we can propagate independently each term of the expansion. Following this procedure, the field at $z = D$ can be expressed as the convolution between the field E_0 at z=0 and a propagator P_D:

$$E_D(r) = \iint_\infty d\bar{r} E_0(\bar{r}) \iint_\infty e^{-2\pi i[f(r-\bar{r})]}e^{-k_z D} df = \iint_\infty E_0(\bar{r})P_D(r-\bar{r})d\bar{r} \tag{2.39}$$

where $r = (x,y)$ represents the coordinates on the image plane (plane after propagation) and $\bar{r} = (\bar{x},\bar{y})$ the one on the object plane, $f = (p,q)$ with p and q spatial frequencies:

$$\begin{aligned} p &= \frac{k_x}{2\pi} \\ q &= \frac{k_y}{2\pi} \end{aligned} \tag{2.40}$$

and the propagator $P_D(r)$ is:

$$P_D(r) = \iint_\infty e^{2\pi i[f(r-\bar{r})]}e^{-ik_z D} \tag{2.41}$$

The equation 2.39 can be rewritten in a more concise way as:

$$E_D(r) = E_0(r) \otimes P_D(r) \tag{2.42}$$

where the symbol $\otimes$ indicates the convolution operation. The field in $z = D$ can be calculated as the convolution between the field E_0 just after the object and the propagator P_D. This equation can be used to determine the field at any distance D from the object interacting with the beam. The calculation of diffracted fields, starting from the expansion in plane waves, generally implies the resolution of integrals whose result cannot be expressed in a closed form. This means that the solution to the eq.2.39 does not give an exact result with a finite amount of data. To solve this issue, sufficiently accurate results can be obtained by introducing some approximations in the diffraction integrals. Among these, the Fresnel and Fraunhofer approximations will be discussed.

2.3.1 Fresnel Approximation

The Fresnel approximation is valid when the field E_0 is assumed to be equal to zero outside of a small region centered in the axis origin, with linear dimensions small with respect to z. Also E_D will be calculated in a region around the position (0,0,z) with linear dimensions small with respect to z. We use the Rayleigh-Sommerfield expression (Gori, 1997) to define the field E_D :

$$E_D(r) = \frac{i}{\lambda} \iint_{\infty} E_0(\bar{r}) \frac{e^{-ikd}}{d} cos(\theta) d\bar{r} \tag{2.43}$$

where

$$\begin{aligned} d &= \sqrt{D^2 + (r - \bar{r})^2} \\ cos(\theta) &= \frac{D}{d} \end{aligned} \tag{2.44}$$

where $r = (x, y, z)$ are the coordinate in the image plane and $\bar{r} = (\epsilon, \eta)$ are the coordinate in the origin plane. The wave field U(x,y) is calculated from the diffraction of a complex aperture placed in the (ϵ,η) plane that is illuminated by the field U(ϵ, η) in the positive z direction (fig. 5.10). Then, in this approximation it is possible to consider:

$$\begin{aligned} cos(\theta) &\approx 1 \\ \frac{1}{d} &\approx \frac{1}{D} \end{aligned} \tag{2.45}$$

An approximated form to the term d that appears in the exponential can be given. However, since this is an oscillating function, the approximation is needed in order to neglect, in the kd argument, only the terms that give a small contribution compared to 2π. We can write d in the form:

$$d = z\left[1 + \frac{(x - \epsilon)^2 + (y - \eta)^2}{z^2}\right]^{1/2} \tag{2.46}$$

and we can approximate d at the first order as:

$$d \approx z + \frac{(x - \epsilon)^2 + (y - \eta)^2}{2z} \tag{2.47}$$

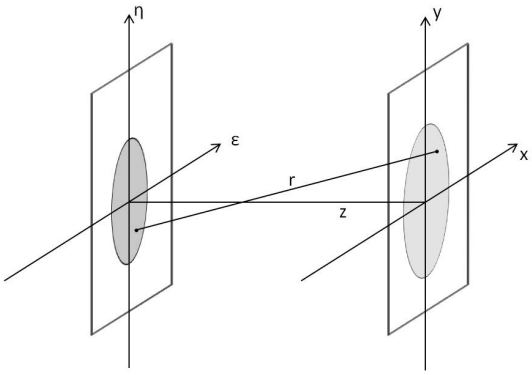

FIGURE 2.7: Schematic representation of the coordinates system: the wave field is defined in the (ϵ,η) plane and propagated until the second plane (x,y). The propagation direction z is orthogonal to both planes.

neglecting the terms from the second order eq.2.43 becomes:

$$E(x,y,z) = \frac{ie^{-ikD}}{\lambda z}\iint_{\infty} E_0(\epsilon,\eta)e^{-ik\frac{((x-\epsilon)^2+(y-\eta)^2)}{2z}}cos\theta d\epsilon d\eta \tag{2.48}$$

which represents the diffraction produced by an object in the Fresnel approximation at z. The integral is extended to the entire plane (ϵ,η) and transverse limitations are taken into account through E_0. Comparing eq.2.48 and eq.2.39, we can write the expression for the Fresnel propagator at a distance $z = D$ in the Fresnel approximation:

$$P_D(x,y) = \frac{i}{\lambda z}e^{-(\frac{i\pi(x-\epsilon)^2+(y-\eta)^2}{\lambda D})} \tag{2.49}$$

Eq.2.49 shows that the propagator P_D acts linearly on the field E_0, so that the propagation process has the same effect as a linear filtering.
Due to this feature, the most natural treatment of the propagation is obtained in the Fourier space. In mathematics the convolution (eq.3.8) corresponds in reciprocal space to a simple multiplication, thus the field E_D measured at $z = D$ can be written in reciprocal space as:

$$\tilde{E}_D(f) = \tilde{E}_0(f)\tilde{P}_D(f) \tag{2.50}$$

where **f** is the spatial frequency conjugated to **r**, and the tilde indicates the Fourier transform.
From eq.2.49 we can rewrite the transfer function in the Fresnel approximation as:

$$\tilde{P}_D(f) = e^{(i\pi\lambda Df^2)} \tag{2.51}$$

Experimentally the intensity of the field E_D is measured as the square module of the field amplitude:

$$I_D(r) = |E_D(r)|^2 \tag{2.52}$$

2.3.2 Fraunhofer Approximation

We want to derive the expression of the diffracted field in the limit of far-field or Fraunhofer approximation. Considering again the expression given before for the propagated field E (eq.2.48), it can be observed that when z tends to infinite, the

terms ϵ and η give a negligible contribution to the argument of the exponential function with respect to 2π .
Under this condition, ϵ and η are omitted and the diffraction integral takes the form (Goodman, 2005):

$$E(x,y,z) = \frac{ie^{-i[kz+\frac{k}{2z}(x^2+y^2)]}}{\lambda z} \iint_{\infty} E_0(\epsilon,\eta) e^{i2\pi\frac{\epsilon x+y\eta}{\lambda}} d\epsilon d\eta \tag{2.53}$$

which is the expression of the diffraction in the far-field limit. The analytic form is now particularly simple because the integral in eq.2.53 is the Fourier transform of E_0 calculated in $\frac{x}{\lambda z}$ and $\frac{y}{\lambda z}$. The condition that ensures the validity of Fraunhofer approximation is:

$$z \gg \frac{\epsilon^2+\eta^2}{2\lambda} \tag{2.54}$$

From this condition the distance of transition between Fresnel and Fraunhofer diffraction regions can be estimated. Assuming that the element generating diffraction is contained within a circle of radius a, the distance at which we are no longer in Fresnel but in Fraunhofer regime is equal to:

$$z \gg \frac{a^2}{2\lambda} \tag{2.55}$$

In practice, already for distances not far from the second term of 2.55, the diffracted field can be described by Fraunhofer approximation. Conventionally, the critical distance of transition is assumed to be:

$$z_c = \frac{\pi a^2}{\lambda} \tag{2.56}$$

The order of magnitude of this distance will be taken in the following to define and distinguish the different regions of formation of the image.

2.3.3 Region of image formation

In this section we will summarize what we saw in sections 2.3.1 and 2.3.2, and define some parameters to distinguish each propagation regime. To define the near and far field approximations, the Fresnel number N_f is used:

$$N_f = \frac{a^2}{\lambda z} \tag{2.57}$$

Different diffraction regimes can be defined as a function of the propagation distance (z) from an aperture (a) at a given wavelength (λ). The condition for the near field regime is satisfied for $N_f >> 1$, while the Fresnel approximation is valid for $N_f \approx 1$ and the Fraunhofer regime applies for $N_f << 1$.

In the near-field regime, the recorded image of the sample is still close to the real image but, at the same time, high contrast is given by sharp changes in the refraction index, e.g. at borders.
In the Fresnel regime, due to the propagation effect, the image of the real sample is almost lost, and the recorded image becomes an interference pattern. This is the region in which we place the sample to perform phase contrast imaging.

In the Fraunhofer regime, the diffracted image losses resemblance with the object. Indeed, in the Fraunhofer region, the image field has the form of the Fourier transform of the field after the object.

2.4 Elements of coherence theory

It is possible to do imaging with different kind of X-ray sources and, as it will be shown later on section 5.6, the coherence degree of the light has a big impact on the image formation process. In particular, the degree of coherence becomes a crucial parameter when using a wavefront sensor.
In this section, we review the elements of the classical coherence theory. The effects of spatial and temporal coherence will be considered separately and we will consider the aspects of the theory of partial coherence that are related to the design of optical instruments.
Coherence is commonly defined as the ability of a field to form interference fringes (Reynolds et al., 1989). Real sources are neither fully coherent nor fully incoherent, but rather are partially coherent. The development of the theory of partial coherence is necessary to quantify the differences between the field produced by a real source and an ideal monochromatic point source.
The theory is formulated in terms of an observable quantity, the mutual coherence function. This function (of a field stationary in time) is defined as the mathematical complex cross-correlation of the field in two points x_1 and x_2:

$$\Gamma_{12}(r) = \Gamma(x_1, x_2, \tau) =< E_1(x_1, t+\tau)E_2^*(x_2, t) > \tag{2.58}$$

where E_1 is the field at the point x_1, E_2 is the field at the point x_2 and $\tau = t_2 - t_1$. Also, $\tau = \Delta l/c$ where Δl is the path difference between the two beams and c is the speed of light in vacuum.
The angular brackets denotes a time average:

$$< f(t) >= \lim_{T\to+\infty} \frac{1}{2T}\int_{-T}^{T} f(t)dt \tag{2.59}$$

The cross-correlation function becomes an autocorrelation function when the two field points coincide. This function is equal to the intensity calculated for the point x_1 for zero time delay : $\Gamma_{11}(0) = I(x_1)$.
The complex degree of coherence $\gamma_{12}(\tau)$ is defined as the normalized mutual coherence function:

$$\gamma_{12}(\tau) = \frac{\Gamma_{12}(\tau)}{\sqrt{\Gamma_{11}(0)\Gamma_{22}(0)}} \tag{2.60}$$

2.4.1 Quasi monochromatic approximation

The quasi monochromatic approximation is satisfied when the spectral width of the radiation ($\Delta\nu$) is very small compared to mean frequency ($\overline{\nu}$):

$$\Delta\nu \ll \overline{\nu} \tag{2.61}$$

In addition, we assume that all path differences in the considered case satisfy the condition:

$$\Delta l \ll c/\Delta\nu \tag{2.62}$$

Under these conditions the radiation behaves like a monochromatic one, with frequency $\overline{\nu}$. Let us consider a two pinhole experiment (fig.2.8), where two plane, linearly polarized waves $E_1(t)$ and $E_2(t)$ are propagating from two apertures S_1 and S_2. Since these two waves are propagated by linear differential wave equations, the field at a generic point P can be represented as a superposition of two contributions:

$$E_P(t) = K_1 E_1(t - r_1/c) + K_2 E_2(t - r_2/c) \tag{2.63}$$

where K_1 and K_2 are propagators and r_1 and r_2 are the distances from P to S_1 and S_2, respectively.

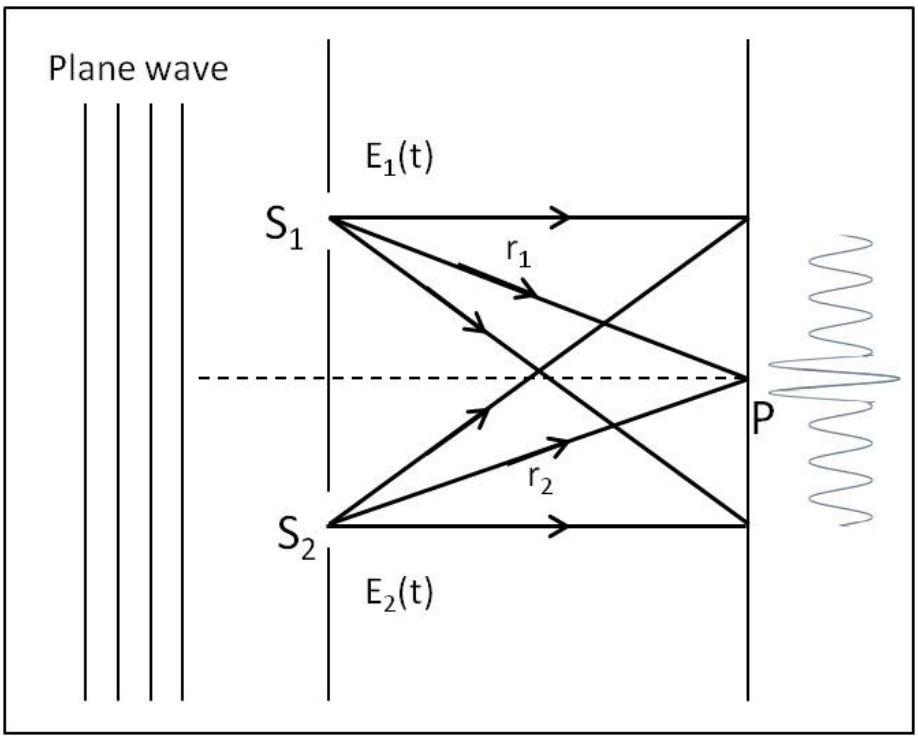

FIGURE 2.8: Schematic two pinholes experiment where P is a general point from the observation plane. The fields from the two apertures S_1 and S_2 are called $V_1(t)$ and $V_2(t)$, respectively. r_1 and r_2 are the distances from P to S_1 and S_2.

The intensity at the point P is given by:

$$I(P) =< E_P(t) E_P^*(t) > \tag{2.64}$$

that can be rewritten as:

$$\begin{aligned} I(P) =< |K_1 E_1(t - r_1/c) + K_2 E_2(t - r_2/c)|^2 >= \\ I_1 + I_2 + 2Re[K_1 K_2^* < E_1(t - r_1/c) E_1^*(t - r_2/c) >] \end{aligned} \tag{2.65}$$

where I_1 and I_2 are the intensities at P due to S_1 and S_2.
The equation 2.65 can be rewritten changing the origin of time:

$$I(P) = I_1 + I_2 + 2Re[K_1 K_2^* \Gamma_{12}(\tau)] \tag{2.66}$$

Eq.2.66 can be called the generalized interference law for partially coherent light.

Let us now define the mutual intensity function as $\Gamma_{12}(0)$. Because K_1 and K_2 are purely imaginary, we can use the notation:

$$\Gamma_{12}(\tau) = |\Gamma_{12}(0)|e^{i\Phi_{12}} = |\Gamma_{12}|e^{i\Phi_{12}} \tag{2.67}$$

where $\Phi_{12} = 2\pi\bar{\nu}\tau + \beta_{12}$. The phase difference is $2\pi\bar{\nu}\tau = (2\pi/\bar{\lambda})(|r_1 - r_2|)$, and $\beta_{12} = arg[\Gamma_{12}(\tau)]$.
Eq.2.66 can be rewritten as:

$$I(P) = I_1 + I_2 + 2|K_1K_2^*||\Gamma_{12}|cos\Phi_{12}] \tag{2.68}$$

Using eq.2.58 we can rewrite eq.2.68 as:

$$I(P) = I_1 + I_2 + 2\sqrt{I_1I_2}|\gamma_{12}|cos\Phi_{12}] \tag{2.69}$$

Eq.2.69 is the generalized interference law for partially coherent quasi-monochromatic light. In terms of $|\gamma_{12}|$, the following types of coherence can be differentiated:

- For $|\gamma_{12}| = 1$: full coherence,
- For $|\gamma_{12}| < 1$: partial coherence,
- For $|\gamma_{12}| = 0$: full incoherence,

Perfect correlation implies a 'perfect' interference pattern ('perfect' in the sense that the interference fringes achieve their maximal visibility) and perfect coherence. Zero correlation implies no interference pattern and complete incoherence. The function $|\gamma_{12}|$ takes into account at the same time spatial and temporal correlations. In particular if $\tau = 0$ it is possible to say that $\gamma_{12}(0)$ describes the spatial coherence properties while if the path traversed by the two signal is equal, $\gamma_{11}(t)$ describes the temporal coherence.
In a pattern of interference fringes, the intensity varies between two limits I_{max} and I_{min}. From Eq.2.69 (with $cos\Phi_{12}$=1) these values correspond to:

$$I_{max} = I_1 + I_2 + 2\sqrt{I_1I_2}|\gamma_{12}(\tau)| \tag{2.70}$$

and

$$I_{min} = I_1 + I_2 - 2\sqrt{I_1I_2}|\gamma_{12}(\tau)| \tag{2.71}$$

We define the fringe visibility V as:

$$V = \frac{I_{max} - I_{min}}{I_{max} + I_{min}} \tag{2.72}$$

it follows that:

$$V = \frac{2\sqrt{I_1I_2}|\gamma_{12}(\tau)|}{I_1 + I_2} \tag{2.73}$$

In the particular case of $I_1 = I_2$, the fringe visibility results to be:

$$V = |\gamma_{12}(\tau)| \tag{2.74}$$

This means that the fringe visibility is equal to the modulus of the degree of partial coherence. Thus, a simple measure of the visibility gives a measure of the complex degree of coherence.

Temporal coherence specifies the extent to which the radiation maintains a definite phase relationship at two different times. Temporal coherence is characterized by the coherence time τ_0, defined as the time for which the field of a "quasi-monochromatic" source keeps the same phase value and for $t > \tau_0$ changes phase abruptly. After each coherence time the phase changes assuming values randomly distributed between 0 and 2π.

From τ_0, we can define the coherent length as:

$$l_c = c\tau_0 \tag{2.75}$$

Considering two beams having a certain path difference between them, the coherent length represents the maximum value of path difference in order to obtain interference fringes. In fact, if the path difference is greater than l_c, the fringe visibility drops.

Let us demonstrate this point in the following discussion. Considering an experimental situation similar to the one shown in fig.2.8, where a beam of light is divided into two beams (with electric fields E_1 and E_2), that are then brought together to produce interference.
The degree of partial coherence can be evaluated assuming that:

$$|E| = |E_1| = |E_2| \tag{2.76}$$

Let us rewrite the normalized mutual coherence function (eq.2.58) for this case (Reynolds et al., 1989):

$$\gamma(\tau) = \frac{< E(t)E^*(t+\tau) >}{< |E|^2 >} \tag{2.77}$$

The time dependence of the field can be expressed as:

$$E(t) = E_0 e^{i\omega t} e^{-i\phi(t)} \tag{2.78}$$

where $\phi(t)$ is a random step function. The equation 2.77 becomes:

$$\gamma(\tau) =< e^{i\omega t} e^{i[\phi(t)-\phi(t+\tau)]} >= e^{i\omega t} \lim_{T\to+\infty} \frac{1}{T} \int_0^T e^{i[\phi(t)-\phi(t+\tau)]} dt \tag{2.79}$$

In the time interval $0 < t < \tau_0 - \tau$ the term $\phi(t) - \phi(t+\tau) = 0$, while for $\tau_0 - \tau < t < \tau_0$ this quantity assumes some random values between 0 and 2π. The same situation is valid for each coherence time interval.

Let us calculate the integral in equation 2.79 for the first interval of coherence time:

$$\frac{1}{\tau_0} \int_0^{\tau_0} e^{i[\phi(t)-\phi(t+\tau)]} dt = \frac{1}{\tau_0} [\int_0^{\tau_0-\tau} dt + \int_{\tau_0-\tau}^{\tau_0} e^{iDt} dt] = \frac{1}{\tau_0} [\tau_0 - \tau + \tau e^{iD}] \tag{2.80}$$

Where $D = \phi(t) - \phi(t+\tau)$ is the random phase difference.
For each coherence time interval we found the same result, aside from the value of D, different for each interval.
Let us calculate the terms which appears in the result of equation 2.80: the average on e^{iD} will be zero, since D is a random value between 0 and 2π. The therm $\frac{\tau_0-\tau}{\tau_0}$ is the same for all the intervals, hence it is equal to the average value of the integral. Taking this analysis in mind, we can find the following results for the complex

degree of coherence (eq.2.79):

- if $\tau < \tau_0$:$\gamma(\tau) = (1 - \frac{\tau}{\tau_0})e^{i\omega t}$
- if $\tau \geq \tau_0$:$\gamma(\tau) = 0$

and then considering the modulus of $\gamma(\tau)$:

- if $\tau < \tau_0$:$|\gamma(\tau)| = (1 - \frac{\tau}{\tau_0})$
- if $\tau \geq \tau_0$:$|\gamma(\tau)| = 0$

As seen before, in the case of equal amplitudes in a two-beam interference arrangement, fringe visibility (V) is equal to $|\gamma(\tau)|$. Remembering that the coherence length is defined as $l_c = c\tau_0$, we may observe fringes only when the path difference between two beams is not greater than l_c.

We can briefly introduce the classical definitions of temporal and spatial coherence, that will be further analyzed in the following. The coherence length can be defined as the half of the maximum visibility value (as defined in eq.2.72). Since visibility is proportional to $(1/\Delta\lambda)$, where $\Delta\lambda$ is the width of the spectrum. Thus, the coherence length depends on the shape of the incident spectrum.
The coherence time will be analyzed starting from the Wiener–Khinchin theorem (section 2.4.4) and some application on real optical system will be also shown.

2.4.2 Spatial Coherence

Spatial coherence describes the correlation between waves at different lateral points in space (Hecht, 1998). To better understand this concept, let us consider a quasi-monochromatic point source and two distinct points P_1 and P_2 in the space, with corresponding electric fields E_1 and E_2 (fig.2.9). The transverse coherence describes

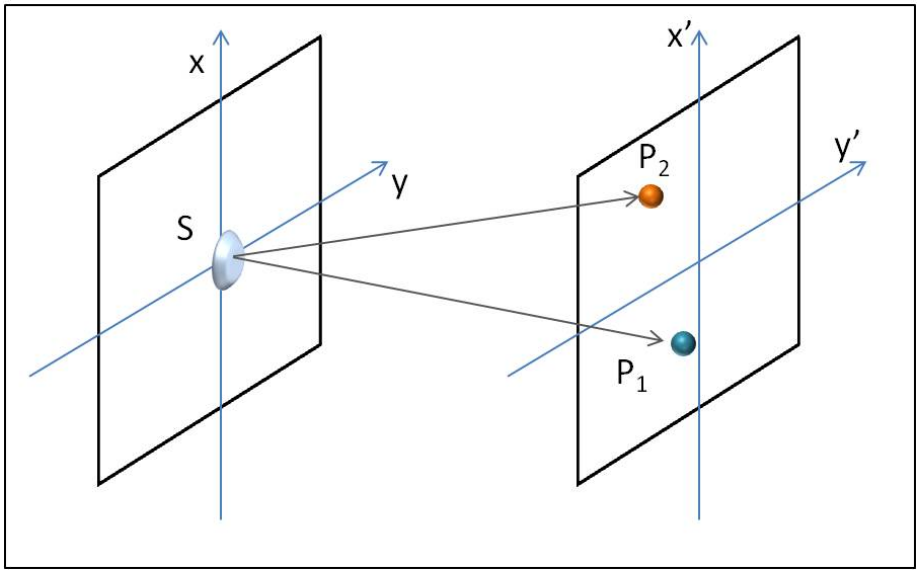

FIGURE 2.9: Schematic representation to show lateral transverse coherence.

the degree to which the phase of the wave is correlated at two distinct points in the transverse plane. If S can be considered as a point source, the time dependence of

the two fields E_1 and E_2 will be the same and they will be mutually coherent. If the source S has a spatial extension, partial coherence will occur.
To simplify the general case of a finite extended source, let us consider the case of a source made by two points (S_A and S_B) and we will look at the lateral coherence from two points P_1 and P_2 (fig.2.9). These two sources have the same characteristic except that their phases vary independently and randomly, so they can be considered as mutually incoherent. The electric fields E_1 and E_2 will be the result of superposition of the contributions coming from S_A and S_B:

$$\begin{aligned} E_1 &= E_{1A} + E_{1B} \\ E_2 &= E_{2A} + E_{2B} \end{aligned} \tag{2.81}$$

The degree of coherence is:

$$\gamma_{12}(\tau) = < \frac{E_{1A}(t)E^*_{2A}(t+\tau)}{\sqrt{I_1 I_2}} > + < \frac{E_{1B}(t)E^*_{2B}(t+\tau)}{\sqrt{I_1 I_2}} > \tag{2.82}$$

where the cross terms vanished since the two point-sources are mutually incoherent. Considering the solution given before for eq.2.80 for $\tau < \tau_0$, we can write:

$$\gamma_{12}(\tau) = \frac{1}{2}\gamma(\tau_A) + \frac{1}{2}\gamma(\tau_B) \tag{2.83}$$

with

$$\begin{aligned} \tau_A &= \frac{d_{(S_A:P_2)} - d_{(S_A:P_1)}}{c} + \tau \\ \tau_B &= \frac{d_{(S_B:P_2)} - d_{(S_B:P_1)}}{c} + \tau \end{aligned} \tag{2.84}$$

where d are the distances between the sources (S_i) and the points (P_i), and c is the speed of light in vacuum. Substituting the expressions found for τ_A and τ_B in the solution given before for eq.2.80 :

$$|\Gamma_{12}(\tau)|^2 \approx \frac{1 + cos[\omega(\tau_B - \tau_A)]}{2}(1 - \frac{\tau_A}{\tau_0})(1 - \frac{\tau_B}{\tau_0}) \tag{2.85}$$

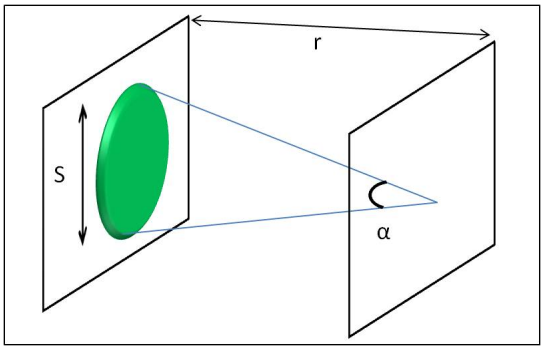

FIGURE 2.10: Schematic drawing to explain the transverse coherence length.

This the equation of the mutual coherence between a fixed receiving point and any

other point being illuminated by the two mutually incoherent sources. If we define r as the mean distance from the sources to the receiving points and s thee distance between the two sources (fig. 2.10), the transverse coherence length is given by:

$$l_t = \frac{r\lambda}{s} \tag{2.86}$$

For an extended source, s corresponds to the source size. Also, the larger the distance r the larger is the coherence length, and the smaller is the source size the lager is the coherence length.

2.4.3 Temporal Coherence

Temporal coherence can be quantified in terms of coherence time which relays the maximum delay in which a wave can be combined with a copy of itself and still produce an interference pattern. The coherence time τ is calculated by dividing the coherence length by the phase velocity of light in a medium:

$$\tau \approx \frac{\lambda^2}{c\Delta\lambda} \tag{2.87}$$

where λ is the central wavelength of the source, $\Delta\lambda$ is the spectral width of the source and c is the speed of light in vacuum. We will now focus on the mathematical representation of temporal coherence, using the Wiener–Khintchin theorem.

2.4.4 Wiener–Khinchin theorem

The Wiener–Khinchin theorem (WKT) states that the power spectral density of a stationary stochastic process in the broad sense is analogous to the Fourier transform of the corresponding autocorrelation function. It was proven by Wiener (Wiener, 1930) and by Khinchin (Shiryayev, 1992) in the 1930s. The WKT is a fundamental theorem used in many disciplines, including statistics, signal analysis, and optics. Especially in modern optics, thanks to the Wiener–Khinchin theorem, the interferometric spectrometer technology has been well established. For example, it is possible to extract the spectral information of light by making a Fourier transform on its time-domain Mach–Zehnder interference (MZI) or Michelson interference (MI) patterns.
We can start writing the relation between one generic field $E(t)$ dependent on time and its Fourier transform:

$$E(t) = \int_{-\infty}^{+\infty} d\omega e^{-i\omega t} E(\omega) \tag{2.88}$$

Let us write the first-order correlation function $G_{(1)}(\tau)$ as:

$$G_{(1)}(\tau) = < E(\tau)E(t+\tau) > = \int_{-\infty}^{+\infty} d\omega' e^{-i\omega' t} \int_{-\infty}^{+\infty} d\omega e^{-i\omega(t+\tau)} < E(\omega')E(\omega) > \tag{2.89}$$

For a stationary and homogeneous light field, $G_{(1)}(\tau)$ depends only on the relative time and displacement. It is very convenient to describe the field by a complex signal, so that the observed field $E(t)$ is its real part. Because $E(\omega)$ is the Fourier-transform of a real function, we can write the complex conjugate of the field $E^*(\omega)$ is equal to $E(-\omega)$.

Applying this result to eq.2.89 we obtained:

$$G_{(1)}(\tau) =< E(\tau)E(t+\tau) >= \int_{-\infty}^{+\infty} d\omega^{'} e^{-i(\omega^{'}-\omega)t} \int_{-\infty}^{+\infty} d\omega e^{i\omega t} < E(\omega^{'})E^{*}(\omega) > \tag{2.90}$$

Because of stationarity, this expression should not have dependence on t. Hence, the correlator should give a delta function:

$$< E(\omega^{'})E^{*}(\omega) >= \delta(\omega^{'}-\omega) < E(\omega)E^{*}(\omega) > \tag{2.91}$$

Therefore, we obtained the final expression for the Wiener–Khintchin theorem:

$$G_{(1)}(\tau) = \int_{-\infty}^{+\infty} d\omega e^{i\omega t} < E(\omega)E^{*}(\omega) > \tag{2.92}$$

From the last expression we can notice that there is a one-to-one correspondence between the spectrum and the correlation function, which can be measured using an interferometer. Theoretically, knowing the function that describes the emitted field of the source we can infer its spectrum thanks to the WKT.
For example if the field can be approximated by a Gaussian function, its Fourier Transform will still be a Gaussian function. Knowing the shape of the spectrum, from eq.2.87, we can assume that the coherence time will be proportional to $(1/\Delta\lambda)$. In many experimental cases we don't know exact shape of the emitted field. Calculating the correlation function of the field, the WKT can be used to estimate the order of magnitude of the emitted spectra, and thus of the coherence time. In fact, since the spectra and the field are connected by a Fourier Transform, we can calculate the trend of coherence time.

2.4.5 Impact of coherence on Hartmann Sensor measurements

In this section we will investigate what it is the effect of the temporal and spatial coherence on Hartmann sensor measurements. Different sources will be compared: the Excillum liquid metal jet anode with a Gallium target (used in section 6.1), a third generation Synchrotron source (used in section 7) with different level of beam monochromaticity and mean energy and, finally, the ID17 Biomedical beamline at ESRF synchrotron, France. We consider separately the ID17 beamline because it presents particular coherence properties due to its large distance from the source. First we considered an estimated source size of $10\mu m$ for the different types of sources (fig.2.11) and we changed the average energy corresponding to each case of interest. In particular, for the Excillum source, we consider both the $K\alpha$ energy of Gallium and the contribution of Bremsstrahlung. We calculate the value $\Delta E/E$, as the ratio between the energy spread and the mean energy value. Typically a $\Delta E/E$ of about 10^{-4} is obtained with a synchrotron beamline monochromator, an optical device that transmits a narrow band of wavelengths of light chosen from a wider range of wavelengths. The mean energies were set to 9 keV to compare with the experimental results obtained with the Excillum source and to 20 keV to fit the experiments performed at ESRF and ELETTRA synchrotrons (see section 7).

We then concentrate on an important parameter that is the transverse coherence length. To calculate its value for each set of parameters we use eq.2.86. It is important to compare the transverse coherence length with the Hartmann mask pitch (distance between two holes) to predict the occurrence of cross-talk between close apertures.

Source	size (µm)	E (keV)	ΔE (keV)	ΔE/E
Excillum (K-alpha)	10	9	10,00E-2	1,11E-02
Excillum (Bremsstrahlung)	10	30	3,00E+01	1,00E+00
Synchrotron	10	9	9,00E-04	1,00E-04
	10	20	2,00E+00	1,00E-01
	10	20	2,00E-03	1,00E-04
ID17 ESRF	10	50	5,00E-03	1,00E-04

FIGURE 2.11: Table reporting the estimated source size, the mean energy and the energy variation for different types of sources: the Excillum liquid metal jet anode with a Gallium target, a third generation Synchrotron source with different level of beam monochromaticity and the ID17 Biomedical beamline at ESRF synchrotron, France.

If the transverse coherence length is larger than the mask pitch, it is possible that the rays reaching two adjacent apertures start to cross-talk. This phenomenon will produce a blurred image and will reduce the accuracy on the final image (see section 5.9.3).

In fig.2.12 we compare the the transverse coherence length with the Hartmann mask pitch for several sources. For the $K\alpha$ of the Excillum source, we calculate a transverse coherence length of 14 μm respect to a pitch of 20 μm, resulting in the absence of cross-talk between apertures. When considering the effect of Bremsstrahlung on Excillum source, the transverse coherence length decreases even more. For the synchrotron sources, the third and fourth line correspond to large distances from source to Hartmann plate, giving a transverse coherence length of about three times the pitch. The different holes can then start to interact and to modify their shape when projected on the detector plane.

Higher values for the transverse coherence length can be seen in the second and last line of fig.2.12 corresponding to a lower energy synchrotron source (9 keV) and with a large distance source-Hartmann plate (80 m) respectively. These two conditions increase the transverse coherence length of about 7 to 9 times the pitch. Under these conditions the image of the Hartmann plate can be distorted and a strong cross-talk between apertures can be observed.

Another important parameter to calculate is the longitudinal coherence length or temporal coherence. To understand if the longitudinal coherence length will have an impact on the Hartmann sensor measurement we compared it with the length Δ as defined in fig.2.13. We consider a Hartmann plate with a given pitch placed at a distance d from a pixelated detector. We then calculate the distance Δ that corresponds to the one needed for the two apertures to shine the same pixel (bottom of fig.2.13). The longitudinal coherence length was calculated using the expression reported in eq.2.87. The values for the different sources are reported in fig.2.14. When the values of the distance Δ are smaller then the longitudinal coherence length, interferences can occur. For the synchrotron sources this condition is verified for monochromatic beams (lines 2, 4 and 5) while for the Excillum (both considering the $K\alpha$ and the

Source	E (keV)	distance source-Hartmann plate (m)	transverse coherence length (µm)	pitch (µm)
Excillum (K-alpha)	9	1	14	20
Excillum (Bremsstrahlung)	30	1	4	20
Synchrotron	9	10	138	20
	20	10	62	20
	20	10	62	20
ID17 ESRF	50	80	198	20

FIGURE 2.12: Table reporting the distance source-Hartmann plate, the transverse coherence length for different types of sources.

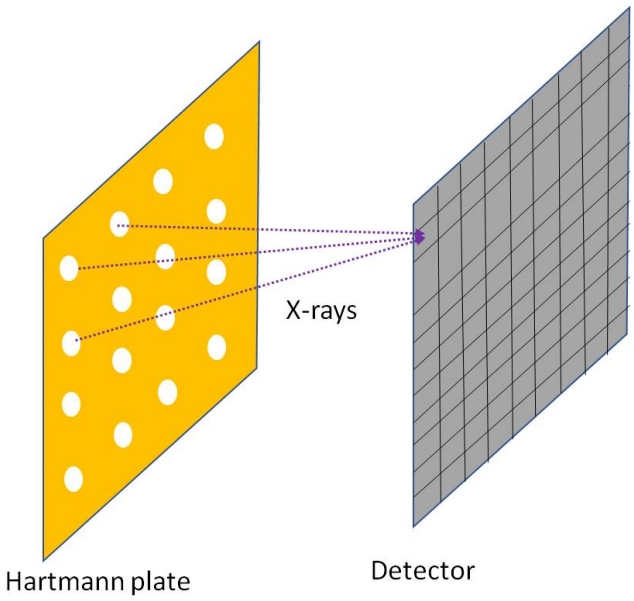

FIGURE 2.13: Drawing to explain the calculation of the longitudinal coherence length.The Hartmann plate with a given pitch is placed at a distance d from a pixelated detector.

Bremsstrahlung energies) and for the sinchrotron with larger spectra (lines 1 and 3) are not.

It is important to note that both spatial and temporal coherence have to be considered to understand the comprehensive response of the system. For example a coherence length of 62 μm for a pitch of 20 μm for the synchrotron source parameters reported in line 3 in fig.2.12. This value was compatible with the occurrence of cross-talk in the image, however while looking at the temporal coherence of the same source we can see that there will be no interference effect due to temporal (line 3, fig.2.14).

Source	longitudinal coherence length (m)	d (m)	Δ (m)
Excillum (K-alpha)	1,24E-08	0,20	1,00E-09
Excillum (Bremsstrahlung)	4,13E-11	0,20	1,00E-09
Synchrotron	1,38E-06	0,20	1,00E-09
	6,20E-10	0,20	1,00E-09
	6,20E-07	0,20	1,00E-09
ID17 ESRF	2,48E-07	0,20	1,00E-09

FIGURE 2.14: Table reporting the longitudinal coherence length, the distance d from the Hartmann plate to the detector, and the distance Δ (as reported in fig.2.13) for different types of sources.

2.5 Conclusion

In this chapter we provided a general introduction of X-ray radiation fundamental proprieties. It is in fact crucial to understand the fundamental interaction mechanisms related with image formation when dealing with imaging techniques.
The x-ray interaction with matter was first introduced using atomic physics principles to understand important parameters connected with X-ray propagation in the medium. Then, the analysis was completed using wave optic approach.
In the last section, we introduced elements of coherence theory since coherence has a big impact on the image formation process. In particular, the degree of coherence becomes a crucial parameter when using a wavefront sensor.

Chapter 3

X-ray Phase Contrast Imaging

Conventional X-ray images use the absorption properties of materials to produce an image. Phase-contrast imaging also visualises the phase changes introduced by the refractive properties of the object. X-ray phase-contrast imaging is a powerful technique which exploits the refraction of X-rays after their interaction with matter (see chapter 2). This method is very suitable to visualize weakly absorbing details like those of soft tissues studied in biology and medicine, and is very sensitive to small variations of electron density (Bravin, Coan, and Suortti, 2012). Phase-contrast imaging founds applications in many fields: biology, material science, industry, cultural heritage and, overall, in the bio-medical field. Recently, many ex-vivo and in-vivo experiments have demonstrated the diagnostic potential of phase-contrast imaging for numerous pathologies, such as breast cancer, neurodegenerative diseases, or regenerative medicine for bones and cartilages (Arfelli et al., 1998).

3.1 Phase-Based Techniques for X-ray Imaging

X-ray phase-contrast imaging provides high contrast visualization of complex samples at high spatial resolution. Several techniques have been developed to detect phase-contrast. In the following sections we will give an overview of the main X-ray phase-contrast imaging methods: Free space propagation imaging (Snigirev et al., 1995), the interferometric technique based on the use of crystals (Bonse and Hart, 1965, Momose et al., 1996), the analyzer-based imaging (ABI) (Förster, Goetz, and Zaumseil, 1980), the edge illumination (Olivo et al., 2001) and the grating interferometric imaging (Weitkamp et al., 2005). The basics of Free space propagation imaging will be described in a separate section since this technique was widely used in this thesis.

3.1.1 Crystal Interferometric Technique

Crystal interferometry is the oldest method of X-ray phase detection (fig.3.1). We will describe the Bonse-Hart interferometer. It requires perfect silicon crystals that split the X-ray beam, with only one-half of the beam traversing the object. In the simplest arrangement, the set-up consists of placing three parallel crystal blades, operating in conditions of Laue, and at the same distance from each other. The beams converge into the detector plane, forming an interference pattern where phase shifts induced by the object can be detected (Bonse and Hart, 1965). Extremely high sensibility in detecting the smallest phase shifts can be achieved with this technique. The field of view is limited because of the nature of the crystal used; moreover, the method is extremely sensitive to vibrations and alignment errors. These difficulties

lead to the fact that this technique is practically no longer used in imaging. Furthermore, crystal interferometry requires a monochromatic parallel X-ray beam, making difficult to use this technique with a laboratory source.

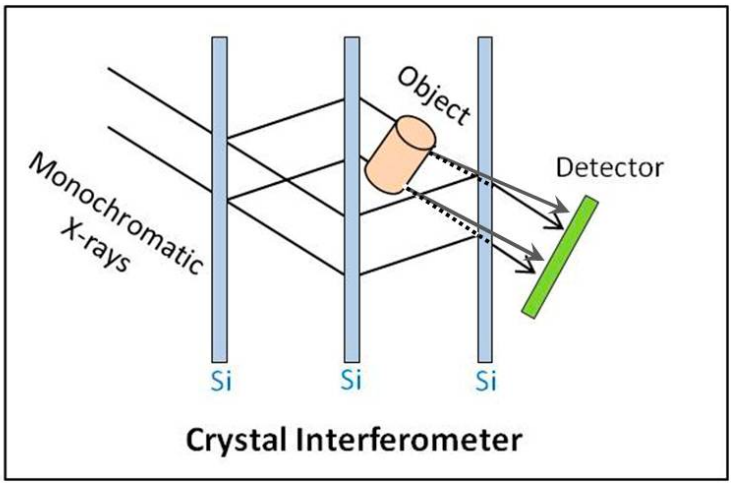

FIGURE 3.1: Bonse-Hart interferometer scheme.

3.1.2 Analyzer-based imaging

The analyzer-based imaging(ABI) or diffraction-enhanced imaging (DEI) makes use of a single crystal as an "analyzer" placed between the sample and the detector in combination with a monochromatic and collimated X-ray beam (fig. 3.2) (Davis et al., 1995). Since the incident beam is refracted by the sample, the analyzer crystal acts as a filter on the radiation emerging from the sample: according to its orientation, only X-rays which meet the Bragg law for diffraction are indeed reflected:

$$m\lambda = 2dsin\theta \tag{3.1}$$

where m is the Bragg angle equal to half of the deviation angle, λ is the wavelength and d is the interrecticular distance of the crystal. The filter function is given by the rocking curve (RC), a bell-shaped function, obtained by rotating the analyzer crystal in the proximity of the diffracted Bragg angle in the absence of the sample and measuring at each step the value of the intensity of the X-rays. ABI enables high phase sensitivity: information on absorption, refraction and scattering signals can be extracted by combining images produced at different positions of the crystal rocking curve. Analyser-based imaging yields relatively large fields of view (in one direction), but depends on an analyser crystal for effective phase detection, which renders the set-up very sensitive to vibrations and other disturbances, and requires monochromatic X-ray radiation.

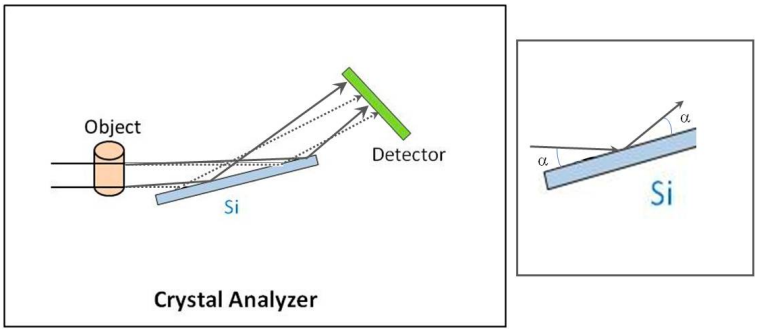

FIGURE 3.2: Analyzer-Based Imaging(ABI) scheme.

3.1.3 Grating interferometry

Grating interferometry with synchrotron radiation requires two gratings placed between an object and the detector to extract X-ray phase information (fig.3.3). The method is based on the phenomenon of Talbot self-imaging. When a grating is coherently illuminated, a diffraction pattern, identical to the grating which creates them is observed at given periodic distances behind the grating, known as Talbot distances, defined by:

$$d_T = m\frac{2p^2}{\lambda} \tag{3.2}$$

where p is the period of the grating and m can be an integer or fractional number.

The interferometer consists of a combination of a phase grating (i.e., a grating whose lines show negligible absorption but substantial phase shift) and an absorption grating. The phase grating acts as a beam splitter and divides the incoming beam essentially into the two first diffraction orders. A phase grating with a phase shift of π or $\pi/2$ illuminated by a plane wave produces self-images of the grating at fractional Talbot distances.

When an object is inserted before or after the grating, perturbations of the incident wavefront lead to a variation of the interference pattern. A standard detector, with micrometric resolution, will not be able to resolve the small shifts produced by the grating. For this reason, the absorption grating is placed at one of the partial Talbot distances immediately in front of the detector. This second grating acts as a transmission mask for the detector and transforms local fringe position into signal intensity variation. The detected signal profile thus contains quantitative information about the phase gradient of the object. The phase signal can be separated from the attenuation by the "phase-stepping" procedure. One of the gratings is laterally shifted with respect to the other in sub-pitch steps, in the direction orthogonal to the beam and the trenches; for each of these positions an intensity image is then acquired. Then, the curve of the intensity variation as a function of the grating steps is recorded for each pixel of the area detector. Comparing the curves obtained with and without the sample, a lateral shift and a reduction in average intensity can be observed.

Implementation of a third grating between the X-ray source and the object has allowed the technique to be successfully applied to conventional clinical X-ray tubes. Grating-based interferometry can be used with the relatively broad spectra provided

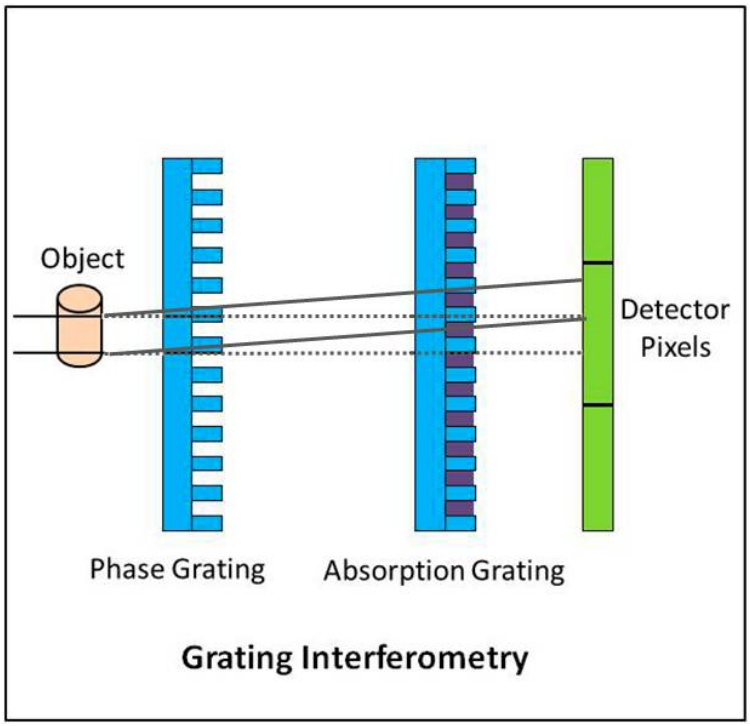

FIGURE 3.3: Grating interferometry scheme.

by conventional X-ray sources and yields fields of view of up to several centimetres in diameter. For these reasons, it is currently the most efficient phase-contrast imaging method when applied to clinical X-ray sources. Furthermore, the technique allows for quantitative imaging.

3.1.4 Edge illumination

In its simplest implementation, the setup of the edge illumination technique consists of two slits with the same opening (some tens of micrometers) that are slightly misaligned (fig. 3.4 d). The first slit is placed before the sample and is used to collimate the beam and a second slit is aligned with the detector so that only a single row of pixels is left uncovered (Zamir et al., 2017). Because of this configuration, to obtain the whole image it is necessary to scan the sample vertically, in the orthogonal direction with respect to the slits and then combining together the single acquisitions. The setup configuration is such that the beam illuminates only one edge of the detector; in the absence of the sample, the detector counts 50% of the incident radiation. When the object is introduced, the beam is refracted and consequently shifted by the quantity $\Delta y = z\ tan(\Delta\theta_y)$, where z is the sample to detector distance and θ_y is the component of the refraction angle in the direction orthogonal to the slits. Multiple projections are acquired at different sub-pixel positions of the object and are later recombined to form a high-resolution projection. The deflection towards the slits causes a reduction of the detected photons, and a negative fringe appears in the collected image; the deflection toward the aperture results instead in an increase of intensity detection, i.e. a positive fringe (fig.3.4). In this way, it is possible to translate the refraction angles into a modulation of the intensity on the detector.
Any particular source coherence requirement is needed, thus the method can work with conventional X-ray sources.

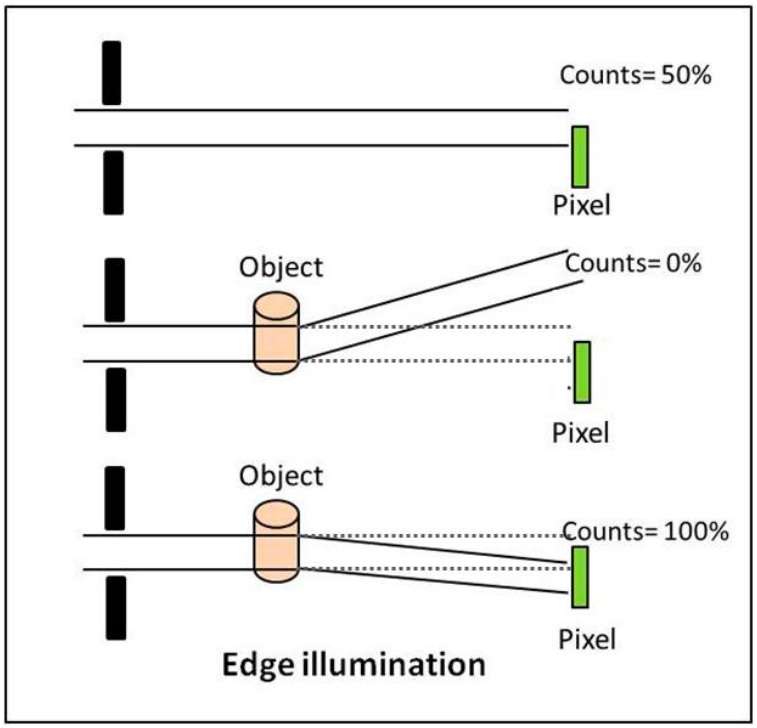

FIGURE 3.4: Edge illumination scheme. The dotted lines represent the propagation of rays without sample.

3.2 Comparison between Phase-Contrast Techniques

We will now focus on the main differences among phase and phase-contrast imaging techniques. Phase imaging techniques can be divided into three groups. Before describing the three techniques, it is important to remind that a phase has no absolute physical meaning since it is defined as the module of two times the flat angle (2π). It thus always possible and physically correct to consider zero the phase at the entrance of the sample or on the part of the beam that did not interact with the sample.

1. Interferometer and holography : In this case, the incoming beam is separated into two beamlets. One will serve as reference and will propagate in air, vacuum or any known media and the second (probe beam) will go through the object. Then the two beams will interfere on the detector to create fringes. Interferometric techniques measure how the sample modify the incident wavefront. Holography instead measures also the wavefront of the probe beam (Eisett et al., 2005). This allows the reconstruction of quasi-3D image: the hologram (Morlens et al., 2006). Although interferometry is a very strong technique, it can fail in retrieving the wavefront if the local phase jump is larger than 2π. Also, X-ray interferometers are technically complex, very sensitive to vibrations, and require either high temporal or spatial coherence.

2. Deflectometry: In this kind of technique the deflection of the incident beam passing through an object is recorded. Namely, these techniques measure the local wave vectors. The phase map is obtained by integrating the local wave vectors ($|2\pi|$). Normally, the phase of the beam propagating on the side of the

object is assumed to be zero, leading to the direct measurement of the phase acquired by the beam passing through the object.

3. Phase-contrast imaging: This technique has been invented in order to increase the contrast of images of samples having low absorption variations. It is based on transforming the variation of the recorded intensity into the deflection induced by variations of the index of refraction. Several phase-contrast methods have been proposed. Along them, coded-aperture or edge-illumination techniques consist in placing an array of blockers near a pixelated detector to stop straight rays. For tabletop sources, it is common to use an additional mask to locally increase the coherence of beamlets or, in other words, to reduce the source size (Olivo and Speller, 2007). Recently, speckle-based imaging has emerged as a new phase-contrast technique (Berujon, Wang, and Sawhney, 2012). All these techniques do not measure the deflection and thus nor the phase. Indeed, the intensity recorded on a pixel is a mix between the local intensities of the straight and deflected beams, the absorption of a neighbour beam that is deflected to the same pixel and the interference effect. Furthermore, intensity is affected by both the detector and background noise. It is not possible to directly measure the phase with such indirect techniques.

We will end this section with a table that summarizes the advantages and limitations of the main phase-contrast techniques (fig.3.5).

Technique	*Limitations*	*Advantages*
Crystal Interferometer	Very monochromatic Parallel beam Complex allignment	High spatial resolution
Free Space Propagation	Monochromatic beam Phase retrieval algorithm	High spatial resolution
Coded Aperture	Very low deflexion accuracy δ mixed with β	High spatial resolution
Crystal Analyzer	High monochromatic beam Parallel beam	High spatial resolution
Grating Interferometer	Very low X-ray transmission Monochromatic beam Acquisition of several positions per angle	Average spatial resolution
Speckle Deflectometry	Long set-up : 1.5 m Monochromatic beam Acquisition of 20 positions per angle Phase retrieval algorithm	High spatial resolution

FIGURE 3.5: Summary of the main advantages and limitations of a set of phase-contrast techniques.

3.3 Free Space Propagation Imaging

Free space propagation imaging has the simplest design among the experimental methods to detect the phase variations with hard X-rays. It does not require any optical element it consists in a coherent/partially coherent X-ray source, the sample and the detector disposed in line with each other. This technique exploits Fresnel diffraction, discussed in the previous chapter (section 2.3.1). The contrast is in fact due to the interference between the beam diffracted by the object and the reference beam. Unlike the interferometric methods described above, there is no need to acquire a reference image without the sample. Since the angular deviations produced by the sample in the hard X-ray region are very small (of the order of μrad), a certain propagation distance between the sample and the detector plane is needed to detect the interference fringes. This is the main modification with respect to the case of standard (absorption based) X-ray imaging, where the detector is positioned immediately behind the sample. Changing the detector-object distance defines the transition between absorption and phase imaging regime.
In the following, we will use wave optic theory for a general description of free space propagation. When considering sources with a low degree of coherence, it is possible to model the system using ray optics, that contains simpler mathematical expression.

3.3.1 Wave optic theory

Most optical phenomena can be accounted for by using the classical electromagnetic description of light. It is the wave optics. In geometrical optics, or ray optics, light will be treated as the form of energy that travels in straight lines known as rays. The simple supposition made in geometrical optics, is that the rays of light propagate along straight lines until they get reflected, refracted, or absorbed. On the other hand, wave optics explains connection between waves and rays of light. This model predicts phenomena such as interference and diffraction, which are not explained by geometric optics. Wave optics is a more general model respect to geometrical optics. We will now start with the explanation of phase-contrast imaging using geometrical optics to later turn to wave optic description. Phase-contrast imaging can be explained as a pure geometrical effect, where the incident rays are deflected from their original trajectory when an object is inserted in the beam path. In fig.3.6 a) a parallel beam geometry is considered, while in fig.3.6 b) a cone-beam geometry is shown. The arrows underline the change in ray's direction when passing through the object. The black line in fig.3.6 d) shows the jump in intensity corresponding to one of the object edges.

In order to perform phase-contrast imaging a small source size is needed, otherwise the refraction peak will be larger and difficult to detect. To explain this phenomena, in fig.3.6 c) we consider the effect of two sources emitting rays displayed with black and green lines respectively. A magnification of the rays in this case is shown in fig.3.6 e), where a different incident angle between the rays and the object will result in a a shift of the refraction peak (green line, fig.3.6 d). Therefore, a larger source size will blur the intensity peak complicating the image analysis.

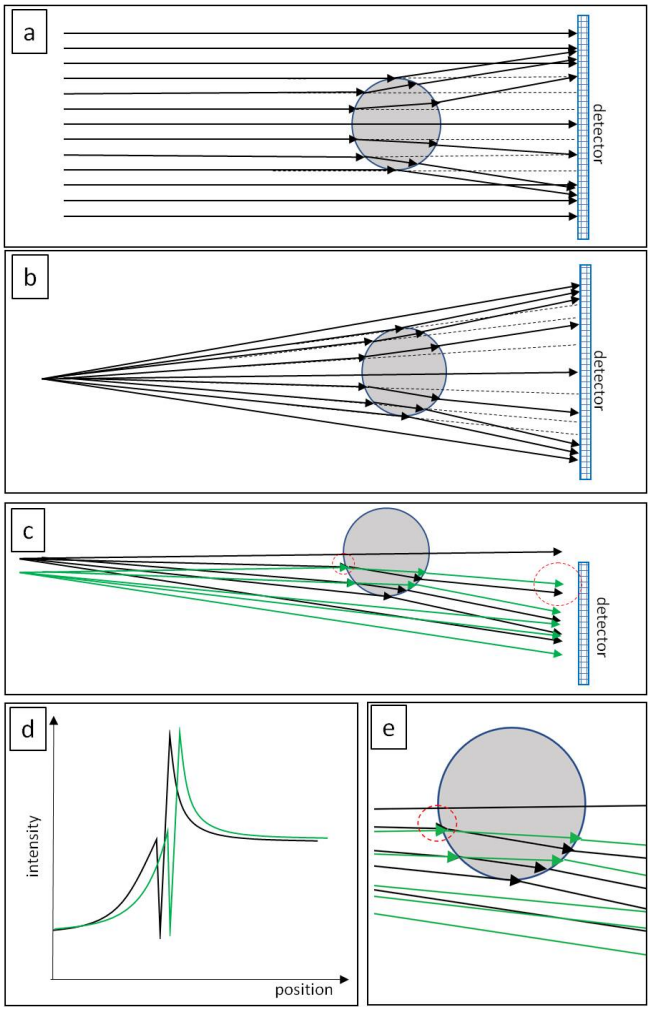

FIGURE 3.6: Phase-contrast imaging; a) parallel beam geometry, b) cone-beam geometry, c) Effect of two sources displayed with black and green lines respectively, d) Intensity plot respect to the position on the detector. The black line jump in intensity corresponds to one of the object edges. The green line corresponds to a different source leading to a shift of the refraction peak. e) Magnification of image c).

3.3.2 Theoretical basis of Free Space Propagation Imaging

The phase shift of X-ray passing through the sample, is given by:

$$\Delta\Phi(x,y) = -\frac{2\pi}{\lambda}\int \delta(x,y,z)dz \tag{3.3}$$

where the beam propagates along the z-axis. This expression was already derived in the previous chapter (section 2.2.1). Reminding that, the local propagation vector will be defined in its orthogonal direction. Assuming the paraxial approximation where the angles between the direction of each ray and the optical axis are assumed to be small ($|\Delta\Phi| << kz$), the local propagator s can be rewritten as (Davis et al., 1995):

$$s(x,y,z) = (-\frac{\partial\phi}{\partial x}, -\frac{\partial\phi}{\partial y}, k) \tag{3.4}$$

After the interaction, the angular deviation $\delta\alpha$ of the beam respect to the incident direction of the wavefront can be expressed as:

$$\delta\alpha \approx |\nabla_{x,y} \int \delta(x,y,z)dz| \tag{3.5}$$

and it thus depends on the variation of the projected refractive index perpendicular to the propagation vector k. Rapid variations in refractive index lead to large deviation of the beam from the propagation axis. The relationship between the angular deviation and the phase shift can be derived by eqs.3.3 and 3.5:

$$\delta\alpha \approx \frac{\lambda}{2\pi}|\nabla_{x,y}\Delta\phi(x,y)| \tag{3.6}$$

Integrating the angular deviations lead to a phase shift $\Delta\phi$ of the interacting beam with respect to the rays freely propagating in the vacuum. The angular deviation is proportional to the phase gradient. For objects with simple geometry, as a sphere or a cylinder, the expression diverges when the ray is tangent to the interface, creating a sharp refraction contrast at the edge of the object. The differences in optical paths produce interference and hence intensity modulations on the detector. The technique transforms phase modulations of the incident beam into amplitude modulations. By recording the intensity of the beam sufficiently far from the sample, the intensity variations due to variations of both the refractive index and sample thickness can be detected as differential phase contrast imaging.

3.3.3 Contrast Transfer Function

Experimentally, the intensity of a propagated field (E_z) at a distance z is recorded on the detector as the square modulus of the field amplitude:

$$I_z(r) = |E_z(r)|^2 \tag{3.7}$$

The amplitude information of the wave can be calculated, while the phase information is lost. Thus, the main challenge in phase contrast imaging is the lack of a direct measure of the phase and therefore several indirect methods have been developed to transform phase modulations into intensity modulations, as previously shown with the interferometric phase contrast techniques or free space propagation.
In this technique the (partial) coherence of the beam is a necessary condition since, when illuminating the object with an incoherent source, the information about the phase is lost just after the object. Therefore, due to the source incoherence, the phase of the incident wave changes in a random way and it will not be possible to differentiate the phase changes produced by the object. We will now derive how the phase contributions are related with the measured intensity.
The coordinate in real space will be denoted as $r = (x, y)$ and the one in the Fourier space as $f = (u, v)$.
The amplitude of the field calculated at the position z, after passing through the object, can be obtained from the expression:

$$E_z(r) = E_0(r) \otimes P_z(r) \tag{3.8}$$

where $\otimes$ is the convolution symbol. In Fourier space the convolution between the field E_0 calculated at $z = 0$ and the propagator P_z becomes a simple multiplication.

Let us consider an incident plane wave of unit amplitude for which the approximation of weak object is valid. The amplitude of the field for the position z can be expressed by:

$$\tilde{E}_z(f) = \tilde{T}(f) \cdot \tilde{P}_z \tag{3.9}$$

where $f = (u, v)$ are the spatial frequencies and $\tilde{T}$ is the Fourier transform of the transmission function (eq.2.29):

$$\tilde{T}(x, y) \approx \delta - \tilde{\mu}_z(x, y) + i\tilde{\phi}(x, y) \tag{3.10}$$

where δ is the Dirac delta function, μ_z is the absorption coefficient in the z-axis and ϕ is the phase. Considering the expression for the propagator $\tilde{P}_z$ in reciprocal space:

$$\tilde{P}_z(f) = e^{-i\pi\lambda z f^2} \tag{3.11}$$

In 2D the expression for the field becomes:

$$\tilde{E}_z = e^{i\pi\lambda z u^2} e^{(\delta - \tilde{\mu}_z + i\tilde{\phi})} \tag{3.12}$$

and in Fourier space it can be rewritten as:

$$\tilde{E}_z = (\delta - \tilde{\mu}_z cos(\chi) - \tilde{\phi} sin(\chi)) + i(\tilde{\phi} cos(\chi) - \tilde{\mu}_z sin(\chi)) \tag{3.13}$$

where $\chi = \pi\lambda z u^2$.
By inverse transforming we obtain E_z as:

$$E_z = (1 - \mu_z \widetilde{cos(\chi)} - \phi \widetilde{sin(\chi)}) + i(\phi \widetilde{cos(\chi)} - \mu_z \widetilde{sin(\chi)}) \tag{3.14}$$

Taking only the first-order terms in ϕ and μ_z, the intensity of the field is:

$$I_z = |E_z|^2 \approx 1 - 2\mu_z \widetilde{cos(\chi)} - 2\phi \widetilde{sin(\chi)}) \tag{3.15}$$

where I_z is the intensity on the image plane placed at a distance z from the sample, considering the weak object approximation. In the Fourier field the final expression of the intensity is:

$$\tilde{I}_z = \delta - 2\tilde{\mu}_z cos(\chi) - 2\tilde{\phi} sin(\chi) \tag{3.16}$$

and replacing the expression for $\chi = \pi\lambda z f^2$:

$$\tilde{I}_z(f) = \delta - 2\tilde{\phi} sin(\pi\lambda z f^2) - 2\tilde{\mu} cos(\pi\lambda z f^2) \tag{3.17}$$

Finally, we obtained an expression where the attenuation and phase contributions are uncoupled; the information on the phase is no longer lost, but is possible to recover it from the recorded intensity. The first term containing Dirac's delta function corresponds to a homogeneous background in the image, due to the direct and non-interacting beam. The second and third terms are called amplitude and phase contrast transfer function respectively. The term with the cosine describes the contribution due to absorption, while the term with the sine represents a modulation of intensity due to phase variation. The factors multiplying $\tilde{\mu}$ and $\tilde{\phi}$ are the contrast factors for amplitude and phase modulation respectively. The free propagation of the wave until the detector plane allow us to observe the phase modulation, due to its interaction with the object, as detectable intensity modulation.
Fig.3.7 shows the plot of the contrast functions $cos(f')$ and $sin(f')$ as a function of the reduced spatial frequency $f' = \sqrt{\lambda z} f$. For $\lambda z |f^2| = 0$, the phase contrast trans-

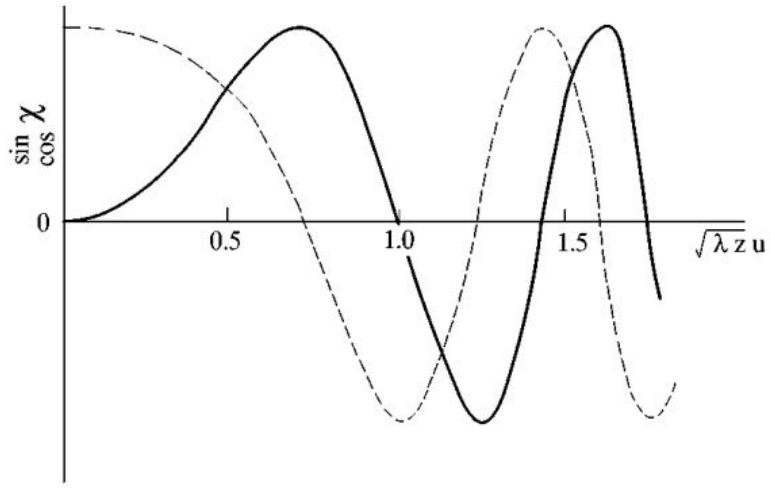

FIGURE 3.7: Absorption (dashed line) and phase (solid line) parts of the Fresnel diffraction optical transfer function as functions of reduced spatial frequency $f' = \sqrt{\lambda z} f$. Figure from Pogany, et al. (Pogany, Gao, and Wilkins, 1997)

fer function (solid line, fig.3.7) is zero, while the absorption contrast (dashed line, fig.3.7) reaches a maximum. While for $\lambda z|f^2| = \frac{1}{2}$, the situation reverses: the phase contrast is maximum, while the absorption contrast is minimum (Pogany, Gao, and Wilkins, 1997).
For this reason, the first value of f for which optimal phase contrast can be obtained is:

$$f_{max} = \frac{1}{\sqrt{2\lambda z}} \tag{3.18}$$

For frequencies around f_{max}, the intensity expression of eq.3.16 can be written as:

$$\tilde{I}_z(f) = \delta(f) - 2\tilde{\phi}(f) \tag{3.19}$$

The distance corresponding to the condition of eq.3.18 is:

$$z = \frac{1}{2\lambda f^2} \approx \frac{d^2}{2\lambda} \tag{3.20}$$

where d is the typical linear size of the object to detect. The ratio $\frac{d^2}{\lambda}$ is called the Fresnel distance.

3.3.4 Phase Retrieval Algorithms

Phase-contrast imaging using the free space propagation technique provides information on both absorption and refraction. However, in this technique the phase cannot be measured directly, but it has to be recovered numerically.
Experimentally only intensity patterns are measured, therefore it is necessary to solve the inverse problem, i.e. "recovering" the information about the phase (and the amplitude) from the measurements of recorded intensities (Shechtman et al., 2015, Burvall et al., 2011). There are different algorithms to recover the phase depending

on the experimental conditions, such as the set-up, the propagation distance or the energy range. In general, the phase retrieval algorithms require two separate intensity measurements taken at two different distances from the source, because the intensity generated by the absorption and by the phase propagates in different ways. Therefore, to apply a phase retrieval algorithm at least two intensity measurements are needed to separate the contributions of phase and absorption (see fig.3.7). For the methods that require only one image at each angle is possible to identify a common basic structure. The input parameter of the algorithm is the intensity $I(r_\perp)$ measured on the image plane as a function of the orthogonal coordinates on the detector plane $r_\perp$. Then a function $g(I(r_\perp))$, depending on the method used, and often corresponding to a normalization, is calculated. Later, the function $g(I(r_\perp))$ is filtered in the frequency domain considering the multiplication of the Fourier transform of $g(I(r_\perp))$ and a filtering function $H_P(w)$, where w are the frequency coordinates. The choice of the filtering function $H_P(w)$ is also dependent on the method used. The final step is to invert the Fourier transform to obtain the function $g_F(f_\perp)$. A function $f(g_F)$ is used to obtain a 2D distribution of the phase $\phi(r_\perp)$ on a plane just after the object.

Multiple-distance method

The following method is an adaptation of a reconstruction method that was fist designed for electron microscopy. The phase retrieval for multiple-distance method that we are going to illustrate is the one described by Zabler et al. (Zabler et al., 2005) for in-line holotomography.
Considering again the equation 3.8 of a wave propagating just downstream of the object in the Fresnel approximation (section 2.3.1):

$$E_z(x,y) = E_0(x,y,z=0) \otimes P_z(x,y) \tag{3.21}$$

where the electric field $E_z(x,y)$ at a propagation distance z is obtained by the convolution of the electric field $E_0(x,y,z=0)$ at $z=0$ with a complex function, which we will refer to as the propagator $P(x,y)$. We are able to simplify this expression by translating it in the reciprocal space where the convolution integral turns into a simple multiplication:

$$\tilde{E}_z(u,v) = \tilde{E}_{z=0}(u,v)\tilde{P}_z(u,v) \tag{3.22}$$

where u and v are the spatial frequencies. Experimentally the measured observable is the intensity. In direct space intensity is calculated by $I = |E(x,y)|^2$.
In the Fourier space the intensity, assuming one dimension for simplicity, is:

$$\tilde{I}_z(u) = \left(\tilde{E}_z(u) * \tilde{E}_z^*(u)\right) = e^{-i\pi\lambda z u^2} \int_{-\infty}^{\infty} d\eta e^{i2\pi\eta u} T(\eta) T^*(\eta - \lambda z u) \tag{3.23}$$

We want to reduce the previous expression to a linear relation between the Fourier transform of the phase and the Fourier transform of the recorded intensity distribution of the Fresnel diffraction images. For this purpose, the slowly varying phase (SPV) approximation, also known as the weak-phase approximation is assumed:

$$\begin{aligned} |\phi(\eta) - \phi(\eta - \lambda z u)| &\ll 1 \\ T(\eta)T^*(\eta - \lambda z u) &\approx 1 + i(\phi(\eta) - \phi(\eta - \lambda z u)) \end{aligned} \tag{3.24}$$

Considering the absorption signal negligible compared to the phase, the expression of the intensity in reciprocal space can be reduced to a linear relation between intensity and phase in reciprocal space:

$$\tilde{I}_z(u) \approx \delta(u) + 2sin(\pi\lambda z u^2)\tilde{\phi}(u) \tag{3.25}$$

where δ is the Dirac distribution at $u = 0$. We calculate the cost function in reciprocal space S_c. S_c is a function of the difference between the experimental intensity and the result of the SVP approximation:

$$S_c = \frac{1}{N}\sum_{m=1}^{N}\int du|\tilde{I}_{z_m}^{exp}(u) - \tilde{I}_{z_m}^{approx}(u)|^2 \tag{3.26}$$

The index N represent the number of images taken at N different propagation distances $z = z_1....z_N$.
We now calculate the minimum of eq.3.26, computing the value of $\tilde{\phi}$ for which $\frac{\partial S_c}{\partial \tilde{\phi}} = 0$:

$$\tilde{\phi}(u) = \frac{\sum_m \tilde{I}_{z_m}^{exp}(u)2sin(\pi\lambda z u^2)}{\sum_m 2sin^2(\pi\lambda z u^2)} \tag{3.27}$$

We obtain an expression similar to (3.25) with an extra cosine term for the absorption:

$$\tilde{I}_z(u) \approx \delta(u) + 2sin(\pi\lambda z u^2)\tilde{\phi}(u) - 2cos(\pi\lambda z u^2)\widetilde{\mu_z}(u) \tag{3.28}$$

with the application of least square minimization, this time with respect to $\tilde{\phi}(u)$ and $\widetilde{\mu_z}(u)$, finally we find the retrieval formulas for phase and absorption separately in reciprocal space:

$$\widetilde{\mu_z}(u) = \frac{1}{2\Delta}(A\sum_m \tilde{I}_{z_m}^{exp}(u)sin(\pi\lambda z u^2) - B\sum_m \tilde{I}_{z_m}^{exp}(u)cos(\pi\lambda z u^2) \tag{3.29}$$

$$\tilde{\phi}(u) = \frac{1}{2\Delta}(C\sum_m \tilde{I}_{z_m}^{exp}(u)sin(\pi\lambda z u^2) - A\sum_m \tilde{I}_{z_m}^{exp}(u)cos(\pi\lambda z u^2) \tag{3.30}$$

with:

$$A = \sum_m sin(\pi\lambda z u^2)cos(\pi\lambda z u^2) \tag{3.31}$$

$$B = \sum_m sin^2(\pi\lambda z u^2) \tag{3.32}$$

$$C = \sum_m cos^2(\pi\lambda z u^2) \tag{3.33}$$

$$\Delta = BC - A^2 \tag{3.34}$$

Single distance: Paganin's Algorithm

In the case of propagation-based imaging, Paganin's algorithm allows the simultaneous extraction of phase and amplitude of the waves from a single phase-contrast image (Paganin et al., 2002). The method overcomes the limitation of multiple-distance approach which requires at least two images to obtain information on the phase. However, what it is calculated is the ratio $\frac{\delta}{\beta}$ and we cannot extract separately the values for these two parameters. In other words, it is not possible to decouple the

contributions due to the phase and the absorption.
The following approximations will be made:

- The irradiated object is considered as composed of a single material (approximation of homogeneous object), that means that absorption is proportional to phase, i.e. the ratio $\frac{\delta}{\beta}$ ratio is constant across the whole object;
- Fresnel approximation is assumed;
- The propagation happens in the Fresnel regime (Fresnel number $N_F \gg 1$), i.e. short distance of propagation.

To obtain a comprehensive discussion of the Paganin algorithm it is useful to introduce the expression of intensity transport equation, that describes the intensity of a monochromatic electromagnetic wave when propagated:

$$\Delta_\perp \cdot (I(r_\perp, z)\Delta_\perp \phi(r_\perp, z)) = -\frac{2\pi}{\lambda}\frac{\partial}{\partial z} I(r_\perp, z) \tag{3.35}$$

where $I(r_\perp, z)$ and $\phi(r_\perp, z)$ are the wave intensity and phase, respectively; λ is the wavelength, $r_\perp$ is the position vector in the plane perpendicular to the optical axis z and finally $\Delta_\perp$ is the gradient applied in the same plane of $r_\perp$. We place the X-ray source at infinite distance, resulting in a plane wave, and the sample will be composed of a single material. Let us consider a plane wave with a constant intensity inside the volume occupied by the object. In sake of easy reading, I will rewrite here the Beer-Lambert law already given in eq.2.31:

$$I(r_\perp, z = 0) = I_{in} e^{-\mu\eta(r_\perp)} \tag{3.36}$$

where $\eta(r_\perp)$ is the projection of the object thickness on the image plane, μ is the linear attenuation coefficient and I_{in} is the intensity of the incident radiation. Considering the thin object approximation, the phase $\phi(r_\perp, z = 0)$ of the beam exiting the object is proportional to the projection of the thickness on the image plane:

$$\phi(r_\perp, z = 0) = -\frac{2\pi}{\lambda}\delta\, \eta(r_\perp) \tag{3.37}$$

where δ is the real part of the material index of refraction. Replacing the expressions from eq.3.37 and eq.3.36 inside the intensity transport equation (3.35) we obtain:

$$-\frac{\delta}{\mu} I^{in} \Delta_\perp^2 e^{-\mu\eta(r_\perp)} = \frac{\partial}{\partial z} I(r_\perp, z = 0) \tag{3.38}$$

Eq.3.38 is a linear equation in $e^{-\mu\eta(r_\perp)}$ and its right side can be estimated using two measures of intensity acquired in two planes placed at a distance R_2 between each other:

$$\frac{\partial}{\partial z} I(r_\perp, z = 0) = \frac{I(r_\perp, z = R_2)}{e^{-\mu\eta(r_\perp)} I^{in}} \tag{3.39}$$

Replacing the previous expression inside the eq.3.38 we obtain:

$$(-\frac{R_2\delta}{\mu}\Delta_\perp^2 + 1)e^{-\mu\eta(r_\perp)} = \frac{I(r_\perp, z = R_2)}{I^{in}} \tag{3.40}$$

Taking the Fourier integral of the images acquired at $z = 0$ and in phase contrast at $z = R_2$ and substituting them in eq.3.40:

$$\Im[e^{-\mu\eta(r_\perp)}] = \mu \frac{\Im[I(r_\perp, z = R_2)]/I^{in}}{r_2\delta|k_\perp|^2 + \mu} \tag{3.41}$$

Calculating the inverse Fourier transform ($\Im^{-1}$) of eq.3.41 and solving with respect to $\eta(r_\perp)$, the final expression can be written:

$$\eta(r_\perp) = -\frac{1}{\mu}\log_e(\Im^{-1}\{\mu \frac{\Im[I(r_\perp, z = R_2)]/I^{in}}{r_2\delta|k_\perp|^2 + \mu}\}) \tag{3.42}$$

Eq.3.42 shows how to solve the intensity transport equation (eq.3.35) from a sample thickness projection $\eta(r_\perp)$ and using images acquired at a single distance. The object thickness $\eta(r_\perp)$ is related to the intensity and to the phase of the radiation after the sample. The thin object approximation is always satisfied in the hard X-ray region and for biological samples. The Paganin algorithm allows to reconstruct images proportional to the phase of an homogeneous object from images acquired at one single distance.

3.4 Conclusion

In this chapter a general introduction to X-ray phase-contrast imaging was given. Being able to resolve weakly absorbing details inside the matters, phase-contrast imaging founds many applications in biology, material science and industry.
The main phase-based techniques were presented, with particular attention to the free space propagation imaging. Wave optic theory was used for a general description of free space propagation.

Chapter 4

Basics of X-ray Tomography

Tomography (from Greek $\tau\grave{o}\mu o\zeta$, "section", and $\gamma\rho\acute{a}\psi\omega$, "to write") indicates an imaging technique which represents the investigated object in layers or sections through the use of any kind of penetrating wave (Hounsfield, 1995, Weissleder et al., 2011), as opposed to conventional radiography which has all the thickness of the object projected on the two-dimensional plane. The method is used in a multitude of science areas, like radiology, biology, astrophysics, atmospheric science, geophysics, materials science, conservation science, etc.

4.1 Radiography and X-ray Tomography

To introduce the main characteristics of X-ray tomography it is useful to start from the main features of the classical 2D radiography. A radiography image is a photographic recording produced by the passage of radiation through a subject onto a photosensitive detector. The final image is a 2D map of the absorption coefficient, μ_z, of the analyzed object. The main limitation of this technique is that the image is the superposition of the signal obtained passing through all the object thickness, making impossible to retrieve the spatial distribution of its internal structures. This limitation was overcome with X-ray tomography. This imaging technique allows to obtain 3D images of a thick object and enables its virtual sectioning. In this way, transverse sections of the object are obtained, called *slices*, which distribution is proportional to the attenuation properties of the object (Suetens, 2009). The sample is divided in elementary volume units called voxel (volumetric picture element) that are the three-dimensional counterpart of the two-dimensional pixel. In a tomographic acquisition the image is formed in the following way: the sample is illuminated with an X-ray beam and the radiation coming out from the sample is measured with a pixelated detector. To allow the tridimensional reconstruction of the object, normally the beam has to be larger than the object size.The field of view of each measurement is defined by the combination of the detector and beam size. This acquisition procedure is repeated for many acquisition angles (fig. 4.1), rotating the sample respect to the detector and the source. The values that are assigned to the pixels in a CT image are associated with the average linear attenuation coefficient μ of the tissue represented within that pixel. The image acquired for each direction represents a bidimensional projection of the object, a classical radiography, that goes under the name of projection. Every projection does not give any tridimensional information of the specimen.
Tomographic images need in fact a reconstruction algorithm to visualize in 3D the object starting from its projection images. For simplicity, we will consider conventional absorption tomography. The expression for the beam intensity attenuation

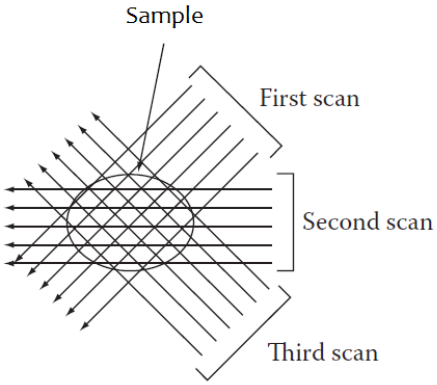

FIGURE 4.1: Scanning procedure of the a tomography scan for a parallel beam geometry.Image adapted from Flower, 2012.

after passing trough an object with thickness Δx is the following:

$$\frac{I_1}{I_0} = \mu(x)\Delta x \tag{4.1}$$

where I_0 is the intensity of the incident beam, I_1 is the intensity of beam after the sample and $\mu(x)$ is the attenuation function. We call L the direction corresponding to each angle. From eq.4.1 follows that:

$$\frac{I_1}{I_0} = e^{-\int_L \mu(x)dx} \tag{4.2}$$

The scan procedure provides the linear integral of the function $\mu(x)$ (eq.4.2) along every direction of acquisition L. From a mathematical point of view tomography is the reconstruction of an unknown function $\mu(x)$ starting from its linear integral. The transform that maps a function in the real space $\Re^2$ into the set of its linear integrals is called Radon Transform (Radon, 1986).

4.2 Projections and Radon Transform

The Radon Tranform connects every point of the cartesian plane (x, y) to the set of its linear integrals in the rotated plane of Radon (r, s) (Flower, 2012). Let us consider a 2D parallel-beam geometry system where $\mu(x, y)$ is the distribution of the linear attenuation coeffient in the plane (x, y) (fig.4.2). We assume that $\mu(x, y)$ equals to

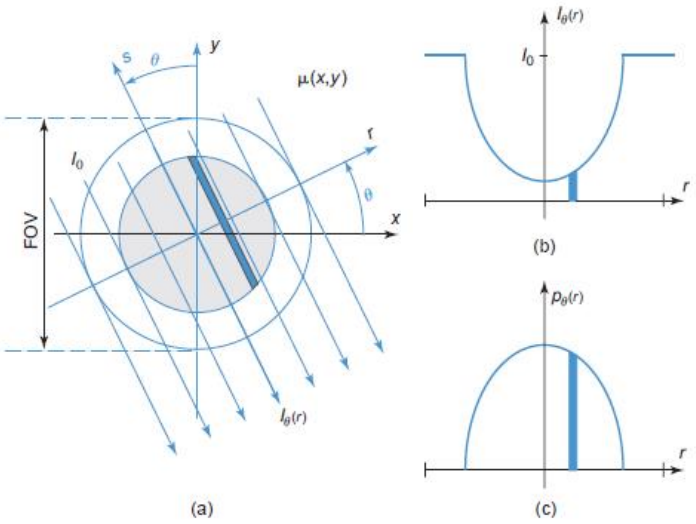

FIGURE 4.2: a) Parallel-beam geometry with coordinate systems. The X-ray beams make an angle θ with the y-axis and are at distance r from the origin. b) An intensity profile $I_\theta(r)$ is measured for every view (defined by an angle θ). I_0 is the unattenuated intensity. c) The attenuation profiles $p_\theta(r)$, obtained by log-converting the intensity profiles $I_\theta(r)$, are the projections of the function $\mu(x, y)$ along the angle θ. Image adapted from (Flower, 2012).

zero outside a circular section of diameter equivalent to the field of view. I_0 is the intensity of the incident beam and θ is the angle between the X-ray beam direction and the y-axis. Applying a rotation of an angle θ to the cartesian plane (x, y) we obtain a new coordinate system (r, s). The following transformations describe how these two coordinates systems are related :

$$\begin{vmatrix} \text{r} \\ \text{s} \end{vmatrix} = \begin{vmatrix} \cos\theta & \sin\theta \\ \text{-sin}\,\theta & \cos\theta \end{vmatrix} \begin{vmatrix} \text{x} \\ \text{y} \end{vmatrix} \; ; \; \begin{vmatrix} \text{x} \\ \text{y} \end{vmatrix} = \begin{vmatrix} \cos\theta & \text{-sin}\,\theta \\ \sin\theta & \cos\theta \end{vmatrix} \begin{vmatrix} \text{r} \\ \text{s} \end{vmatrix} \tag{4.3}$$

For every angle θ the measured intensity as a function of the coordinate r (fig.4.2 b) is defined by:

$$I_\theta(r) = I_0 e^{-\int_{L_{r,\theta}} \mu(x,y)ds} = I_0 e^{-\int_{L_{r,\theta}} \mu(r\cos\theta - s\,\sin\theta, r\sin\theta + s\,\cos\theta)ds} \tag{4.4}$$

where $L_{r,\theta}$ is the line that forms an angle θ respect to the y-axis at a distance r from the axis origin. To simplify the expression, in eq.4.4 the energy dependence has been omitted. The beam intensity for each direction is transformed in an attenuation function :

$$p_\theta(r) = -ln\frac{I_\theta(r)}{I_0} = \int_{L_{r,\theta}} \mu(r\cos\theta - s\,\sin\theta, r\sin\theta + s\,\cos\theta)ds \tag{4.5}$$

where $p_\theta(r)$ is the projection of the function $\mu(x,y)$ along the axis θ(fig.4.2 c). The projection function $p_\theta(r)$ can be measured for each angle θ between 0 and 2π, but the projections corresponding to supplementary angles will create identical images. It is thus sufficient to measure $p_\theta(r)$ in a range between 0 and π (fig.4.3). Considering all

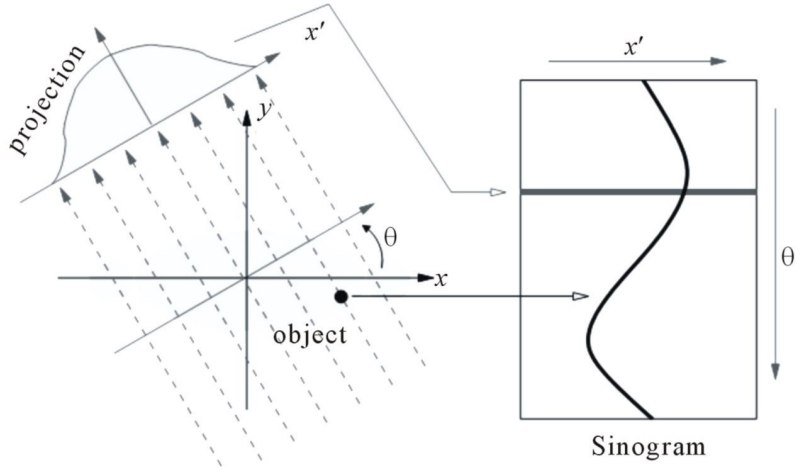

FIGURE 4.3: Illustration of mapping between the object space and the sinogram space (left). A sinogram is formed by stacking all of the projections of different views, so that a single projection is represented by a horizontal line in the sinogram. The projection of a single point forms a sinusoidal curve in the sinogram space. Image from (Hsieh, 2003).

the projection together, we obtain a set of bidimensional data $p(r,\theta)$ called *sinogram* (fig.4.4). Once the direction r is fixed, the projection function $p(r,\theta)$ has a sinusoidal shape. Mathematically the transformation of every function $f(x,y)$ in its sinogram $p(r,\theta)$ is called Radon Transform:

$$p(r,\theta) = \Re[f(x,y)] = \int_{-\infty}^{+\infty} f(rcos\theta - s\,sin\theta, rsin\theta + s\,cos\theta)ds \tag{4.6}$$

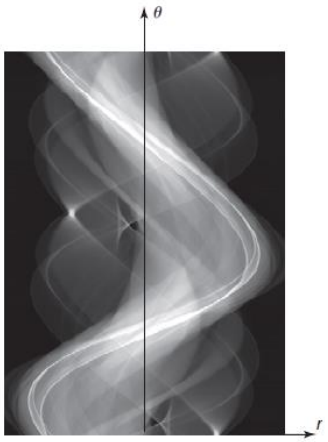

FIGURE 4.4: A sinogram is a 2D dataset $p(r,\theta)$ obtained by stacking the 1D projections $p_\theta(r)$. Image from (Flower, 2012).

4.3 Backprojection

In order to reconstruct the analyzed object it is necessary, given the sinogram $p(r,\theta)$, to reconstruct the distribution $\mu(x,y)$ of the linear attenuation coefficient. One possible solution to this problem is to assign the value of $p(r,\theta)$ to all the points (x,y) belonging to a given line (r,θ). This operation is then repeated for all the angles θ between 0 and π. This algorithm is called Backprojection and it can be expressed with the following mathematical expression:

$$b(x,y) = B[p(r,\theta)] = \int_0^{\pi} p(x\,cos\theta + y\,sin\theta, \theta)d\theta \tag{4.7}$$

To link the sinogram with the original function $f(x,y)$, we need to apply the inverse Radon transform :

$$f(x,y) = \Re^{-1}[p(r,\theta)] \tag{4.8}$$

This mathematical problem is solved by the *Projection Theorem* that will be discussed in the following (Hsieh, 2003). Let us define $F(k_x,k_y)$ as the 2D Fourier transform (FT) of the function $f(x,y)$ and $P_\theta(k)$ as the 1D Fourier transform (FT) of $p_\theta(r)$. If we consider θ as a variable, $P_\theta(k)$ becomes a 2D function of $P(k,\theta)$. The projection theorem states that:

$$P(k,\theta) = F(k_x,k_y) \tag{4.9}$$

with:

$$k_x = kcos\theta; k_y = ksin\theta; k = \sqrt{k_x^2 + k_y^2}. \tag{4.10}$$

In other words, the theorem affirms that $P(k,\theta)$, that is the 1D FT of the Radon transform of a generic 2D function $f(x,y)$, equals $F(k_x,k_y)$, the 2D FT of the same function $f(x,y)$.
It is possible to calculate the function $f(x,y)$ for each point (x,y) starting from its set of projections $p_\theta(r)$ with θ defined inside the interval (0 ,π) .
The image reconstruction problem can be easily solve by the Projection Theorem (Francesco and Silva, 2004): starting form the projections of the desired function $f(x,y)$ for a series of angles θ, applying a 2D FT to $p_\theta(r)$ we can calculate $P_\theta(k)$ for a certain number of radial directions (fig.4.5 a). Theoretically, assuming an infinite number of projections, the values of the function $P_\theta(k)$ will be known for every point and the object function $f(x,y)$ could be calculated with a 2D inverse Fourier transform. However, in a real tomographic acquisition the number of projections is finite and to approximate the function $F(k_x,k_y)$ an interpolation between the points in the polar plane (r,s) and in the cartesian plane (x,y) is needed (fig.4.5 b). The function $f(x,y)$ is finally calculated with a 2D inverse Fourier transform of $F(k_x,k_y)$. There are two problems related with this approach.

First, the data collected in the Fourier domain lie on a radial grid, while the algorithms performing the inverse transformation, such as the Fast Fourier transform, require a Cartesian grid. This means that we will have to apply interpolation in the Fourier domain which causes strong reconstruction artefacts.
Second, the sampling distribution in the Fourier domain is much denser near the origin respect to the outer regions. Therefore, the lowest frequencies (which lie close to the origin) are over-sampled, meaning that they will be reconstructed fairly accurately. On the other hand, the high frequencies (where most of the finer details of the object are located) are under-sampled and cannot be accurately reconstructed after the inverse Fourier transform: this will lead to blurry images.

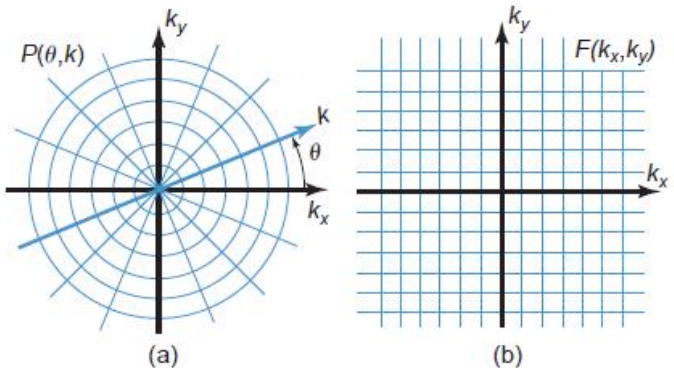

FIGURE 4.5: a) The function $P_\theta(k)$ is defines in a polar reference system. b) The calculation of $F(k_x, k_y)$ in a cartesian coordinate system is needed to reconstruct the image represented by $f(x, y)$.

The reconstruction method called filtered backprojection (FBP), based on the Fourier slice theorem, overcomes these limitations: it avoids the occurrence artefacts by interpolating the data in real space and introduces an additional filtering step. This practical approach will be described in the following section.

4.3.1 Filtered Backprojection

We are now finally ready to make an attempt at recovering the object function by means of filtered backprojection, which involves two steps: a filtering and a backprojection step. In the Filtered Backprojection (FBP) algorithm the interpolation step on raw data is avoided by applying a filter on the sinogram $p(r,\theta)$ and backprojecting the filtered sinogram (Flower, 2012). Let us analyze this technique more in detail.
The function $f(x,y)$ can be rewritten as its 2D inverse Fourier transform in polar coordinates:

$$f(x,y) = \int_0^{\pi} \int_{-\infty}^{+\infty} P(k,\theta)|k|e^{i2\pi kr} dk d\theta \tag{4.11}$$

with $r = xcos\theta + ysin\theta$. Let us define:

$$P^*(k,\theta) = P(k,\theta)|k| \tag{4.12}$$

and

$$p^*(r,\theta) = \int_{-\infty}^{+\infty} P^*(k,\theta)e^{i2\pi kr} dk \tag{4.13}$$

Taking into account the last two equations, we can rewrite the eq.4.11 as:

$$f(x,y) = \int_0^{\pi} p^*(r,\theta) d\theta \tag{4.14}$$

The function $f(x,y)$ can thus be reconstructed backprojecting $p^*(r,\theta)$, that is the 1D inverse Fourier transform respect to the variable k of $P^*(k,\theta)$. The function $P^*(k,\theta)$ was calculated multiplying $P(k,\theta)$ with the filter $|k|$.
Mathematically, a multiplication in the Fourier space corresponds to a convolution in the reciprocal space, so $p^*(r,\theta)$ can be rewritten as:

$$p^*(r,\theta) = \int_{-\infty}^{+\infty} P(r',\theta)q(r-r')dr' \tag{4.15}$$

with

$$q(r) = F^{-1}\{|k|\} = \int_{-\infty}^{+\infty} |k|e^{i2\pi kr} dk \tag{4.16}$$

The function $q(r)$ is called nucleus of the convolution.
In summary, the FBP reconstruction algorithm can be described by two main steps:

- *Sinogram filtering* $p(r,\theta)$:
  $p^*(r,\theta) = p(r,\theta) \star q(r)$ or $P^*(k,\theta) = P_\theta(k) \cdot |k|$
- *Backprojection of the filtered sinogram* $p^*(r,\theta)$:
  $f(x,y) = \int_0^{\pi} p^*(xcos\theta + ycos\theta, \theta)d\theta$

Backprojecting considering only a few directions θ, will reduce dramatically the accuracy in the object reconstructed. A sufficient number of acquisition angles (projections) needs to be acquired to resolve the inner details of complex objects. In fig.4.6 the result of a chest tomography using successive filtered backprojections, considering different number of projections from 1 to 1024, is shown. This shows how successive filtered backprojections under different angles can be used to achieve a good reconstruction of the space domain.

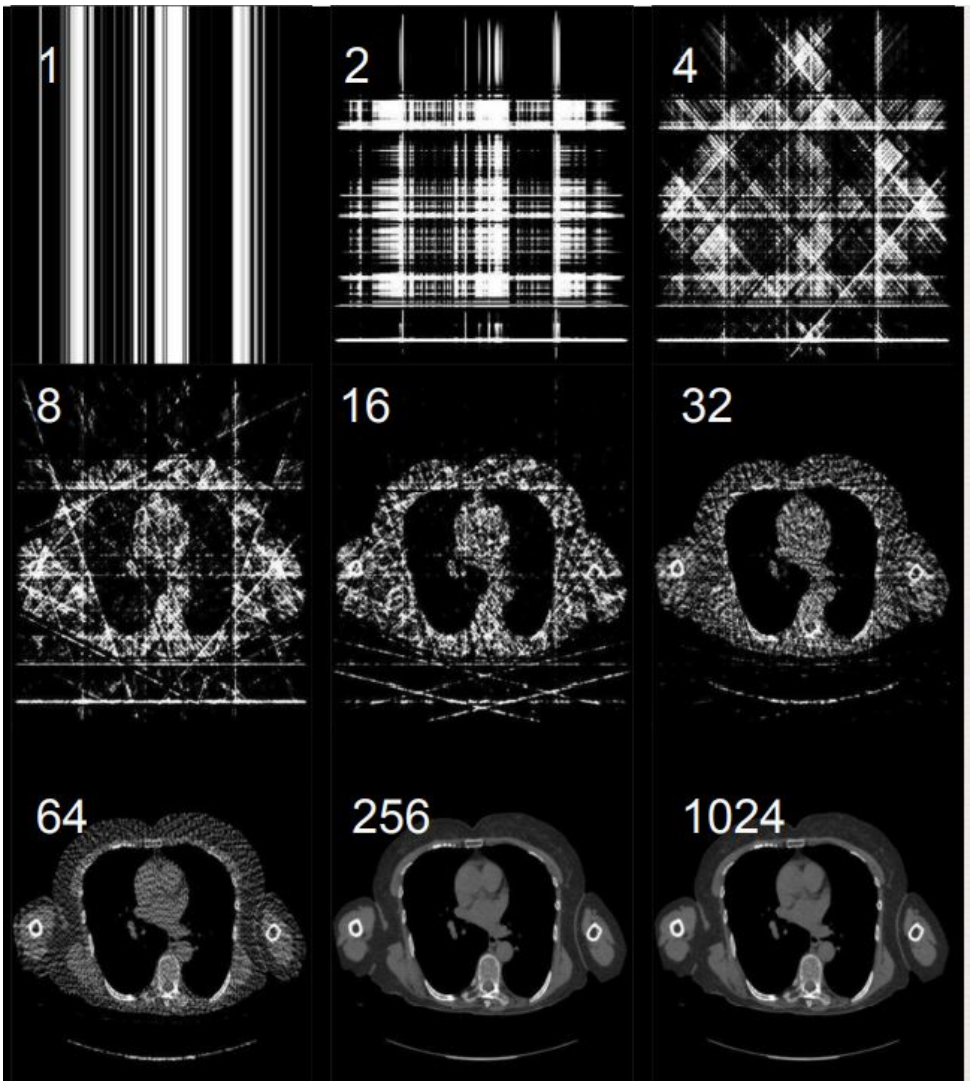

FIGURE 4.6: Chest tomography reconstruction using successive filtered backprojections. Successive filtered backprojections using 1, 2, 4, 8,16, 32, 64, 256, and 1024 projections. Image from (*Diagnostic Radiology Physics* 2014).

4.3.2 Cone beam Filtered Backprojection

The reconstruction algorithm described before can be applied if the data have been acquired in a parallel beam geometry. All the table-top sources normally used in a laboratory set-up present a cone beam geometry, where the X-rays are divergent, forming a cone. Both the coordinates (r, θ) used in parallel beam geometries and the coordinates (γ, β) used in cone beam geometries are shown in fig.4.7, with the detector placed along a circular arc. The angle between the source and the y-axis is β, and γ is the angle between the ray through (x, y) and the center line of the associated cone. We define the cone angle as the angle formed by the cone. For simplicity, to

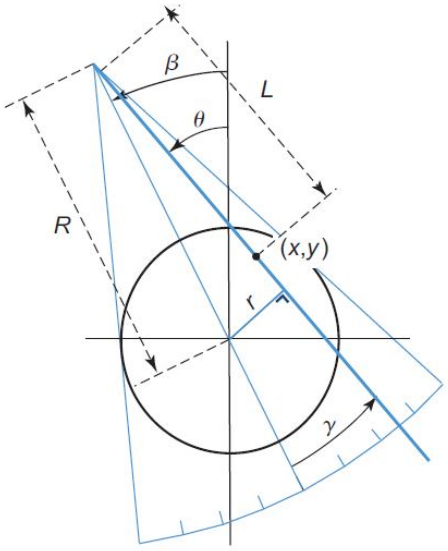

FIGURE 4.7: Cone beam geometry with detector placed on a circular arc: β is the angle between the center line of the cone and the y-axis, γ is the angle between the center line and the ray through point (x, y). L is the distance from the source to (x, y). Image from Suetens, 2009.

describe the reconstruction algorithm in cone beam geometry we assume to have data corresponding to β from 0 to 2π. Two possible reconstruction approaches exist:

- Rebinning involves the reordering of the data into parallel data and requires interpolation,
- An adapted equation for filtered backprojection can be used.

Substituting eq.4.15 in eq.4.14 and limiting $r^{'}$ in the integration to $[FOV/2, FOV/2]$ (with FOV = Field Of View) yields:

$$f(x,y) = \frac{1}{2}\int_0^{2\pi}\int_{-FOV/2}^{FOV/2} p(r^{'},\theta)\cdot q(xcos\theta + ysin\theta - r^{'})dr^{'}d\theta \tag{4.17}$$

The coordinate transformations from parallel to cone beam geometry are the follow-

ing:

$$\begin{aligned} \theta &= \gamma + \theta \\ r &= Rsin\gamma \end{aligned} \tag{4.18}$$

where R is the distance from the top of the cone, i.e. the position of the source, to the center of the FOV. Introducing these new coordinates and after a few calculations,the following cone beam reconstruction formula can be derived (Kak and Slaney, 1988):

$$f(x,y) = \int_0^{2\pi} \frac{1}{L^2} \int_{-(cone-angle)/2}^{(cone-angle)/2} [Rcos\gamma' \cdot p(\gamma',\beta)] \frac{1}{2} sin\Big(\frac{\gamma-\gamma'}{sin(\gamma-\gamma')}\Big) q(\gamma-\gamma') d\gamma' d\beta \tag{4.19}$$

where L is the distance from the image point (x, y) to the top of the cone. Note that this expression is a modified Filtered Backprojection weighted with $\frac{1}{L^2}$. The inner integral is a convolution of $p(\gamma,\beta)$, weighted with $Rcos\gamma$, with a modified filter kernel $\frac{1}{2}(\frac{\gamma}{sin\gamma})^2 q(\gamma)$.
A similar equation can be derived if the detector lies on a straight line perpendicular to the center line of the cone. In this configuration the coordinates (α,β) are used; where α is the distance from the origin to the ray through (x, y) measured parallel to the detector array.
It can be shown (Kak and Slaney, 1988) that the weighted Filtered Backprojection can now be written as:

$$f(x,y) = \int_0^{2\pi} \frac{1}{(U/R)^2} \int_{-\infty}^{+\infty} \Big[\frac{R}{\sqrt{R^2+\alpha'^2}} \cdot p(\alpha',\beta)\Big] \cdot \frac{1}{2} q(\alpha-\alpha') d\alpha' d\beta \tag{4.20}$$

where U is the projection of distance between the source a generic point (x,y) onto the central ray of the cone.

4.3.3 Iterative Algorithms

Among the reconstruction algorithms for tomography, filtered back-projection (FBP) is the most widely used. As previously seen, in FBP algorithm images are created by back-projecting individual attenuation measurement for each point in space.
Recently, iterative methods have been proposed (Tessa et al., 2007), such the simultaneous algebraic reconstruction techniques (SART) and the simultaneous iterative reconstruction technique (SIRT).
The first iterative technique was the algebraic reconstruction technique (ART) (Raparia, Alessi, and Kponou, 1997). To understand the ART reconstruction algorithm, we can start from the following linear algebraic problem:

$$W \cdot \vec{v} = \vec{P} \tag{4.21}$$

where $\vec{v}$ is a vector that contains the values of all the pixels in the image, $\vec{P}$ is the vector of the projections for every ray per angle and W is the weight matrix.
The most important parameter is the matrix W, that contains the weights of every pixel for all the different rays in the projection.
The ART algorithm is based on spreading the density values in the reconstruction space and then modify this values at each iteration. Basically, the grayness of pixels on the intersections of the rays are changed to make the ray sum correspond to the

measured projection. In the following we will concentrate on a brief description of the two main iterative algorithms: SIRT and SART

SIRT

The simultaneous iterations reconstruction technique (SIRT) is one of several reconstruction algorithms of the ART family (Gilbert, 1972,Hansen and Jørgensen, 2017). The main issue faced by the ART algorithm is that one pixel can be crossed by many rays during one iteration. Updating the grid after every ray will thus create artefacts in the image. To solve this problem, SIRT updates the pixel values only at the end of each iteration. In this way, the efficiency and precision are both improved. Also, SIRT algorithms require several iterations to reach convergence.

SART

The simultaneous algebraic reconstruction technique (SART) was introduced in 1984 as a great improvement of ART and SIRT (Jiang and Wang, 2001). In contrast with ART, the grid correction in the SART approach is not performed with ray-by-ray updates. Here the pixels are updated after a computation of the whole projection image at a certain angle. This means that the error correction terms are applied simultaneously for all rays of a certain projection.

4.4 Conclusion

In this chapter we introduced the main aspects of X-ray tomography, starting from a comparison with the bidimensional radiography technique and considering the mathematical transformations that are need to reconstruct an object in 3D. The Back-projection algorithm is described to link the 2D projection data acquired at different angles with the volumetric reconstruction.

Chapter 5

Phase Imaging with the Hartmann Wavefront sensor

Here we will discuss about the use of the Hartmann wavefront sensor in a non classical way. This technique can be used to perform imaging of biological samples (see section 6.7), to retrieve information about the components of the index of refraction (δ and β) (see section 7) and to infer the chemical properties of a given material.

5.1 Introduction

In order to optimize the classical Hartmann sensor for X-ray imaging application, there are several aspects to consider. To answer many open questions on the Hartmann sensor's design a precise simulation tool is needed.
The simulation results were divided in several parts to asse different issues. In the first section we consider the features connected with the propagation process (section 5.9) from one set-up element to the other: source energy, aperture shape, pitch and set-up distances.
In the second section (section 5.10) several parameters connected with the detection process have be analyzed : first, the capabilities of classical detection algorithms (First Moment, Weighted First moment, Gaussian Three-Point Fitting) will be studied for a theoretical spot (gaussian shape), with particular attention to effect of threshold level applied to binarized images. To improve the detection performance, more advanced algorithms (Iterative Gaussian Weighted and 2D Gaussian Fit) will be also described.
Later, the results of these two sections will be combined together to analyze the outcome of several detection algorithms to a propagated spot (Bessel and Sinc function). Finally, the same analysis will be applied to a real experimental spot. In fig.5.1 a general overview of the performed analysis is given.
Concerning the first section (fig.5.1), parameters connected with the source has to be consider. The choice of mask material and thickness are in fact strictly related with the source properties. The degree of coherence will not be considered in this section since we discuss extensively the effect of coherence level on the design of an Hartmann sensor (section 5.6).
For the Hartmann plate array several geometries can be proposed, we will concentrate on a 2D repetitive pattern with square or circle apertures. The two parameters to optimize are the aperture size and the pitch size (distance between the centers of two apertures).
Particular attention should be given to the effect of wave propagation. Since in our code we use free space propagation, the distances between every component will be

related with different diffraction regimes (from near-field to Fraunhofer diffraction regime, see chapter 5.9.1). Regarding the detection part of the analysis (fig.5.1), the

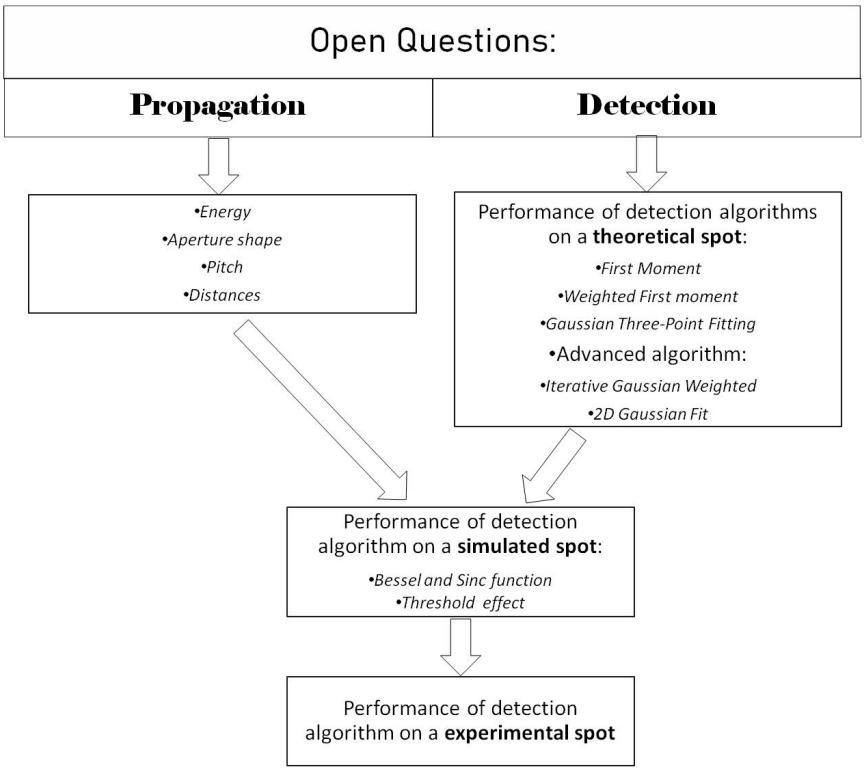

FIGURE 5.1: General overview of the analysis connected with the Hartmann sensor design. First, aspects connected with the wave propagation from one set-up element to the other are considered . After, features connected with the spot detection are examined for a theoretical spot. Finally, these two analysis are combined together to examine the detection capabilities after propagation and on a real experimental example.

first open question is which detection algorithm works better for different aperture geometries. Classical and advanced centroid algorithms will be thus applied to a theoretical spot (gaussian shape), to a simulated spot after propagation (square and circular aperture) and finally to our experimental results.
Both classical mask geometries based on absorption and phase-contrast mask will be considered.

5.2 Wavefront definition

As a wave propagates, its disturbance according to the Huygens-Fresnel principle is given by the superposition of secondary spherical wavelets weighted by the amplitudes at the points where they originate on the wave (Mahajan, 1998). Each element of the surface of the wave in fact will propagate and becomes a source of a spherical wave, where the amplitude will be proportional to the surface element (fig.5.2). The wavefront is defined as the group of points in space where the wave has the same phase (Goodman, 2005). It is usually quantified as the deviation from a plane or spherical wavefront measured in meter or in radians. The phase difference can thus be quantified as the difference of optical path $\Delta(x, y)$ between two points P(x,y),

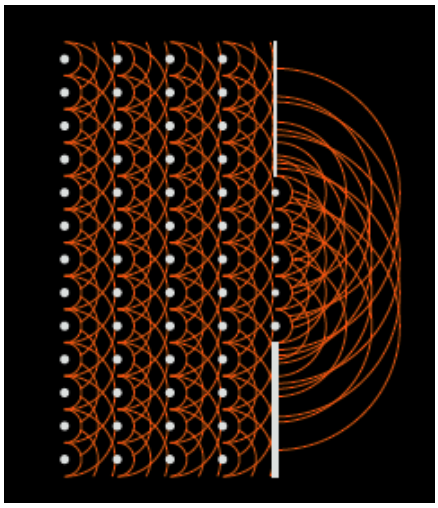

FIGURE 5.2: Illustration of the Huygens-Fresnel principle showing the gradual propagation of a plane wave through the excitation of secondary waves. Image adapted from Peatross and Ware, 2010.

P'(x,y), belonging respectively to the surface of the reference plane wave and of the wave surface under study (fig. 5.3). Taking a monochromatic radiation of wavelength λ, the phase difference can be expressed as:

$$\Delta\phi = \frac{2\pi}{\lambda}\Delta(x,y) \tag{5.1}$$

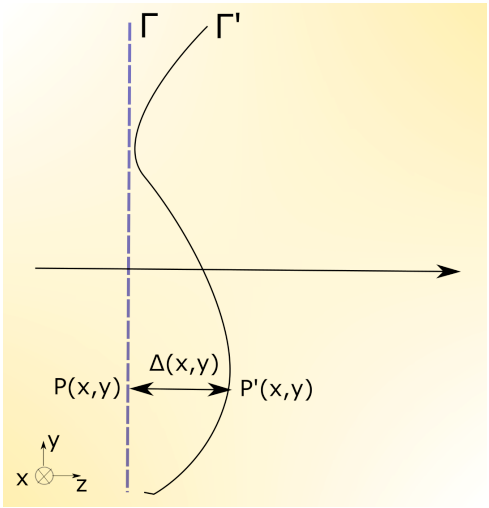

FIGURE 5.3: The wavefront of a wave Γ' is quantified by the difference of the optical path $\Delta(x,y)$ respect to a plane wavefront Γ and it can be expressed as meter or fraction of the wavelength λ .

5.3 Wavefront detection

A wavefront sensor is a device capable of measuring the phase of the incoming light (Hartmann, 1900, Born and Wolf, 1980). Several techniques have been proposed to measure the incident wavefront in the X-ray regime. For soft X-ray lasers Hartmann sensors have been proposed with array of holes (Le Pape et al., 2002,Mercère et al., 2003), zone plate (Baker et al., 2003) or refractive lenses (Mayo and Sexton, 2004). Curvature sensors (Baker, 2003), which measure the Laplacian of the phase, and two-dimensional interferometers (Bonse and Hart, 1965,Tejnil et al., 1997,Baker, 2009,Vogt et al., 2005,Filevich et al., 2004), based on two orthogonal phase gratings in the same plane, can be also implement to measure the wavefront of an X-ray beam. However, in general, Hartmann masks are simpler to fabricate, easy to scale up to areas of several centimeters (see chapter 6.6), can be applied at higher X-ray energies, and are tolerant to defects, imperfections, and polychromatic beams (see chapter 7). The Hartmann sensor was invented to perform optical metrology, and its applications ranges from adaptive optics to laser wavefront characterization. We will focus on the implementation of an Hartmann wavefront sensor for phase contrast images. The Hartmann wavefront sensor consists of a hole array mounted at a certain distance from the detector. The incident X-ray beam will be sampled by the aperture array where each hole will locally sample the incident wavefront generating a series of beamlets.
The wave front sensor measures the tilt over each aperture by comparing the measured positions of the diffracted spots to the positions of the diffracted spots for a reference input beam (fig.5.4). The deplacement of each spot is, in fact, directly proportional to the local derivative of the wavefront in that point.
These tilt measurements are then converted into a local measure of the wavefront by performing an integration called wavefront reconstruction (Fried, 1977, Southwell, 1980, Hudgin, 1977). In a Hartmann wavefront sensor the incident X-ray beam will

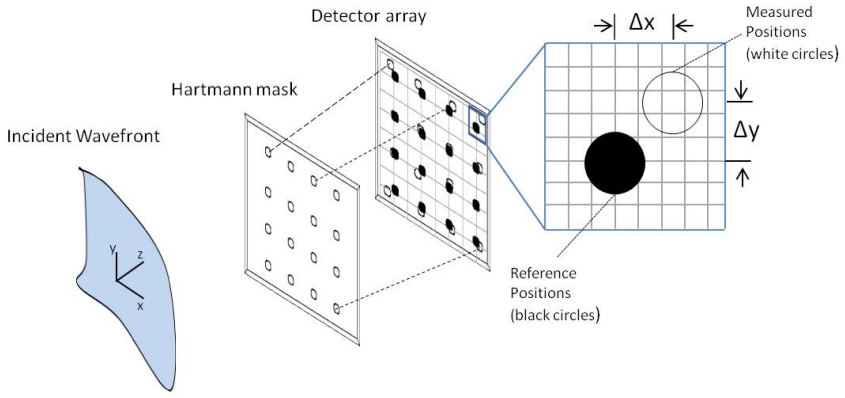

FIGURE 5.4: Drawing of the Hartmann wave front sensor operation. Showing an incident wave front traveling along the z-axis illuminating an aperture array and the diffracted spots illuminating a detector and the displacement of a single diffracted spot from the reference location on the detector.

be sampled by the aperture array where each hole will locally sample the incident wavefront generating a series of beamlets (see section 5.2).
The wave front sensor measures the tilt over each aperture by comparing the measured positions of the diffracted spots to the positions of the diffracted spots for a

reference input beam. Fig 5.4 shows the schematic diagram of the sensor operation. In order to measure the incident wavefront with the Hartmann wavefront sensor, the first step is to determine the location of the diffracted spots. We define the z-axis as the optical axis normal to the planes of the detection and of the aperture arrays. The x and y axes are located in the plane of the detector.
Spots positions are determined from the reference image by calculating their centroids or first moments (Spiricon, 2004) along both the x-axis and the y-axis. The centroid in the x direction, $\bar{x}$, of an arbitrary intensity pattern is given as:

$$\bar{x} = \frac{\int_{-\infty}^{+\infty}\int_{-\infty}^{+\infty} I(x,y)xdxdy}{\int_{-\infty}^{+\infty}\int_{-\infty}^{+\infty} I(x,y)dxdy} \tag{5.2}$$

where I(x,y) is the intensity function for the point (x,y) on the detector plane. Although, in reality, the detectors are composed of a discrete set of pixels that will be described by the variable i along the x-axis and j along the y-axis.
Thus, this discretization of the Hartmann system allows us to transform continuous variables into a discrete form, replacing the integral of eq.5.2 with a summation. Furthermore, we have to change the limits of the integration to apply this formula to measure an array of diffracted spots.
The standard strategy to calculate the positions of the diffracted spots is to sample the grid of spots with an array of small rectangular sections that are centered on each projection of the aperture and with sides as long as the aperture spacing. These rectangular sections are named area-of-interest (AOI).
The centroid integration will be then performed inside these sections for each aperture. Finally, the general first moment centroid equation can be rewritten as:

$$\bar{x} = \frac{\sum_i \sum_j I(i,j) i\, s}{\sum_i \sum_j I(i,j) i} \tag{5.3}$$

where the indexes i and j corresponds to the rectangular integration areas in the x and y-axis respectively, I(i,j) is the intensity measured by the pixel in the i^{th} row and j^{th} column and s is the spacing of pixels along the x or y axes.
The equivalent equation can be used to determine the position of the diffracted spot along the y-axis. To minimize the effects of noise due to the camera and due to the diffracted light, the intensity I(i,j) is usually thresholded. If the intensity is below the threshold, the intensity at this pixel is set to zero. Otherwise, the intensity minus the threshold is used in the calculation.
To perform any measurement, the Hartmann wavefront sensor is illuminated with a beam whose wavefront, $\Phi(x,y)$ is being measured and the diffracted spot positions are determined from the detctor image using the centroid algorithm. The slope of the measured wave front is determined by measuring the spatial displacement of a diffraction pattern from that due to a reference wave incident on the same aperture array.

The wavefront slope can be calculate starting from the geometry described in fig.5.5:

$$\begin{aligned} R^2 &= r^2 + (R - \Phi(r))^2 \\ \Phi(r) &= R - \sqrt{r^2 - R^2} \end{aligned} \tag{5.4}$$

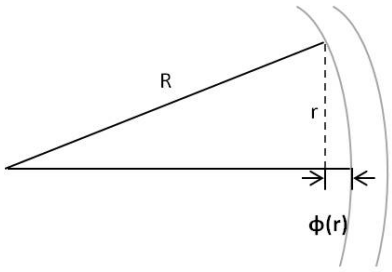

FIGURE 5.5: Showing two successive wavefronts (gray lines) with a radius of curvature, R, and the phase as a function of radius, r, from the optical axis.

Expanding the wavefront and assuming the paraxial approximation (R » r) we get:

$$\Phi(r) \approx \frac{r^2}{2R} \tag{5.5}$$

Thus the slope of the wavefront respect to r is :

$$\frac{\Phi(r)}{dr} \approx \frac{r}{R} \tag{5.6}$$

In the Hartmann wavefront sensor this slope is determined by measuring the spatial displacement of a diffraction pattern from the one of a reference wave incident on the same aperture array.

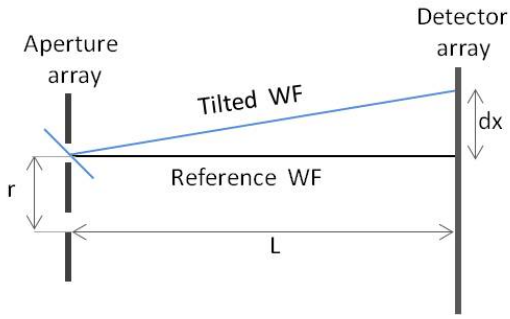

FIGURE 5.6: Schematic representation of the diffraction spot displacement on the detector due to the slope of the wavefront at the aperture array.

The local gradient of the wavefront over the aperture diameter along the x-axis (and in the same way for the y-axis) is calculated using the equation:

$$\begin{aligned} \frac{\partial \Phi(x,y)}{\partial x} &= \frac{\partial x}{L} \\ \frac{\partial \Phi(x,y)}{\partial y} &= \frac{\partial y}{L} \end{aligned} \tag{5.7}$$

where L is the distance between the aperture array and the detector array.

5.3.1 Centroiding Methods

The accuracy of the reconstructed wavefront is largely dependent on the determination of the spot centers, commonly referred to as "centroiding" . The most used method is intensity-based and it is called the first moment calculation (eq. 5.3). It allows to have a fast and robust centroid calculation, even if its performances decrease when noise level increases. We will investigate different existing centroiding methods (Ferstl, 2016; Nightingale and Gordeyev, 2013) : First Moment centroid, a Weighted First Moment centroid, Gaussian Three-Point Fitting centroid, an Iterative Gaussian Weighted centroid and a 2D Gaussian fit centroid.

In the **Weighted First Moment centroid**, the weighting function W(x,y) has a Gaussian shape and its initial central position is given by previous centroiding runs (for instance with the first moment algorithm):

$$W(x,y) = \frac{1}{2\pi^2} e^{-((x-\bar{x})^2+(y-\bar{y})^2)/(2\sigma^2)} \tag{5.8}$$

where W(x,y) is a Gaussian centered in ($\bar{x}$,$\bar{y}$) and with FWHM= 2 $\sigma\sqrt{ln(2)}$.
Then the position moments are calculated up to the second order:

$$\begin{aligned} S_W &= \sum_{x,y} I(x,y)W(x,y), & S_x &= \sum_{x,y} xI(x,y)W(x,y) \\ S_{xx} &= \sum_{x,y} x^2 I(x,y)W(x,y), & S_{yy} &= \sum_{x,y} y^2 I(x,y)W(x,y) \end{aligned} \tag{5.9}$$

The centroid positions are then calculated in the following way:

$$\begin{aligned} \bar{x} &= \frac{S_x}{S_W} \\ \bar{y} &= \frac{S_y}{S_W} \end{aligned} \tag{5.10}$$

The **Gaussian Three-Point Fitting centroid** is a simple fitting technique (Tremsin et al., 2003) that starts from a one-dimensional Gaussian model and, applying the logarithm on both sides, finds a quadratic function dependent on x_0, the central peak position:

$$lnI(x) = -\left[x_0^2 - 2x_0x + x^2 + 2\sigma^2 ln\frac{\sigma\sqrt{2\pi}}{A}\right]/2\sigma^2 \tag{5.11}$$

where A is the amplitude, x_0 is the central peak position and σ is the standard deviation. By fitting this parabola into three equidistant points $I_{i-1}(x_{i-1})$,$I_i(x_i)$ and $I_{i+1}(x_{i+1})$, the maximum x_0 can be expressed as:

$$x_0 = P\frac{lnI_{i+1} - lnI_{i-1}}{2[2lnI_i - lnI_{i-1} - lnI_{i+1}}] + iP \tag{5.12}$$

where P denotes the fixed distance between the three points. For our application, this distance represents the size of a pixel. In order to obtain the centroid, the fit

has to be applied in y-dimension as well. Therefore, five points are required in total, since the central point I_i is the same for both dimensions.

The **Iterative Gaussian Weighted centroid** follows the same logic of the Gaussian Weighted centroid, but the central position of the weighting function W(x,y) iteratively adjusts based on the previous iteration's weighted first moment calculation: The newly computed spot center becomes the weighting functions center for the next iteration and this process is repeated until the computed spot positions in both the x- and y-directions converge to within the chosen accuracy (for example 0.001 pixels of the previous iteration).

The **2D Gaussian fit** centroid method is based on a weighted regression model (Anthony, 2009). It transforms the equation of the intensity of a 2D circular Gaussian:

$$I(x,y) = Ae^{-\{[(x-x_0)^2+(y-y_0)^2]/(2\omega^2)\}} \tag{5.13}$$

to a linear equation using logarithms:

$$c_1 x_i + c_2 y_j + c_3 lnI(i,j) + c_4 = (x_i^2 + y_j^2) \tag{5.14}$$

where c_1, c_2, c_3, and c_4 are unknown coefficients defined as follows:

$$\begin{aligned} c_1 &= 2\bar{x}; \qquad c_2 = 2\bar{y} \\ c_3 &= -2\omega^2; \quad c_4 = -2\omega^2 ln(A) - \bar{x}^2 - \bar{y}^2 \end{aligned} \tag{5.15}$$

with the centroid coordinates estimation defined as ($\bar{x}$,$\bar{y}$) (eq. 5.3).
Eqs.5.15 are set of linear equations which may be solved using a linear least-squares regression model (Akondi, Roopashree, and Prasad, 2009).

5.3.2 Basic data treatment: OpenCV python library

We will now introduce the main features of the Python library that have been used to perform the First Moment algorithm in many analysis shown in this manuscript.
OpenCV(Bradski, 2000) is the most popular computer vision library in the world that includes several hundreds of different algorithms. We will concentrate on a brief explanation of the image processing modules, in particular on the contour detection and centroid calculation.
Using contour detection, we can detect the borders of objects, and localize them easily in an image. It is often the first step for many interesting applications, such as image-foreground extraction, simple-image segmentation, detection and recognition. The contour is an outline representing or bounding the shape or form of an object.
Typically, a specific contour refers to boundary pixels that have the same color and intensity. OpenCV provides two main algorithms for contour detection: CHAIN-APPROX-NONE where all the boundary line points are stored and CHAIN-APPROX-SIMPLE that saves just two end points of that line.
We will now explain all the needed steps for detecting contours in OpenCV:

- **Read the Image and convert it to Grayscale Format**: Converting the image to grayscale (fig.5.7 a) is very important as it prepares the image for the next step (thresholding), which in turn is necessary for the contour detection algorithm to work properly.

- **Apply Binary Thresholding**: This converts the image to black and white (fig.5.7 b), highlighting the objects-of-interest and making the contour-detection step easier. Thresholding turns the border of the object in the image completely white, with all pixels having the same intensity.
- **Find the Contours**:The algorithm can now detect the borders of the objects from these white pixels. It uses the findContours() function to detect the contours (fig.5.7 c) in the image.

After finding the contours of an object, we can use this analysis to calculate some features like the center of mass of the object or the area of the object.
Some of these properties of the image are found via image moments. For a 2D continuous function t(x,y) the moment of order (p + q) is defined as :

$$M_{pq} = \int_{-\infty}^{+\infty} \int_{-\infty}^{+\infty} x^p y^q t(x,y) dx dy \tag{5.16}$$

for p,q=0,1,2,...
After converting the image to a scalar (grey scale) image with pixel intensities I(x,y), raw image moments M_{ij} are calculated by :

$$M_{ij} = \frac{\sum_x \sum_y x^i y^j I(x,y)}{\sum_x \sum_y I(x,y)} \tag{5.17}$$

where the division by I(x,y) is done considering the image as a probability density function.
The centroid coordinates can be easily calculated by :

$$\{\bar{x}, \bar{y}\} = \left\{ \frac{M_{10}}{M_{00}}, \frac{M_{01}}{M_{00}} \right\} \tag{5.18}$$

The function cv.moments() gives a dictionary of all moment values calculated (fig.5.7 (d)).
A visual scheme of the OpenCV contour algorithm is given in fig.5.7.

However, there are some cases where the contour algorithm might fail to deliver meaningful and useful results. In fact, the contours associated with each object can be clearly identified when it is strongly contrasted against its background. While, when a bright object (fig.5.8,dog) is mixed up with a background with the same brightness as the object of interest (fig.5.8,dog), multiple unwanted contours stands out in the background (fig.5.8,green selection).

5.4 Wavefront reconstruction

Once the local wavefront slopes have been determined, the wavefront can be reconstructed by integrating the gradient measurements. The works of Fried (Fried, 1977), Hudgin (Hudgin, 1977) and Southwell (Southwell, 1980) set the foundation of the classical wavefront reconstruction algorithms which influenced most of the methods used nowadays.
The zonal reconstruction method was developed by Fried and Hudgin, while Southwell presented a phase-retrieval method known as modal reconstruction method, depending on whether the estimate is a phase value in a local zone or a coefficient

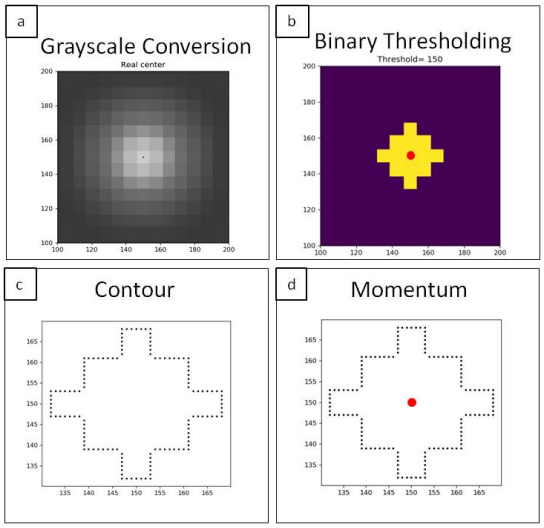

FIGURE 5.7: (a) Convert a test image to grayscale format, (b) apply binary thresholding (thr=150), (c) find the contours, (d) calculate the moment of the image and the centroid coordinates (red dot).

FIGURE 5.8: Left – input image with a white dog and a lot of other edges and background colors. Right – the contour detection results overlaid. The contours are not complete, and the detection of multiple or incorrect contours due to clutter in the background.

of an aperture function. In the following sections we will present the classical zonal and modal reconstruction algorithms.

5.4.1 Zonal Reconstruction

Starting from the slope measurement (obtained, e.g., from the centroid method eq.5.2), the zonal algorithm consists on a linear model that connects the unknown phase value ϕ with the phase slopes (eq.5.7) via a finite difference approach.
The grid positions for the x- and y-slopes measurements are shown in fig.5.9.

The formulation of the problem depends on where the actual slope measurements are taken: Southwell (fig.5.9 a)), Hudgin (fig.5.9 b)) and Fried (fig.5.9 c)). The goal of this series of algorithms is to construct a function or a model of the phase that can be least-squared-fitted on the slope measurement data.
Considering the data configuration given in (fig.5.9 a)) , we assume that the phase dependence between the grid points in the x direction is represented by the polynomial:

$$\phi = c_0 + c_1 x + c_2 x^2 \tag{5.19}$$

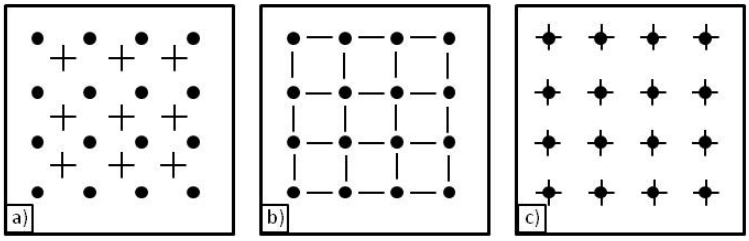

FIGURE 5.9: Slope measurement sampling geometry and wavefront mesh points. The horizontal lines indicate positions of x-slope sampling. The vertical lines are the y-slope sampling positions. The dots are the estimated phase points. Configuration (a) is from Southwell, (b) is from Hudgin and (c) is from Fried.

And the slope is :

$$S^x = c_1 x + 2c_2 x \tag{5.20}$$

In this configuration, since we have two slopes measurements for each phase point it is possible to retrieve both c_1 and c_2 of eq.5.20. This will produce the following relationships, for a grid of (NxN) phase points :

$$\begin{aligned} \frac{(S^x_{i+1,j} + S^x_{i,j})}{2} &= \frac{(\phi_{i+1,j} - \phi_{i,j})}{h} \quad for\ i = 1, N-1; \\ & \qquad\qquad\qquad\qquad\qquad\quad j = 1, N, \\ \frac{(S^y_{i+1,j} + S^y_{i,j})}{2} &= \frac{(\phi_{i,j+1} - \phi_{i,j})}{h} \quad for\ i = 1, N; \\ & \qquad\qquad\qquad\qquad\qquad\quad j = 1, N-1, \end{aligned} \tag{5.21}$$

where h = D/N and D is the width of the aperture.
Having a set of slopes measurements S^x and S^y, from eqs.5.21 we can apply the least-squared technique.
The previous expressions can be written in the following matrix equation:

$$S = A\,\phi \tag{5.22}$$

where S is a vector containing all the slope measurements and ϕ is the vector containing the N^2 unknown phase values.
The standard solution of this problem is to calculate the transpose matrix of A (A^T) and solving a least-squared problem. However, every constant wavefront added to the solution will satisfy the model and thus the matrix $A^T A$ is singular. For large arrays, we can use iterative matrix methods for solving eq.5.22.
In the following, we will describe the Successive Over-Relaxation (SOR) method.
We start from the matrix describing the eqs.5.21:

$$DS = A\,\phi \tag{5.23}$$

where D is a matrix that performs the adjacent slope averaging.
The corresponding normal equations are:

$$(A^T A)\,\phi = A^T D S \tag{5.24}$$

Writing just the nonzero matrix element components :

$$\phi_{jk} = \bar{\phi}_{jk} + b_{jk}/g_{jk} \tag{5.25}$$

where $\overline{\phi_{jk}}$ is the nearest-neighbor phase average, $b_{jk} = (S^y_{j,k-1} - S^y_{j,k} + S^x_{j-1,k} - S^x_{j,k})h$ and g factors are the diagonal elements of A^TA.
Eq.5.25 is the basis of an iterative solution, where the right side of the equation is calculated for each current value of ϕ.
The result after m iterations is :

$$\phi^{(m+1)}_{jk} = \bar{\phi}^{(m)}_{jk} + b_{jk}/g_{jk} \tag{5.26}$$

By adding and subtracting ϕ_{jk} on the right-hand side of eq.5.26 and introducing the relaxation parameter ω, we have:

$$\phi^{(m+1)}_{jk} = \phi^{(m)}_{jk} + \omega[\bar{\phi}^{(m)}_{jk} + b_{jk}/g_{jk} - \phi^{(m)}_{jk}] \tag{5.27}$$

The optimal value of ω is known for this class of matrices:

$$\omega = \frac{2}{1 + sin[\pi/(N+1)]} \tag{5.28}$$

The convergence is achieved when the quantity in brackets on the right-hand side becomes small.

5.4.2 Modal Reconstruction

In the modal reconstruction algorithm, the wavefront is expanded in a set of orthogonal unitary functions, where its coefficients are estimated from the slopes measurements. For the decomposition of phase elements, the Zernike polynomials are often used for circular apertures and Legendre polynomials for square apertures.

The wavefront can be expanded in a set of orthogonal functions:

$$\phi(x,y) = \sum_{k=0}^{M} a_k n_k F_k(x,y) \tag{5.29}$$

where a_k are the coefficients to be determined, n_k are the normalization constants, and F_k are the two-dimensional functions that are orthogonal over the sampled aperture. We choose F_k to have zero mean. The slope model is obtained by differentiating eq. 5.29 :

$$\begin{aligned} S^x &= \sum_{k=1}^{M} a_k n_k \frac{\partial F_k}{\partial x} \\ S^y &= \sum_{k=1}^{M} a_k n_k \frac{\partial F_k}{\partial y} \end{aligned} \tag{5.30}$$

The numerical complexity is highly reduced by replacing the initial problem of N^2 phase point with M phase expansion coefficients a_k (eq. 5.30). We can reshape eq.5.30 in matrix form:

$$S = Aa \tag{5.31}$$

where A is a rectangular matrix with M columns and $2N^2$ rows.
Since all the other terms in the expansion have zero mean, the corresponging normal equations can be solved using the standard least-squares solution:

$$A^T A a = A^T S \tag{5.32}$$

and the coefficient matrix a is :

$$a = (A^T A)^{-1} A^T S \tag{5.33}$$

where $A^T A$ is an M by M symmetric matrix, and $A^T S$ is a vector of length M whose components are weighted sums (or moments) over the slope data.

5.5 Wavefront sensor precision and accuracy

There are different sources of uncertainty in wavefront sensor, that can be divided into precision and accuracy of the wavefront sensor (Daniel R. Neal, 2002).

Precision is defined as the repeatability of the sensor. Therefore, it is the variation of the measurement for an unchanged incident wavefront. It is normally quantified by the root-mean-square (RMS) of the measurement difference.

Accuracy is the ability of a wavefront sensor to measure a known incident wavefront.

These two factors are influenced by the camera readout noise, the finite pixelization, the cross-talk between two close spots and several other effects.
In the following sections we will describe several sources of error that can affect the design of a Hartmann sensor.

5.5.1 Alignment and calibration

Alignment and calibration effects are sources of systematic errors in the system. The relative orientation between the Hartmann aperture mask and the detector may be subject to tilt, tip or rotation. Since the reference centroids are recorded for each image acquisition, the measurements are essentially differential and these systematic errors are minimized. It is thus crucial to maintain the alignment between the aperture array and the detection plane when performing a series of acquisitions.
Also, the distance between the array and the detector is an important parameter and it has to be measured with high accuracy to avoid a calibration offset.

5.5.2 Precision: Centroid estimation error

The repeatability of a wavefront sensor is affected by the finite signal to noise ratio of real detectors. The error on the centroid estimation can be obtained repeating the same measurement many times and then analyzing the centroid positions. Considering an array with K apertures for N repeated measurements:

$$V^2 = \frac{1}{N} \sum_{n=1}^{N} \left(\frac{1}{K} \sum_{k=1}^{K} (x_k - \bar{x}_k)^2 + (y_k - \bar{y}_k)^2 \right)_n \tag{5.34}$$

where V^2 corresponds to the standard deviation of the centroids. In eq. 5.34 we assume that the centroid measurements in x and y are statistically independent. In the calculation of the wavefront sensor precision, we can suppose that the error is mainly coming from stochastic noise. Averaging the result with N meaurements, will improve the centroid estimation as the root-mean-square of N.

5.5.3 Accuracy: Centroid pixelization error

To evaluate this type of error, the estimated position is compared to the position of an ideal spot. The relative position of the source respect to the Hartmann array is varied in a known way and compared to the estimated centroid location:

$$\sigma_{px}^2 = \langle (\widetilde{x} - x_I)^2 \rangle \tag{5.35}$$

where σ_{px}^2 is the pixelization error, x_I is the ideal spot position and $\widetilde{x}$ is the real measured position.

5.6 Simulation Tool

Many experimental parameters need to be optimized to design a Hartmann wavefront sensor dedicated to imaging applications. A precise simulation tool is thus needed. In particular, the architecture of the Hartman hole plate, the distances between the different elements of the set-up and the source properties are some of the crucial issues that determine the performances of the entire system. In this thesis, we developed a 3D wave propagation model based on Fresnel propagator (Goodman, 2005). The model can manage any degree of spatial coherence of the source, enabling the accurate simulation of a wide range of X-ray emission processes, such as tabletop sources, synchrotron facilities or X-ray free-electron lasers (Begani Provinciali et al., 2020). The technique used to describe beam divergence is physically consistent with the definition of spatial coherence of an emitting source (see section 5.6.7). In the following sections the different components of the simulation tool, implemented in Python, will be described.

5.6.1 Fresnel Propagator

The radiation emitted from the source is propagated step-by-step to each optical element using a Fresnel Propagator. The wave field U(x,y) is calculated from the diffraction of a complex aperture placed in the (ϵ,η) plane that is illuminated by the field U(ϵ,η) in the positive z direction (fig. 5.10).

The propagator was implemented following its classical derivation from the Huygens-Fresnel principle (Goodman, 2005) :

$$U(x,y) = \frac{z}{j\lambda} \int_{-\infty}^{+\infty} \int_{-\infty}^{+\infty} U(\epsilon,\eta) \frac{e^{ikr}}{r^2} d\epsilon d\eta \tag{5.36}$$

where λ is the wavelength, k is the wave vector, U(x,y) and U(ϵ,η) are the wave fields in the (x,y) and in the (ϵ,η) planes, respectively, and z is the propagation distance. Finally, the distance r is given by:

$$r = \sqrt{z^2 + (x - \epsilon^2) + (y - \eta^2)} \tag{5.37}$$

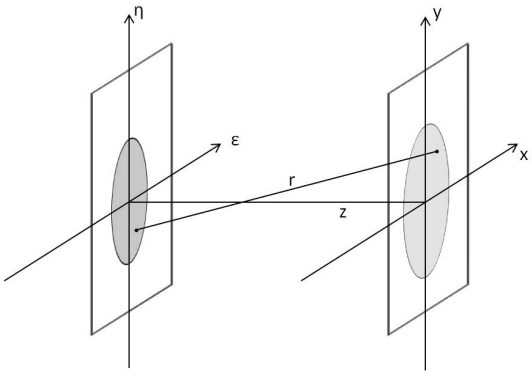

FIGURE 5.10: Schematic representation of the coordinates system: the wave field is defined in the (ϵ,η) plane and propagated until the second plane (x,y). The propagation direction z is orthogonal to both planes.

To reduce the Huygens-Fresnel to a simpler expression, we introduced a binomial expansion for the distance r and keep only the constant and quadratic terms of the expansion:

$$r \approx z\left[1 + \frac{1}{2}(\frac{x-\epsilon}{z})^2 + \frac{1}{2}(\frac{y-\eta}{z})^2\right] \tag{5.38}$$

Inserting eq.5.38 inside eq.5.36 we can rewrite the field at (x,y) as a convolution in the following form:

$$U(x,y) = \int_{-\infty}^{+\infty}\int_{-\infty}^{+\infty} U(\epsilon,\eta)h(x-\epsilon, y-\eta)d\epsilon d\eta \tag{5.39}$$

where the convolution kernel h(x-ϵ,y-η) is defined as:

$$h(x,y) = \frac{e^{ikz}}{j\lambda z}e^{\frac{ik(x^2+y^2)}{2z}} \tag{5.40}$$

and factorizing the term $e^{\frac{ik(x^2+y^2)}{2z}}$ outside the integral we found:

$$U(x,y) = \frac{e^{ikz}}{j\lambda z}e^{\frac{ik(x^2+y^2)}{2z}}\int_{-\infty}^{+\infty}\int_{-\infty}^{+\infty} U(\epsilon,\eta)e^{\frac{ik(\epsilon^2+\eta^2)}{2z}}e^{\frac{-2j\pi(x\epsilon+y\eta)}{\lambda z}}d\epsilon d\eta \tag{5.41}$$

Eq.5.41 is the Fourier transform of the product of the initial complex field U(ϵ,η) and a quadratic phase factor $e^{\frac{ik(\epsilon^2+\eta^2)}{2z}}$. Eq.5.41 is called Fresnel diffraction integral. This approximation is valid when the observation distance r is many wavelengths larger than the aperture ($r \gg \lambda$) and is called the near-field of Fresnel diffraction region (see section 2.3.3). The propagated field U_2(x,y) after a distance z, equals the inverse Fourier transform of the multiplication of the Fourier transform of the initial field U_1(x,y) and the propagator H(f_x, f_y):

$$U_2(x,y) = FT^{-1}\Big\{FT[U_1(x,y)]H(f_x,f_y)\Big\} \tag{5.42}$$

where the direct and inverse Fourier transform are indicated with FT and FT^{-1}, respectively, $U_1(x,y)$ is the initial field and the propagator H(f_x, f_y) can be expressed

by:

$$H(f_x, f_y) = e^{j\pi\lambda z f^2} e^{jkz} \tag{5.43}$$

where f=(f_x, f_y) ($f_x = \frac{x}{\lambda z}, f_y = \frac{y}{\lambda z}$) are the spatial frequencies.
In this way, we were able to compute the convolution integral in eq.5.41 as simple Fourier transforms.

5.6.2 Discrete Fourier Transform

When implementing Fourier optics simulations on the computer, it is necessary to represent the functions by discrete arrays of sampled values and apply transform and processing methods designed for these discrete signals.
The main challenge in Fourier optics simulations is to find a balance between acceptable sampling artifacts and available computer resources (Voelz, 2011). In the following sections we will discuss the sampling of continuous functions and the Shannon–Nyquist sampling theorem.
Let us consider a 2D analytic function g(x,y), uniformly sampled in the x and y directions with a sample interval Δx and Δy respectively:

$$g(x, y) \rightarrow g(m\Delta x, n\Delta y) \tag{5.44}$$

where m and n are integer indices of the samples. The respective sample rates are $1/\Delta x$ and $1/\Delta y$.
In practice, the sampled space is finite. Assuming it is composed of M x N samples in the x and y directions, respectively, m and n are often defined with the following values:

$$m = (-\frac{M}{2}, \frac{M}{2} - 1); \;\; n = (-\frac{N}{2}, \frac{N}{2} - 1) \tag{5.45}$$

The sampled space is shown in fig. 5.11, where L_x is the length along the x side of the sampled space and L_y is the length along the y side; they are called side lengths. They represent physical distances and are related to the sampling parameters by:

$$L_x = M\Delta x; \;\; L_y = M\Delta y \tag{5.46}$$

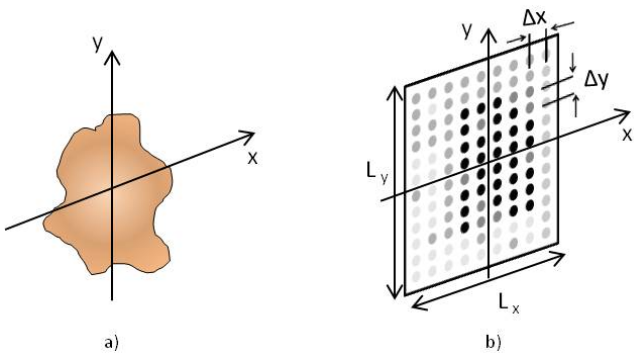

FIGURE 5.11: Two-dimensional function: (a) analytic and (b) sampled versions.

One fundamental issue is whether the sample intervals of the analytic function are small enough to preserve the features of g(x,y). For functions where the spectral content of the signal is limited to a finite range of frequencies (band-limited functions),

a continuous function can be recovered exactly from the samples if the sample interval is smaller than a specific value.
The Shannon–Nyquist sampling theorem extended to two dimensions set this parameter to:

$$\Delta x < \frac{1}{2B_x}; \;\; \Delta y < \frac{1}{2B_y} \tag{5.47}$$

where B_x is the bandwidth of the spectrum of the continuous function along the x direction and B_y is the bandwidth along the y direction.
If we indicate with $|G(f_x, f_y)|$ the magnitude Fourier transform of the function g(x, y), the bandwidth is commonly defined as a half-width measure of $|G(f_x, f_y)|$.
Aliasing effects occur when the condition stated in eq. 5.47 is not satisfied: this results in undersampling high-frequency components in the signal that are interpreted erroneously as low-frequency signals.

We will now discuss only the critical simulation aspects in the implementation of the Discrete Fourier Transform (DFT), for more details see (Robert M. Gray, 1995;Oppenheim Alan V., 2009) .
The analytic Fourier transform of a function g(x,y) of two variables x and y is defined as:

$$G(f_x, f_y) = \int_{-\infty}^{+\infty} \int g(x,y) e^{-j2\pi(f_x x + f_y y)} dxdy \tag{5.48}$$

We assume that g(x,y) is sampled following eq.5.44 and eq.5.45 and to simplify the notation we call $g(m\Delta x, n\Delta y)$ as $\widetilde{g}(m,n)$.
Next, the integrals in 5.48 can be approximated with a Riemann sum:

$$\int_{-\infty}^{+\infty} \int (...) \; dxdy \rightarrow \sum_{n=-N/2}^{N/2-1} \sum_{m=-M/2}^{M/2-1} (...) \; \Delta x \Delta y \tag{5.49}$$

where the sampling parameters Δx and Δy are multiplied subsequently to the DFT operation.
The frequency domain is conventionally divided into M and N evenly spaced coordinate values, called f_x and f_y. The discrete set of frequencies are thus defined by:

$$f_x \rightarrow \frac{p}{M\Delta x}, \;\; where \;\; p = \frac{-M}{2}, ..., \frac{M}{2} - 1; \tag{5.50}$$

$$f_y \rightarrow \frac{q}{N\Delta y}, \;\; where \;\; q = \frac{-N}{2}, ..., \frac{N}{2} - 1; \tag{5.51}$$

where p and q are integers indexes, and the frequency sample intervals are:

$$\Delta f_x = \frac{1}{M\Delta x} = \frac{1}{L_x}, \;\; and \;\; \Delta f_y = \frac{1}{N\Delta y} = \frac{1}{L_y} \tag{5.52}$$

The spatial (m,n) and frequency (p,q) arrays have the same number of elements.
Incorporating eq.5.51 and eq.5.52 into the complex exponential of eq.5.48 we have:

$$exp(-j2\pi(f_x x + f_y y)) = exp(-j2\pi(\frac{pm}{M} + \frac{qn}{N})) \tag{5.53}$$

And the final form for the DFT is:

$$\widetilde{G}(p,q) = \sum_{n=-N/2}^{N/2-1} \sum_{m=-M/2}^{M/2-1} \widetilde{g}(m,n) exp(-j2\pi(\frac{pm}{M} + \frac{qn}{N})) \tag{5.54}$$

where $\widetilde{G}(p,q)$ represents the DFT of $\widetilde{g}(m,n)$.
The inverse discrete Fourier transform (DFT^{-1}) is derived in a similar way and is written as:

$$\widetilde{g}(m,n) = \frac{1}{MN} \sum_{p=-N/2}^{N/2-1} \sum_{q=-M/2}^{M/2-1} \widetilde{G}(p,q) exp(j2\pi(\frac{pm}{M} + \frac{qn}{N})) \tag{5.55}$$

The term $\frac{1}{MN}$ comes out when numerically evaluating a forward Fourier integral followed by an inverse Fourier integral. This allows the DFT followed by the DFT^{-1} to return the original function values, which is consistent with the Fourier integral theorem.

5.6.3 Coordinates definition and Shifting

In the simulation square grids and uniform sampling in the two axis were used: Δx=Δy, N=M, and L_x= L_y=L.
The coordinates in the real plane and the spatial frequency coordinates are derived by eq.5.50-5.52 and described in fig.5.12.

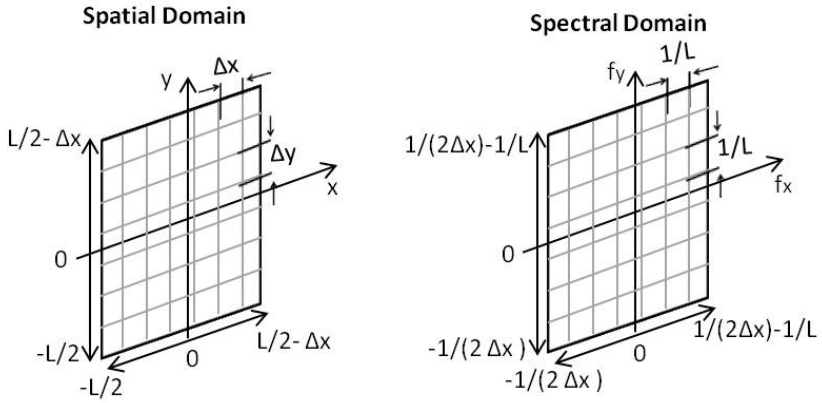

FIGURE 5.12: Spatial coordinates of the samples (Left) and the respective spatial frequency coordinates (Right) assuming a FT relationship between the spatial and spectral domains

The integer index variables introduced before (m and n, as well as p and q) span from negative to positive values. However, software applications use positive integer values for vector or array (matrix) indexing. It is common to put the zero coordinate at the center of the grid, corresponding to the (M/2+1) index.
Nevertheless, in the majority of the coding language, the zero coordinate is placed in the first index position when dealing with the Fourier Transform algorithms. Thus, a "shift" of the centered vector values is needed before a Fourier Transform operation.

5.6.4 Fresnel Two-Step Propagator

In a free-space propagation code the source size and the detector extension can be simulated inside planes with very different side lengths. Computationally, each field is normally defined as a 2D array of data. In order to propagate the source field of a certain distance multiplication between matrices are performed. To perform this operation, the number of samples for each matrix cannot change during the propagation. In some cases, the field dimensions vary during the propagation due to

magnification or demagnification processes. A possible solution is to sample differently each plane, changing the side dimensions defining each field.
It is thus convenient in many geometries to define a two-step propagation method where the side lengths can be chosen independently. The approach was derived in the 1980s and takes advantage of two artificial Fresnel propagations (Tyler and Fried, 1982).
The first propagation is from the source field $U_1(x_1, y_1)$ to a virtual plane field $U_V(x_V, y_V)$ situated after a distance z_1. The second propagation is from the observation plane field $U_2(x_2, y_2)$ to the virtual plane after distance z_2 (fig. 5.13).

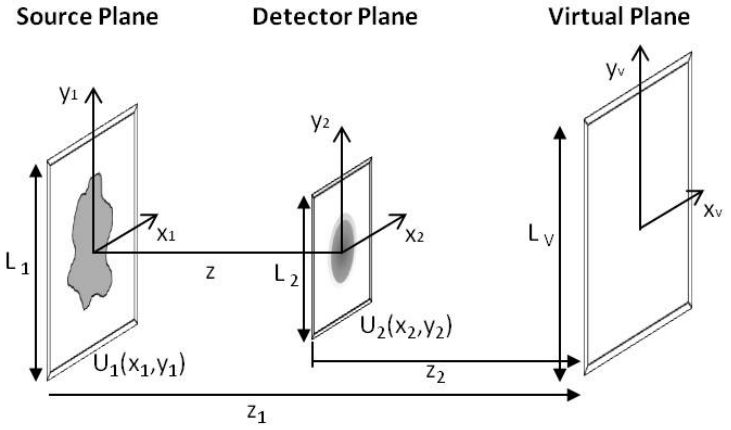

FIGURE 5.13: Fresnel two-step propagation concept

These propagations can be separately written using the definition given by Fresnel (eq. 5.41) and then equating the virtual plane fields we found:

$$\begin{aligned} U_2(x_2,y_2) = \frac{z_2}{z_1} exp[jk(z_1-z_2)]\ \ exp\Big[-j\frac{k}{2z_2}(x_2^2+y_2^2)\Big] \\ *F^{-1}\Bigg\{exp\Big[-j\frac{k}{2}\Big(\frac{1}{z_1}-\frac{1}{z_2}\Big)(x_d^2+y_d^2)\Big] \\ *F\Big\{U_1(x_1,y_1)exp\Big[j\frac{k}{2z_1}(x_1^2+y_1^2)\Big]\Big\}\Bigg\} \end{aligned} \tag{5.56}$$

The propagation distance from the source to the observation plane is given by :

$$z = z_1 - z_2 \tag{5.57}$$

The virtual plane coordinates are related to the transform frequencies in the source and observation planes by:

$$x_v = \lambda z_1 f_{X1} = \lambda z_2 f_{X2} \tag{5.58}$$

where the same equation can be written for the y-dimension parameters.
With discrete sampling, the source and observation plane side lengths are given by:

$$L_1 = M\Delta x_1, \quad L_2 = M\Delta x_2 \tag{5.59}$$

where M is the number of samples and Δx_1 and Δx_2 are the respective sample intervals. Applying 5.58 and considering that, in frequency space, f_{X1} = p/2 Δx_1 and f_{X2} = p/2 Δx_2, where p is the progressing index of the simulated plane, we find:

$$\frac{z_1}{z_2} = \frac{L_1}{L_2} = \frac{\Delta x_1}{\Delta x_2} \tag{5.60}$$

Considering eq. 5.57 we can derive:

$$z_1 = z\Big(\frac{L_1}{L_1 - L_2}\Big) \;\; ; \;\; z_2 = z\Big(\frac{L_2}{L_1 - L_2}\Big) \tag{5.61}$$

Performing some algebra, we can rewrite eq. 5.56 as :

$$\begin{aligned} U_2(x_2, y_2) = \frac{L_2}{L_1} exp(jkz) \;\; exp\Big[-j\frac{k}{2z}(\frac{L_1 - L_2}{L_2})(x_2^2 + y_2^2)\Big] \\ *F^{-1}\Bigg\{ exp\Big[-j\pi\lambda z \frac{L_1}{L_2}(f_{x1}^2 + f_{y1}^2)\Big] \\ *F\Big\{ U_1(x_1, y_1) exp\Big[j\frac{k}{2z}\frac{(L_1 - L_2)}{L_1}(x_1^2 + y_1^2)\Big]\Big\}\Bigg\} \end{aligned} \tag{5.62}$$

The expression 5.62 is the basis for the two-step propagator, where the source and observation plane side lengths, L_1 and L_2 respectively, can be chosen independently.

5.6.5 Sampling considerations in the two-step method

The two-step propagation method described in the previous section can be affected by sampling issues.
We will first define the oversampled regimes analyzing the terms of eq.5.62. The source contribution is expressed as:

$$exp\Big[j\frac{k}{2z}\frac{(L_1 - L_2)}{L_1}(x_1^2 + y_1^2)\Big] \tag{5.63}$$

and is oversampled when $\Delta x_1 \leq \lambda z_1 / L_1$. Using the relation for z_1 in eq.5.61 yields:

$$\Delta x_1 \leq \frac{\lambda z}{|L_1 - L_2|} \tag{5.64}$$

In the same way for the term in the observation plane:

$$exp\Big[-j\frac{k}{2z}(\frac{L_1 - L_2}{L_2})(x_2^2 + y_2^2)\Big] \tag{5.65}$$

the requirement for oversampling is $\Delta x_2 \leq \lambda z_2 / L_2$. Inserting eq.5.60 the expression for Δx_1 can be rewritten as:

$$\Delta x_1 \leq \frac{L_1}{L_2}\frac{\lambda z}{|L_1 - L_2|} \tag{5.66}$$

Finally, for the frequency term:

$$exp\Big[-j\pi\lambda z \frac{L_1}{L_2}(f_{x1}^2 + f_{y1}^2)\Big] \tag{5.67}$$

This part is oversampled when:

$$\Delta x_1 \geq \frac{\lambda z}{L_2} \tag{5.68}$$

Equating eq.5.64 and eq.5.66, results in the condition $L_1 = L_2$. Thus, critical sampling requires the side lengths to be equal. Also, under critical sampling eq.5.68 gives the familiar critical sampling criterion $\Delta x_1 = \lambda z_2 / L_1$. Thus, choosing L_1 and L_2 to be different forces non-critical sampling. Sampling criteria depend on the relationship between L_1 and L_2. In general, the two-step method is capable of resampling the observation plane grid within the propagation process, but does not alleviate the sampling constraints for the Fresnel propagators.

5.6.6 Fresnel Propagator validation

To validate the implementation of our Fresnel propagator, we simulated the propagation of a fully coherent beam using an object that leads to a well-known diffraction pattern.
We looked at the diffraction pattern of a coherent source from a rectangular aperture for various normalized distances from the aperture, as represented by different Fresnel numbers. We remind that the Fresnel number $N_f = (a^2/z\lambda)$ is the ratio between the aperture size (a) and the product of the distance of the screen from the aperture (z) and the incident wavelength (λ).
The simulation was performed with $\lambda = 1.38 \times 10^{-10}$ m, M x M samples with M=1000, the distance z and the aperture size were adjusted for each value of N_f.
The diffraction patterns generated with our code are reported in fig.5.14 a) ,while results tabulated in Goodman, 2005 (p. 86) are given in fig.5.14 b) for N_f = 1, 4, 10. For each plot the size of the aperture is given. The results coming from the sim-

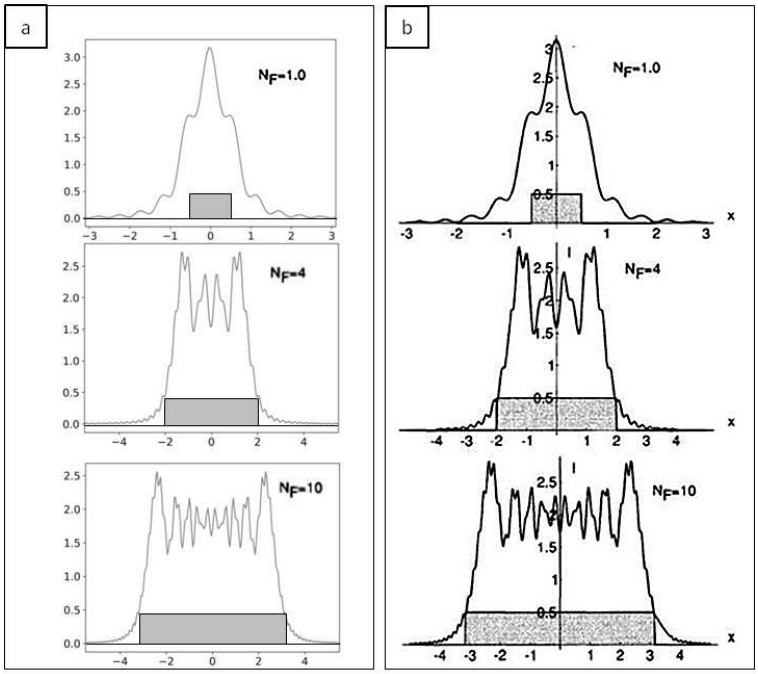

FIGURE 5.14: Diffraction patterns from a rectangular aperture changing the Fresnel number (N_f). (a) Simulation results for N_f = 1, 4, 10; aperture size is shown in dark grey. (b) Theoretical results for N_f = 1, 4, 10; aperture size is shown in dark grey.

ulation are well represented by the theoretical diffraction pattern of a rectangular aperture. This test validates the reliability of the Fresnel propagator implemented in the simulation code.

5.6.7 Definition of source coherence

Many techniques are currently available to describe partially coherent beams by a superposition of coherent but mutually uncorrelated light beams (Vahimaa and Turunen, 2006, Gbur and Visser, 2010, Shi et al., 2014). In the Gaussian Schell model (GSM) (Starikov and Wolf, 1982) the beam represents a broad class of partially coherent beams, whose intensity and degree of coherence both satisfy Gaussian distributions. In the twisted Gaussian Schell model (TGSM) (Simon and Mukunda, 1993) partially coherent beams can carry two special kinds of phase (i.e., twist phase and vortex phase) besides the usual quadratic phase.
Recently, great attention has been paid to partially coherent beams whose degree of coherence does not satisfy a Gaussian distribution, so-called partially coherent beams with nonconventional correlation functions (Cai, Chen, and Wang, 2014). An alternative approach consists in propagating the wavefront by a linear superposition of Gaussian beam wavefronts (Idir et al., 2011). Each beam is propagated independently throughout the optical system and then superimposed to calculate the propagated field. Here we describe a modified version of the superposition of Gaussians

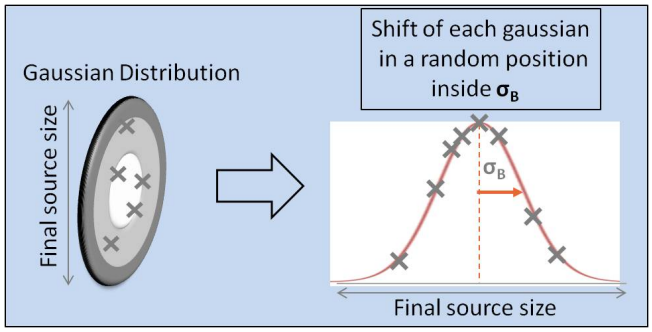

FIGURE 5.15: Description of source architecture: each Gaussian beam is first shifted to a random position chosen inside a larger Gaussian distribution (with standard deviation σ_B) that defines the final source size.

approach. The model described here is based on a modified version of the Huygens-Fresnel principle, replacing the spherical waves with Gaussian beams. Before the propagation, each Gaussian beam is first shifted to a random position chosen inside a larger Gaussian distribution (with standard deviation σ_B) (fig. 5.15) , that defines the source size, and then multiplied by a random phase factor $e^{(i\phi(x,y))}$.
Afterwards, the propagation is applied and the electric fields are added together at the end of each cycle to generate the final field. The logic of the loop that generates this superposition of Gaussians is described in fig. 5.16.

The final expression for the electric field for N Gaussian beams inside the source is:

$$E^{tot} = \sum_{i=1}^{N} E(x_i^{r_i}, y_i^{r_i}) exp(i\phi_i(x_i^{r_i}, y_i^{r_i})) \tag{5.69}$$

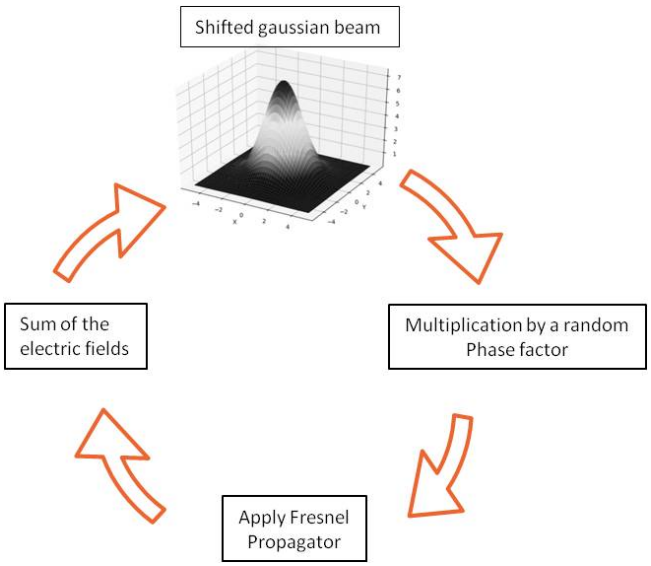

FIGURE 5.16: The beams are propagated independently up to the detector plane, where the electric field of every beam is summed together. Prior to propagation, each beam is multiplied by a random phase factor and is shifted in a random position chosen inside a larger Gaussian distribution with standard deviation σ_B that defines the source size.

where E^{tot} is the total electric field, $E(x_i^{r_i}, y_i^{r_i})$ is the electric field calculated in each position $(x_i^{r_i}, y_i^{r_i})$ randomly distributed inside the source and $exp(i\phi_i(x_i^{r_i}, y_i^{r_i}))$ is a random phase factor.
All the simulation results showed here have been performed with a monochromatic beam.
A typical image of a simulated incoherent beam is shown in fig. 5.17. The outcome of this process is a partially coherent source obtained using Fresnel propagators, that can reproduce any type of sources from fully coherent to incoherent.
In order to prove the reliability of our numerical model to treat the Fresnel propagator in the case of a fully coherent or partially coherent illumination, we first simulated a fully coherent source (N = 1) and we observed its capability of creating a diffraction pattern after passing through a sharp edge (red curve, fig.5.18) looking at its normalized intensity pattern.

The effect on the diffraction pattern shape for an incoherent illumination was studied with the simulation tool previously described. The simulation was performed with the following parameters: incident radiation wavelength $\lambda = 1.38 \times 10^{-10}$ m, M x M samples with M=3000, and a propagation distance z = 40 cm between the source and the detection plane. The oscillations that can be seen on the black line of fig.5.18 a) for a low number of Gaussians inside the source (N = 5) are due to its high level of coherence.
The measured fringe visibility is related in fact to the magnitude of the complex degree of coherence within the illumination beam (Smith et al., 2003a).
Taking the same experimental condition but increasing the number of Gaussian sources (N = 100), makes the beam partially coherent. The oscillations vanished (blue line in fig.5.18 a)) since they are averaged between many shifted beams. The

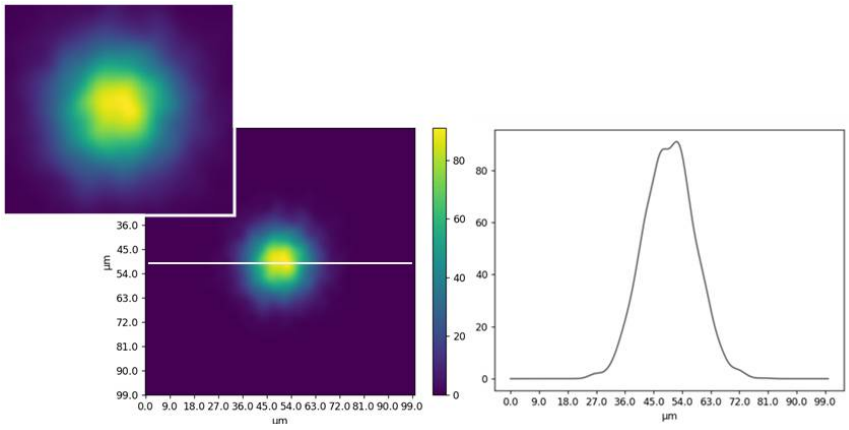

FIGURE 5.17: Simulation of an incoherent source (left) and a single line plot corresponding to the white line (right). Screen size L=100 µm, λ = 1.38 × 10^{-10} m, M x M samples with M=1000, propagation distance z=20 cm.

diffraction pattern created by the object in the case of a coherent illumination corresponds to the one tabulated in the literature (fig.5.18 b)) (Valasek, 1950 (p. 180)). The developed simulation tool well represents the diffraction patterns both for incoherent and coherent illuminations. In the next section a simple experimental set-up will be studied.

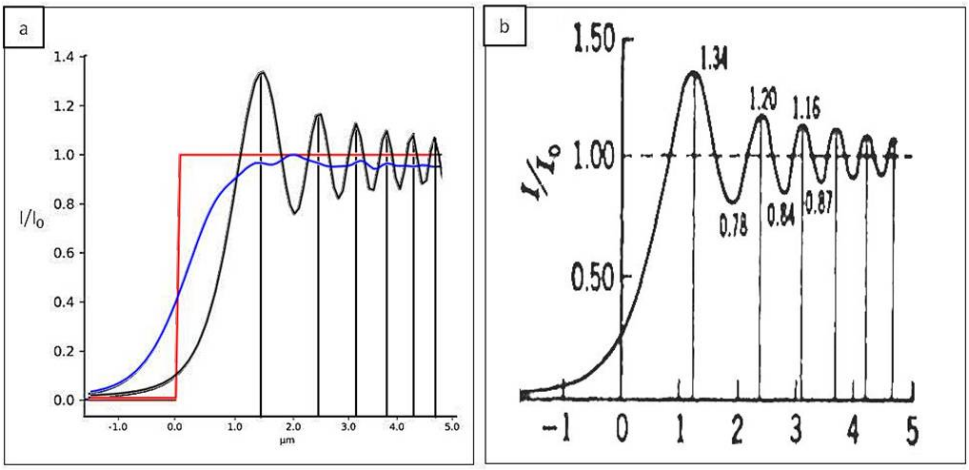

FIGURE 5.18: Diffraction pattern from a plane wave incident to a sharp edge(red line) in the case of coherent and incoherent illumination. (a) Result from the simulation for N = 5 (black line) and N = 100 (blue line). (b) Theoretical result for coherent illumination.

5.6.8 Diffraction from a Test Object

In this section we will show the results from the simulation of a standard experimental situation, where a simple object was taken as an example.
The interaction of the incident beam with an object is described through its transfer function. The wave electric field E(x,y) after the interaction with the object can be expressed as:

$$E(x,y) = A_0(x,y) * exp(\frac{2\pi i\delta\Delta L}{\lambda}) * exp(-\frac{2\pi\beta\Delta L}{\lambda}) \tag{5.70}$$

where ΔL is the object thickness, A_0(x,y) is the amplitude of the incident wave, λ is the wavelength, δ and β are the real and imaginary parts of the index of refraction.
The simulated sample was a 3D cylinder composed of Polymethylmethacrylate (PMMA). The material is described by its index of refraction $n(\omega) = 1 - \delta(\omega) + i\beta(\omega)$, where ω is the wave pulsation.
After the design of the source, to perform the simulation we used two propagators: one from the source to the object plane and one from the object plane to the detector plane.
The simulation was performed with the following parameters: Energy=9 keV (λ= 1.377 10^{-10} m), M x M samples with M=3000, standard deviation of each Gaussian source σ = 0.03 μm, source-object distance (z_1)=30 cm, object-detector distance (z_2)=142 cm, detector pixel size= 0.2 µm. The number of initial Gaussians in the source (N) was set at N=50 to simulate a coherent source while for an incoherent illumination N=150.
The detector was placed far from the object ($z_2 \gg z_1$) to better observe the diffraction from the edges of the cylinder.
The design of the 3D cylinder (1 mm diameter) is shown in fig.5.19 a).
The thickness of the object is evaluated at each (x,y) point. The propagation inside the sample is not yet considered. Since the deflection angles are very small, in the 100 nrad to μrad range, the rays might be considered as being shifted laterally by a negligible amount inside the sample.

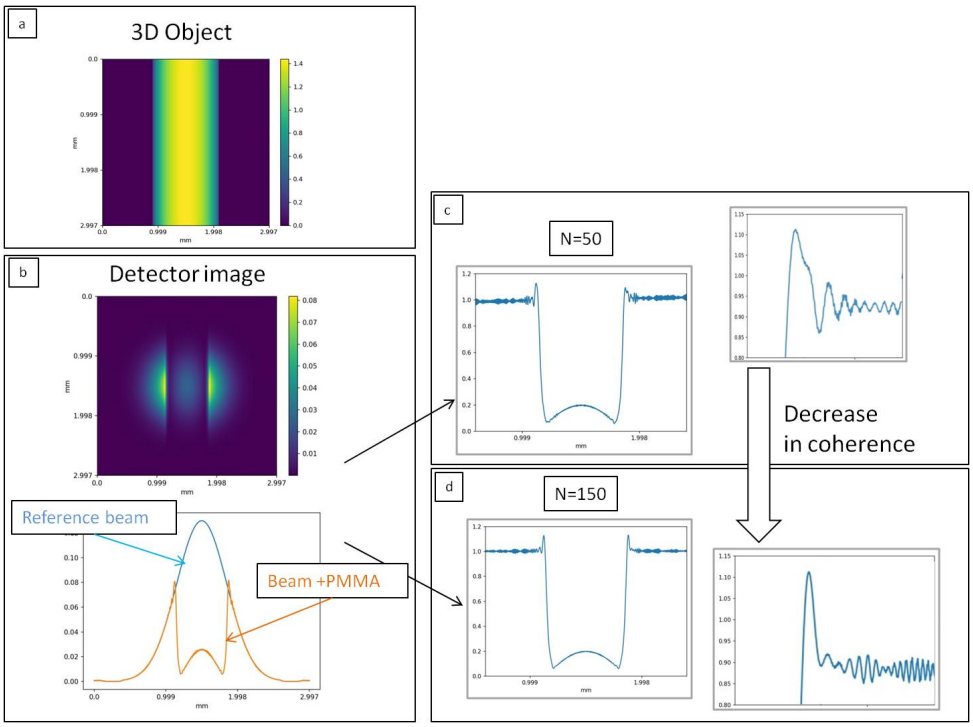

FIGURE 5.19: Effect of the degree of coherence of the source on a test object (PMMA cylinder). (a) Design of the 3D cylinder (1 mm diameter). (b) Image of the object after the propagation at the detector plane. In the 2D image we can see the interaction between the incident gaussian beam and the test object. Graph : single line plot of the reference beam (blue line) and of the detector image (orange line). (c) Case of highly coherent source (N=50): we can observe many oscillations at the edge and a broad peak. (d) case of lower coherence with higher number of sources (N=150) :the amplitude of the peak decreases.

The image acquired at the detector plane is shown in fig.5.19 b). In the 2D image, we can see the result of the interaction between the incident Gaussian beam and the test object. In the graph below we find a single line plot of the reference beam (blue line) and of the detector image (orange line).
To study the effect of the degree of coherence of the source, we run the simulation with the same parameters varying the number of initial Gaussians (N) inside the source. For a highly coherent source (N=50) we can observe many oscillations near the edge and a broad peak at the edge (fig.5.19 c). While decreasing the level of source coherence, so increasing the number of sources (N=150), the amplitude of the peak decreases (fig.5.19 d). In fact the resulting signal will be the average of many different small sources and this will blur the final image.
From this last example we can see how the design of the source coherence level plays a crucial role on the detected diffraction pattern.
A similar test was performed increasing the spatial resolution of the detector (pixel size of the detector= 0.13 μm) and varing the distance source-object to z_1 = 5 cm and the distance object-detector to z_2= 5 cm. The other parameters remained unchanged from the previous simulation.
The diffraction pattern from a PMMA cylinder was studied for N = 1, 10, 100 and 1000 Gaussian sources.

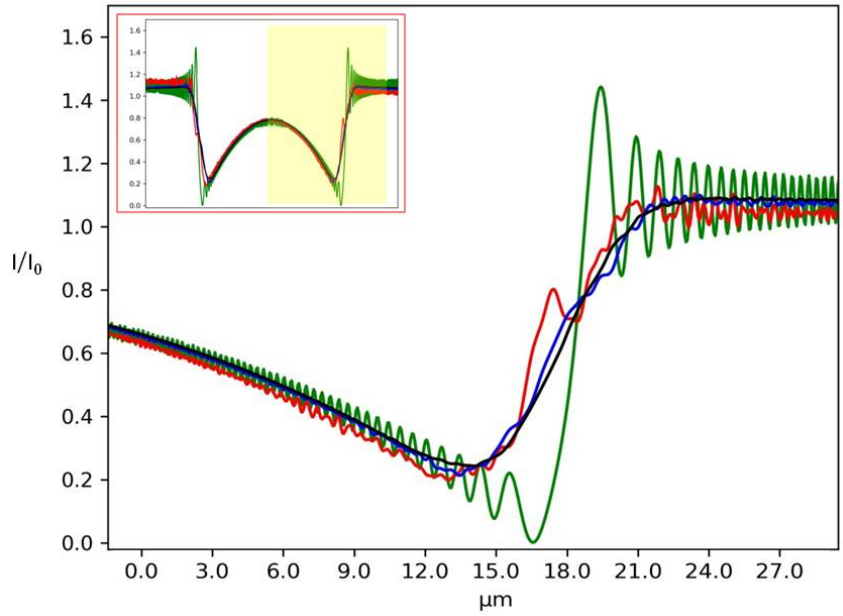

FIGURE 5.20: Single line plot at the edge of a PMMA cylinder varying the level of coherence of the source. Green line (N = 1) represents the case of fully coherent illumination, while the red line is for N = 10, the blue for N = 100 and the black for N = 1000. The inset shows the full line plot.

Horizontal plots (fig. 5.20) are shown to appreciate the evolution of the diffraction patterns between the different cases. The shape of the incident Gaussian beam can be seen at the centre of the intensity plot (fig. 5.20) since the low absorption properties of PMMA are not completely attenuating the incident beam.
Many contrasted oscillations can be seen in the case of fully coherent illumination (green line, N = 1), while with a small number of sources (red line, N = 10) the signal appears noisy due to the multiple interferences.
The incoherent illumination can be simulated using a high number of sources (black line, N = 1000). In this case, the diffraction pattern is completely smoothed out due to the random superposition of the electric fields coming from the very large number of sources.
The case N = 100 represents an intermediate coherence level and still exhibits very weak oscillations.

5.6.9 Modelling of image formation with compact Hartmann Sensor

The previous part validates the relationship between the coherence of the source and its effect on the imaging procedure. This is an important step in the understanding of the behavior of optical systems with respect to the characteristics of the illuminating source.

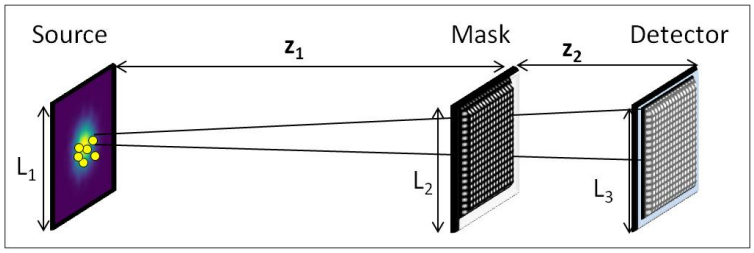

FIGURE 5.21: Schematic representation of the simulated set-up: the Hartmann mask is placed in the beam path between the source and the detector. z_1 is the source to mask distance and z_2 is the mask to detector distance.The small circles in the source plane represents each Gaussian propagated independently.

The design of a highly sensitive wavefront sensor, such as the X-ray Hartmann sensor, requires the optimization of many parameters. We simulate the beam after the Hartmann mask, that was designed as an absorbing plate with regularly spaced holes having 100% transmission (fig.5.21). The reported images display the beam after the propagation through a Hartmann mask with 3 μm square holes and 5 μm pitches (distance between the centers of two adjacent holes). The simulated plane is composed of M x M samples with M=5000 and standard deviation of each Gaussian source σ = 0.03 μm. The incident energy is set at 9 keV. The distance source-mask is z_1 = 5 cm and the distance mask-detector is z_2 = 1 cm.The pixel size of the detector is 0.066 μm.

Since the reconstruction of the wavefront is based on the integration of the signal of each beam to calculate their displacement (Mercère et al., 2003,Southwell, 1980), we are going to investigate the occurrence of diffraction and the cross-talk between adjacent holes when changing the coherence of the illuminating beam. In fig.5.22,

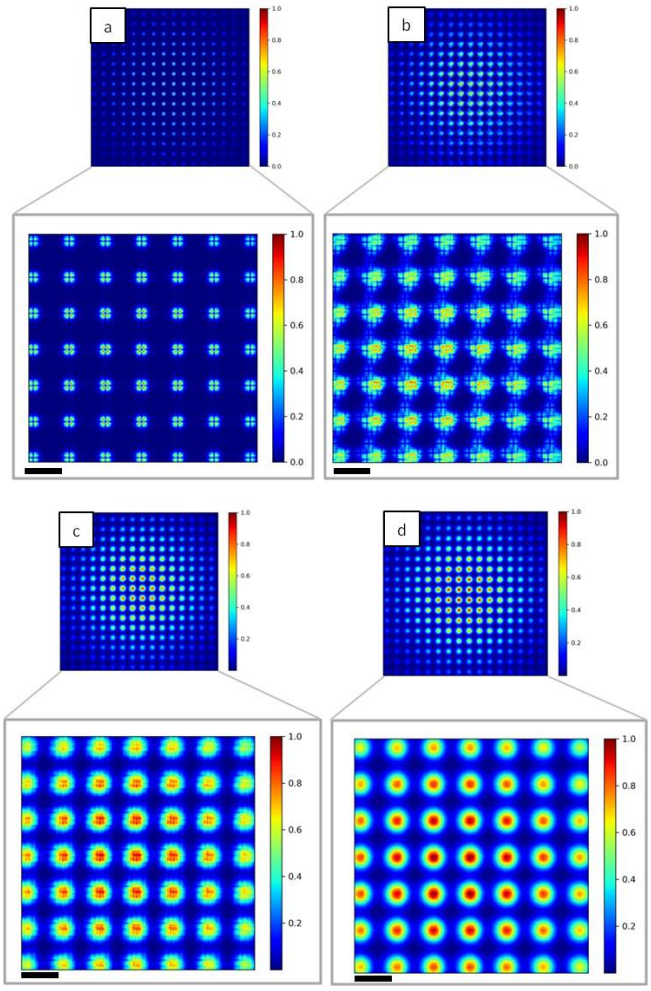

FIGURE 5.22: 2D intensity maps of the simulated Hartmann mask imaged at the detector plane for different values of N. (a) N = 1, (b) N = 10, (c) N = 100 and (d) N = 1000. The diffraction pattern created with coherent illumination (a) will become more noisy increasing N, reaching a Gaussian shape in the incoherent case (d). Insets show a magnification of the central part of the mask. Scale bars are 16 μm.

images of the Hartmann patterns in the case of N = 1, 10, 100 and 1000 are reported. Single line plots of each case shown in fig.5.22 are reported in fig. 5.23. Diffraction effect from the hole edges is clear in the case of coherent illumination (N = 1, fig.5.22 a)), while the displacement of the sub-sources associated with the interference of the propagated beams induces a strong change on the pattern N = 10 (fig.5.22 b)).
Decreasing the degree of coherence of the incident beam decreases the visibility of the diffraction pattern (N = 100, fig.5.22 c)), and in the case of strongly incoherent illumination (N = 1000, fig.5.22 d)) a Gaussian shape for the diffraction pattern of each hole can be seen. In this case the image of the source is convolved with the diffraction pattern.
The Hartmann patterns shown in fig.5.22 are characteristic of compact wavefront sensors. They have been observed on the high numerical aperture EUV sensor (Ruiz-Lopez et al., 2017,Li et al., 2020). The mask parameters, like the spacing between two holes or their dimension, can be optimized with respect to the degree of coherence

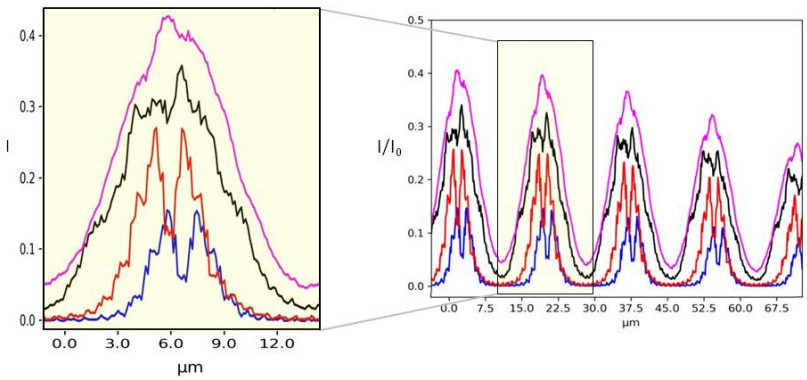

FIGURE 5.23: Single line plot of the 2D images shown in fig.5.22 varying N. N = 1 (blue line), N = 10 (red line), N = 100 (black line) and N = 1000 (purple line).

of the source (see section 5.9.3).

In the Hartmann mask studied in Section 5.6.9 the pitch is comparable with the aperture size and the detector was placed at 1 cm from the mask.
Standard experimental conditions for Hartmann imaging usually requires a larger pitch and to move the detector plane further (Smith et al., 2003b).
To meet these criteria, a second Hartmann mask was modelled with 3 μm square holes and 25 μm pitches. The simulated plane is composed of of M x M samples with M=5000 and each Gaussian source has standard deviation σ= 0.03 μm. The incident energy is set at 9 keV. The distance source-mask is z_1 = 20 cm and the distance mask-detector is z_2= 20 cm. The detector pixel size is 0.13 μm. The results are displayed in fig.5.24 . This configuration differs from the previous one in the sense that

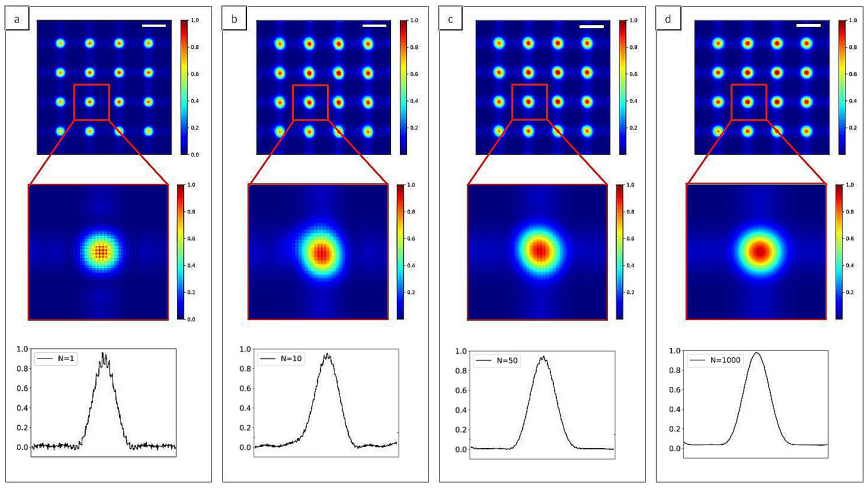

FIGURE 5.24: 2D Intensity map of Hartmann mask with 3 μm square apertures and 25 μm pitches for different illuminating sources. The number of Gaussians N inside the source are N = 1 (a), N = 10 (b), N = 50 (c) and N = 1000 (d). Oscillations can be seen in the detected spots with coherent illumination (a) while they become quite smooth in the incoherent case (d). White scale bars are 38 μm.

the detector is placed after the Fraunhofer distance, given by $L = 2d^2/\lambda$, where d is the aperture size.
Within the modeling conditions, L = 0.13 m that is about half the distance mask-detector.
As a consequence, the diffraction patterns for all the cases are exhibiting the well-known Airy pattern. It is also important to remember that for partially coherent sources, the pattern is convolved with the image of the source formed by each hole. For totally incoherent beam, the pattern is (like in fig.5.23) the image of the source.
When we look at the image obtained with the highest degree of coherence, the diffraction of one hole extends far up to the neighboring hole, inducing undesirable cross-talk.
In the full coherent case (fig.5.24 a) small oscillations can be seen for each spot, while they tend to disappear with incoherent illumination (fig.5.24 d). Such oscillations are not detectable on a standard Hartman sensor since the pixel size is about 1 μm, compared to 0.13 μm in the current modeling.

5.6.10 Talbot effect with a coherent source

In this section we want to validate the design of the degree of coherence of the simulated source.
One of the well-known phenomena connected with coherent illumination of regularly spaced diffractive objects is the Talbot effect (Valasek, 1950).
From the given definition for source coherence, the parameters of the simulation were optimize to analyse the occurrence of this phenomenon.
In 1881, Lord Rayleigh was the first to prove that this phenomenon is a consequence of the diffraction interference of highly spatially coherent (plane) waves after the interaction with a periodic structure, such as a grating.
When a plane coherent wave interacts with a periodic structure, it reproduces the exact pattern of the grating after a certain distance, called Talbot distance.
At the Talbot distance z_T, all the diffraction orders are reinforced:

$$z_T = 2m\frac{d^2}{\lambda} \tag{5.71}$$

where d is the period of the grating and m can be a positive fractional or integer value. Each value of m goes to a plane where the image of the periodic structure is reproduced.
We perform a simulation of the Hartmann mask at the first Talbot plane with different degree of coherence (fig.5.25). Illuminating the Hartmann mask with a fully coherent beam (fig.5.25 a) reproduces the periodic square apertures of the mask, as expected.
Decreasing the level of coherence of the source induces a blurring effect (fig.5.25 b),c) as well as a superposition of the signal coming from different holes. At the highest number of individual sources (N = 1000, fig.5.25 d)) the image of the periodic structure is completely lost.
This last example shows the consistency of our simulation given a certain degree of coherence of the source: the system is reproducing the exact period structure at the Talbot distance as a consequence of the diffraction interference phenomena, while this effect cannot be seen in the case of an incoherent illumination.

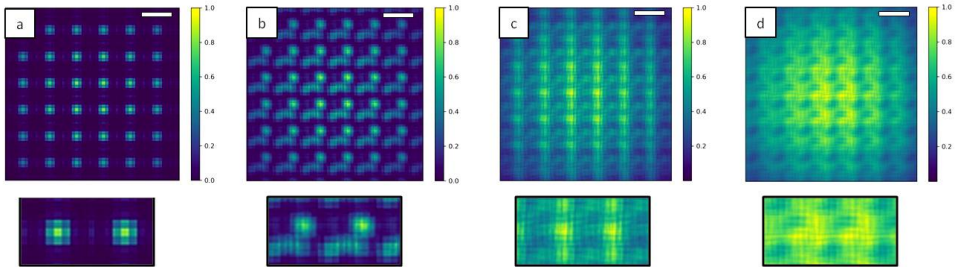

FIGURE 5.25: 2D intensity map of the Hartmann mask at the Talbot plane increasing N. For N = 1 (a) the square pattern of the mask is exactly reproduced, while for N = 10 (b) and for N = 100 (c) the image is blurred. In the incoherent case N = 1000 (d) the square shape is completely lost. Insets show a magnification of the central part of the mask. Scale bars are 15 μm.

5.7 Modelling to estimate sensor accuracy

In order to determine the Hartmann sensor accuracy, it is necessary to vary some parameters in a known way. Using the apparatus of fig. 5.26 it is possible to vary the tilt in a systematic and rigorous manner. It is thus possible to perform experiments or modelling. We have chosen this last solution since our access to X-ray sources is very low.

The simulated set-up is composed of a Gaussian fully coherent source, the Hartmann plate and a detector. The parameter of the simulation are the following: MxM samples with M=500, E=20keV, source diameter=2 μm, detector pixel size=0.2 μm,z_1=50 cm,z_2=11 cm. The source was shifted in the direction parallel to the y-axis and the

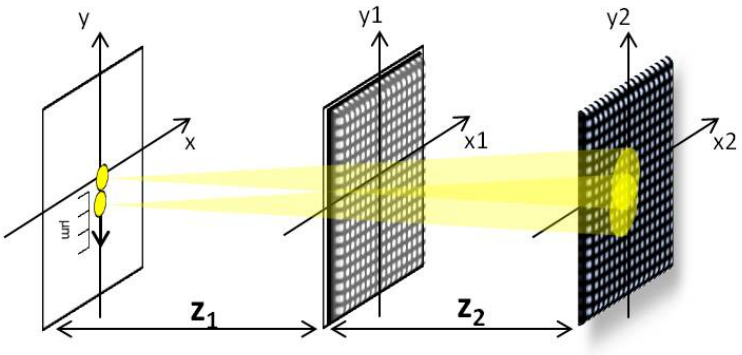

FIGURE 5.26: Description of the set-up used to test the Hartmann sensor accuracy. The source position was shifted several times in y-axis direction (yellow spots on the left). An Hartmann plate and a detector were placed after. The position of the same aperture at the detector plane was recorded while shifting the source.

image of the same aperture at the detector plane was recorded while shifting the source. The total shift of the source was of 2 μm.
Fig.5.27 shows images of one aperture on the detector plane for different source shifts. On the bottom a magnification of each image is reported. The Gaussian

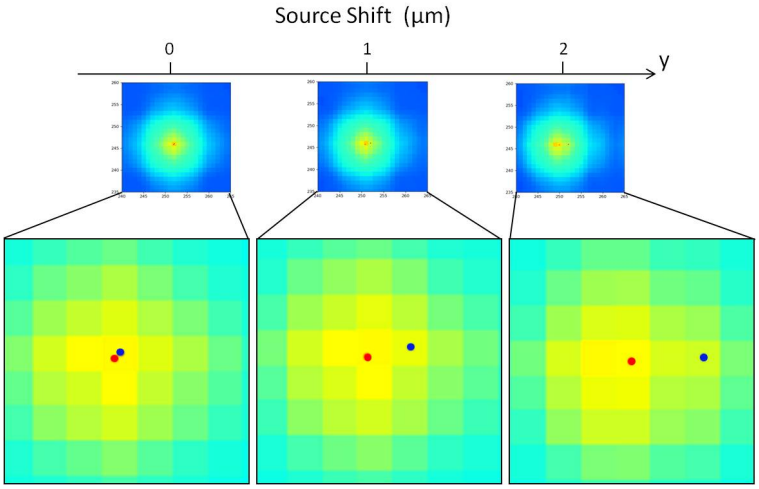

FIGURE 5.27: Images of one aperture on the detector plane are reported for different source shifts. Magnification of the same images are reported just below. The Gaussian source was centered in a known point (blue dot) and the centroid was calculated with the classical first moment algorithm (red dot) while shifting the source.

source was centered in a known point (blue dot) and the centroid was calculated with the classical first moment algorithm (red dot) while shifting the source.

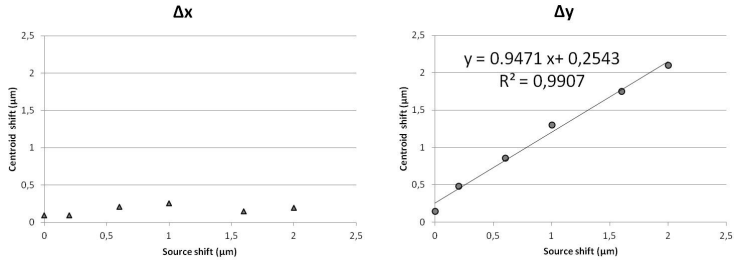

FIGURE 5.28: Plots of data shown in fig.5.27. Difference between the real center and the centroid calculation as a function of the source shift for both axis. For the shift along the y-axis, we calculate the values for a linear regression model. The value of the regression parameter is $R^2 = 0.9907$.

In fig.5.28 we report the difference between the real center and the centroid calculation as a function of the source shift. Since the source was moved only parallel to the y-axis, the centroid calculation in the x direction was not affected. Only small oscillations do to the algorithm accuracy can be observed (for the x-axis, the root mean square (RMS) of the values is 0.09).
For the shift along the y-axis, we calculate the values for a linear regression model. The value calculated for the slope using the best-fit curve is 0.9471, while the theoretical slope value should be one. The value found for the regression parameter is $R^2 = 0.9907$. This procedure is used in reality to calibrate the Hartmann wavefront sensor, where both the mask or the source can be moved to create a known tilt.
To quantify the level of calibration of the Hartmann sensor with this simulation parameters, we measure the tilt as a function of the input tilt with a larger shift of the

source (total shift 24 μm). We performed a linear best fit procedure on the resulting curve (fig.5.29), with a $R^2 = 0.9898$. This sensor is accurately calibrated with a slope close to 1, with a slope error of less than 3%.

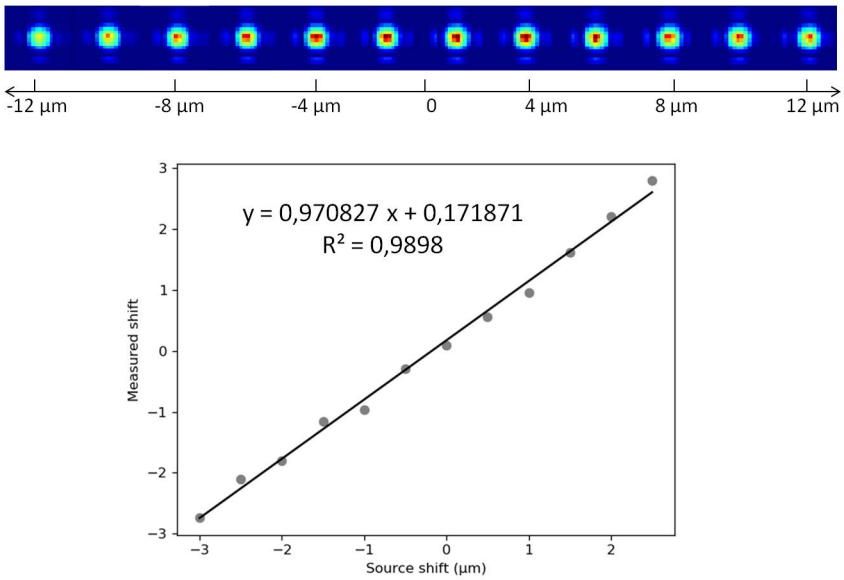

FIGURE 5.29: Measured average tilt as a function of input tilt. At the top images of the aperture corresponding to each source shift. The source for shifted, in both the positive and negative direction of the x-axis, for a total shift of 24 μm. We performed a linear best fit procedure on the resulting curve. The slope error is 0.3% and the $R^2 = 0.9898$.

5.8 Hartmann sensor design: simulation results

The need of simulating many parameters related with the Hartmann sensor design was already stated at the beginning of this chapter(5.1). In fig.5.1 a general overview of the performed analysis is given.
The simulation results were divided in several parts to asses different issues. In the first section we consider the features connected with the propagation process from one set-up element to the other: source energy, aperture shape, pitch and set-up distances.
In the second section several parameters connected with the detection process have been analyzed : first, the capabilities of classical detection algorithms (First Moment, Weighted First moment, Gaussian Three-Point Fitting) will be studied for a theoretical spot (gaussian shape), with particular attention to effect of threshold level applied to binarized images. To improve the detection performance, more advanced algorithms (Iterative Gaussian Weighted and 2D Gaussian Fit) will be also described. Later, the results of these two sections will be combined together to analyze the outcome of several detection algorithm to a propagated spot (Bessel and Sinc function). Finally, the same analysis will be applied to a real experimental spot.

5.9 Analysis of propagation related parameters

In this section, we will explain in details the analysis performed on the propagation parameters. First, we will study the correlation between the incident X-ray energy and the propagation distance from the Hartmann mask to the detection plane.

5.9.1 Diffraction regimes

Before simulating the entire Hartmann mask, we will concentrate on the effect of propagation on a single aperture. As previously seen, the Fresnel number $N_f = a^2/(z\lambda)$ is used to define the near and far field regimes (see section 5.9.1). We remind here that the condition for the near field regime is satisfied for $N_f >> 1$, while the Fresnel approximation is valid for $N_f \approx 1$ and the Fraunhofer regime applies for $N_f << 1$.
We investigates numerically the diffraction patterns of single circular and square apertures as a function of the propagation distance from the aperture plane at a given illumination wavelength. The aperture size (a) was set at $3\mu m$, the pixel size at 0.1 μm and the wavelength (λ) was chosen equal to $6.2x10^{-11}$ m. Three different diffraction regimes were identified by the following propagation distances (z): for the near field regime z=0.05m (corresponding to $N_f = 8.064$),for the Fresnel diffraction regime z=0.4m (corresponding to $N_f = 1.008$) and for the Fraunhofer regime z=10m (corresponding to $N_f = 0.0403$). The results of the simulation for a square aperture are shown in fig.5.30. The diffraction patterns change accordingly to the three diffraction regimes. In the near field, the signal is quite oscillating and the square shape can be clearly seen; while in the Fresnel regime the oscillations around the peak get smoother. At a larger distance, in the Fraunhofer regime, the signal becomes smoother and the oscillations are weak.

The same simulation was repeated for a circular aperture with the same size and wavelength. The results are shown in fig.5.31. The oscillations are reduced respect to the square aperture (fig.5.30) at the same propagation distance. In particular, the

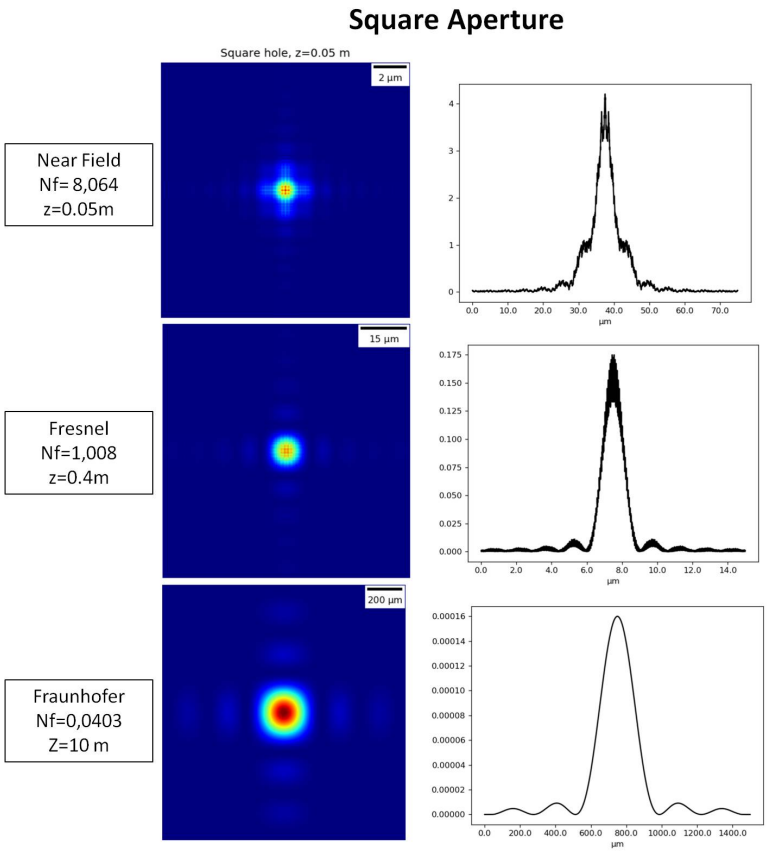

FIGURE 5.30: Diffraction patterns from a square aperture a= $3\mu m$, considering a wavelength $\lambda = 6.2x10^{-11}$ and different propagation distances z=0.05, 0.4, 10 m. The 2D images and the corresponding line plots are reported for three diffraction regimes: for the near field regime ($N_f = 8.064$), the Fresnel diffraction regime ($N_f = 1.008$) and the Fraunhofer regime ($N_f = 0.0403$).

oscillations near the central peak are smaller in both the Fresnel and the Fraunhofer regimes.

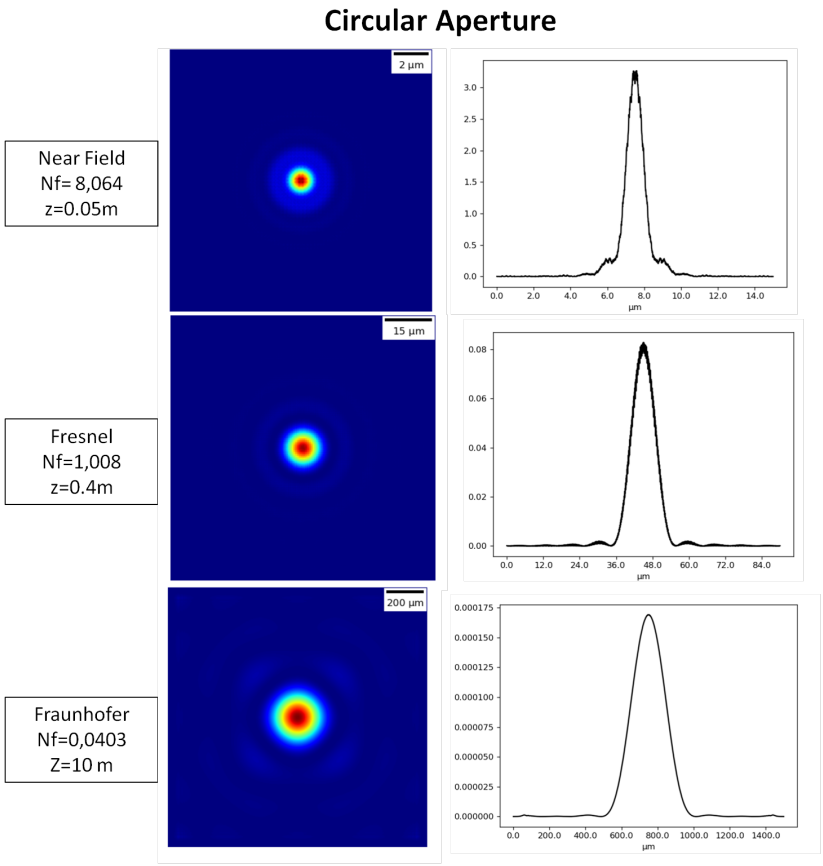

FIGURE 5.31: Diffraction patterns from a circular aperture a= $3\mu m$, considering a wavelength $\lambda = 6.2x10^{-11}$ and different propagation distances z=0.05, 0.4, 10 m. The 2D images and the corresponding line plots are reported for three diffraction regimes: for the near field regime ($N_f = 8.064$), the Fresnel diffraction regime ($N_f = 1.008$) and the Fraunhofer regime ($N_f = 0.0403$).

5.9.2 Incident X-ray energy

In this section, the set-up consists of an Hartmann mask and a pixelated detector. The simulation is performed at two different incident monochromatic energies (10 and 20 keV) and three propagation distances from the Hartmann mask to the detector (z= 0.1, 1 and 5 cm). The source is fully coherent and MxM samples with M=1000 are used. The apertures have a circular shape with diameter=3 μm and pitch=8 μm, detector pixel size = 0.1 μm. The mask is an ideal absorption mask, where the X-ray transmission inside the aperture is one and zero outside.

For an incident energy of 10 keV, when the propagation distance is very small, only the edge effect coming from each aperture can be seen (fig. 5.32 a)). A series of spikes can be observed both in the inner and outer parts of each aperture.
At z=1 cm (fig. 5.32 b)) the diffraction becomes stronger and close holes start to interfere creating small oscillations between the bigger peaks.
Propagating even further from the Hartmann mask, z=5 cm (fig. 5.32 c)), the spot image becomes very noisy and the peaks interfere strongly. Although there is a collective effect, the image of the mask is not sharpened by talbot effect. Indeed, the first Talbot plane with an incident energy of 10 keV and 8 μm pitch it is at around 80

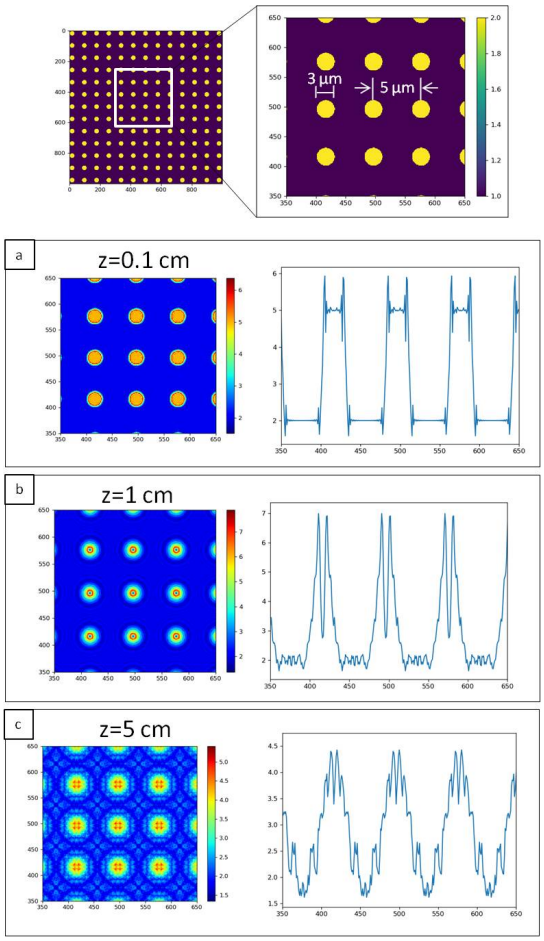

FIGURE 5.32: Top: A scheme of the designed Hartmann plate and the values for the circular aperture (diameter=3 μm) and the pitch (8 μm). The incident monochromatic energy is 10 keV. Images corresponding to three propagation distances from the Hartmann mask to the detector (a) z= 0.1 cm, (b) 1 cm, (c) 5 cm) are reported. Single line plot corresponding to the center of the plate are shown for each z.

cm.
Since the simulated source is fully coherent, small propagation distances were chosen. Placing the detection plane further, the high coherence level will create strong diffraction fringes and the strong cross-talk between close apertures will make impossible to distinguish the signal coming from different holes in the image .
The same simulation code was run a second time with the same parameters given before, except for the energy value that was increased to E= 20 keV.
In fig. 5.33 a), the diffraction pattern at z=0.1cm is reported. A similar trend can be observed respect to the lower energy case (fig. 5.32 a)), even if the oscillations at the edge are less pronounced.
For z=1 cm (5.33 b)) the diffraction pattern is quite spiky and a small cross-talk contribution can be detected. Remarkably, moving the detector plane further (z=5 cm, 5.33 c)), each aperture creates a peaked diffraction pattern even if the interaction between apertures increases respect to the previous case.
Let us compare the plot shown in fig.5.33 c) with the one from a single hole (fig.5.31

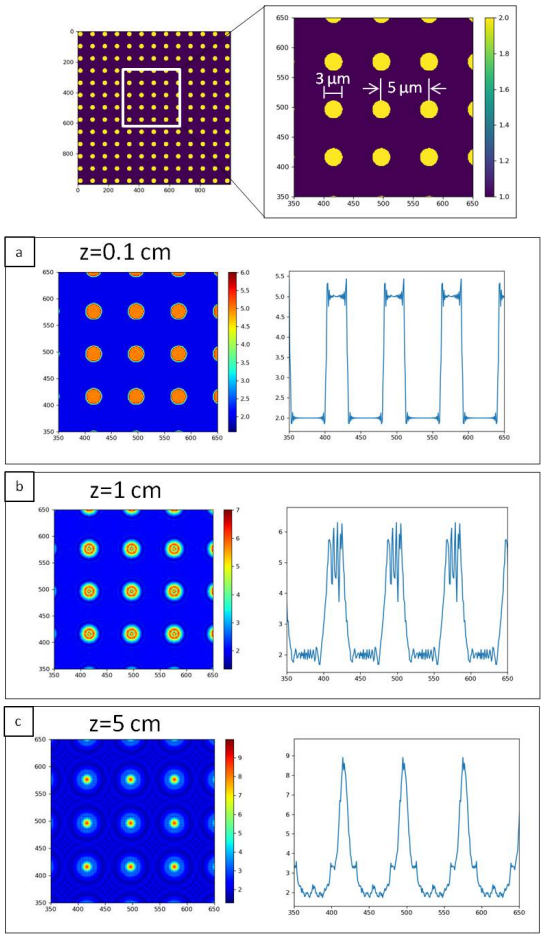

FIGURE 5.33: Top: A scheme of the designed Hartmann plate and the values for the circular aperture (diameter=3 μm) and the pitch (8 μm). The incident monochromatic energy is 20 keV and the images corresponding to three propagation distances from the Hartmann mask to the detector ((a) z= 0.1 cm, (b) 1 cm, (c) 5 cm) are reported. Single line plot corresponding to the center of the plate are shown for each z.

Near Field) obtained with the same simulation parameters. It is clear that the oscillations present in fig.5.33 c) are related with the cross-talk between the apertures, since they are not present in the plot of the single hole.
The main goal of this study was to understand the effect of the incident energy on the diffraction pattern. In this sense, here we underlined a strong correlation between the energy of the incident beam and the propagation distance.

5.9.3 Pitch and Aperture shape

Designing the aperture plate is a crucial step for the Hartmann sensor system. The principal parameters that need to be optimized are the aperture geometry and the pitch. For each chosen geometry of the aperture, a corresponding diffraction pattern will be formed.
In this section we will consider an ideal absorption mask. Simple geometry were chosen in the mask design: square and circle apertures. The pitch of two adjacent holes was progressively decreased to study the occurrence of cross-talk, since this parameter can limit the resolution of the system. The simulation parameters were the following: fully coherent incident beam, square side/circle diameter=3 μm, MxM samples with M=1000, detector pixel-size= 0.1 μm, energy=20 keV, propagation length z=5 cm.

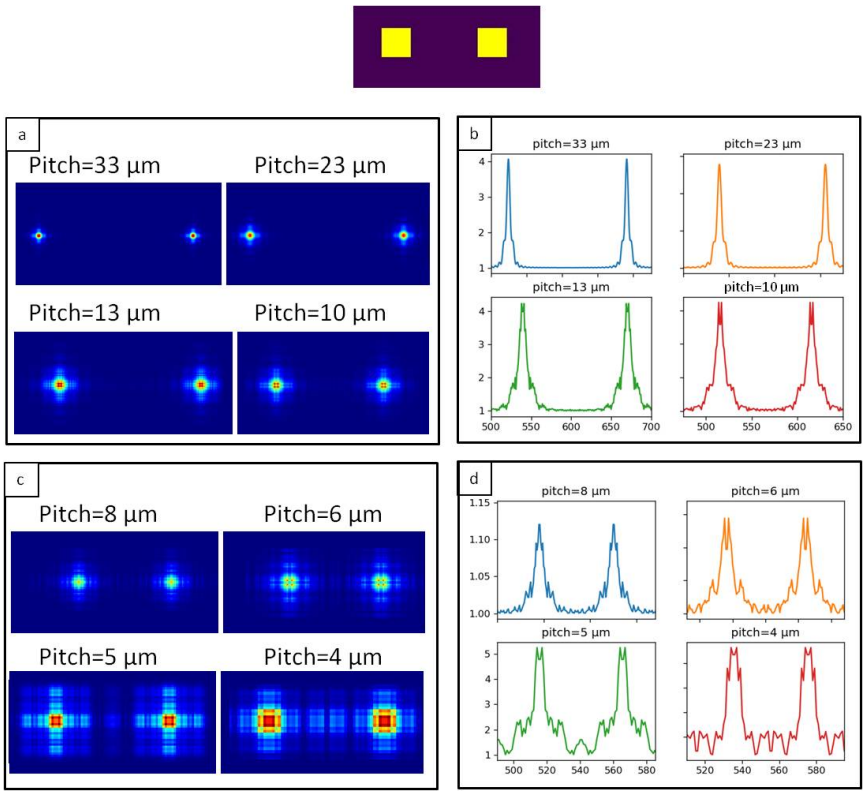

FIGURE 5.34: Top: Design of two square apertures with side=3 μm. a) Images obtained varying the pitch, putting the apertures progressively closer. Pitch from 33 μm to 10 μm. b) Single line plot corresponding to the images shown in a). c) Images obtained varying the pitch: pitch from 8 μm to 4 μm. d) Single line plot corresponding to the images shown in c). The scale is different for plots in b) and d), since varying the pitch will change the relative distance of the peaks.

Cross-talk can be clearly seen in fig.5.34 where the pitch is progressively decreased. For pitches from 33μm to 23μm (fig.5.34), the diffraction is equal to the one of a single aperture. While for a pitch equal to 13μm a small interaction between the holes can be observed. Decreasing even more the pitch size (from 8 to 4 μm, fig.5.34) the diffraction pattern appears very oscillating and the square aperture shape can be seen. This can be explained thinking that we are close to a Talbot plane, with a Talbot distance $z_T = 2m\frac{d^2}{\lambda}$ with m=16.

The same simulation code was run a second time with the same parameters given before, but changing the aperture geometry with a circle. Considering the mask with

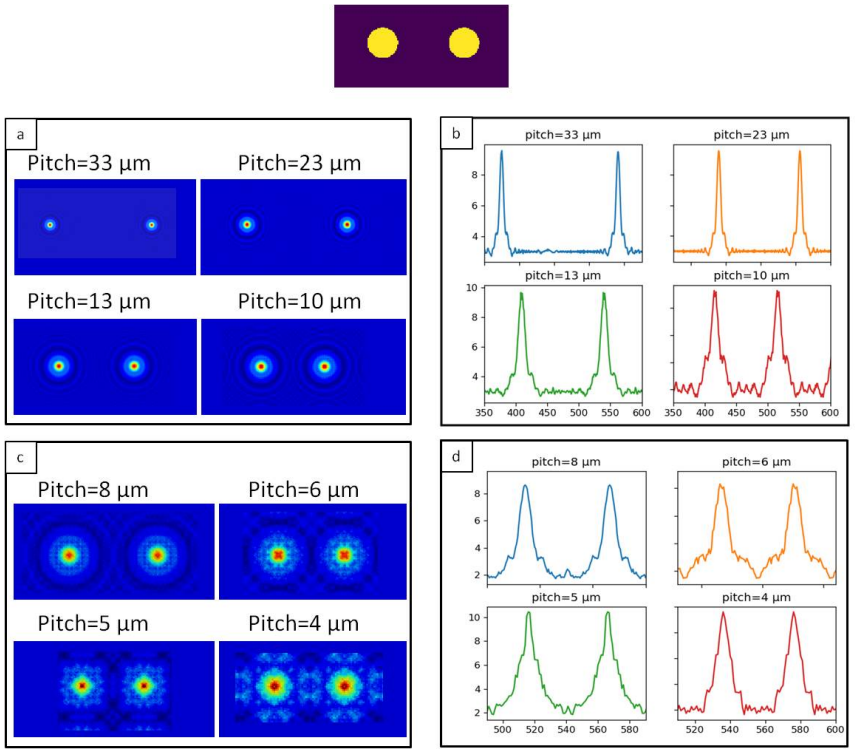

FIGURE 5.35: Top: Design of the two circular apertures with diameter=3 μm. a) Images obtained varying the pitch, putting the apertures progressively closer. Pitch from 33 μm to 10 μm. b) Single line plot corresponding to the images shown in a). c) Images obtained varying the pitch: pitch from 8 μm to 4 μm. d) Single line plot corresponding to the images shown in c). The scale is different for plots in b) and d), since varying the pitch will change the relative distance of the peaks.

circular apertures fig.5.35, the width of all the peaks appears broadened respect to the square mask. We can see how, even when the pitch is quite large (fig.5.35), many small oscillations are already present. The typical diffraction figure from a circular aperture is completely lost from pitch=6 μm (fig.5.35). The mutual interaction of the apertures creates very large and noisy peaks (fig.5.35), making harder the spot detection.

In general, we can conclude that circular holes start to interact at larger pitch size than square holes; making possible to put the square holes closer in the Hartmann plate. In this way the sampling rate of the incident wavefront will be higher, bringing to higher spatial resolution in the final image.

It is important to note that in the last two simulations the illumination was fully coherent and pixel-size was very small. In a real experiment it would be very hard to reach this spatial resolution, making difficult to resolve all the small oscillations that we can see in the simulation.

5.9.4 Phase Hartmann Mask

In this section, we will analyze the capabilities of a different type of masks. In the previous analysis, classical absorption masks were simulated, where the substrate is completely absorbing the incident X-ray beam while the transmission in each aperture is set to one.

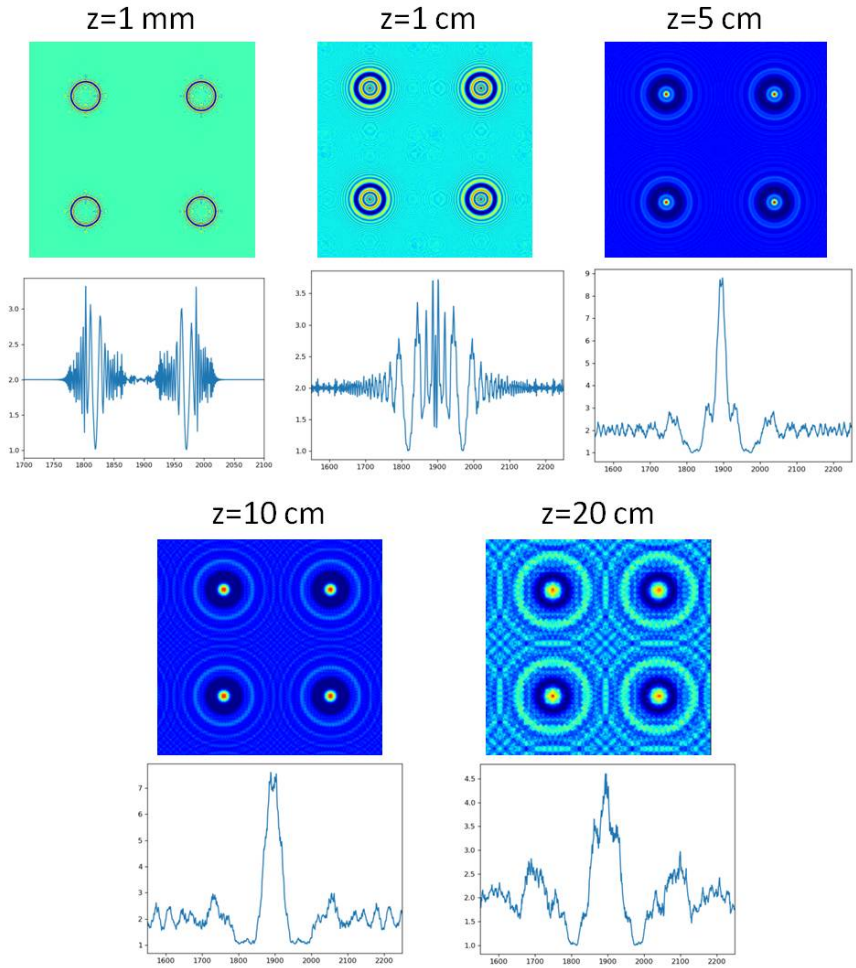

FIGURE 5.36: Images of a phase mask with phase shift of π, varying the propagation distance z from the mask to the detector plane. Single line plot of one aperture are shown for each z. Edge diffraction is visible for small propagation lengths (z=1mm and z=1cm).The diffraction pattern is sharper and the corresponding peak are clearly visible for z=5cm and z=10cm. At z=20 cm, close apertures start to interfere producing a noisy signal.

For the Hartmann mask another design is possible: the whole surface of the mask is completely transparent to the X-rays and only inside each aperture a phase shift is produced. In practice, this type of masks can be fabricated with the periodic deposition of metallic (gold...) structures on a substrate (silicone...). The phase shift in this configuration will be proportional to the thickness and to the element used.
In the simulated set-up a series of circular apertures and two different phase shifts (π and $\pi/2$) were used. Each aperture was defined with a function : $e^{i\Delta\phi}$ with $\Delta\phi$

equal to the phase shift. The simulation parameters were the following: fully coherent incident beam, circular apertures diameter=5 μm, pitch=20μm, MxM samples with M=3000, detector pixel-size= 1.48 μm, energy=20keV. The pixel size was chosen to simulate the performances of the HASO HXR prototype (see section 6.2).
Images obtained with a phase shift of π and different propagation distances can be seen in fig.5.36. Many oscillations can be seen as a result of edge diffraction for small propagation lengths (fig.5.36, z= 1mm and z=1cm). While, putting the detection plane further, the diffraction pattern becomes sharper and the peaks corresponding to each aperture are clearly visible (fig.5.36, z= 5cm and z=10cm). However, at z=20 cm, close apertures start to interfere producing a noisy signal. Here, the signal to noise ratio is highly compromised and the detection accuracy will also drop.
The same parameters were use to run again the same code with a phase shift of $\pi/2$. The diffraction pattern are similar to the one described before ($\Delta\phi=\pi$ fig.5.36) for short propagation distances (fig.5.37 z= 1mm and z=1cm). When increasing z, strong oscillations are still present for z=5cm, while the cross-talk between close aperture is weaker (fig.5.37 z=20cm) than for the same distance at $\Delta\phi=\pi$. The results shown for the phase mask are very promising since, in certain experimental conditions, it is possible to generate sharp diffraction peaks. Nevertheless, the system is very sensible to the set-up parameters, especially for different diffraction regimes corresponding to different propagation distances.
Other aperture shapes and pitch distances can be investigated in the future to improve the system performances.

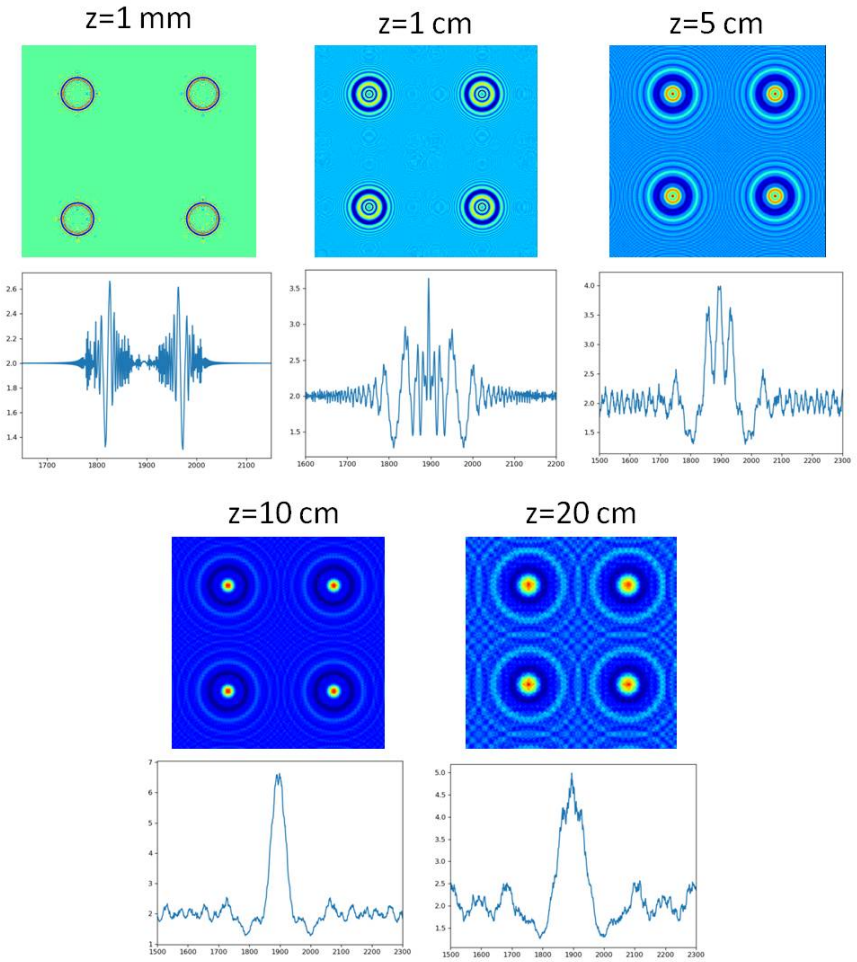

FIGURE 5.37: Images of a phase mask with phase shift of $\pi/2$, varying the propagation distance z from the mask to the detector plane. Single line plot of one aperture are shown for each z. Edge diffraction is visible for small propagation lengths (z=1mm and z=1cm).The diffraction pattern is sharper and the corresponding peak are clearly visible in the other cases.(z=5cm, z=10cm and z=20 cm).

5.10 Analysis of detection related parameters

In this section, we will explain in details the analysis performed on the detection parameters (fig.5.1). In particular, several centroiding methods are presented and their characteristics are discussed based on comprehensive data simulation carried out in Python. All the algorithms used in this section were previously described in Section 5.3.1 and were developed in-house: First Moment, Weighted First moment, Gaussian Three-Point Fitting, Iterative Gaussian Weighted, Iterative Gaussian Three-Point Fitting and 2D Gaussian Fit.

5.10.1 Performance of detection algorithms on a theoretical spot

The analysis of the detection algorithm performances was first done on a simulated theoretical spot. A Gaussian distribution with different full width half maximum (FWHM) was chosen. We concentrated on this parameter since we wanted to un-

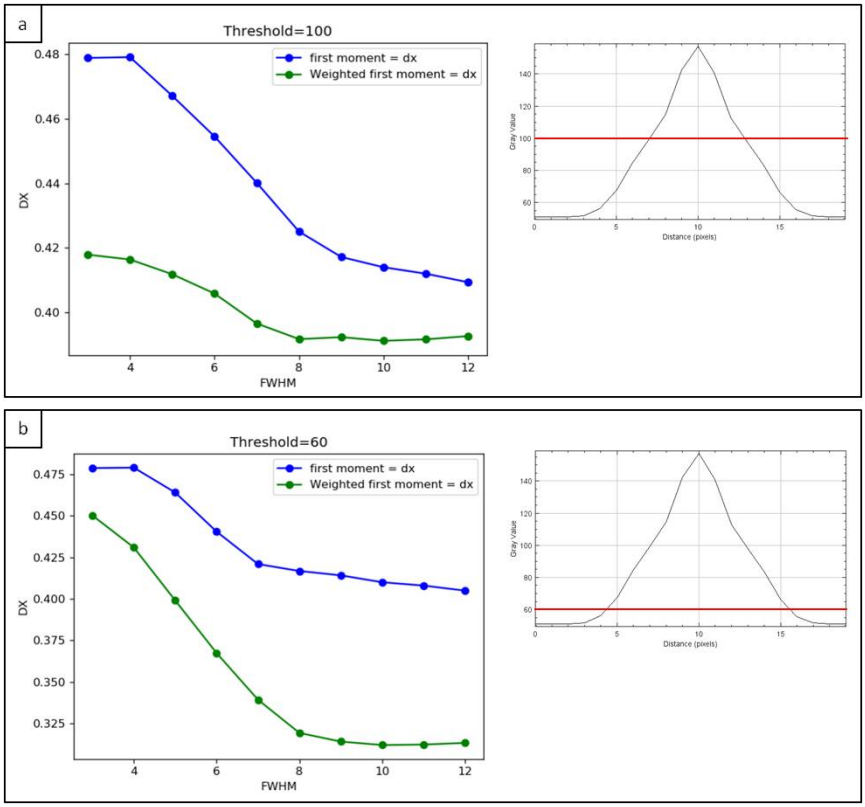

FIGURE 5.38: Performance of the Weighted First Moment algorithm respect to the First Moment: the plots shows DX (difference from the value of the real center) as a function of FWHM of the Gaussian test spot. The weighting function it is a 2D Gaussian with FWHM=4. Two different threshold values (t) were applied : a) t=100, b) t=60. The corresponding single line plot of one spot and the applied threshold can be seen on the right side of the image.

derstand if and how the centroid algorithms are influenced by the number of shined pixels corresponding to a single aperture.
The first algorithm we tested is the Weighted First Moment in comparison with the standard First Moment. Different weighting functions can be used (Gaussian distribution, Bessel function, Sinc function etc.). As it is better if the weighting function resembles the shape of the target spot, a two-dimensional Gaussian function was applied to generate the discrete weighting function. Also, the initial central position of the weighting function is normally given by a previous centroid estimation (first moment centroid was used in this case).
Since thresholding the initial spot image is a standard procedure before running the centroid detection algorithms, two different levels of threshold were considered.
In fig.5.38 the performance of the Weighted First Moment algorithm respect to the First Moment are reported in therms of DX (difference from the value of the real center) as a function of FWHM of the Gaussian test spot. The weighting function is a 2D Gaussian with FWHM=4 pixels and maximum intensity of 155 a.u. A high threshold level (t=100, MAX/1.55) was used in fig.5.38 a) while a lower value (t=60,MAX/2.58) was considered in fig.5.38 b). Both algorithm performances improved by increasing the FWHM of the test spot.

It is also important to note that, while the outcome of the First Moment is not extremely sensible to the threshold level, the Weighted first moment decreases its error with a lower threshold value (fig.5.38 b).
For a threshold value correspondent to 66% of the maximum (fig.5.38 a) and a FWHM of 12, the Weighted first moment algorithm returns a $DX = 0.39$; while the same point for a threshold value correspondent to 40% of the maximum (fig.5.38 b) $DX = 0.312$.
For both threshold values, the algorithms reach a plateau for Gaussian test spots with FWHM>= 8. In addition to that, a second analysis was performed on the definition of the weighting function parameters. In particular, we estimated the accuracy of the algorithm on the same test spot changing the FWHM of the weighting function. A Gaussian test spot of FWHM=5 was choosen, and the Weighted First Moment algorithm was run several times changing the FWHM of the weighting function. In fig.5.39 a plot of the DX (distance from the real spot center) as a function of the weight FWHM can be seen. An image of the test spot is also presented (fig.5.39, bottom right corner).

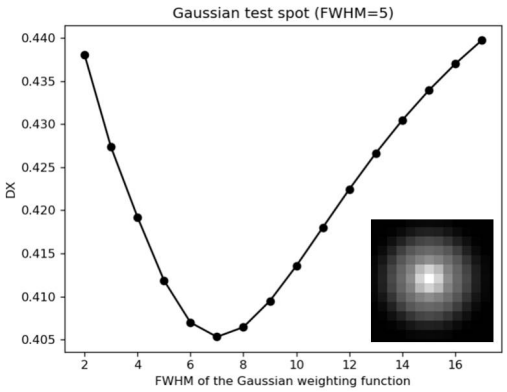

FIGURE 5.39: Performance of the Weighted First Moment algorithm on a gaussian test spot of FWHM=5 (bottom right corner). Plot of DX (distance from the real spot center) as a function of the FWHM of the gaussian weighting function. A small percentage variation can be observed in DX (around 6% decrease) for increasing FWHM values.

A small percentage variation can be observed in DX (around 6% decrease) for increasing FWHM values. Therefore, the performances of the Weighted First Moment algorithm are affected by the definition of the weighting parameters. Small improvement in the centroid detection can be seen decreasing the value of FWHM, reaching a minimum for FWHM=7. The accuracy in the spot detection decreases for FWHM larger than 7. This can be explained with the relative dimensions between the test spot and the weighting function. The test image was a Gaussian with FWHM=5, considering a weight much larger than the spot increases the error in the spot detection.
The second algorithm that was taken in to consideration is the Gaussian Three-Point Fitting. Notably, the initial centroid estimation is crucial for this method, as it determines the pixels that are included in the fit. For this reason we performed the same analysis on the Gaussian test spots (varying their FWHM), considering two different guessing for the initial central position of the Gaussian fit: one calculated with the First Moment algorithm and the second giving the exact theoretical center. A plot of DX (distance from the real spot center) as a function of the spot FWHM

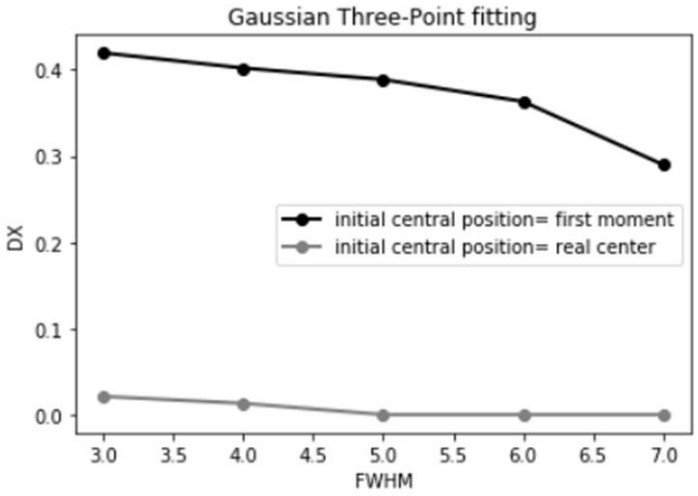

FWHM	X(first moment)	X(real center)
3	0.4193	0.0220
4	0.4017	0.0140
5	0.3885	0.0012
6	0.3631	0.0012
7	0.2901	0.0110

FIGURE 5.40: Performance of the Gaussian Three-Point Fitting algorithm on a Gaussian test spots (varying FWHM). Plot of DX (distance from the real spot center) as a function of the spot FWHM for two initial central position of the gaussian fit: one from the First Moment algorithm and the second giving the exact theoretical center. The plotted values are reported on the table on the right.

is shown in fig.5.40. The algorithm accuracy is dramatically influenced by the initial central position passed to the Gaussian fit. Its performance is comparable with the one obtained with the Weighted First Moment algorithm (green line, fig.5.38) when the outcome of the first moment is given as an initial central position. While, the DX estimation become extremely accurate (around 0.1%) when the real center is considered. When the real center is considered, the minimum value for DX is found for FWHM=5 and 6; while the values increases of about 10 times when FWHM=3,4 and 7. Even small oscillations in the initial fitting parameters could generate the divergence of the Gaussian Three-Point Fitting (Ferstl, 2016).

Since this algorithm is deeply influenced by the first centroid guessing, it is not convenient to use it when we want to reach sub-pixel accuracy in the centroid estimation.
These first three algorithms (First Moment, Weighted First moment, Gaussian Three-Point Fitting) are an example of the basic centroid techniques that can be used. On average these centroid estimations, when the initial centroid position is unknown, can reach an accuracy up to 0.3 times better that the pixel size. Thus, two more

advanced calculations can be performed to improve the centroid estimation: an iterative approach (Iterative Gaussian Weighted and Iterative Gaussian Three-Point Fitting) can be considered to let the calculation converge or a full 2D gaussian fitting procedure (2D Gaussian Fit). In the Iterative Gaussian Weighted, after calculating an initial guessing for the centroid, the result of each iteration is used for centroid estimation in the subsequent computation. In fact, by performing multiple iterations, the weighting function W is shifted towards the target position.
We looked at the number of iterations needed in order to converge to the real centroid value. The results obtained for a gaussian test spot of FWHM=4 are reported in fig.5.41. The convergence is quite fast since after 20 iterations (fig.5.41 a)) the result it is already 10 times better than the non-iterated version of the algorithm. Almost 1/100 of pixel accuracy can be achieved in 30 iterations. Finally, the algorithm is close to high accuracy after 40 iterations. In fig.5.41 b) the set of centroid coordinates for each iterative step are overlaid on the spot image. The black arrow direction in the magnified image shows the results for an increasing number of iterations.

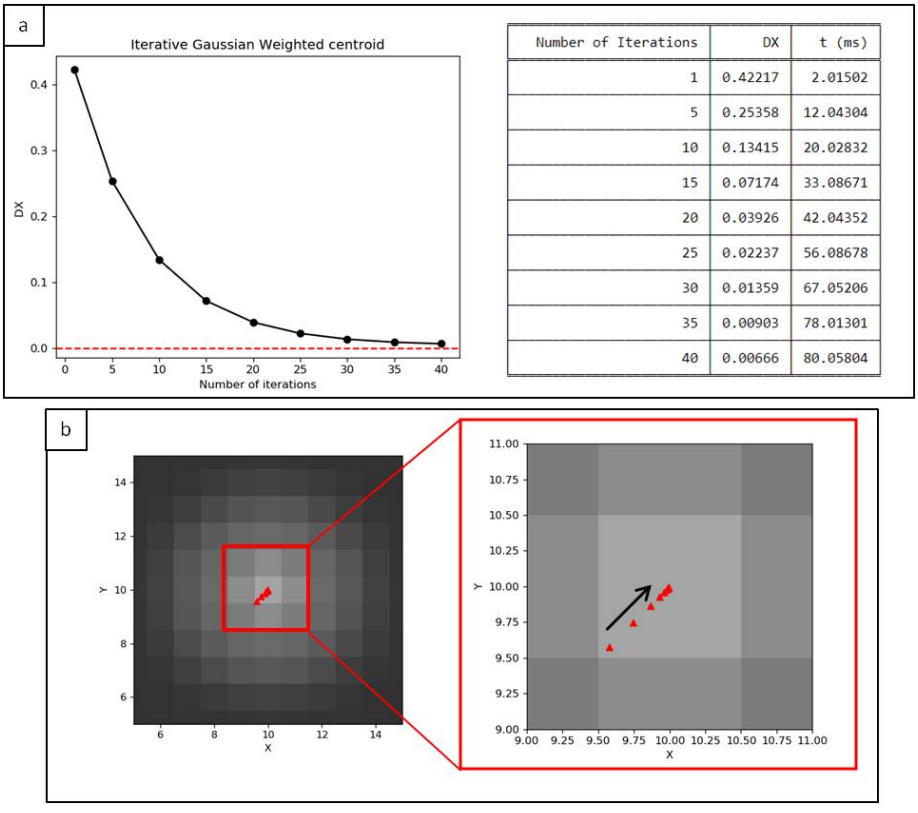

Number of Iterations	DX	t (ms)
1	0.42217	2.01502
5	0.25358	12.04304
10	0.13415	20.02832
15	0.07174	33.08671
20	0.03926	42.04352
25	0.02237	56.08678
30	0.01359	67.05206
35	0.00903	78.01301
40	0.00666	80.05804

FIGURE 5.41: Results from Iterative Gaussian Weighted algorithm. (a) Plot of the DX (distance from the real spot center) respect to the number of iterations for a gaussian test spot of FWHM=4 . The plotted data and the computational time in ms are reported on the table. (b) Set of centroid coordinates(red triangles) for each iterative step are overlaid on the spot image. The black arrow shows the evolution of the results for an increasing number of iterations.

The same iterative approach was used to improve the results from the standard Gaussian Three-Point Fitting. This algorithm after only 2 iterations improved the estimation of the centroid (5.42 a)). Compared to the iterative version of the Gaussian Weighted centroid, where convergence is achieved slowly and constantly, here

the centroid value remains stable after 2 iterations. Even if the Iterative Gaussian Three-Point Fitting algorithm can reach a good sub-pixel estimation, the obtained value (0.01349) cannot be improved by increasing the number of iterations.

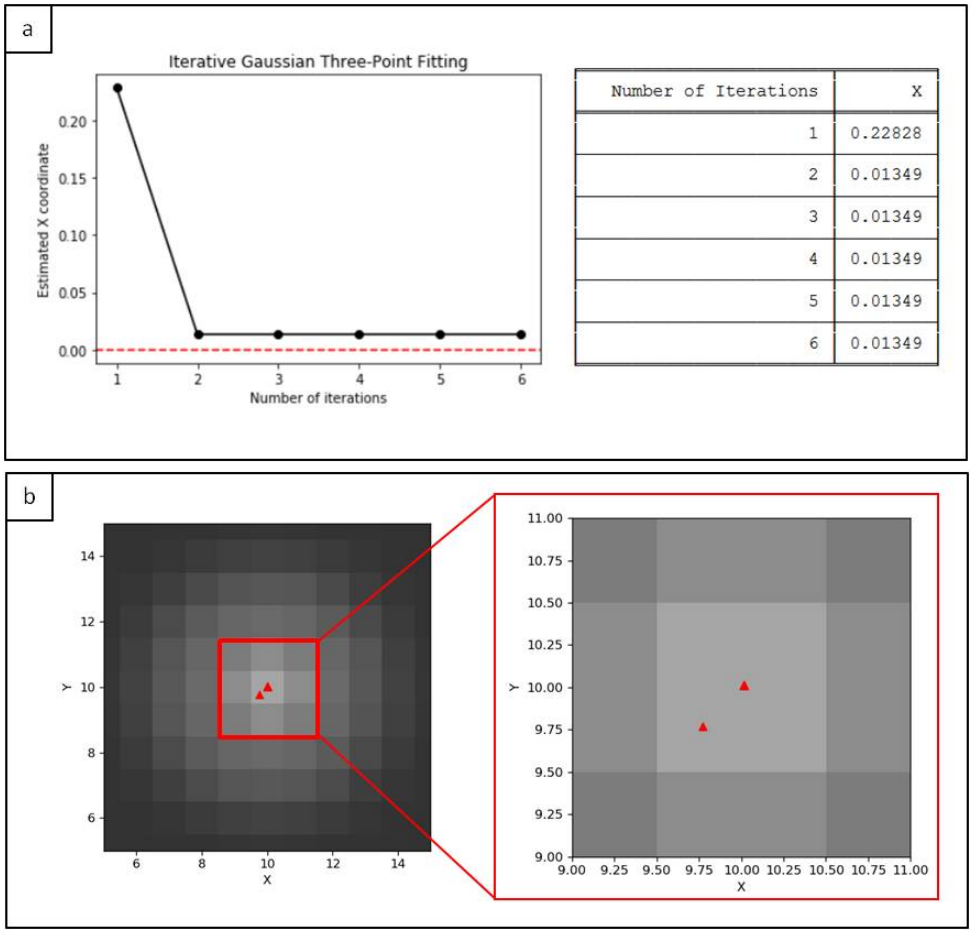

Number of Iterations	X
1	0.22828
2	0.01349
3	0.01349
4	0.01349
5	0.01349
6	0.01349

FIGURE 5.42: Results from Iterative Gaussian Three-Point Fitting. a) Plot of the DX (distance from the real spot center) respect to the number of iterations for a gaussian test spot of FWHM=4 . The plotted data are reported on the table. b) Set of centroid coordinates for each iterative step are overlaid on the spot image.

We will now consider an advanced algorithm: the 2D Gaussian Fit centroid method. It calculates the centroid by fitting a 2D Gaussian to the 2D distribution of the data using a 2D non-linear least-squares minimisation process.
Even taking a small test spot (FWHM=3) the 2D Gaussian fit algorithm increases the accuracy to around 1/26 th pixel (fig.5.43). When the size of the detectable spot increases the accuracy goes up to around 1/275 th pixel. It is important to note that from FWHM=3 to FWHM=4 pixels the accuracy is improved by a factor of 8. The high performances and high stability of this algorithm makes it one of the more efficient among the other considered here.

Finally, a comparison of the computational time for each centroid method is given in fig.5.44. For the Iterative Gaussian Weighted method the time for one iteration is reported. The Iterative Gaussian Three-Point method had the same computational time of the Iterative Gaussian Weighted method.

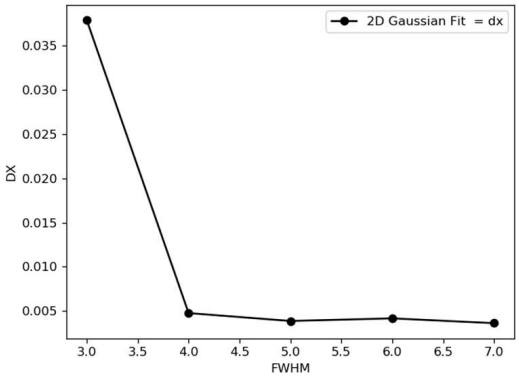

FWHM	X	t (ms)
3	0.03787	34.88600
4	0.00476	33.52353
5	0.00387	29.23406
6	0.00417	30.16856
7	0.00363	31.01646

FIGURE 5.43: Results from 2D Gaussian Fit algorithm : The plot shows DX (difference from the value of the real center) as a function of FWHM of the gaussian test spot. The plotted values and the computational time in ms are reported in the table.

Centroid Algorithm	t (ms)
First Moment	1.0
Gaussian Weighted	3.0
Iterative Gaussian Weighted	1.1
Gaussian Three-Point Fitting	1.0
2D Gaussian Fitting	30.0

FIGURE 5.44: Computational time corresponding to each centroid algorithm.For the Iterative Gaussian Weighted method the time for one iteration is reported.

5.10.2 Performance of detection algorithm on known diffraction patterns

To understand the interaction between the propagation process and the spot detection, the three basic centroid algorithms (First Moment, Weighted First moment, Gaussian Three-Point Fitting), already described in section 5.10.1, will be tested on known diffraction distributions.
In the Fraunhofer approximation, the diffraction pattern of an aperture is obtained mathematically via the Fourier Transform of the aperture function: the diffraction pattern produced by a circular aperture is described by the Bessel function, while for a square aperture is proportional to the sine cardinal. This two distributions will be used in the following analysis as test functions.
The Bessel functions are canonical solutions y(x) of Bessel's differential equation:

$$x^2 + \frac{d^2y}{dx^2} + x\frac{dy}{dx} + (x^2 - \alpha^2)y = 0 \tag{5.72}$$

for an arbitrary complex number α, the order of the Bessel function.
Bessel functions of the first kind, denoted as $J_\alpha(x)$, are solutions of Bessel's differential equation. $J_1(x)$ is known as a Bessel function of the 1^{st} kind and 1^{st} order. The general definition for the n-th order is:

$$J_n(x) = \sum_{m=0}^{\inf} \frac{(-1)^m}{m!(n+m)!}\left(\frac{x}{2}\right)^{(2m+n)} \tag{5.73}$$

The angular distribution of intensity of light diffracted by a circular aperture is :

$$\frac{I(\theta)}{I(0)} = \left[\frac{2J_1(\rho)}{\rho}\right]^2 \tag{5.74}$$

where $\rho = \frac{2\pi sin(\theta)}{\lambda}\frac{a}{2}$ and a is the diameter of the aperture.

The other function that we are going to use is the sine cardinal, also called sinc function. Denoted by sinc(x),the normalized sinc function is defined for $x \neq 0$ by:

$$sinc(x) = \frac{sin(\pi x)}{\pi x} \tag{5.75}$$

A sinc function is an even function with unity area. A sinc function passes through zero at all positive and negative integers (i.e., X=0,$\pm$1,$\pm$2...) but for x=0 it reaches its maximum of 1.
The zero-order Bessel function and the sinc function are reported in fig.5.45.
The 2D Bessel intensity function was tested to simulate the diffraction from a circular aperture. Since this function is characterized by many oscillations, we decide to consider only the central first ring .
The width of the first ring was set at 15 pixels. The classical three centroid algorithms were tested (First Moment, Weighted First moment,Gaussian Three-Point Fitting).
The results are shown in fig.5.46. Considering that the real center is around (x=12, y=11.5), both the First Moment and the Weighted First moment gave an accurate result (pixel/100). While the Gaussian Three-Point Fitting returned a wrong guessing for the X coordinates. This could be explained by the lack of symmetry between x and y at the very center of the spot, that let the Gaussian fit fails in one direction.
An iterative approach was also performed on the Gaussian Three-Point Fitting to increase the accuracy of the result, but no improvement on the centroid estimation

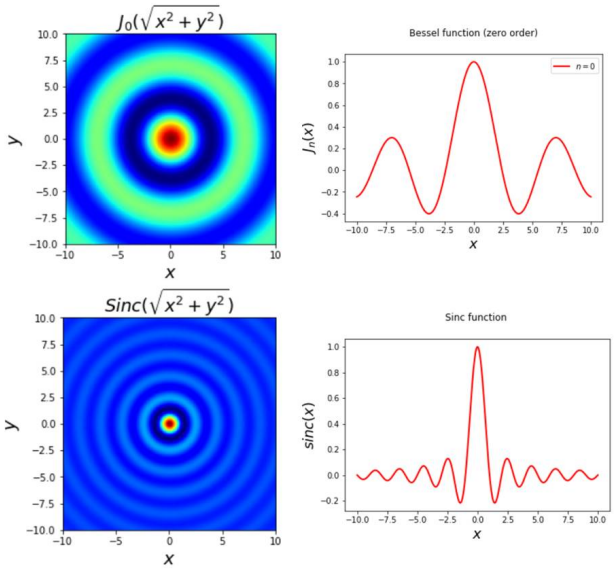

FIGURE 5.45: The intensity of zero-order Bessel function and of the Sinc function. Single line plot can be seen for the two functions.

was found. Since the Gaussian Three-Point Fitting interpolates in 2D the spot image using 5 points and not using a real fitting procedure, the algorithm cannot improve with iterations.

After that, the diffraction from a square aperture was investigated. A 2D sinc function was simulated and, as in the previous case, only the central ring was considered.
In fig.5.47 the centroid guessing from the classical three centroid algorithms were tested (First Moment, Weighted First moment, Gaussian Three-Point Fitting).
The estimated x and y coordinates are reported, while the real center coordinates are around (x=14.5,y=13.5). All the three algorithms returned an accurate guessing for the centroid coordinates: the first moment and the Gaussian Three-Point Fitting find exact center, while the Weighted First moment performed with 1/100 th pixel accuracy. The basic algorithm performed better for the sinc function than the Bessel function. One possible explanation is that the peak is narrower in the sinc function and the centroid calculation it is more accurate.

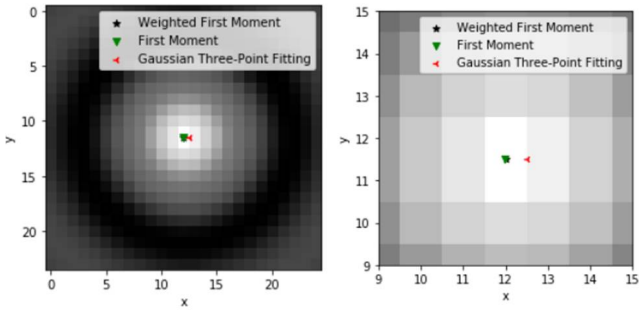

	X	Y
First Moment	11.99135	11.50033
Gaussian Weighted	12.01152	11.50029
Gaussian Three-Point Fitting	12.49467	11.50000

FIGURE 5.46: Test of the centroid algorithm (First Moment, Weighted First moment,Gaussian Three-Point Fitting) on a 2D Bessel function to simulated the diffraction from a circular aperture. Only the first ring was considered and the real center coordinates are around (x=12,y=11.5). The First Moment and the Weighted First moment gave an accurate result, while the Gaussian Three-Point Fitting returned a wrong guessing for the X coordinates.

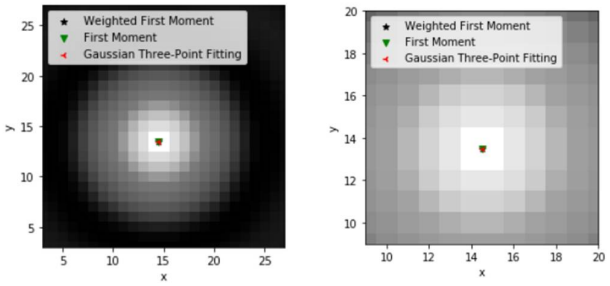

	X	Y
First Moment	14.50100	13.50000
Gaussian Weighted	14.49890	13.50000
Gaussian Three-Point Fitting	14.50000	13.50000

FIGURE 5.47: Test of the centroid algorithm (First Moment, Weighted First moment,Gaussian Three-Point Fitting) on a 2D sinc function to simulated the diffraction from a square aperture. Only the first ring was considered and the real center coordinates are around (x=14.5,y=13.5). All the three algorithms gave an accurate result.

5.10.3 Performance of detection algorithm on a experimental spot

We will conclude the dissertation on the accuracy of the detection algorithms, applying them to a real experimental spot.
The data was acquired at the SYRMEP beamline at the Elettra synchrotron (Italy). In the results reported here, the incident spectrum was a filtered pink beam with peak energy at 15.8 keV. A visible CCD detector (2056*2062) pixels with 1.48μm pixel size combined with a LuAG crystal and image relay system was used. The pitch of the Hartmann mask was 20μm and the apertures were tilted squares. All the details about the experiment will be given in the following sections (section 6) of this chapter.
An image of a small portion of the Hartmann pattern is reported in fig.5.48 a) together with a line plot of the first raw of apertures. The profile corresponding to each spot is not homogeneous: small fluctuations in each peak maximum and shape can be noted.
We run the centroid algorithms previously described in Section 5.3.1 (First Moment, Weighted First moment, Gaussian Three-Point Fitting, Iterative Gaussian Weighted, Iterative Gaussian Three-Point Fitting ,2D Gaussian Fit) for all the spots. Here we only report as an example the outcome for the top-left aperture that can be seen in the magnified red inset. The (x,y) coordinates given by each algorithm are overlaid on the spot image and reported on the table in fig.5.48 b). The plotted (x,y) coordinates are reported in the table in fig.5.49.

From a visual analysis, the spot center looks like around (x=8.0,y=7.4). In this case we cannot give a theoretical value for the center because the data are experimental. The two iterative algorithms gave very accurate results (Iterative Gaussian Weighted and Iterative Gaussian Three-Point Fitting) and the 2D Gaussian Fitting reached around 3/1000 th pixel accuracy in spot detection for the x-axis.
The error in the centroid estimation from the basic First Moment and Weighted First Moment algorithms were quite large compared to the more advanced algorithms. The accuracy was of 40/100 th pixel for the First Moment and 23/100 th pixel for the Weighted First Moment.

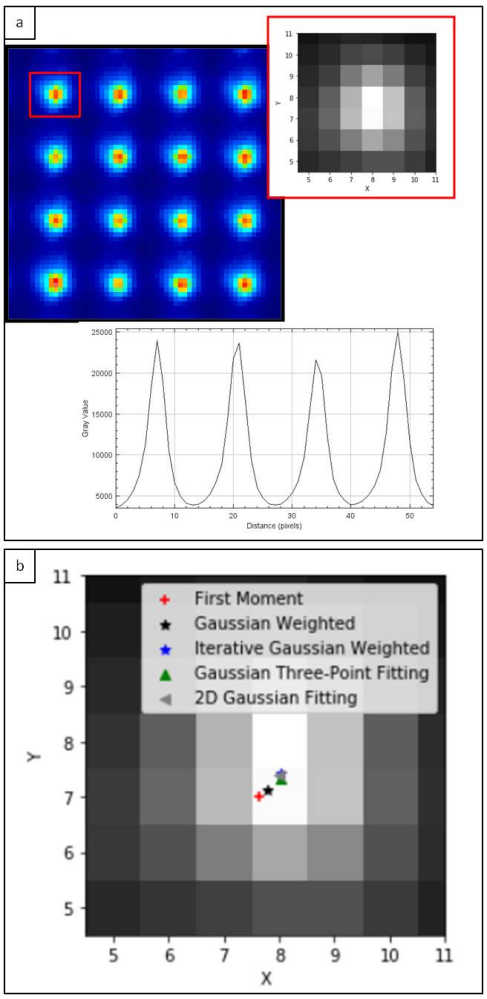

FIGURE 5.48: a) Experimental image of a small portion of the Hartmann mask acquired at the SYRMEP beamline (Elettra synchrotron, Italy). A magnification of the studied aperture can be found in the red inset. Single line plot corresponding to the first raw of the mask. b) Set of centroid coordinates for each algorithm are overlaid on the spot image.

	X	Y
First Moment	7.65257	7.00107
Gaussian Weighted	7.77537	7.13015
Iterative Gaussian Weighted	8.0209	7.43348
Gaussian Three-Point Fitting	8.04278	7.34818
2D Gaussian Fitting	8.00287	7.39941

FIGURE 5.49: Table of the (x,y) coordinates shown in fig.5.48 b) for different algorithms.

5.10.4 Conclusion on detection algorithms

In this last section, we have analyzed the capabilities of the principal detection algorithms both on a theoretical and experimental spots. The accuracy of the detection algorithm has a crucial impact on the final accuracy in the reconstructed absorption and phase images. To reach a high angular sensitivity (0.1 μrad) an accuracy of about 1/100 the pixel size is needed. The first moment and the weighted first moment methods have an accuracy of 40/100 and 30/100 the pixel size respectively. The standard 3-point-fitting algorithm, reaches a very high accuracy (4/1000 the pixel size), only when the exact center is given as an input, that is an hard information to have a priori. The iterative methods are the only one that reach 1/100 th pixel accuracy. We consider a Gaussian test spot (FWHM=4) and define dx as the difference from the calculated to the real x coordinate of the spot. The iterative 3 points-Gaussian algorithm calculate a dx=0.01359 with only 2 iterations in 2 ms. While, the iterative Gaussian weighted calculate a dx=0.01349 with 30 iterations in 67 ms. This discrepancy can be explained considering that 3 points-Gaussian algorithm interpolates 5 points on a 2D Gaussian function, that is the same function used for the test spot. We repeat the same test on an experimental spot acquired at the Elettra synchrotron (Italy). The iterative Gaussian weighted gives a dx=0.021046 with 30 iterations in 37 ms; while the iterative 3 points-Gaussian gives a dx=0.27465 with 30 iterations in 4 ms. Even if the iterative 3 points-Gaussian is computationally faster, the accuracy obtained with the iterative Gaussian weighted algorithm is higher (about 2/100 of pixel size) respect to the 27/100 of pixel size in the other case. Together with the detection algorithm optimization, it is also important to measure the system angular precision. In future we will concentrate on the estimation of the Hartmann sensor accuracy using synchrotron radiation. The simplest experiment that can be performed in this sense is to compare the theoretical values of the diffraction pattern from a pinhole with the experimental one. The experimental limitation of this system will be that, at high energies, the diffraction angles become very small. This problem can be overcome looking at the refraction generated by a prism for different incident angles.

5.11 Conclusion

In this chapter we defined the concept of wavefront using the Huygens-Fresnel principle and the different ways to detect it.
To calculate the incident wavefront, the zonal and modal wavefront reconstruction methods were presented.
The next section was dedicated to the description of a 3D wave propagation simulation tool based on Fresnel propagator. The model can manage any degree of spatial coherence of the source. Validation analysis for the modelling of image formation and coherence proprieties are provided.
A separate part was dedicated to the simulation results on Hartmann wavefront sensor imaging. First, features connected with the propagation processes were examined. Later, parameters connected with the detection algorithms have be analyzed.
Later, the results of these two sections will be combined together to analyze the outcome of detection algorithms to a propagated spot.

Chapter 6

Optimization of the design of Hartmann wavefront sensor for phase imaging

As we have seen in the previous sections, the design and the conception of the Hartmann sensor is strictly related with properties of the radiation emitted by the source. There are many differences from a parallel beam geometry (synchrotron measurements) and a cone beam geometry (laboratory measurements).
It is important to note that when using a Hartmann wavefront sensor with a cone beam geometry, the magnification of each aperture on the detection system will result in a different number of shined pixels respect to parallel beam. It is thus crucial to calculate accurately the distances between the set-up components in order to reach the desired magnification on the final image.
Also, in these two cases the level of coherence will generate different diffraction patterns and, consequently, the aperture design and the spacing in the Hartmann plate have to be adapted.
Finally, the acquisition time are largely different in this two cases due to the higher brilliance of synchrotron radiation respect to laboratory sources. In fact, the greater the brilliance, the more photons of a given wavelength and direction are concentrated on a spot per unit of time.
In this chapter we will show the experimental results for the laboratory set-up and in the next chapter (see chapter 7) for the synchrotron measurements.

6.1 Hartmann wavefront sensor: Laboratory set-up

In this section, we will present the implementation and the results of X-ray phase imaging obtained thanks to the use of the X-ray Hartmann sensor on a laboratory set-up.
The system was designed by the company Imagine Optic, France. The X-ray source is an Excillum liquid gallium metal jet, which has a brilliance of approximately of 5×10^{11} photons/(s mm^2 $mrad^2$ 0.1 % B.W.) (Wansleben et al., 2019), one order of magnitude higher than conventional microfocus sources. In this new kind of sources an electron beam is focused onto the liquid-metal jet resulting in X-ray generation.
Three different Hartmann plates were tested. All the images were reconstructed using the WAVEVIEW metrology software provided by Imagine Optic.
Results coming from every set-up will be discussed in the following sections.

6.2 Compact X-ray Hartmann wavefront sensor: edge detection

The first system under test is the HASO HXR: Hartmann wavefront sensor for Hard X-ray imaging (fig.6.1). The sensor is very compact since it measures about 50 cm in length. It is compatible with both focused and unfocused beams. The system works

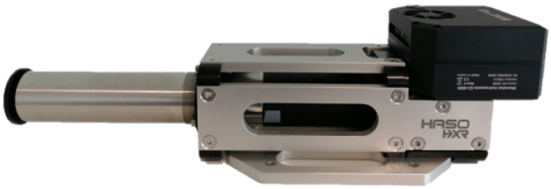

FIGURE 6.1: Picture of the HASO HXR Hartmann wavefront sensor for Hard X-ray imaging from Imagine Optic. Image courtesy of *Imagine Optic*.

with its own reconstruction program. The sensor is composed of an amplitude Hartmann mask, located in front of a scintillator and a visible relay imaging system. It works for energies ranging from 5 to 25 keV. It has a field of view of 3x3 mm^2, and a deflection sensitivity of 100 nrad (La Rochefoucauld et al., 2021,La Rochefoucauld et al., 2020).
The first measurements performed with this sensor are 2D images of test samples: empty polycarbonate tubes (wall tickness=50μm), tube filled with oil and with nylon fibers (diameter=500μm and 120 μm) . In this case, the main goal of the experiment was to test the ability of a known X-ray wavefront sensor to perform phase imaging. From the raw images of the Hartmann mask it was possible to reconstruct the absorption map integrating the signal coming from each aperture, the deflection maps in the two directions X and Y, and finally the wavefront. The reconstructed images are shown in fig.6.2 for different samples.
The first sample was an empty polycarbonate tube and it was possible to resolve its 50μm wall (Signal to Noise Ratio (SNR)=5.38 ; fig.6.2 column a1-d1). Then, a polycarbonate tube was filled with oil (fig.6.2 column a2-d2). The absorption signal changes respect to the previous sample. A double edge is visible on the Y slope of the empty polycarbonate tube (fig.6.2 b1) while only one edge is visible when the tube is filled with oil (fig.6.2 b2). This effect can be explained considering that the index of refraction is similar for oil and polycarbonate. In the third column (fig.6.2 column a3-d3) a nylon fiber of 500μm diameter was inserted inside the empty tube. The two edges from air to polycarbonate and from polycarbonate to nylon can be observed.
The last sample we considered are two nylon fibers of 120 μm diameter braided together placed in air. The quality of the absorption image is quite poor (SNR=4.37)

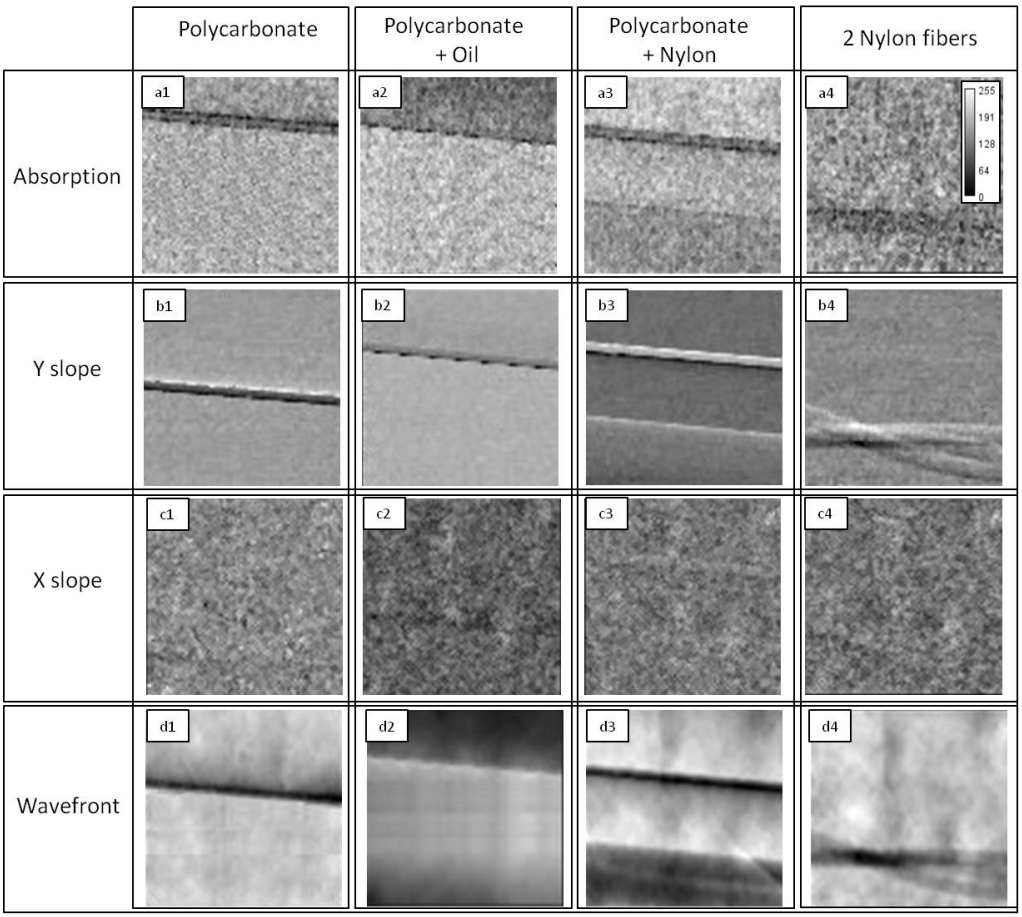

FIGURE 6.2: Images acquired with the HASO HXR Hartmann wavefront sensor from Imagine Optic. Four samples(columns) were imaged (columns): empty polycarbonate tubes (wall tickness=50μm), tube filled with oil, tube with one nylon fiber (diameter=500μm) and two nylon fibers braided together (diameter= 120 μm). For each sample, the absorption, the deflection in the two directions X and Y and the wavefront were reconstructed (rows). The grey scale is the same for all the images and it is shown in the panel a4).

for this sample (fig.6.2 a4). This can be explained considering the small absorption of nylon fibers.
It is important to note that the samples are not detectable calculating the slope in the x direction (fig.6.2 row c1-c4) since they were placed parallel to that axis. The absorption images appear noisier than the deflection, since the absorption is calculated directly from the detector signal while deflection results from the centroid calculation.
From the wavefront images different information on the sample properties can be understood. For example the phase is homogeneous for the empty tube (fig.6.2 d1) except for the jump at the interface with the air, while for the oil (fig.6.2 d2) it is clear that the phase value changes between inside and outside the sample. The same properties couldn't be seen looking at deflection Y only (fig.6.2 b2).
In fig.6.3 a single line plot of the wavefront reconstruction of the polycarbonate tube filled with oil (fig.6.2 d2) can be seen.The sample modifies the reference beam and acts as a diverging lens, because the refractive index is less than one.

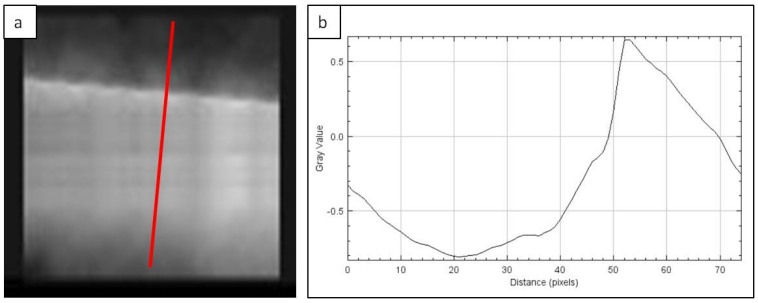

FIGURE 6.3: a) 2D wavefront reconstruction of the polycarbonate tube filled with oil b) single line plot of the wavefront performed perpendicularly to the tube surface.

This underlines the need of reconstructing the same object with complementary signal (absorption, phase etc.) to reach a comprehensive knowledge on sample properties.
Single line plot of absorption and deflection in the Y direction are shown for the first three samples shown in fig.6.2 (a1-a3,b1-b3) are reported in fig.6.4.
In the absorption plots the signal is noisy (SNR=4.37) and it is difficult to differentiate between materials. While in the deflection plots the discontinuity, corresponding to the presence of an edge between two materials, can be clearly appreciated.
In particular, for the sample composed of polycarbonate and one nylon fiber, in the deflection image (fig.6.4,bottom right plot) it is possible to see the two jumps corresponding to the two edges while only one can be detected in absorption (fig.6.4,upper right plot). The double jump (positive and negative) that can be seen in the deflection image, corresponding to the sample edge, is connected with the deflection obtained by the object contours that generates positive and negative peaks. This is a first example where the advantages of deflection and, consequently, phase image can improve the quantitative separation between different materials.

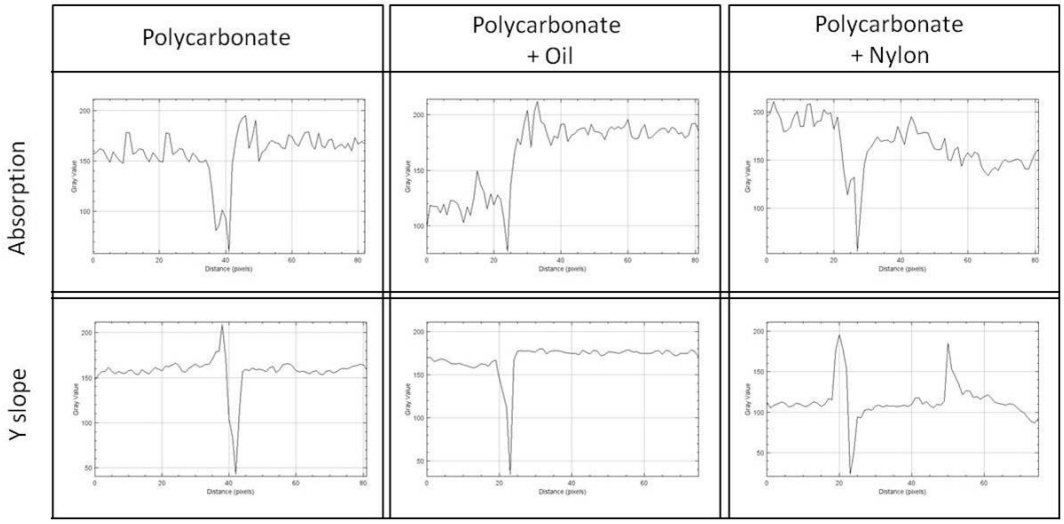

FIGURE 6.4: Single line plot of absorption and deflection in the Y direction for the first three samples shown in fig.6.2 (a1-a3,b1-b3). The edge detection between different material is improved using the deflection respect to the classical absorption images.

6.3 Impact of the reference image

The Hartmann sensor measures the tilt respect to a reference position for each aperture. The detection process is based on the relative shift of each aperture position between one image taken without the sample (reference) and one acquired with the sample (see section 5.2). Since this step is the basic mechanism for experimental measures, we will concentrate on the impact of the reference image on the deflection and absorption reconstruction. We will show how the visibility of details inside the sample is related with how the reference image is taken. It is important to note that in phase reconstruction the presence of the sample modifies the reference beam and acts as a diverging lens. If the object is embedded in a material (like water, ethanol, paraffin etc.) the incident wavefront will be modified by both the sample and its surrounding material.

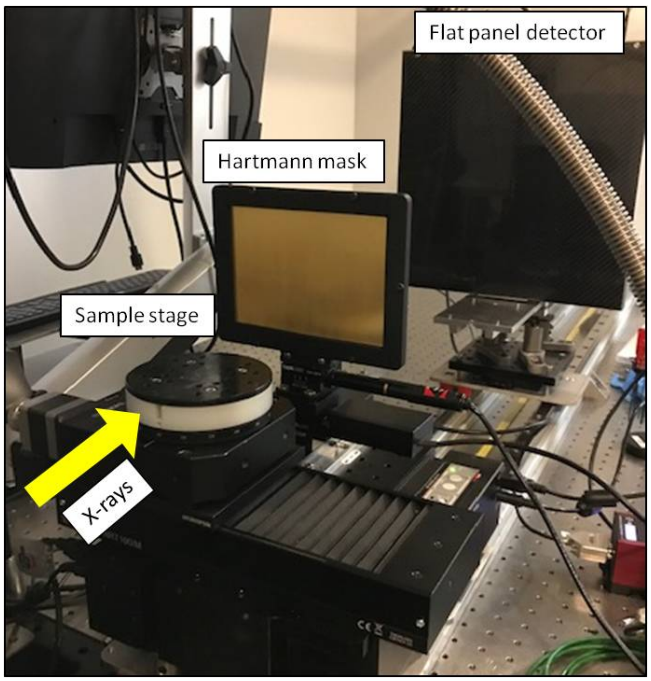

FIGURE 6.5: Picture of the laboratory set-up in Imagine Optic. An X-ray source and an Hartmann mask located in front of a Flat-Panel detector with a 50 μm pixel size. The sample is placed on a translation and rotational stages.

Several tests were performed to understand the impact of the sample preparation on the image reconstruction. The imaging system used for the experimental results is composed of an X-ray source and an Hartmann mask located in front of a Flat-Panel detector with a 50 μm pixel size. The X-ray source is a 70kV Excillum liquid gallium metal jet. The sensor has a field of view of 10x10 cm^2, and a theoretical deflection sensitivity of few μrad. The distance from the source to the sample was set at 25 cm and the distance from the source to the mask at 50 cm (fig.6.5). Considering the magnification, the same sample was imaged in air and in a Ependorff filled with water. One grape was used as a test sample and the following tests were performed:

- Test 1: Sample measured in air and reference taken in air,
- Test 2: Sample measured in water and reference taken in air,
- Test 3: Sample measured in water and reference taken in water.

Absorption and deflection images were reconstructed for each of this experimental condition. The reference in water was acquired using the same cylindrical container

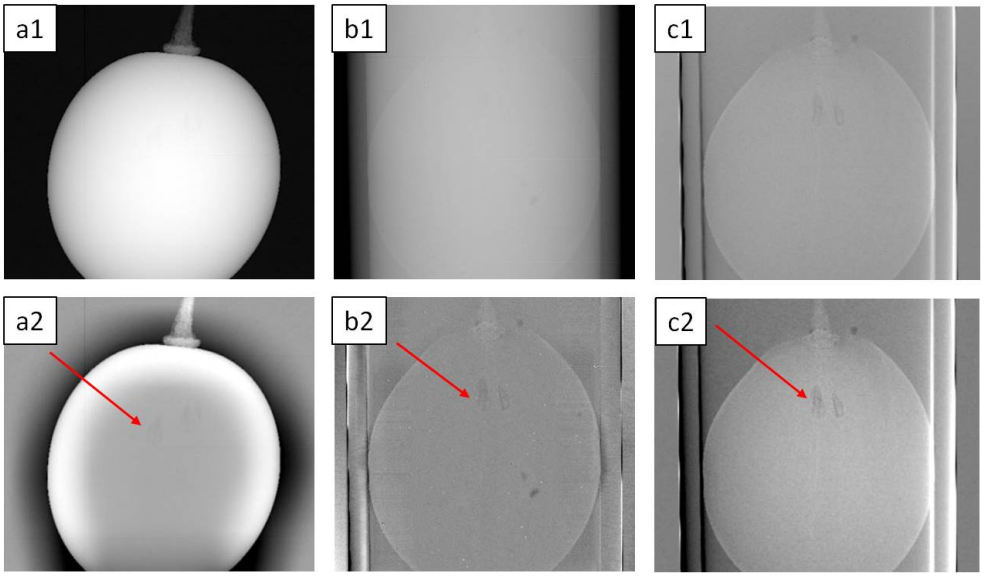

FIGURE 6.6: Absorption reconstruction of one grape: (**a1**) Sample measured in air and reference taken in air, (**b1**) Sample measured in water and reference taken in air, (**c1**) Sample measured in water and reference taken in water. The same images after the application of median filter (size 200*200 pixels) for artefacts reduction (**a2**),(**b2**),(**c2**) respectively. The arrows point at the internal seeds of the grape.

filled with water and without the sample. The results from the absorption reconstruction are shown in fig.6.6. The image acquired with the parameters defined in Test 1 can be seen in fig.6.6 a1, for Test 2 in fig.6.6 b1 and for Test 3 in fig.6.6 c1. The same images after the application of a median filter (size 200*200 pixels) for artefacts reduction are shown in fig.6.6 a2, fig. 6.6 b2, fig.6.6 c2 respectively.
For the filtering part, the plugin Fast Filter available in ImageJ software was used. This plugin is based on unidirectional filters (mean, min, max, median), i.e. filters that can be applied to rows or columns in an image. The median filter with a rectangular n*m kernel area is obtained by replacing the initial pixel values by the median of the pixels within the defined kernel.
When both the sample and reference images are taken in air (fig.6.6 a2), the object contours are visible and a slowly varying signal can be seen inside the sample and the internal structures are hard to differentiate. Inserting the sample in water and taking the reference in air (fig.6.6 b2), the signal is more homogeneous but the internal seeds are still hard to see. In the last figure (fig.6.6 c2) both the reference and the sample images were taken in water. The inner details of the object can be retrieved. The red arrows point to the seeds present inside the grape that cannot be seen in the sample measured in air.
The same absorption images shown in fig.6.6 a1 and c1 were further analyzed. In this images, for the reference image and for the sample the same medium was used. In fig.6.7 a, we can see the absorption reconstruction when the sample is measured in air and reference taken in air. A magnification of the area where the seeds are located, shows that, adjusting the image contrast, it is possible to observe them. On the right, a single line plot of the grape shows the absorption variation inside the sample and two small oscillations corresponding to the seeds (red arrows). On the

other hand, when the sample is measured in water and the reference is taken in water (fig.6.7 b), the single line plot profile appears more linear. The signal inside the grape is more flat and the contrast of the inner details increases (red arrows).
We quantify the depth of the signal coming from the seeds as the ratio of the peak-to-valley intensity variation (ΔI) and the average intensity ($< I >$) outside the seed, for the two cases for the samples measured in air and in water. For the sample in air (fig.6.7 a) we calculated a $\Delta I / < I >= 0.47$ and for the sample in water (fig.6.7 b) we calculated a $\Delta I / < I >= 0.015$. The ratio is increased by 31 times considering the sample measured in water.
It is clear that the choice of the medium can affect the image quality: when the absorption difference between the sample and the surrounding medium is large (such in the case of air), the signal of the inner details is very small.

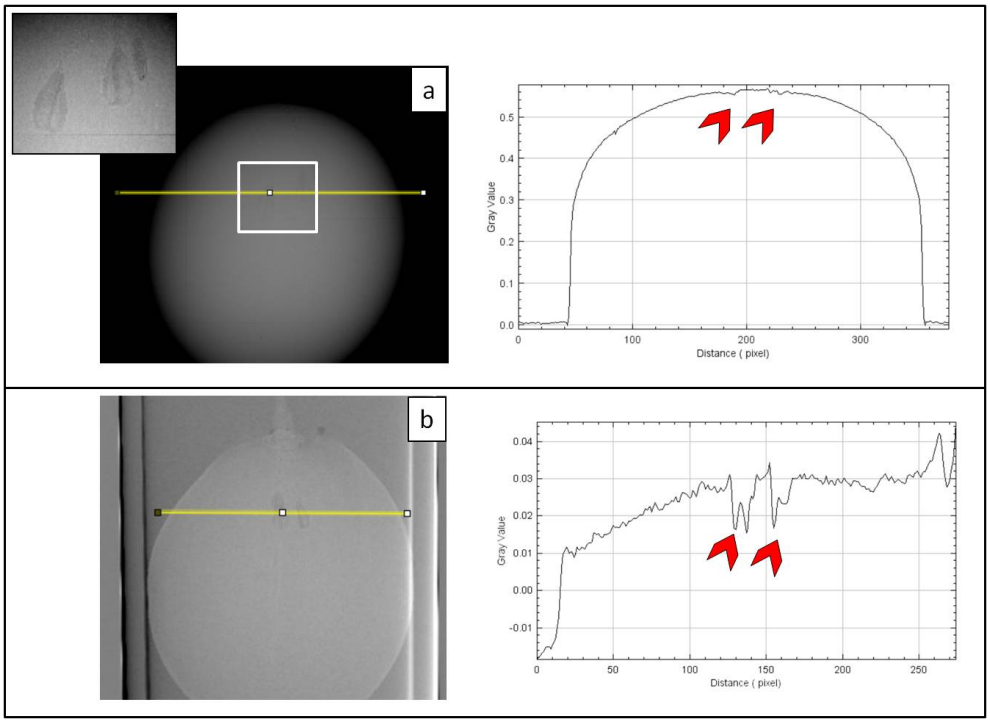

FIGURE 6.7: Absorption reconstruction of one grape. a) Left: Image of the sample measured in air and reference taken in air, Magnification : Adjusting the contrast it is possible to see the seeds. Right: Single line plot of the absorption image. The red arrows points at the small oscillations corresponding to the seeds. b) Left: Image of the sample measured in water and reference taken in water. Right: Single line plot of the absorption image. The red arrows corresponds to the seeds position.

Moiré fringes are visible on the detector plane. A moiré pattern is created by superimposing two patterns of regular geometry, but with different spatial frequencies, such as two sets of evenly spaced lines or apertures (Gustafsson, 2000). In that case, the mask is not totally flat inducing local modifications of the apparent spatial frequency that no longer fit with the detector frequency.
To better understand the impact of moiré fringes, the full deflection image of the sample acquired in air, can be seen in fig.6.8. The presence of black and white fringes affects deeply the image quality. For the single line plot reported on the right part of fig.6.8, the signal coming from the sample is distorted by the moiré pattern. The

deflection of the object is thus mixed with the artefact, complicating the image analysis. The deflection coming from the grape should be symmetrical, while in the plot we do not observe this due to the presence of fringes. Also, fringes correspond to deflections of about 25 μrad, a value much larger than the theoretical accuracy of few μrad.

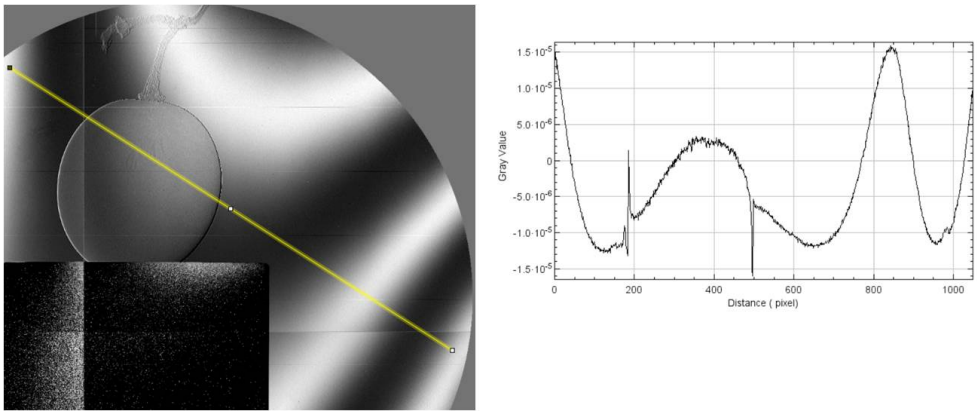

FIGURE 6.8: Deflection reconstruction image of one grape. The moire fringes are clearly visible on the image. Right: Single line plot of the sample profile distorted by the moiré fringes.

Thanks to the Hartmann wavefront sensor, from the same raw data-set it was possible to reconstruct also the deflection images of the sample for the two axis X and Y in the object plane (fig.6.9). Due to the symmetry of the chosen sample the deflection reconstruction in the two axis gave similar outcomes. For this reason only the deflection in the horizontal X-axis is reported in fig.6.9.
Moiré fringes appear in the images taken with the reference in air (figs.6.9 a1 (zoom of fig.6.8) and b1). The intensity of the moiré pattern decreases when the reference is acquired in water (fig.6.9 c1). When the filter is not applied, both in absorption (fig.6.6 c1) and in deflection (fig.6.9 c1), the sample visibility increases when the sample is inside water and the reference is taken in the same medium. The same images have been numerically treated with a median filter (size 200*200 pixels) in order to reduce the artefacts. The results are shown in figs.6.9 a2, b2, c2 respectively. The moiré fringes are now nearly invisible. To better understand how the filtering procedure can attenuate the visibility of the moiré fringes, single line plot of deflection images with and without the filter are shown in fig.6.10. In the image without filter (fig.6.10 a1) the signal inside the grape appears distorted because of the moiré fringes. It is possible that the application of a median filter (fig.6.10 a2) smooths out the deflection variations inside the grape. Sharper peaks coming from the sample edges can be seen, respect to the non-filtered image.
In this section we show how the presence of moiré fringes can be attenuated by changing the medium where the reference image is acquired and also by post-processing the images with the application of a filter.

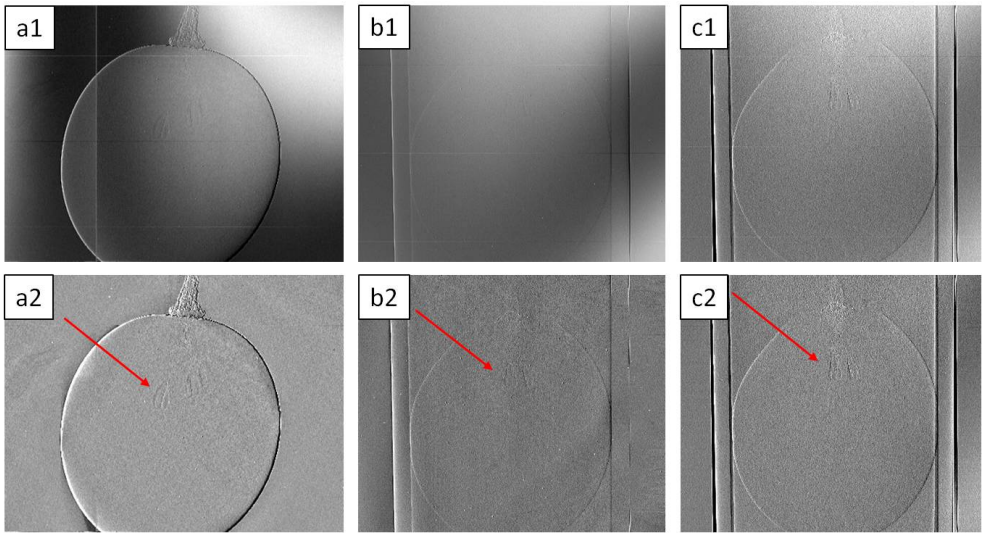

FIGURE 6.9: Deflection reconstruction of one grape for the X-axis: (**a1**) Sample measured in air and reference taken in air, (**b1**) Sample measured in water and reference taken in air, (**c1**) Sample measured in water and reference taken in water. The same images after the application of median filter (size 200*200 pixels) for artefacts reduction (**a2**),(**b2**),(**c2**) respectively. The arrows point at the internal seeds of the grape. The contrast is the same for all the images.

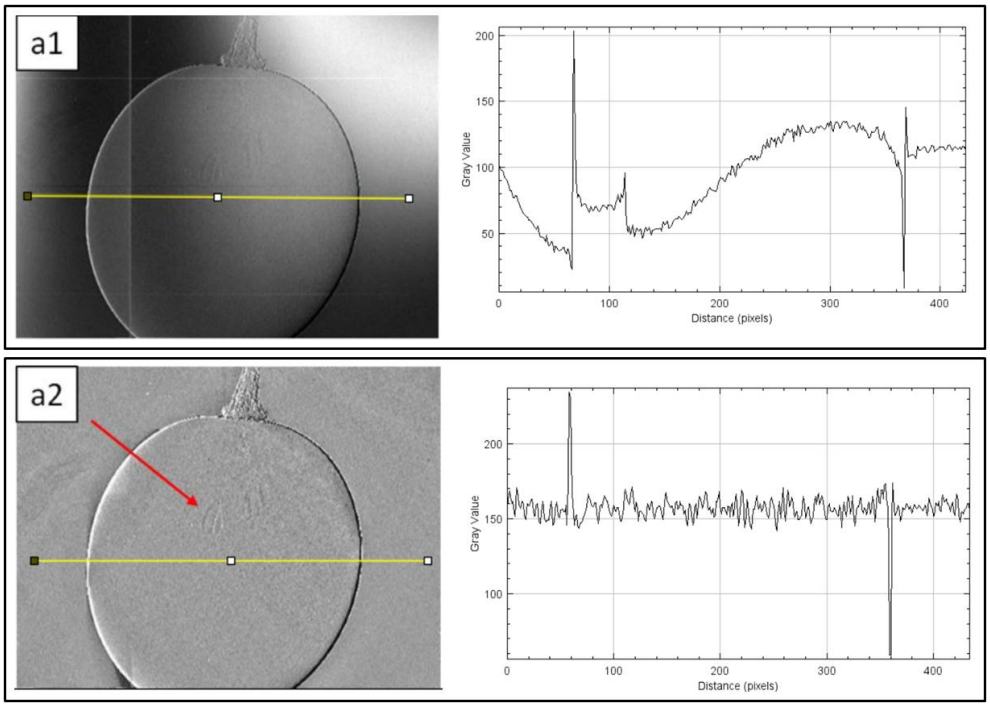

FIGURE 6.10: Deflection reconstruction of one grape for the X-axis: (**a1**) Sample measured in air and reference taken in air, (**a2**) Same image after the application of median filter (size 200*200 pixels).

6.4 Compact Hartmann wavefront sensor: propagation effect

After interacting with the sample, the refracted X-rays will superimpose with rays traveling in straight lines outside and near the object. This effect is predominant on the object edges, creating what it is normally called 'edge enhancement'. Since the diffraction angles are very small in the hard X-ray region, a certain propagation distance is needed to observe this effect. We will study here how the propagation distance affects the sample visibility.
Changing the propagation distance, near and far field approximations can be defined by the Fresnel number. As previously mentioned, the Fresnel number $N_f = (a^2/z\lambda)$ is the ratio between the aperture size (a) and the product of the propagation distance from the aperture (z) and the incident wavelength (λ). For $N_f >> 1$, the regime is in near-field, for N for $N_f \approx 1$ the regime is Fresnel and for $N_f << 1$ the regime is Fraunhofer. Another set of measurements were performed using the Hartmann sensor HASO HXR, already described in the previous section 6.2.
In this experiment we changed the relative distance between the sample and the wavefront sensor.
The distances used in this set-up were the following:
For the first experiment the distance source-sample is 39.5 cm and the distance sample-detector is 6 cm, while for the second experiment the distance source-sample is 33.5 cm and the distance sample-detector is 27 cm.
If we assume the typical size of the Excillum X-ray source (20μm) and the energy corresponding to the peak of the gallium anode (E= 9.2 keV); the second group of distances (propagate field) are closer to the Fresnel approximation requirements (N_f =49) while the first one are better described by the near field regime (N_f =11).

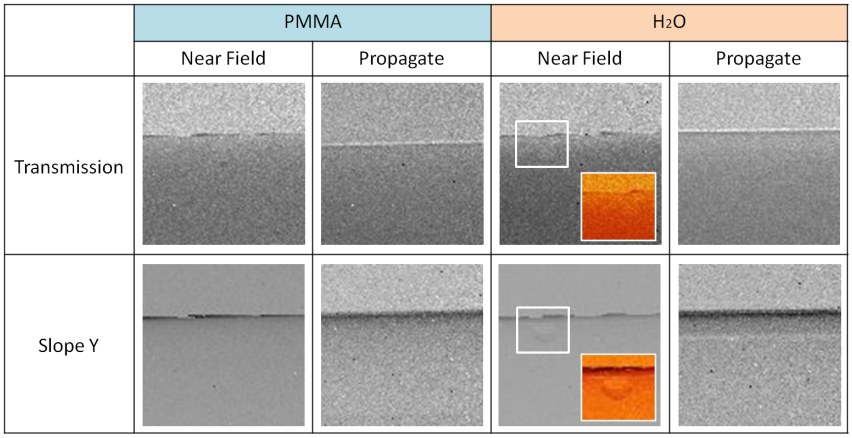

FIGURE 6.11: Images acquired with the HASO HXR Hartmann wavefront sensor from Imagine Optic varying the relative distance between the sample and the wavefront sensor. We defined as near field image the one acquired with distance sample-detector is 6 cm, while for the propagate field the distance sample-detector is 27 cm. Both the transmission and the deflection on the Y axis are presented. Magnification: it was possible to see the presence of an air bubble inside the tube in the deflection image that cannot be resolved in the corresponding transmission image.

The test samples that were used are an acrylic (PMMA) rod with 2mm diameter and an empty polycarbonate tube with 2 mm diameter filled with water.

The edge between air and the material can be clearly seen both for the near and the propagate fields. Notably, imaging the water sample in the near field (zoom fig.6.11), it was possible to see the presence of an air bubble inside the tube in the deflection image that cannot be resolved in the corresponding transmission image reconstructed from the same raw data.
We compared the experimental results obtained of the deflection on the Y axis for the water changing the propagation distance between the object and the detector. A single line profile plot of the near field image is shown in fig.6.12 a) and the one corresponding to the propagated field in fig.6.12 b).
We quantify the depth of the signal as the ratio of the peak-to-valley intensity variation (ΔI) and the average intensity ($< I >$) outside the peak. For the image after propagation we find a $\Delta I / < I >= 0.244$, while for the near field a $\Delta I / < I >= 0.694$. The depth of the signal corresponding to one edge is larger in the propagated case. We also quantify the Full Width Half Maximum (FWHM) of the two plots: for the near field the FWHM=2 pixels while for the propagated one FWHM=7 pixels. Thus the width of the signal is larger after propagation.

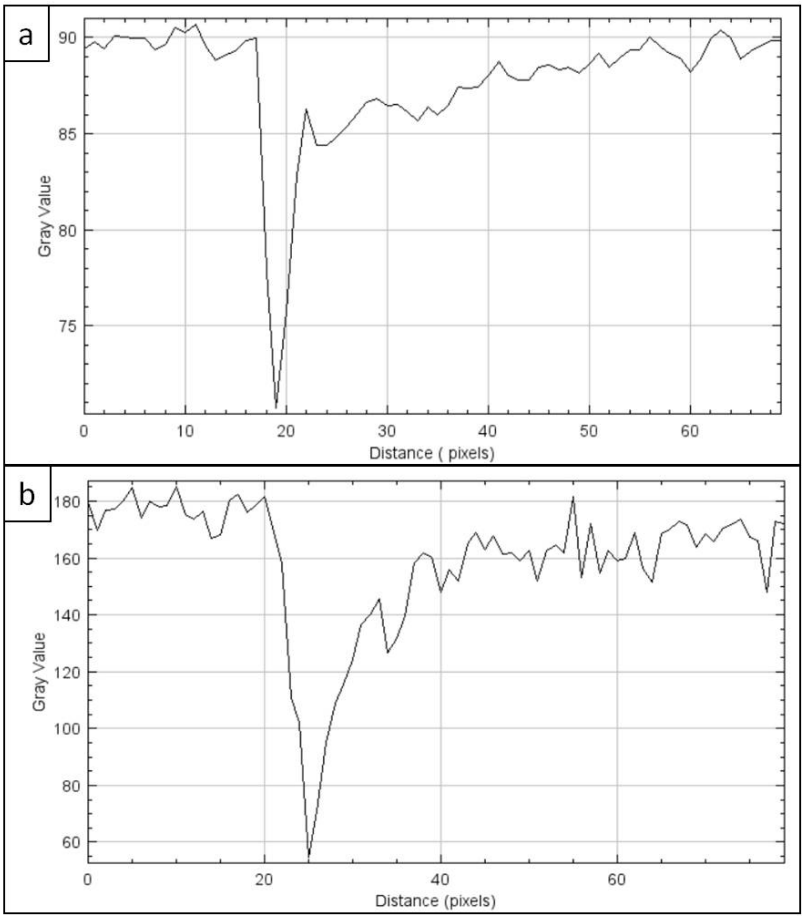

FIGURE 6.12: Single line plot for the slope on the Y axis for water in the near field a) and in the propagated field b) (see fig.6.11, water).

We will now present the results from the simulation code that was run with the same parameters of the experimental set-up discussed in this section. To make the comparison with the simulation easier, we reconstructed the transmission of the samples and their deflection in one of the two axis (Y axis). The image obtained from the

PMMA and the water samples are reported in fig.6.11.
The simulation tool described in section 5.6 was used for the comparison. The experimental parameters described before were used in the simulation. The X-ray transmission T through a material of thickness d was calculated as:

$$T = exp(\frac{i2\pi\delta d}{\lambda}) * exp(-\frac{2\pi\beta d}{\lambda}) \tag{6.1}$$

where δ and β are the components of the index of refraction of the material and λ is the wavelength.
We will first show the results for the near field imaging (fig.6.13), so the detector placed few cm after the sample, for both water and PMMA.
The simulation was performed with an incident energy of 9 keV, with a screen size MxM=200*200 pixels and a pixel size of 1 μm.
On the left we can see the experimental image (6.13 a,d) and on the middle the result of the simulation (6.13 b,e) . A single line plot is reported for both images (6.13 c,f) .
The image of the PMMA is well represented by the simulation, the single line plot (6.13 c) shows a similar trend in the simulated data respect to the experimental one .
On the other hand, the transmission for the water samples appears to be slightly lower in the experimental data (6.13 f).

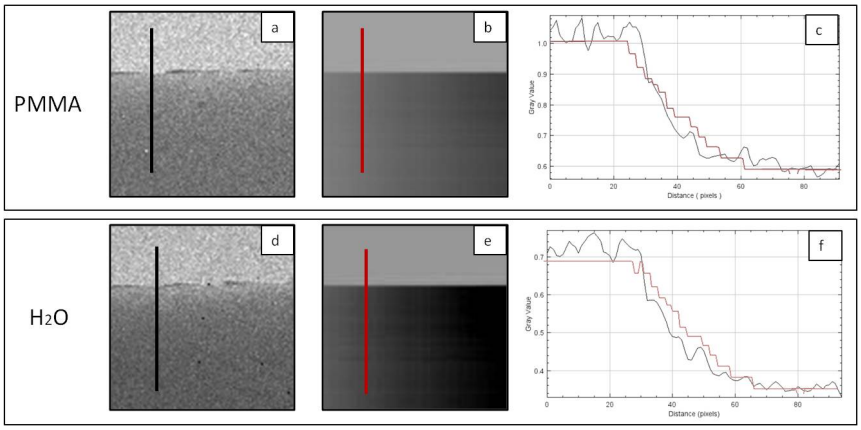

FIGURE 6.13: Transmission images for the near field of the two test samples of PMMA (a,b) and water (d,e). The experimental data is shown on the right (a,d) while the simulated data is shown in the middle (b,e). Single line plot for the two samples are shown (c,f) (red=theoretical data, black=experimental data).

The data corresponding to the propagated field were simulated in the same way for water and PMMA samples (fig.6.14). In this case, the edge enhancement effect and its corresponding peak is well represented for the water sample (water, red line fig.6.14). The simulated profile of the PMMA sample is smoother than the experimental one. One possible explanation can be found in a different PMMA composition of the real sample (so in the given values for δ and β) respect to the tabulated ones. In this section we analyzed what is the effect of wave propagation when the distance between the sample and the Hartmann plane is changed. The wavefront changes when propagates in free space.
With the propagated field we are not completely in the Fresnel regime but we can still observe the changing of regime, for water we can see a jump at the edge (fig.6.14, water) due to propagation that is not visible in the near field image (fig.6.13, water).

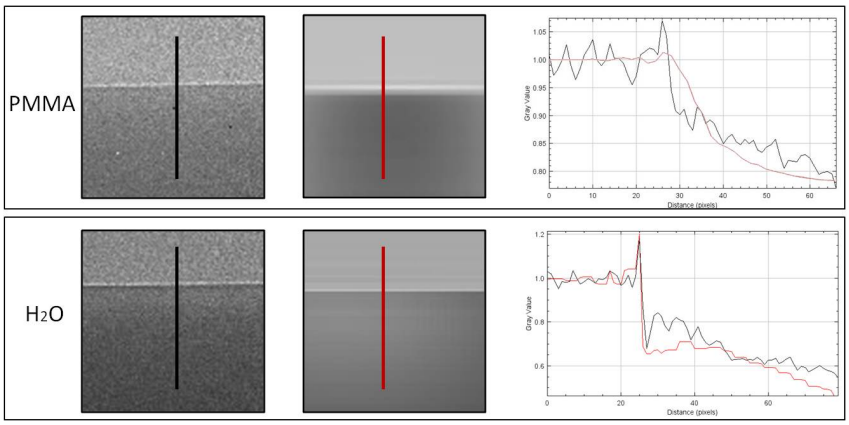

FIGURE 6.14: Transmission images for the propagated field of the two test samples of PMMA and water. The experimental data is shown on the left while the simulated data is shown on the middle. Single line plot for the two samples are shown (red=theoretical data, black=experimental data).

The transmission profiles were compared for the experimental and the simulated data for the near and propagated field. From the results obtained we can conclude that the Fresnel Propagator can be used to predict the experimental outcomes.

6.5 First prototype of the large-field of view Hartmann wavefront sensor

A new Hartmann system was designed by Imagine Optic with a larger field of view. The system is composed of a Hartmann mask, located in front of a Flat-Panel detector. It has a field of view of 3x3 cm^2 and a theoretical deflection sensitivity of 1 μrad. The distance from the source to the sample was set at 22 cm and the distance from source to mask to 43.8 cm.
In this experience, the first tomography measurement on a series of test samples was performed. Cylinders of 2mm diameter were imaged: PMMA, graphite and a polycarbonate tube filled with glass micro-spheres (diameter 1.5μm). The resulting spatial resolution on the sample plane was 25 μm.
The tomography was acquired over 400 projections corresponding to 360°. Every projection was treated with a reconstruction program developed by Imagine Optic to obtain the absorption and the deflection on the Y axis. For the tomography reconstruction the open-source toolbox TIGRE (Biguri et al., 2016) was used. It allows fast and accurate 3D tomographic reconstruction for any geometry (including the cone-beam). It uses iterative algorithms and it has been optimized to run on GPUs for improved speed. A filtered backprojection algorithm was applied to obtain the tomographic volume. A 3D image of the three samples is shown in fig.6.15 a).
Thanks to the tomographic reconstruction the volume can be sliced in different symmetry planes. In particular, the images on the sagittal (fig.6.15 orange plane) and the axial planes (fig.6.15 yellow plane) are the result of a maximum intensity projection on 20 tomographic slices. In fig.6.15 b2-c2), from left to right, we find the graphite, the PMMA and the polycarbonate tube filled with glass micro-spheres.
It is important to remark that in the absorption image (fig.6.15 b2) the tubes appear smooth and with a well-defined shape. On the other hand, in the deflection image

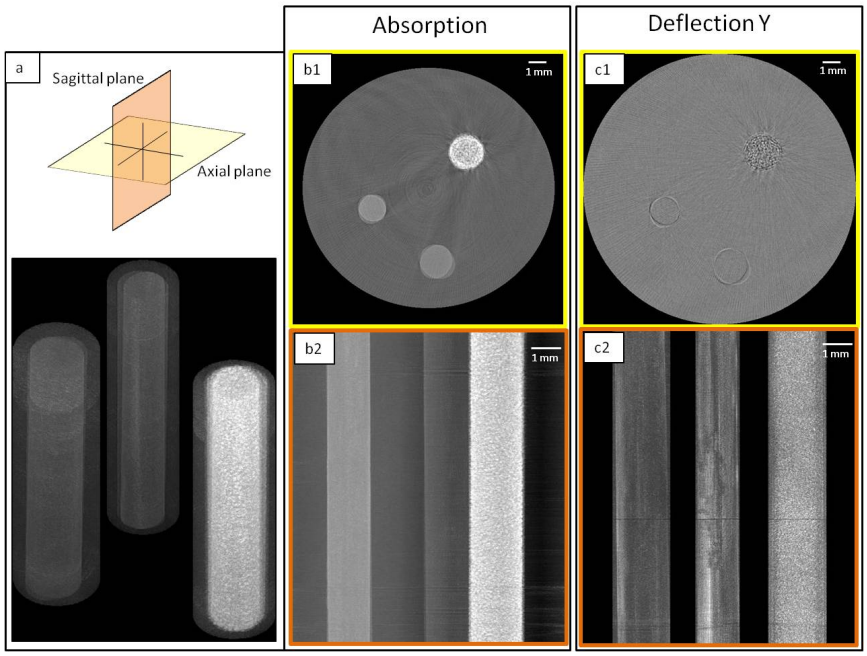

FIGURE 6.15: Tomography images of a series of cylinders of 2mm diameter: graphite (left), PMMA (center), and a polycarbonate tube (right) filled with glass micro-spheres (diameter 1.5μm). a) 3D image of the three samples and an explanation of the symmetry planes. b1-b2) Absorption reconstruction in the axial (yellow plane) and the sagittal plane (orange plane). From left to right, there is the graphite, the PMMA and the polycarbonate tube filled with glass micro-spheres, c1-c2) Reconstruction deflection on the Y axis in the axial (yellow plane) and the sagittal plane (orange plane).

(fig.6.15 c2) many imperfections can be seen inside the carbon and the PMMA tubes. Once again this result underlines the importance of phase imaging as it gives complementary information respect to the classical absorption imaging.
Another important point to notice it is the capability of the system to resolve the glass micro-spheres (diameter 1.5μm) thanks to the high deflection sensitivity of the system. They can't be exactly resolved because of the limited spatial resolution but their presence is clear in both absorption and deflection images.
In the images shown for the axial plane (fig.6.15 b1-c1) many star-like artifacts can be seen. The artifact is caused by the small number of acquired projections. This results in a loss of contrast and resolution in the reconstructed image and, if the number of projections can be increased, the streak artifact is expected to be reduced.

6.6 Second prototype of the large field of view Hartmann wavefront sensor

A different Hartmann mask was designed to image larger samples , still using the same Flat-Panel detector as the first prototype previously described (section 6.5).
It has a field of view of 10x10 cm^2 and a theoretical deflection sensitivity of 1 μrad. The spatial resolution on the sample plane was 37.5 μm. The distance from the source to the sample was set at 30 cm and the distance from the source to the mask at 60 cm.
The goal was to perform a tomographic experiment on a large test sample with an interesting inner structure to visualize in 3D. We decided to image a snail, since it is composed of a calcareous shell coiled in a spiral pattern around a central axis.
The tomography was acquired with 1000 projections covering 360°. Every projection image was treated with a reconstruction program designed by Imagine Optic to obtain the absorption and the deflection images. For the tomography reconstruction the open-source toolbox TIGRE (Biguri et al., 2016) was used.
The first step in the analysis was to treat the artefact on the raw projections to reduce the quantity of noise in the reconstructed volume. The used Flat-Panel is composed of four smaller screens joined together. This results in a slightly different gray level between different screens. Also, many dark lines, corresponding to dead lines on the detector, are visible (fig. 6.16 a).
A median filter (kernel area 200 pixels) was applied both on the vertical and horizontal axis to reduce the number of artifacts on the projection (fig. 6.16 b). This procedure was applied to all the projections. The tomographic volume was reconstructed

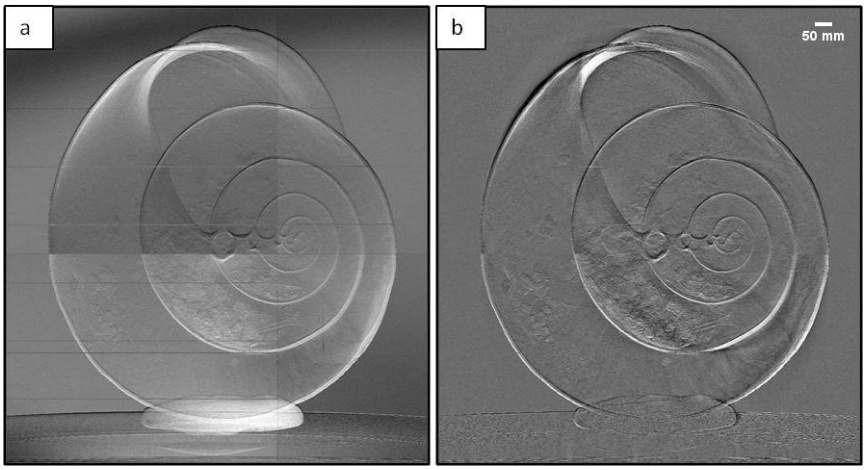

FIGURE 6.16: Projection images of a snail shell performed with the second prototype of the Hartmann wavefront sensor. The resulting spatial resolution on the sample plane is 37.5 μm. a) Projection image, the lines corresponds to dead lines on the detector. b) Same projection image after applying a median filter.

using a cone beam geometry and two reconstruction algorithms were tested on the deflection images: the Filtered Back-Projection (FBP) algorithm and the Simultaneous Iterative Reconstruction Technique (SIRT) algorithm with 150 iterations and a relaxation parameter of 0.2 (fig.6.17).
The details in the image appear blurred and less defined in the SIRT reconstruction. Increasing the number of iterations will decrease the blurring effect in the image, but

at the cost of a dramatic increase of the reconstruction time. After performing this reconstruction test on several slices, the FBP was used to reconstruct the full volume. The 3D reconstruction of both the absorption and the deflection maps allowed us to

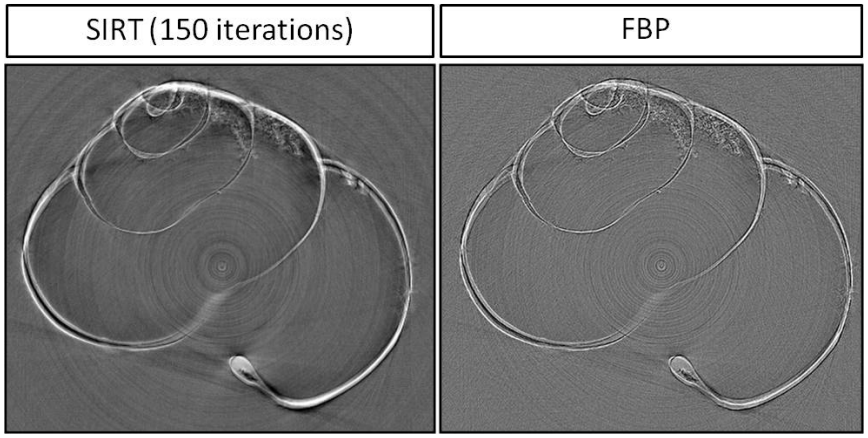

FIGURE 6.17: Tomographic reconstruction images of the deflection performed with the Filtered Back-Projection (left) and Simultaneous Iterative Reconstruction Technique (right) algorithm. For the SIRT algorithm 150 iterations and a relaxation parameter of 0.2 was used. The details in the image appear blurred and less defined in the SIRT reconstruction.

further investigate the sample.
The 3D rendering was done with the data analysis software Volume Graphics VGStudio Max 2.2.6. A picture of the sample is shown fig.6.18 a), together with its 3D rendered images of the absorption fig.6.18 b) and deflection fig.6.18 c).
For the 3D rendering false color based on the gray value were used. The surface was rendered completely opaque for the absorption image while the outer part of the shell (purple) was set transparent in the deflection image. In this way it was possible to see the segmentation (blue) of the inner spiral structure inside the shell. Optimizing the rendering parameters, many small details can be seen on the surface

FIGURE 6.18: a)Picture of the sample (snail shell). b) 3D rendering of the absorption map. c) 3D rendering of the deflection map. Opaque surface was rendered for the absorption image while it was set transparent in the deflection image.In the segmented part (blue), the inner spiral structure inside the shell.

of the shell in the deflection reconstruction (fig.6.19 b). Also, the presence of a crack on the outside of the shell can be seen on the 3D rendering of the deflection (fig.6.19 b) while it is absent on the absorption reconstruction (fig.6.19 a). The same rendering parameters were used for the two images. This is the first step towards the 3D

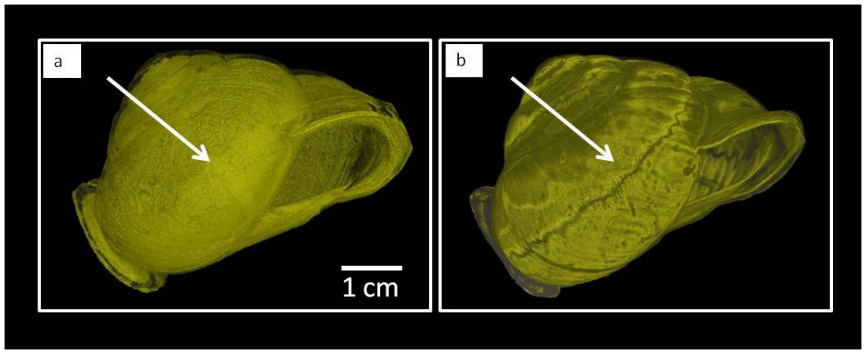

FIGURE 6.19: 3D rendering of the snail shell. a) Absorption reconstruction, b) Deflection reconstruction. The presence of a crack on the outside of the shell can be seen on the 3D rendering of the deflection while it is absent on the absorption reconstruction.

imaging of structured large samples, thanks to the larger field of view and the high deflection sensitivity of the prototype described here.

6.7 3D imaging of biological samples with the second prototype

The Hartmann mask described in section 6.6 coupled with a Flat-Panel detector was tested for 3D imaging of biological samples. The tomography was acquired with 3000 projections covering 360°.
Every projection image was treated with a reconstruction program designed by Imagine Optic to obtain the absorption and the deflection images. For the tomography reconstruction the open-source toolbox TIGRE (Biguri et al., 2016) was used.
Results from two biological samples will be discussed: a mouse brain perfused with microfil solution (Vasquez et al., 2011) and a rat spine together with some part of the ribcage. The samples were imaged in one Eppendorf filled with distilled pure water. To image the inner structures of mouse brain, casting agents can be used to increase the contrast inside the tissue. Specifically, Microfil contrast agent, a low viscous silicone rubber injection compound containing lead pigments, has been used to perfuse the vascular system for tomography measurements. In this perfusion method the lumen of vessels are filled with contrast agent. The lead pigments in the Microfil provide high contrast compared to the background tissue needed to acquire a 3D image of the vascular structure (Walker et al., 2011). The blood in the cerebral vessels is drained out through an incision and the Microfil is perfused right after the complete drainage of blood. Tomographic reconstruction of a mouse brain perfused with Microfil are shown in fig.6.20. Maximum intensity projection of 100 tomographic slices were performed. The 3D reconstruction of the absorption is visible in fig.6.20 a) and the 3D deflection in the y axis in fig.6.20 b).

The yellow arrow is pointing at the same image detail both in absorption and deflection. Since the deflection image is calculated on one of the two axis, the structures manly oriented in the other axis (perpendicular to one considered) cannot be seen. The visibility of the internal structures are limited by the spatial resolution, leading to the visualization of the bigger brain arteries and not of the small capillary

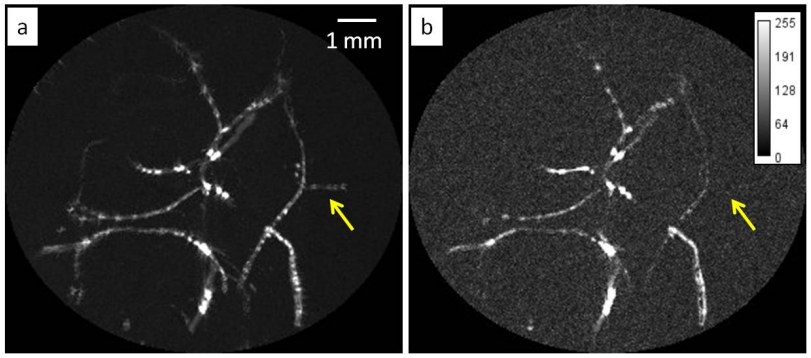

FIGURE 6.20: Tomographic reconstruction of a mouse brain perfused with Microfil, maximum intensity projection of 100 tomographic slices of the 3D absorption a), and of the 3D deflection in the y axis b). The yellow arrow is pointing at the same image details that can't be seen in the deflection image since only one axis on the images plane is considered.

arrangements. The contrast agent (Microfil) enhances the visibility of the brain vascularization that thus appears as bright structures inside the volume. The presence of white clusters inside each vessel can be related with the perfusion procedure. It is possible that the contrast agent could not reach homogeneously all the desired parts inside the tissue. The contrast appears to be more concentrated in some part of the vascularization (white dots) and less visible in others. From the images analysis we can conclude that the perfusion procedure did not work perfectly and that the sample preparation has to be optimized. Notably, the 3D reconstruction performed with the Hartman sensor was capable of visualizing the presence of clusters inside the vessels and can be used as a diagnostic tool to compare different sample preparations. Also, we were able to retrieve qualitative information about the vascularization.

The second sample that was imaged with the same set-up is a rat spine with a part of the ribcage. The spatial resolution on the image plane is 32.5 μm and the theoretical deflection sensitivity is about 1 μrad. The tomography was acquired with 3000 projections covering 360°. Thanks to the large field of view, the full spine was imaged inside an Eppendorf filled with distilled pure water. One slice from the tomographic reconstruction of the absorption is shown in fig.6.21 a) and for the deflection in the y-axis in fig.6.21 b). In the absorption image (fig.6.21 a, inset) the internal tissue of the skeletal bone called spongy bones or trabecular bones can be observed. This inner part of the bones composed of a porous network divided in tiny lattice-shaped units forming this tissue. In the deflection image (fig.6.21 b, inset) it is possible to visualize the internal orientation of this porous tissue in the direction parallel to the considered deflection axis. The two images of the same sample (absorption and deflection on the y-axis) gave complementary information on the sample structure and tridimensional arrangement.

A maximum intensity projection of 100 tomographic slices of both signals was performed (fig.6.22) to better observe the entire sample. The vertebreae are the highly specialized bones which collectively make up the spinal column. Their tridimensional arrangement can be observed in the absorption reconstruction (fig.6.22 a). The part of the ribs attached to the spine can be also seen. From the same acquisition, the deflection image in the y-axis was reconstructed (fig.6.22 b). Comparing the magnification shown in the insets, the 3D shape of each vertebra of the bone can be seen

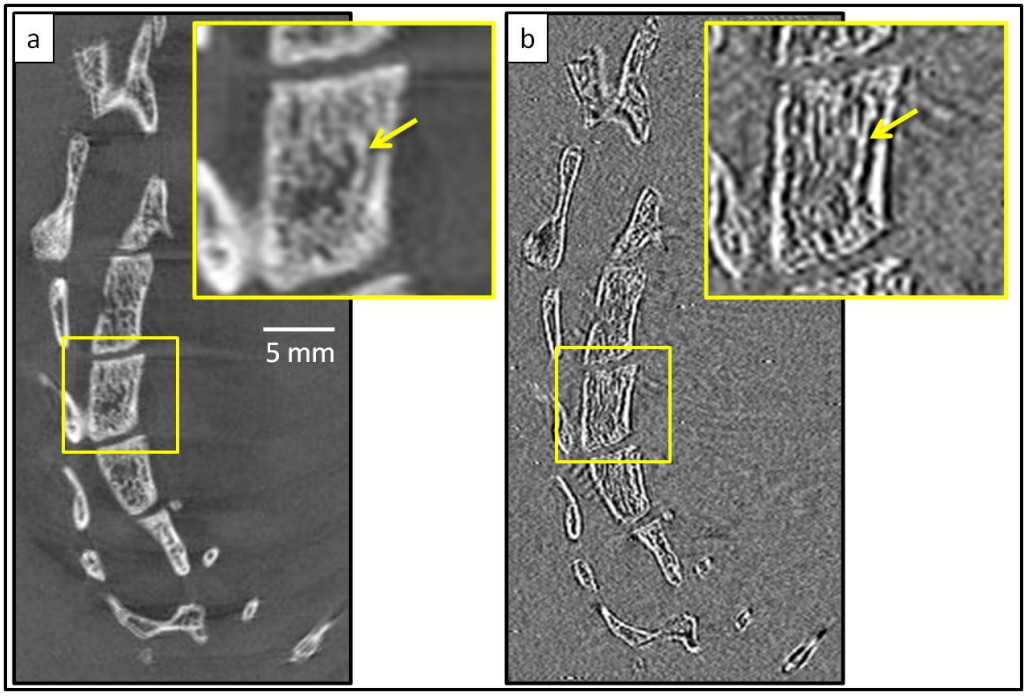

FIGURE 6.21: One reconstructed slice of rat spine sample. Absorption reconstruction a) and deflection reconstruction in the y-axis b). In the inset a magnification of the internal spongy bones can be compared for absorption and deflection images.

in absorption while the orientation of several structures constituting each bone can be analyzed in deflection. Once again, since the ribs are mostly oriented in the x-axis, they are not visible in the reconstruction of deflection on the y-axis. Finally, a 3D rendering of the sample done with the data analysis software Volume Graphics VGStudio Max 2.2.6. is shown in fig.6.23. In this way the tomographic volume can be inspected in 3D and the spatial organization of each element can be visualized.

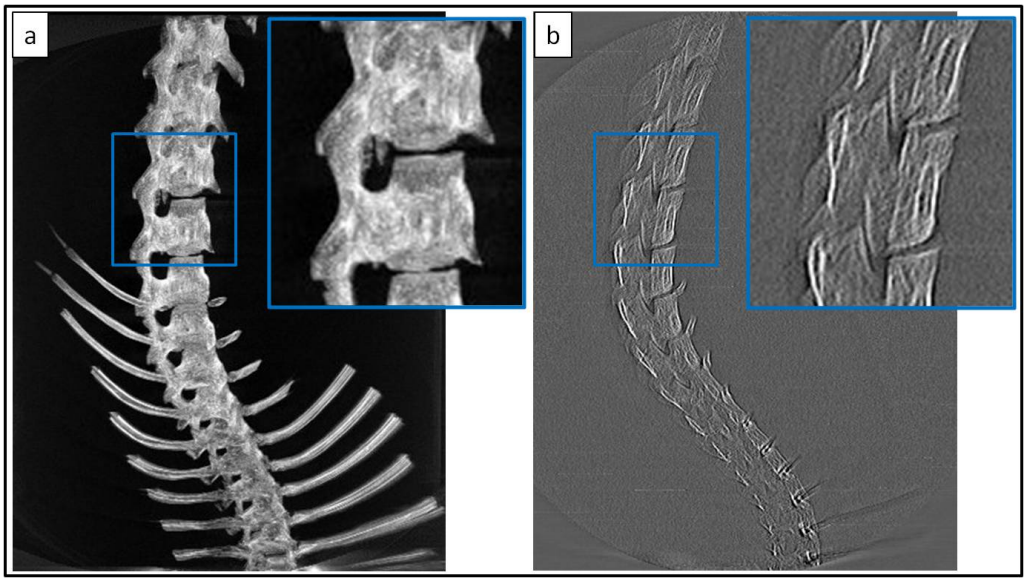

FIGURE 6.22: Maximum intensity projection of 100 tomographic slices of the rat spine. a) absorption reconstruction and b) deflection reconstruction in the y-axis. The structure of the vertebrae can be compared in the two insets.

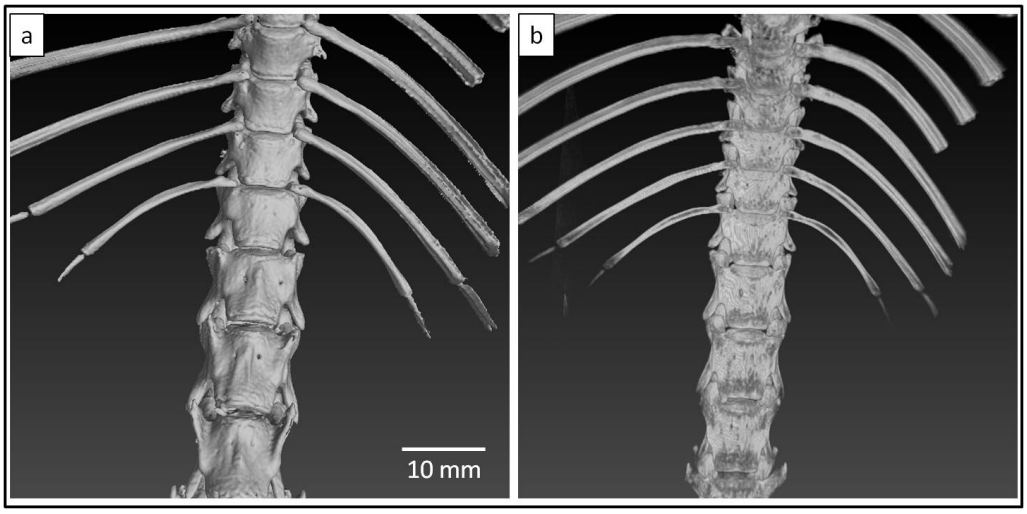

FIGURE 6.23: 3D rendering of the rat spine and initial part of the ribs connected with the spine. a) 3D of the absorption reconstruction, b) 3D of the deflection reconstruction in the y-axis.

6.8 Optimized set-up for biological imaging

A new Hartmann mask was used to perform an experiment focus on biological imaging. The experiment took place at the Syrmep beamline of Elettra synchrotron (Italy) with an incident "white" beam, an electron energy of E=2 GeV and a current I=300 mA.

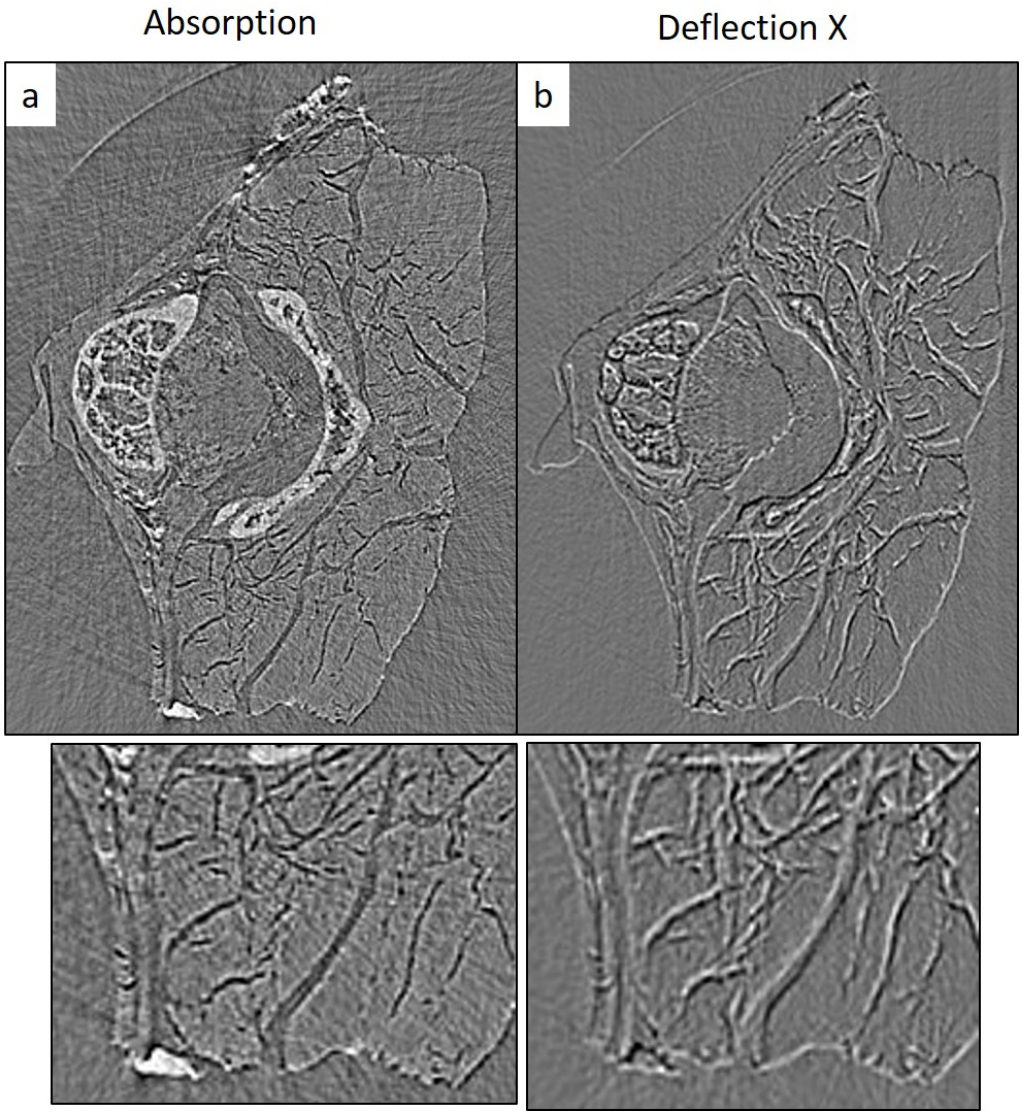

FIGURE 6.24: Single tomographic slice reconstruction of a mouse backbone obtained with the optimized prototype Hartmann wavefront sensor. a) Absorption reconstruction of the sample, b) Deflection reconstruction of the sample. In the lower insets a magnification in the soft tissue area where the vessels are located is given.

The samples stage was composed of an Hexapod, a compact six degrees of freedom parallel robotic motion platform, and a rotational stage to allow tomographic measurements.
The Hartmann mask was placed on a second Hexapod stage to allow the alignment of the mask respect to the incident X-ray beam. The detector was a CMOS (3.9 μm pixel size) from the standard beamline set-up. The spatial resolution on the sample

was 20 μm.
The optimization of the data analysis parameters allowed the reconstruction in 3D both the absorption and the detection signal of biological samples. Many details of a mouse backbone can be seen in a single tomographic slice both in absorption (fig.6.24 a) and deflection (fig.6.24 b). The porosity of the bone as well as the vascular organization can be appreciated in the two images. Complementary information on the sample can be retrieved using 3D absorption and deflection reconstruction. A 3D rendering of the absorption map is shown in fig.6.25 .

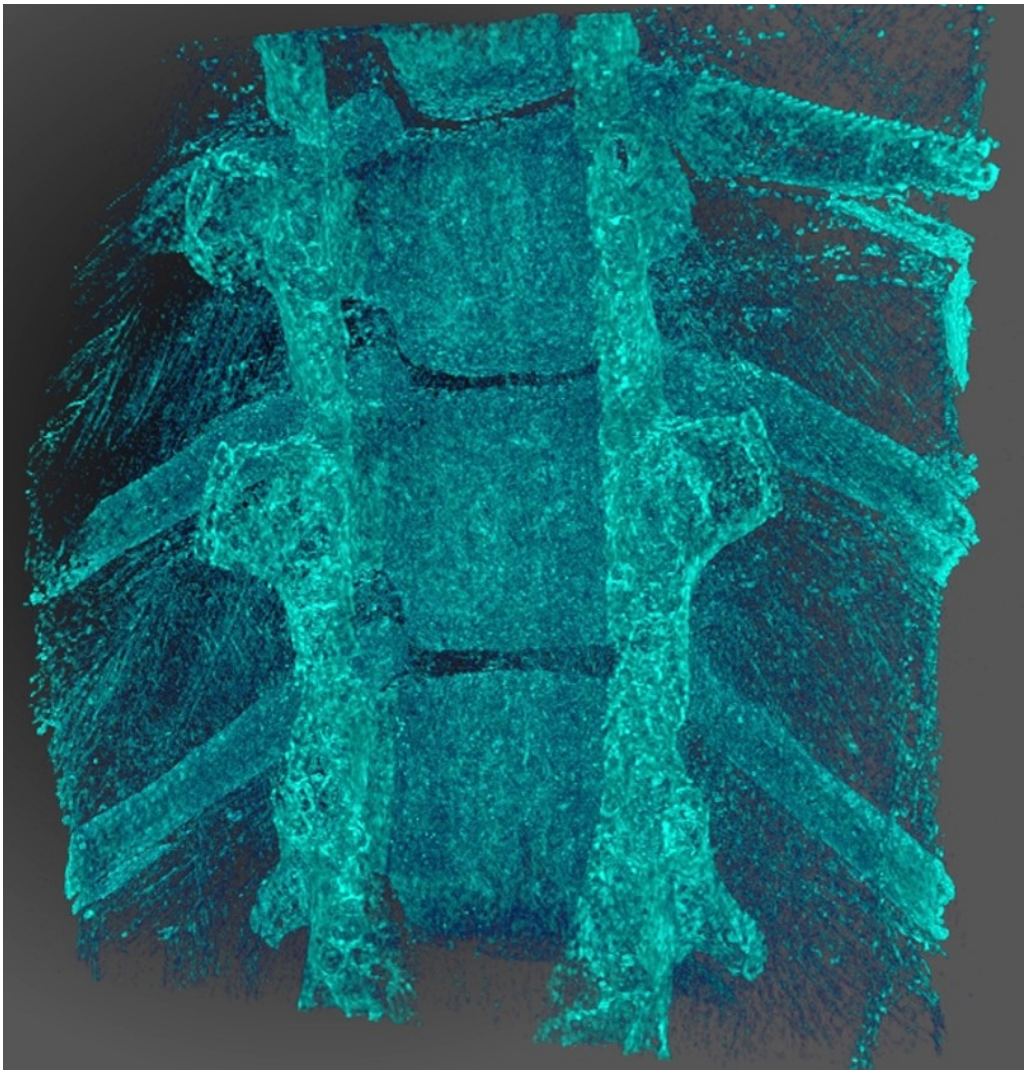

FIGURE 6.25: 3D rendering of the absorption reconstruction.

6.9 Conclusion

In this chapter experimental results with the X-ray Hartmann wavefront sensor were shown both for the laboratory set-up and for the synchrotron measurements.
Three different Hartmann plates were tested: a compact X-ray Hartmann wavefront sensor and two prototypes with a larger field of view.
Results using laboratory sources on edge detection and propagation effects are presented for the compact X-ray Hartmann wavefront sensor. Also, the second prototype was tested for 3D imaging of biological samples.

Chapter 7

Density and Chemical Composition Discrimination

Here the Hartmann sensor was used to retrieve the chemical composition of test objects composed of known material. The chemical composition could be inferred starting from a direct and independent measurements of the real part (δ proportional to the phase) and the imaginary part (β proportional to the absorption) of the sample refractive index (n). The comparison of the trend of δ and β respect to the incident energy with the tabulated curves can give information on the chemical composition of unknown material.
In order to compare the experimental results with the theoretical values, we imaged a series of μspheres of known chemical composition and dimensions.
Finally, from the absorption and phase reconstruction the real δ and imaginary part β of the refractive index for each of the chemical element was calculated.
We performed experiments on synchrotrons that have a sufficient flux to allow using a monochromator but also to reduce the spectral width with a set of specially designed filters. These two experiments (polychromatic and monochromatic measurements) will be described and discussed below.

7.1 Polychromatic set-up

The HASO HXR was used to perform the experiment on the Syrmep beamline at Elettra synchrotron (Italy) with an incident "white" beam, an electron energy of E=2 GeV and a current I=308 mA. A picture of the experimental set-up can be found in fig.7.1.
First, a filter wheel provided by the beamline was used to mount six different filters in front of the beam. It could rotate respect to a central axis, allowing to use a combination of different materials to shape the incident spectrum. Since a different resulting flux was calculated for each filter, the acquisition time was adapted consequentely. All the details about the filters will be described later.
The samples stage was composed of an Hexapod, a compact six degrees of freedom parallel robotic motion platform, and a rotational stage to allow tomographic measurements.
The wavefront sensor was placed on a second Hexapod stage to allow the alignment of the Hartmann mask respect to the incident X-ray beam.
The following steps were performed during the experiment:

- Alignment of the HXR wavefront sensor with the Hexapod motion platform,
- Alignment of the filter holder respect to the beam direction,

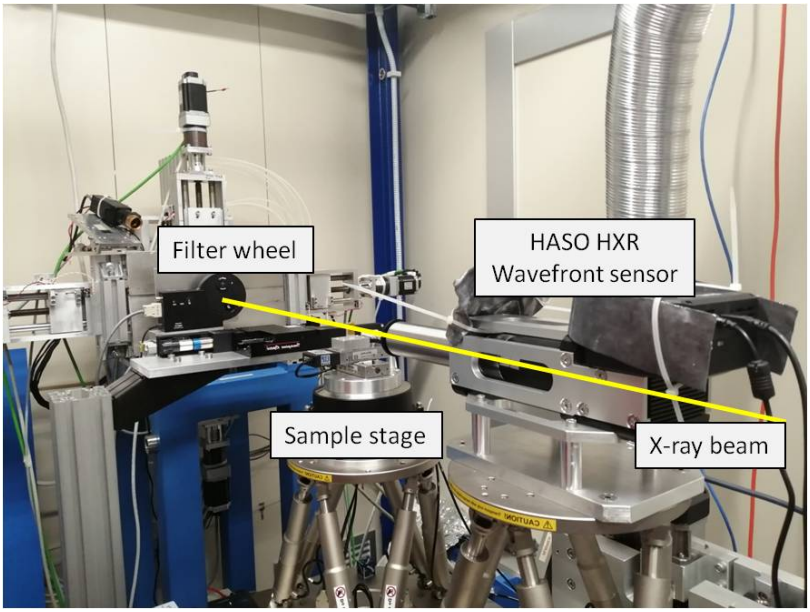

FIGURE 7.1: Picture of the set-up on Syrmep beamline. A filter wheel was used to mount six different filters in front of the beam. The samples stage was the combination of an Hexapod and a rotational stage to allow tomographic measurements. The wavefront sensor was placed on a second Hexapod stage to allow the alignment of the Hartmann mask.

- Acquisition of images with six different filters, without sample and adjustment of the integration time for each filter,
- Alignment of the center of rotation on the sample stage using a pin,
- Alignment of the sample and acquisition of 2D test images,
- Run acquisition of 2D images.

7.2 Calculation of the incident spectra

The calculation of the white beam flux was provided by the beamline. The flux was calculated as the number of photons per second per unit of bandwidth for a 300 mA current up to a photon energy of 45 keV. To calculate the resultant spectrum we adjust the white beam values for each beam filtration.
The white beam flux is first multiplied by the transmission function ($T_{filters}$) of each filter. To calculate $T_{filters}$, the absorption coefficient μ as a function of energy was taken from the National Institute of Standards and Technology (NIST) database (Hubbell and Seltzer, 2004) and the thickness of each material was given from Goodfellow company.
A list of the combination of filters and their respective acquisition time is reported in fig.7.2.

Then, considering the distances of our set-up, the transmission of 1 m of propagation in air (T_{air}) was also calculated.
Finally the absorption ($Abs_{crystal}$) of the scintillator coupled with the CDD detector inside the wavefront sensor was considered.

Filter Number	Acquisition Time (s)
1	0.5
2	3
3	6
4	1
5	10
6	2

FIGURE 7.2: A list of the combination of elements used as filter and their the respective acquisition time.

The resulting spectrum was calculated in the following way:

$$N_{greenphotons}/s = (N_{x-rayphotons}/s) * T_{air} * T_{filters} * Abs_{crystal} * \epsilon \tag{7.1}$$

where $N_{greenphotons}/s$ is the final number of photons incident on the CCD that are emitted in green light because of the properties of the crystal and $(N_{x-rayphotons}/s)$ is the white beam flux of the beamline.

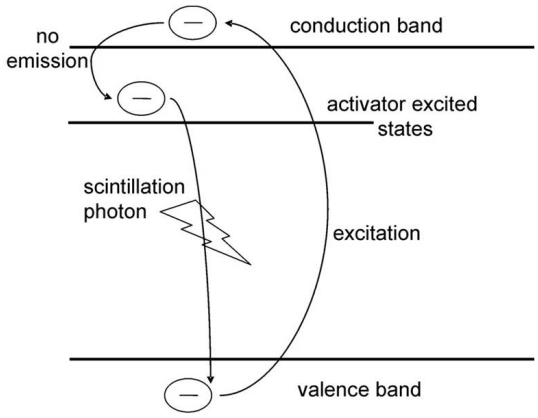

FIGURE 7.3: The electronic band structure of an activated inorganic crystal scintillator. When an X-ray photon interacts with the scintillator material, electrons move from the valence band to the conduction band. It can fall down into one of the excited states of the activator without emission. When it is transmitted from the activator energy band back to the ground state, a photon is emitted. These de-excitations are in the visible-light band. Figure adapted from (Graafsma and Martin, 2008)

Finally, to understand the meaning of the therm $Abs_{crystal} * \epsilon$, it is important to concentrate on the properties of a scintillator screen. Detectors used for tomography often use a converter screen to convert X-ray photons to visible-light that is subsequently detected by a photodetector, mostly of the CCD type. This conversion is done via a scintillation or luminescence process.
These scintillation materials have an energy-band diagram similar to the one of

semiconductors, with a valence band separated by an energy gap from the conduction band.
When an X-ray photon is absorbed, energy is deposited in the crystal and electrons in the valence band can be excited to the conduction band, leaving holes in the valence band (fig.7.3). When an excited electron falls back to the valence band and recombines with a hole, the excess energy is dissipated by emission of photons with energy equal to the width of the bandgap.
For intrinsic scintillators the efficiency of the radiative de-excitation process is, however, low and the bandgaps are, in general, too large. To overcome this limitation scintillators are doped with typical fluorescent ions such as europium (Eu), terbium (Tb) or cerium (Ce).
The emission efficiency (light yield) of a scintillator can be evaluated by determining the X-ray to light conversion efficiency. The absolute efficiency ϵ is defined by the ratio between the number of detected visible photons to the number of incident X-ray photons.
Finally, in eq.7.1 the absorption($Abs_{crystal}$) of the crystal was calculated considering its thickness and this therm was multiplied by the efficiency factor (ϵ) of the conversion between X-rays and visible light given by the manufacturer.
The resulting spectrum for each of the filtration numbered in fig.7.2 and calculated as expressed in eq.7.1 is shown in fig.7.4.

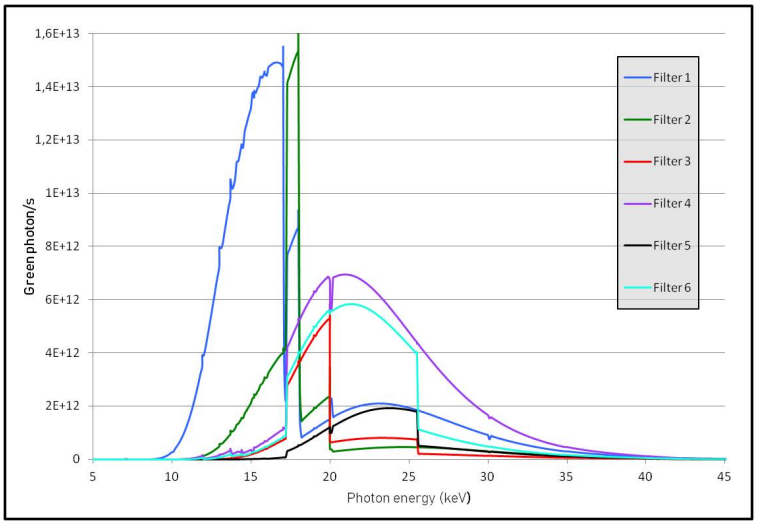

FIGURE 7.4: Resulting spectrum for each of the filtration numbered in fig.7.2 and calculated as expressed in eq.7.1.

7.3 Sample description

In order to compare the experimental results with the theoretical values, we imaged a series of μspheres of known chemical composition and dimensions. An image acquired with an optical microscope of the sample can be seen in fig.7.5. The material, the chemical composition, the diameter and the density of each of the μspheres are reported in fig.7.6.
Due to the small field of view of the optical microscope, several images were acquired with a pixel size of 0.38 μm and were combined together afterwards to reproduce the spatial arrangement of the μspheres during the experiment.

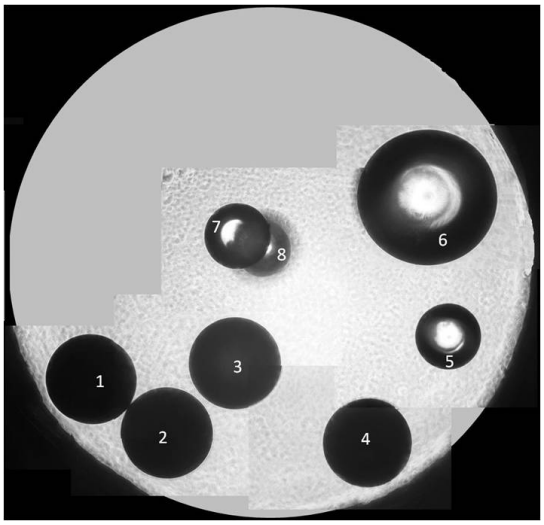

FIGURE 7.5: Image of the samples acquired with an optical microscope (pixel size of $0.38\mu m$).The chemical composition of each of the μspheres is the following: sphere 1 is Si, spheres 2 and 3 are Al_2O_3, spheres 5,7 and 8 are SiO_2 and sphere 6 is soda lime glass.

Material	Chemical composition	Diameter (mm)	Density (g/cm^3)
Silicon	Si	0.48	2.33
Aluminium oxide	Al_2O_3	0.50	3.99
Silicon dioxide	SiO_2	0.35	2.19
Soda lime glass	$Si_{70}O_{172}Na_{30}Ca_{10}Mg\,B_2\,Al_2$	0.70	2.50

FIGURE 7.6: The material, the chemical composition, the diameter and the density of each of the μspheres shown in fig.7.5.

7.4 Detectivity of the Hartmann wavefront sensor

To understand the detection capability of the Hartmann wavefront sensor we compare the absorption and deflection signals of the same objects.
We consider two μspheres of SiO_2 (number 7 and 8 shown in fig.7.5 that show an overlap. We consider the absorption and deflection in the x axis signal for on specific incident spectrum (filter 1, fig.7.4).
The deflection profile along the x-axis given by the superposition of the two SiO_2 μspheres is explained in fig.7.7. The blue line corresponds to the first sphere and the green to the second sphere alone. The orange line is the resulting deflection considering the two spheres together.
We also analysed the absorption plot (blue line, fig.7.8), where it is impossible to differentiate the two spheres.
However, looking at the deflection plot (red line, fig.7.8) the two spheres appear very clearly. In particular, in the deflection along the x-axis, the deflection at the border is modified by the presence of the other sphere. This is an important result because it shows a high sensitivity of the system as well as an exceptional sensitivity for occluded objects.

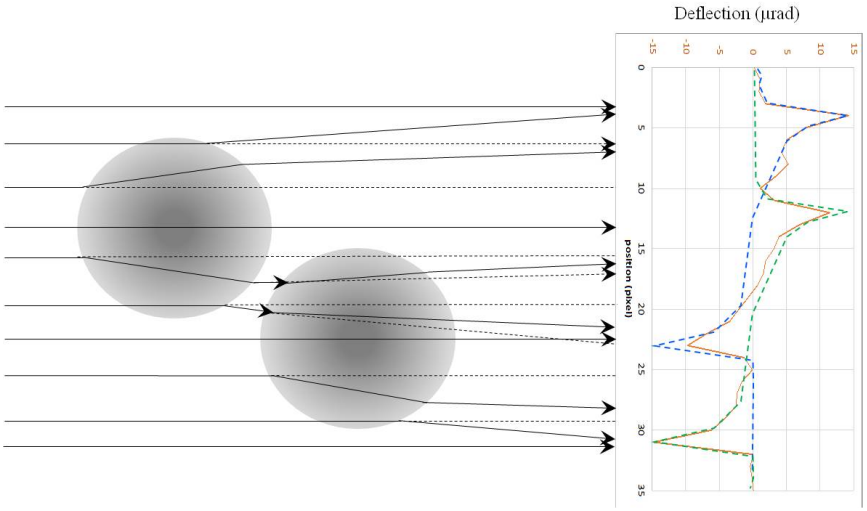

FIGURE 7.7: Explanation of the deflection profile along the x-axis for the superposition of the SiO_2 μspheres 7 and 8 shown in fig.7.5. The blue line corresponds to one sphere and the green to the other sphere alone. The orange line is the resulting deflection considering the two spheres.

7.5 Experimental Results with polychromatic beam: retrieving δ and β.

The data analysis was focused on the reconstruction of the real part (δ proportional to the phase) and the imaginary part (β proportional to the absorption) of the sample refractive index (n) as function of the incident energy.
The experimental results were compared with the tabulated index of refraction for compound materials available online on the Center for X-Ray Optics website (Henke, Gullikson, and Davis., 1993). The weighted theoretical values for δ and β were calculated by multiplying the values at different energies with the calculated number of photons at this energy and then dividing by the total number of photons in the spectral window. To estimate the refractive index, the average energy for each spectra was calculated. The results are reported in fig.7.4.
The same test sample (μspheres) was imaged several times changing the filtration of the white beam, intensity and deflection maps were first reconstructed. From this first analysis it was also possible to obtain images corresponding to the sample absorption and wavefront.
The value of β was calculated from the transmission image, obtained as the ratio between the intensity recorded with the sample and the reference intensity without the sample. The transmission value (T) of each μsphere was calculated from the profile plot taken at the center of the sphere.
In order to retrieve β, we start from the Beer-Lambert's law for X-ray transmission ($T = e^{-\mu\Delta X}$), where μ is the mass attenuation coefficient and ΔX is the object thickness.
Finally, to obtain the formula written on fig.7.9 a), we rewrite the Beer-Lambert's law and consider that $\beta = (\mu\lambda)/4\pi$ and that the thickness $\Delta X = d$, the μsphere diameter.
The wavelength λ was calculated from the mean energy corresponding to each filter. For δ instead, the absolute phase value was used, that is calculated in μm from the

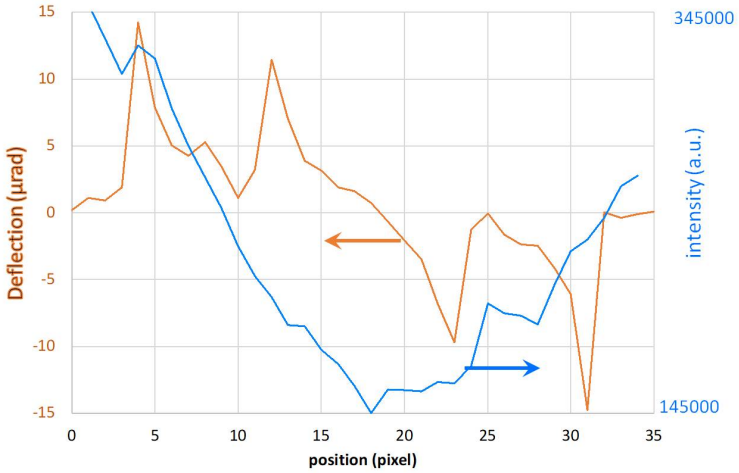

FIGURE 7.8: Single line profile plot of deflection along the x-axis (red line) and absorption (blue line) of the SiO_2 μspheres 7 and 8 shown in fig.7.5.

reconstruction program. To obtain the correct value of δ, the experimental phase difference ($\Delta\Phi$) from the profile plot of the wavefront image was thus divided by the diameter of each sphere (fig.7.9 b)).
It is important to note that the maximum value of the phase was not constant on the two edges of each sphere. To overcome this experimental fluctuation, the average value between the two edges (y_1 and y_2) was considered. Several factors can be analyzed from the acquired experimental data:

1. Regarding the incident spectrum reported in fig.7.4: Filter 4 (purple line) is very broad with contributions from high energies. Also, filter 6 (red line) presents a lower number of photons respect to the others.

2. Considering the μspheres composition in fig.7.5: the soda lime glass has a complicated chemical composition ($Si_{70}O_{172}Na_{30}Ca_{10}MgB_2Al_2$). Also, the exact chemical composition might depend on the production process of each company. For this reason the results obtained for β and δ with this sample were not in agreement with the theoretical one.

To better understand the acquisition problem with different incident spectra, we show an image of the same sample acquired with filter 1 and filter 6 (fig.7.10). On fig.7.10 a) we can see the reconstructed intensity for the spectra corresponding to filter 1, ranging from 10 to 18 keV and with high photon flux, while on fig.7.10 b) the same intensity image was reconstructed with a broader spectra (filter 4) with photon energies up to 40 keV and lower photon flux.
In particular, for filter 4 the visibility of each sphere is reduced and the noise level value is increased. The white arrows point to the SiO_2 μspheres, that it is almost not detectable when imaged with filter 4.
For this reason it was not possible to perform the analysis on the index of refraction for the spectrum corresponding to filter 4 and filter 6. Also, as mentioned before, because of the complex chemical composition of the soda lime glass μsphere it was not possible to reconstruct the index of refraction with high accuracy.
The images acquired for the same sample described in fig.7.5 are shown in fig.7.11 : the transmission (fig.7.11 a), the deflections in the X and Y directions (fig.7.11 b and

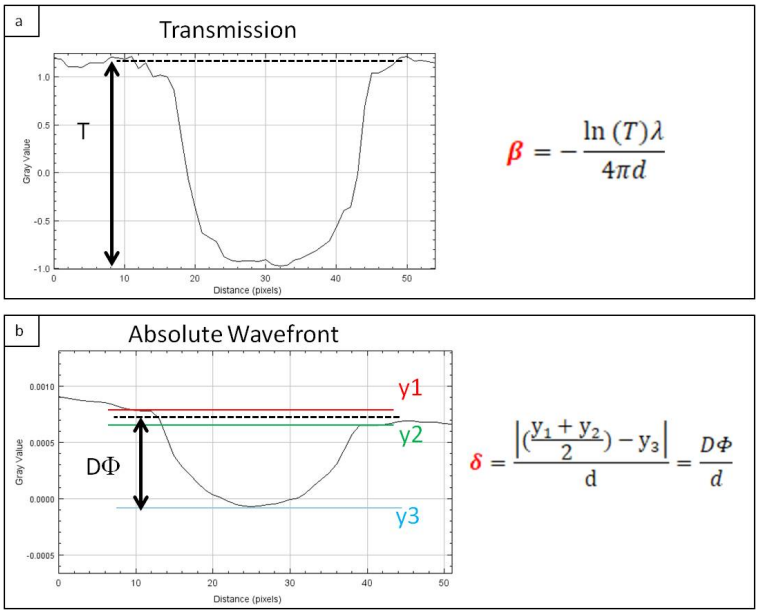

FIGURE 7.9: Example of the profile plot of the μspheres used to calculate the β and δ components of the refraction index. a)The value of β was calculated from the transmission image, obtained as the ratio between the intensity recorded with the sample and the reference intensity without the sample. The formula used is reported on the right, where T is the transmission, λ the wavelength and d is the sphere diameter. b) The value of δ was calculated from the experimental phase difference ($D\Phi$) divided by the sphere diameter d.

c respectively), and the reconstructed phase (fig.7.11 d). Results were obtained for two different incident spectra: one centered around 16 keV (filter 1 of fig.7.4, upper row in fig.7.11) and the second one at 22 keV (filter 4 of fig.7.4, lower row in fig.7.11). As the energy increases, all the spheres start to be transparent to X-rays, and the transmission map is noisier. At 22 keV, it is difficult to differentiate the soda lime (red), Al_2O_3 (green) and Si (black) spheres from the absorption map, while, we can easily differentiate the Al_2O_3 (green) from the Si (black) spheres on the phase map.
Following the procedure explained in fig.7.9, a first estimation for β of each chemical composition as a function of the incident energy was performed. The reconstruction of β was done for the μspheres of SiO_2, Al_2O_3 and Si. The following peak energies of each spectrum were considered: E=(15.8, 17.6, 20.5, 22.5) keV.
The plots of the measured values (dark gray) for β respect to the energy for each element, and the corresponding data, are shown in fig.7.12. The theoretical values are shown with a continuous line (light gray).
The experimental data are globally in good agreement (trends) with the theoretical values (fig. 7.13), but with still residual errors especially for Al_2O_3 (orange background) and Si (green background).

Since different sources of error can arise when performing a series of measurements on experimental data, we analyze the same data again with a new approach.
The general idea was to increase the measurements points for every element on the transmission plot and the corresponding sphere thickness.
In order to use all the pixels describing each μsphere, several points on the sphere diameter were considered. In fig.7.14 a profile plot corresponding to the center of

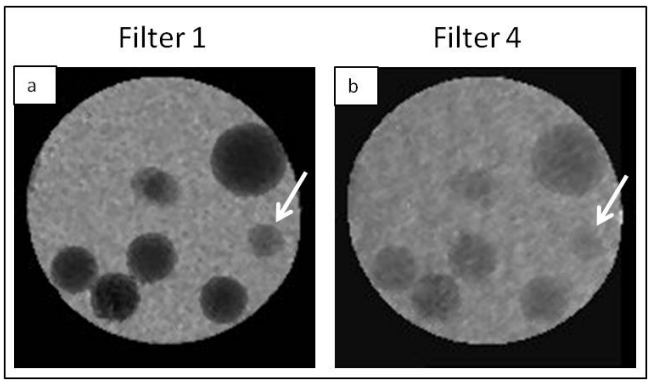

FIGURE 7.10: Intensity images of the same sample with μspheres changing the incident spectrum. a) Image reconstructed with filter 1. b) Image reconstructed with filter 4, the visibility of each sphere is reduced and the noise level is increased. The white arrows point to the SiO_2 μspheres, that it is almost not detectable when imaged with filter 4.

one sphere is shown. Each cross represents a point (i) where the transmission (T_i) and the corresponding sphere thickness(ΔL_i) were measured.
In this way, for each element six different estimations of β were made (formula in fig.7.14) and the average among them was considered as the final estimation for β.
A drawing of how the transmission calculation was done on each sphere is also given. The measurements were repeated for each element following the procedure described on fig.7.14, that will be called '3D measurement'. Both β and δ were reconstructed. The new measurements obtained for β are shown in fig.7.15 and the corresponding data is shown in fig.7.16.
Generally speaking, the experimental data (dark gray) are in good agreement with the theoretical value (light gray line).
The biggest variations from the theoretical trend are observed for Al_2O_3, especially the β value corresponding to energy E= 22.5 keV is around 50% lower then the theoretical one. Also, a slight underestimation of all the calculated values can be seen for Si. The plotted data is reported on the table in fig.7.16.

In the same way, the 3D measurement was also performed to estimate the values of δ for each element. The measurements for δ are shown in fig.7.17. The experimental data follows the expected theoretical trend. The analysis performed on the images corresponding to the energy E=20.5 keV shows an underestimation of the value of δ for both Al_2O_3 and Si. This effect can be connected with a problem on the phase reconstruction. The plotted data is reported on the table in fig.7.18.

High accuracy in the estimation of δ and β can be reached using the Hartmann wavefront sensor. This analysis opens the way to a precise density estimation of samples of unknown composition. Also, in future it will be possible to infer the chemical composition of a sample analysing the index of refraction's components in comparison with the theoretical trends of each material.
When applying this method to a biological sample, the main open question is related to the chemical and structural complexity of this kind of materials. Minimum prior knowledge on the analysed structure dimension and composition will help to decrease the error in the reconstruction of δ and β.

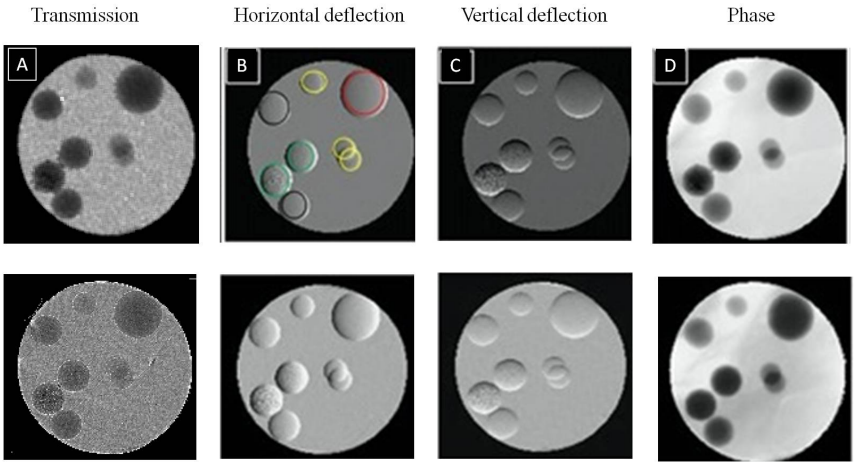

FIGURE 7.11: Absorption, horizontal and vertical deflections, and phase reconstruction from one experimental acquisition. The upper row corresponds to a mean energy of 16 keV (filter 1, fig.7.4), while the bottom row corresponds to 22 keV (filter 4, fig.7.4). The color code is used to differentiate the 4 kinds of spheres: soda lime in red, Al_2O_3 in green, Si in black and SiO_2 in yellow.

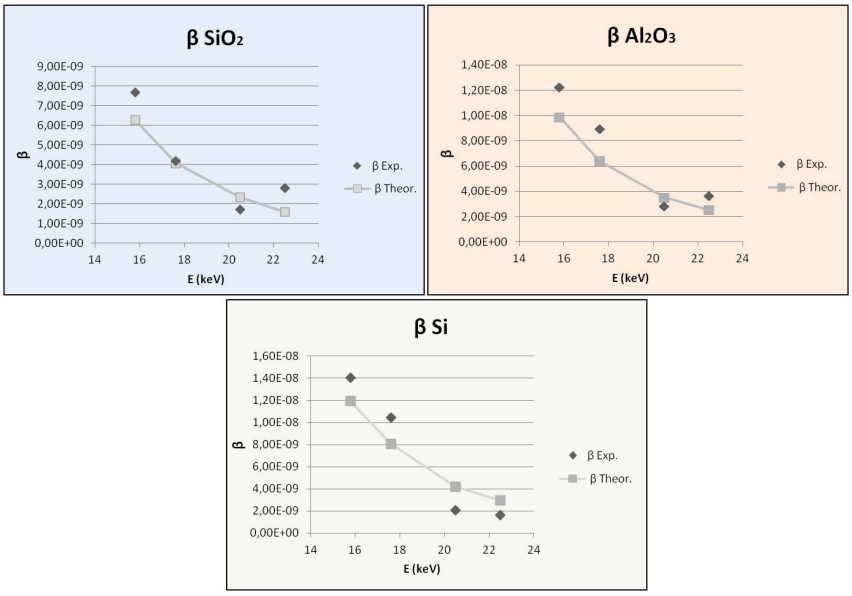

FIGURE 7.12: Reconstruction of β for μspheres of SiO_2, Al_2O_3 and Si. The peak energies of each spectrum was considered: E=15.8, 17.6, 20.5, 22.5 keV. The measured values (dark gray) for β respect to the energy for each element and the corresponding data are shown. The theoretical values are reported with a continuous line (light gray).

	Si02		Al2O3		Si	
E (keV)	β Exp.	β Theor.	β Exp.	β Theor.	β Exp.	β Theor.
15,80	7,69E-09	6,28E-09	1,22E-08	9,87E-09	1,40E-08	1,19E-08
17,60	4,19E-09	4,07E-09	8,95E-09	6,40E-09	1,04E-08	8,04E-09
20,50	1,73E-09	2,33E-09	2,83E-09	3,51E-09	2,08E-09	4,19E-09
22,50	2,80E-09	1,59E-09	3,64E-09	2,51E-09	1,59E-09	2,96E-09

FIGURE 7.13: Measured and theoretical values for β respect to the energy for each element.

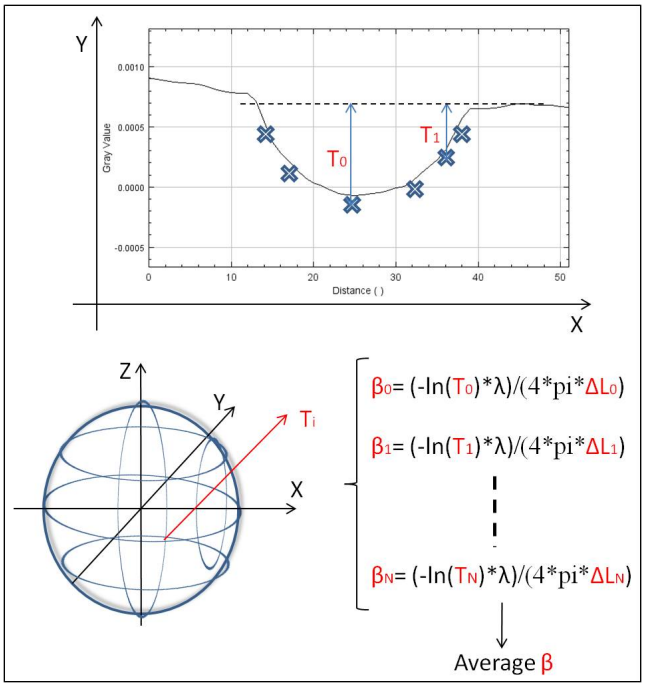

FIGURE 7.14: New measurement of β: several points for each sphere on the sphere diameter were considered. A profile plot (up) corresponding to the center of one sphere is shown. Each cross represents a point(i) where the transmission (T_i) and the corresponding sphere thickness(ΔL_i) were measured. Six different estimation of β were made for each element and the average among them was considered the final estimation for β (down,right).A drawing (down, left) of how the transmission calculation was done on each sphere is shown.

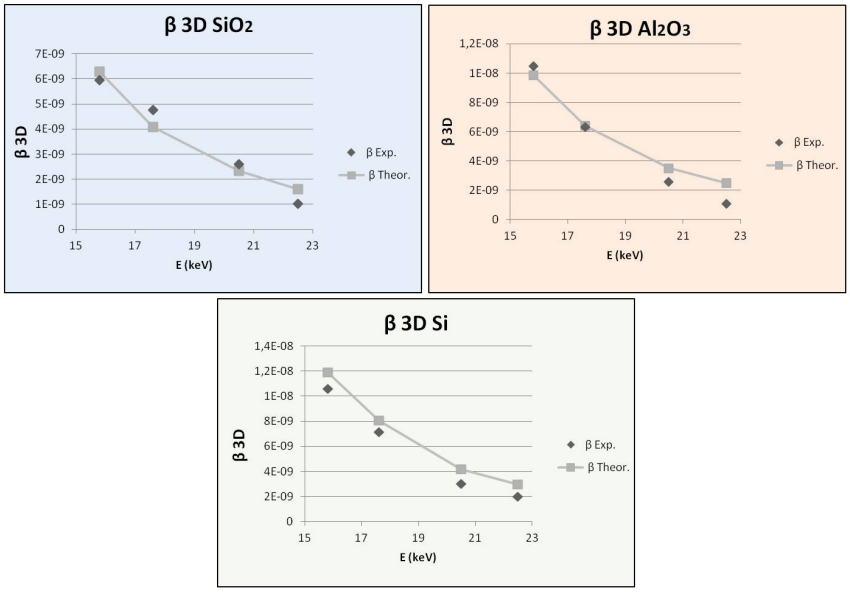

FIGURE 7.15: New measurement of β considering the procedure described in fig.7.14. A series of μspheres of SiO_2,Al_2O_3 and Si were used. The peak energies of each spectrum was considered: E=(15.8,17.6,20.5,22.5) keV. The measured values (dark gray) for β respect to the energy for each element are shown. The theoretical values are reported with a continuous line (light gray).

	Si02		Al2O3		Si	
E (keV)	β 3D Exp.	β 3D Theor.	β 3D Exp.	β 3D Theor.	β 3D Exp.	β 3D Theor.
15,80	5,95E-09	6,28E-09	1,5E-08	9,87E-09	1,06E-08	1,19E-08
17,60	4,76E-09	4,07E-09	6,31E-09	6,40E-09	7,14E-09	8,04E-09
20,50	2,60E-09	2,33E-09	2,58E-09	3,51E-09	3,00E-09	4,19E-09
22,50	1,02E-09	1,59E-09	1,06E-09	2,51E-09	2,00E-09	2,96E-09

FIGURE 7.16: Measured and theoretical values calculated in 3D for β respect to the energy for each element.

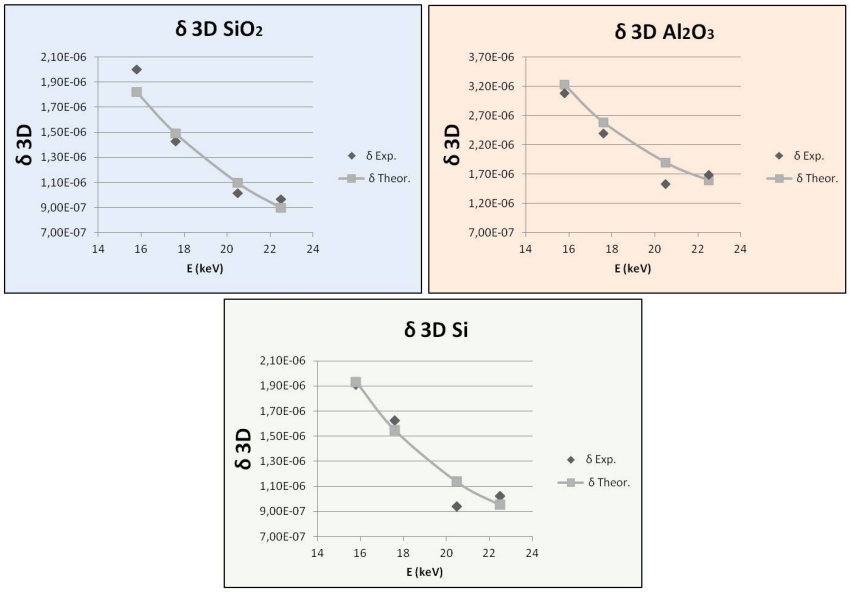

FIGURE 7.17: New measurement of δ considering the procedure described in fig.7.14. A series of μspheres of SiO_2,Al_2O_3 and Si were used. The peak energies of each spectrum was considered: E=(15.8,17.6,20.5,22.5) keV. The measured values (dark gray) for β respect to the energy for each element. The theoretical values are reported with a continuous line (light gray).

	Si02		Al2O3		Si	
E (keV)	δ 3D Exp.	δ 3D Theor.	δ 3D Exp.	δ 3D Theor.	δ 3D Exp.	δ 3D Theor.
15,80	2,00E-06	1,82E-06	3,08E-06	3,22E-06	1,91E-06	1,93E-06
17,60	1,43E-06	1,49E-06	2,40E-06	2,59E-06	1,63E-06	1,55E-06
20,50	1,01E-06	1,10E-06	1,53E-06	1,90E-06	9,40E-07	1,14E-06
22,50	9,69E-07	8,99E-07	1,69E-06	1,59E-06	1,02E-06	9,52E-07

FIGURE 7.18: Measured and theoretical values for δ respect to the energy for each element.

7.6 Experimental Results with monochromatic beam: retrieving δ and β.

The monochromatic experiment has been performed on the BM05 beamline of European Synchrotron Radiation Facility (ESRF, France). A picture of the set-up is reported in fig. 7.19. After the monochromator, the energy spread was around 10 eV

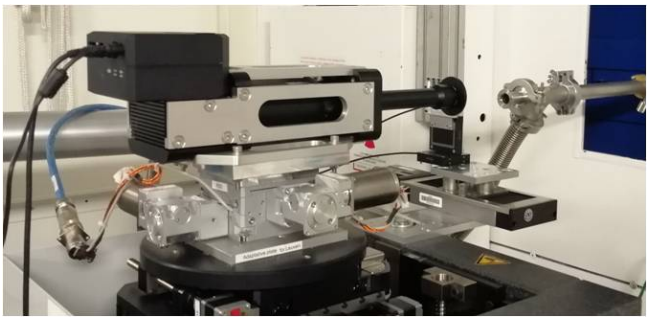

FIGURE 7.19: Picture of the Hartmann X-ray phase imaging system as installed in the BM05 beamline of ESRF.

while the central energy was set at 10 keV, 12 keV and 14 keV respectively. The X-ray beam was parallel. We used the same sample used for the polychromatic measurements, the set of 8 spheres already described in section 7.3. From the images with and without sample, the four maps (transmission, horizontal and vertical deflections, and the phase) could be measured, as illustrated fig.7.20 at 12 keV. As illustrated, it is difficult to differentiate Si and Al_2O_3 spheres from the transmission map, but differences are noticeable on the phase map. On the contrary, Si and SiO_2 look different on the transmission map while more similar on the phase. From the

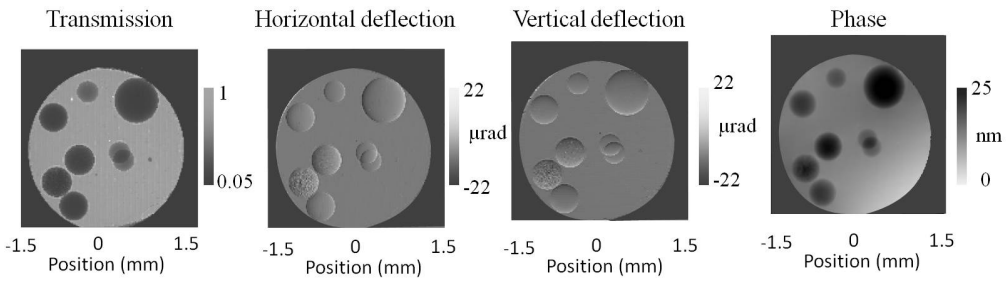

FIGURE 7.20: False color maps of the transmission, horizontal and vertical deflection, and phase measured at 12 keV for the set of 8 spheres.

transmission and phase maps, and knowing the thickness of the spheres, it is possible using the procedure explained in fig.7.9 to measure experimentally δ and β of the different spheres and at the different energies (10, 12 and 14 keV). Results have been reported in the graphs fig.7.21. The experimental data (red dots) fit very well with theory (blue crosses), within less than 10% error.
It is worth noting that the values of δ with energy for Si and SiO_2 are very similar ($4.11x10^{-6}$ and $4.08x10^{-6}$ respectively at 10 keV, and Si: $2.38x10^{-6}$ and SiO_2: $2.17x10^{-6}$ at 14 keV) preventing to differentiate them only from the δ but the values of their β are sufficiently different. The ability to get both δ and β information at few

energies allows to distinguish Si from SiO_2.
Another example is given by the β forSiO_2 ($3.91x10^{-8}$) and Al_2O_3 (6.2810^{-8}) that are easily differentiable at 10 keV but become much closer at 14 keV (SiO_2: $1.01x10^{-8}$; Al_2O_3:$1.59x10^{-8}$) making the differentiation more delicate. However, δ at 14 keV are quite different for SiO_2 ($2.32x10^{-6}$) and Al_2O_3 ($4.11x10^{-6}$). Knowing only β in this example would not have been enough. The knowledge of both δ and β at few energies allows to confirm the initial guess based on β values.

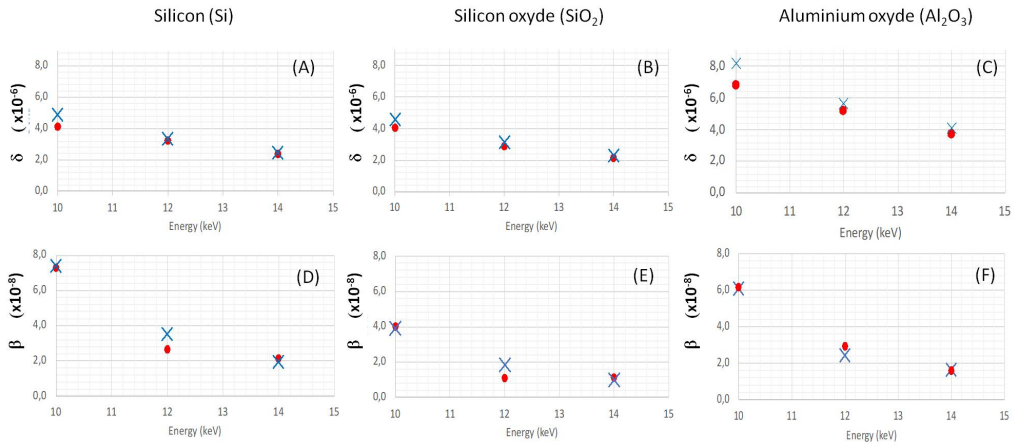

FIGURE 7.21: Comparison of experimental values (red dot) of δ versus theoretical ones (crosses) for Si (a), SiO_2 (b) and Al_2O_3 (c) and β for Si (d), SiO_2 (e) and Al_2O_3 (f). The vertical error bars have not been displayed since they are of few percent's and will not be visible.

These examples show that the ability to directly and independently measure δ and β on a single acquisition with the HXPI is a key advantage for chemical differentiation. Also, it appears clearly that the measurement of δ and β at few energies is needed to ensure a high degree of confidence.

7.7 Conclusion

This chapter is dedicated to experimental results performed with synchrotron light to retrieve the density and the chemical composition of test objects composed of known material. The same samples were analyzed with a polychromatic and monochromatic incident beam.

Chapter 8

Study of Neurodegenerative Diseases with Free Space Propagation Tomography

In this chapter we will focus on the study of neurodegenerative diseases and what are their main consequences on the central nervous system. Neurodegenerative diseases are a set of over 600 diseases, that involve the gradual loss of motor, sensory functions, as well as cognitive and behavioral deficits due to neuronal cell death. The most common are : Alzheimer Disease (AD) , Parkinson, Huntington and Amyotrophic Lateral Sclerosis (ALS). They occur sporadically in the population and the main risk factors are advanced age, mitochondrial DNA mutation and oxidative stress damage.
The main idea of this section was to exploit the capabilities of X-ray phase contrast imaging for the investigation of the effects of neurodegenerative diseases on the central nervous system.
The results from two experiments will be presented: the first one was carried out on mouse brain samples affected by an animal model of Alzheimer and the second one was performed on mouse spinal cord samples affected by an animal model of Amyotrophic Lateral Sclerosis. In this chapter, the experimental results obtained with X-ray phase contrast tomography will be discussed. The results were obtained with the free space propagation technique, where the sample is placed on a rotational stage after the source and the images are recorded by a detector placed far from the object. All the images described in the following were obtained with synchrotron light at the beamline ID17 of ESRF (France).

8.1 Brain Imaging : Alzheimer Disease

X-ray Phase contrast tomography (XPCT) measurements obtained in free space propagation were performed on (20-22) and (12-15) months old male mice brains affected by Alzheimer's disease. Male wild type mice of the same age were used as reference sample. The samples were provided by the NeuroSpin laboratory (France).
Animal models are commonly used to understand the mechanisms underneath neurodegenerative diseases. They use transgenic mouse that have been artificially modified at a genetic level to include a foreign sequence, or transgene. This often involves the insertion of a human gene into the mouse's genome (Colpo et al., 2017).
Animal models mimic human diseases and have enhanced the understanding of the molecular pathogenesis of Alzheimer's disease (AD), Parkinson's disease (PD), frontotemporal dementia (FD), and amyotrophic lateral sclerosis (ALS).

This study was focus on the APP/PS1 animal model of AD. Alzheimer's disease is the most prevalent neurodegenerative disorder worldwide that causes memory loss and confusion, resulting in personality and cognitive decline over time. It is characterized by $A\beta$ protein deposition and the formation of intracellular neurofibrillary tangles (NFTs) in the brain regions involved in learning and memory (O'brien and Wong, 2011). Extracellular $A\beta$ proteins, that derive from the amyloid precursor protein (APP), accumulates in senile plaques. The APP/PS1 is a transgenic mouse model that overproduces the $A\beta$ proteins and is often used to study the mechanisms of neuropathology of AD (Lok et al., 2013).
The XPCT experiment was performed at beamline ID17 (ESRF synchrotron, France) with a monochromatic incident energy of 48.5 keV. The sample was set at a distance of 2.3 meters from the CCD camera that has a pixel size of 3.5 μm. The tomography has been acquired with 4000 projections covering a total angle range of 360°.
Data pre-processing, phase retrieval and reconstruction were performed using the SYRMEP Tomo Project software (Massimi et al., 2018).
Filtered back-projection algorithm was used to reconstruct the tomographic volume and a ratio $\delta/\beta = 200$ was used in Paganin's algorithm for phase retrieval (see section 3.3.4).

8.1.1 Artifact Removal

In this section, we will present how image artifacts were removed from the reconstructed tomographic slices of the brain. The most recurrent artifact in tomographic images are the so-called *ring artifacts*, which appear as concentric rings around the center of rotation of the sample. Temporal variations in the beam intensity, nonlinearities in the detector response or inhomogeneities of the optical elements are among the main causes of these artifacts. To reduce this artefact several options are possible. We will explain how ring removal can be applied after image reconstruction with the ImageJ image processing software (Rueden et al., 2017). First, the reconstructed slice is transformed into polar coordinates, assuming the center of rings as the center of the Cartesian-to-polar conversion.

The rings will thus become strips in the new coordinate system. Then a filter with a defined size is applied on the columns to attenuate the stripes. After testing, we assessed that the best choice for our images is given by median filter, set to replace each pixel of the column with the median of the pixels within a certain distance. The filter size is data-dependant, and it has been adapted to the specific need of the data-set. Polar-to-Cartesian coordinate transformation is performed to conclude the de-ringing process. The original image showing the artifact can be seen in fig.8.1 a) and the result of the ring removal procedure is shown in fig.8.1 b). From the image insets the artefact suppression can be appreciated (yellow arrows).
Another common artefact that occurs in tomography is the oscillations of the gray values on tomographic projections acquired at different time. This artefact is normally connected with the fluctuation of the maximum intensity of the incident X-ray beam. To correct from the gray-value oscillations an histogram equalization is needed. A standard histogram equalization algorithm, present inside ImageJ software, was used on all the tomographic slices. The algorithm takes the square root of the histogram values and divide each slice with this value, resulting in a series of normalized histogram. This procedure suppresses the gray value oscillations among the tomographic slices.

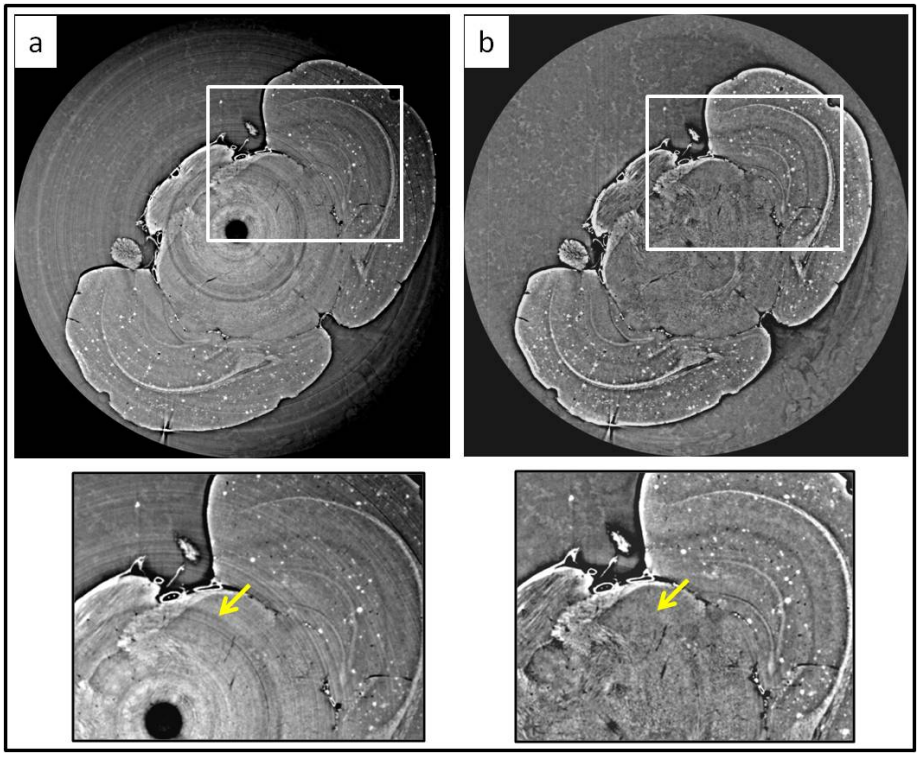

FIGURE 8.1: Effect of ring removal process on a XPCT of a mouse brain. a) Original tomographic slice of the brain, b) The same slice after the ring removal procedure. The ring shaped artefacts are suppressed.

In fig.8.2 a) one tomographic slice presenting stripes artefact can be seen. The effect of the histogram equalization filter is visible in fig.8.2 b).

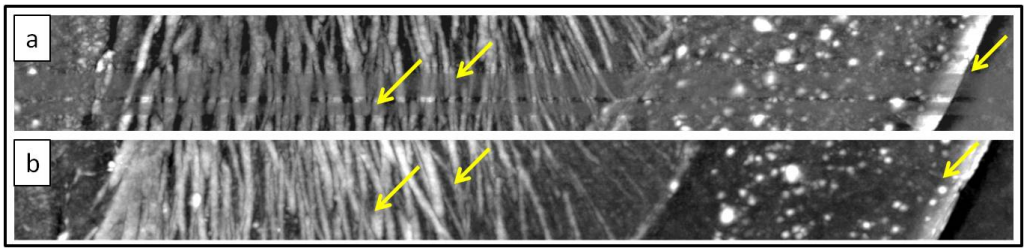

FIGURE 8.2: XPCT of a mouse brain. a) Raw tomographic slice presenting stripe artifact (yellow arrows) connected with the gray values oscillations, b) Tomographic slice after the application of the histogram equalization filter. The artefacts are suppressed after the equalization filter.

8.1.2 3D visualization of the brain

To better understand the results of this chapter, we will start with a concise description of the morphology of mouse brain. In fig.8.3 the main areas of mouse brain are described by different colours. For the study of Alzheimer, we will mainly concentrate on the two areas that are mostly involved by the disease: the cerebral cortex (light blue) and the hippocampus (green).

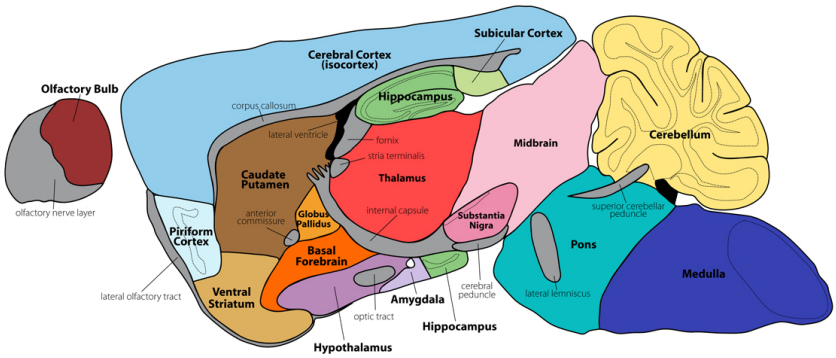

FIGURE 8.3: Drawing of the mouse brain highliting the different brain regions with different colours. Image from: GENSAT Project at Rockefeller University, Mouse Brain Atlas.

The first step on the data analysis was to observe the tomographic volume and its internal structures. To enhance the visualization of inner details inside the sample we performed maximum intensity projections every 150 μm slices. A sketch of the projection direction (green arrow) inside the brain volume is given in fig.8.4 a).
A region of interest was chosen inside each projection image to visualize the structures of interest (white inset, fig.8.4 b). Different parts of the brain tissue can be visualized, such as nerve fibers (white tubular structures in the images) and plaques (white spots). The images were acquired with a pixel size of 3.5μm. Maximum intensity projections of the chosen inset, following the green arrow direction are shown in fig.8.5. Thanks to the high spatial resolution (about 9 μm) obtained with XPCT, many morphological details inside the tissue can be seen. To understand the effect of Alzheimer disease on the brain we will concentrate on the spatial characterization and quantitative analysis of Aβ plaques (yellow star, fig.8.5) and on brain fibers (yellow cross, fig.8.5).

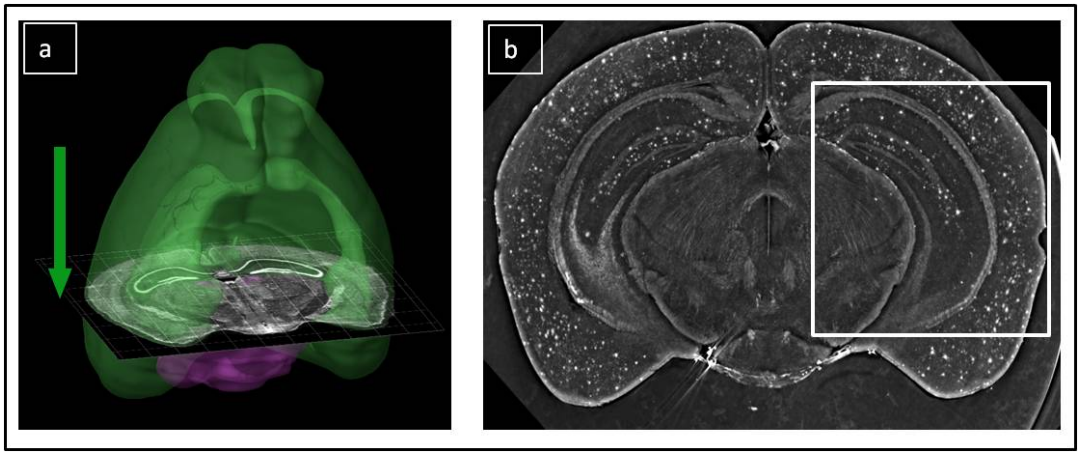

FIGURE 8.4: Maximum intensity projections of the XPCT data of a mouse brain affected by AD. a) A sketch of the projection direction (green arrow) inside the brain volume, b) Definition of a region of interest (white inset) inside the projection images.

As previously said, plaques agglomerates are normally observed in AD affected brain therefore understand their size and position in the brain is a crucial issue.
Also, it has been proposed recently that alterations in myelination are an important factor that can be connected with the occurrence of AD. Myelin is an electrical insulator that wraps around nerve fibers and is essential for action potential conduction to the neuronal axons of the central nervous system (Nave, 2010).
Therefore, demyelination may serve as a trigger process leading to pathological events that can affect the regional nervous system connectivity.

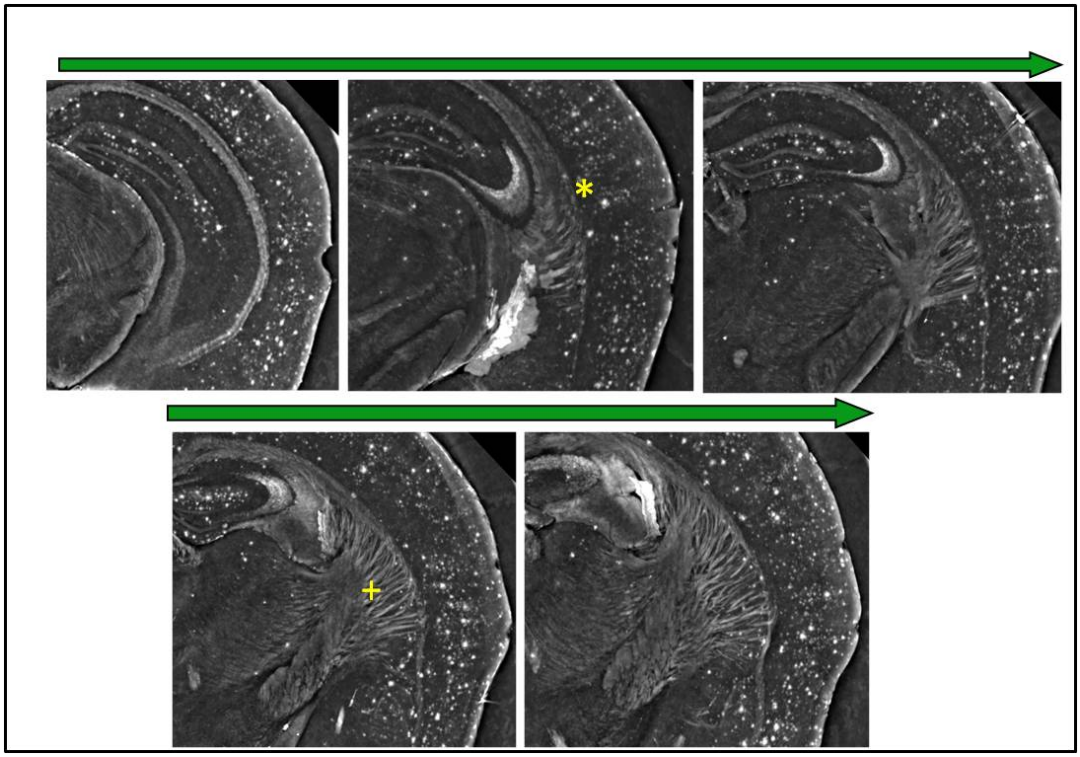

FIGURE 8.5: Maximum intensity projections of the chosen inset. The analysis will be concentrated on the Aβ plaques (yellow *) and on brain fibers (yellow +). The projections direction inside the brain volume is given by the green arrow.

8.1.3 Qualitative analysis of AD progression in mouse brain

A series of maximum and minimum intensity projections of the acquired samples were performed to visualize complementary structures inside the tissue. A comparison among the maximum intensity projections, corresponding to a thickness of about 100 μm, of the wild type, the AD affected APP/PS1 (12-15) month old and the AD affected APP/PS1 (20-22) month old sample are shown in fig.8.6. The appearance of many bright agglomerates in the brain cortex can be seen in the AD affected samples (fig.8.6 b,c), while they are not present in the wild type sample (fig.8.6 a). The bright dots that appear in the images are compatible with Aβ amyloid plaques that characterize AD. The presence of ions of zinc (Zn), copper (Cu), iron (Fe), and calcium (Ca) has been observed in amyloid plaques on XPCT images (Rasmussen et al., 2017). As a result, the plaques creates a strong signal making them easy to detect. The number of Aβ amyloid agglomerates increases with the disease progression, especially in the brain cortex, an area connected with language, memory, and thought.
Magnifications of the cortex and of the hippocampus are shown in the central and bottom parts of fig.8.6 for the different time-points.

During the standard sample preparation for mouse organs extraction, the blood is cleared from the vessels before the tissue fixation. The internal lumen of the vessels should appear as a (empty) low density tissue, that corresponds to a dark gray value in XPCT images. As a result, when performing the minimum intensity projection, the dark structures in the images represent the brain vascular system.

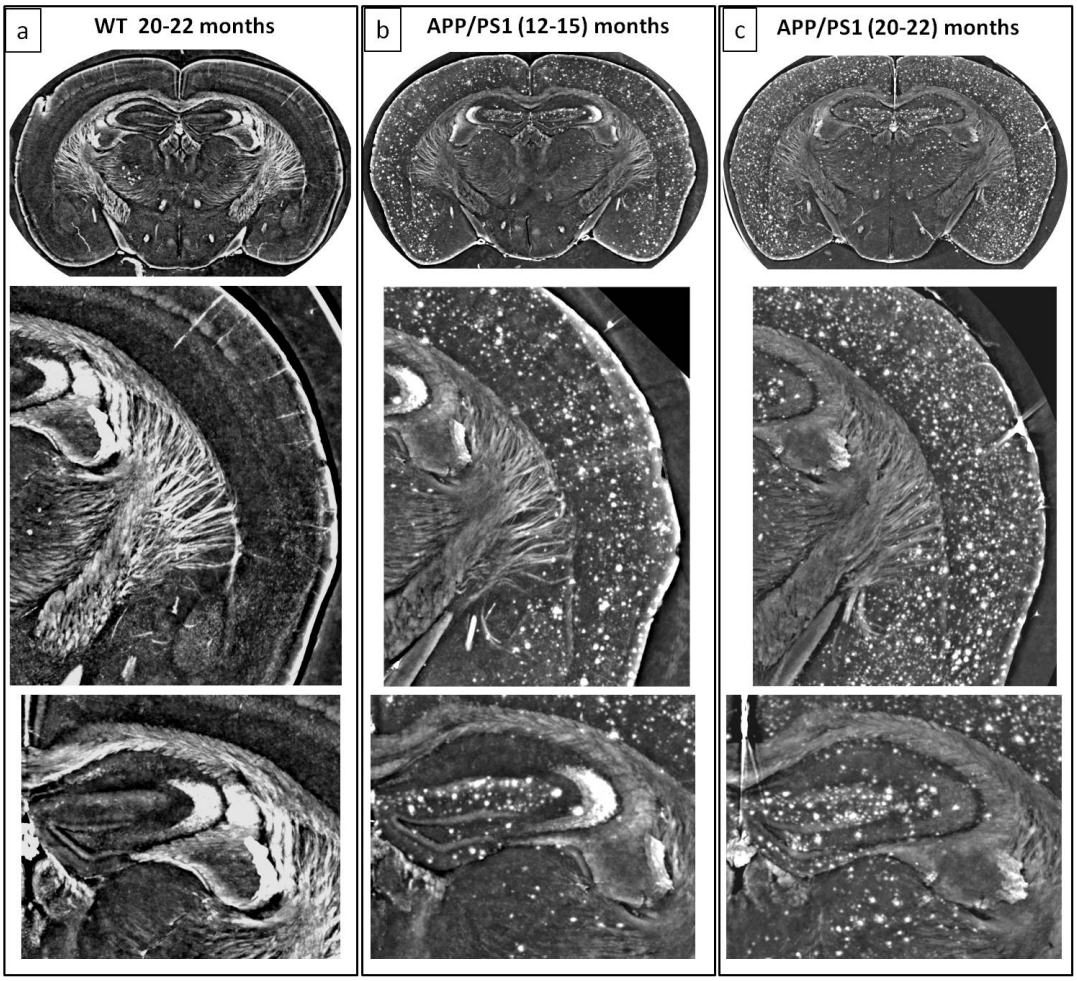

FIGURE 8.6: Maximum intensity projection of XPCT brains corresponding to a thickness of about 100 μm. a) Wild type brain, b) AD affected APP/PS1 (12-15) month old, c) AD affected APP/PS1 (20-22) month old. Magnifications on the cortex and of the hippocampus region are shown.

The minimum intensity projection were performed on the same areas already considered for the maximum. The projected volume corresponds to a thickness of about 100 μm. The minimum intensity projection of wild type, AD affected APP/PS1 (12-15) month old and AD affected APP/PS1 (20-22) month old sample are shown in fig.8.7. The yellow arrow in the magnification of the hippocampus in the wild type sample (fig.8.7 a) points to a series of vessels (black dots) following the direction of the dentate gyrus (spiral structure shown in the magnification).
A different vessel organization can be seen for the AD affected (12-15) month old sample (fig.8.7 b) respect to the wild type. Increasing the age of the AD affected sample, only few vessels are still visible. As it can been seen from this qualitative analysis, the vascular architecture is altered in the samples affected by AD. At the latest time-point the spatial organization of the vascularization in the AD affected brain is not yet comparable with the wild type images.
Recent studies (Jack, 2010) focused on the vascular contribution in Alzheimer disease, involving an increased permeability of blood vessels and consequently neurotoxicity. Vascular dysfunction also includes a diminished brain capillary flow

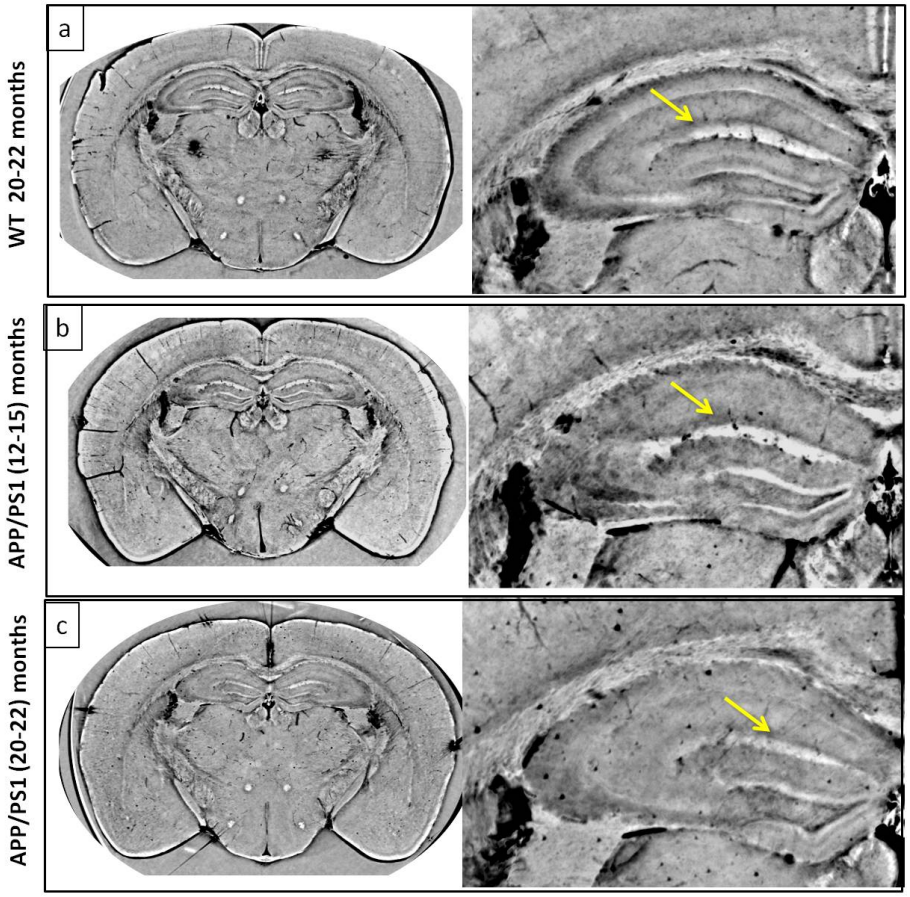

FIGURE 8.7: Minimum intensity projection of XPCT brains corresponding to a thickness of about 100 μm. a) Wild type brain, b) AD affected APP/PS1 (12-15) month old, c) AD affected APP/PS1 (20-22) month old. Magnification on a part of the hippocampus region are shown.

causing neuronal alterations. Cerebrovascular lesions in white matter have been observed in AD and microvascular lesions are also common pathological events (White et al., 2002).

As a result, we perform maximum and minimum projections of the same area of the brain in the wild type and in the AD affected APP/PS1 (12-15) month old mice. Artery and vessels have an external tubular structure composed of three external distinct tissue layers and an internal lumen through which blood flows (fig.8.8). The external layers are called tunics and they are largely composed of living cells and their products, including collagenous and elastic fibers.
In XPCT images white structures corresponds to tissues with higher density, while what appears dark is less dense. In the minimum projection of the wild type sample (fig.8.9 a1) no tubular dark structure compatible with vascularization can be seen. Instead, many white vessels are visible in the maximum projection image (yellow arrows,fig.8.9 b1). This bright signal is compatible with the external denser walls of the vessels.
The opposite situation can be seen in the AD affected mouse sample (red arrows,

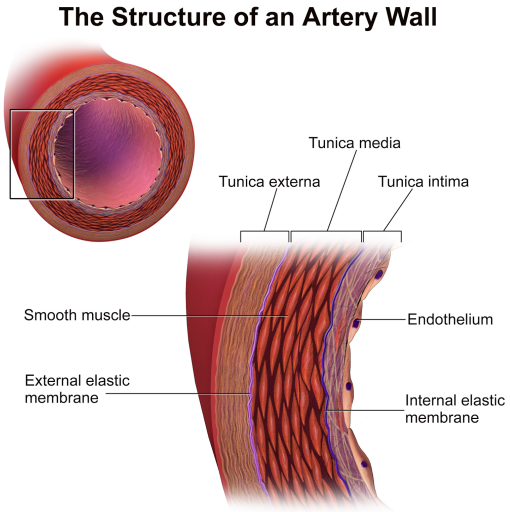

FIGURE 8.8: Drawing of the structure of an artery wall.

fig.8.9 a2) where the vessels appear as dark filaments. These structures are thus compatible with the inner lumen of the vessels where the blood flows.
The samples affected by AD present a strong alteration in the vascular architecture, leading to a permeability of the blood vessels that will thus appear darker in XPCT images.

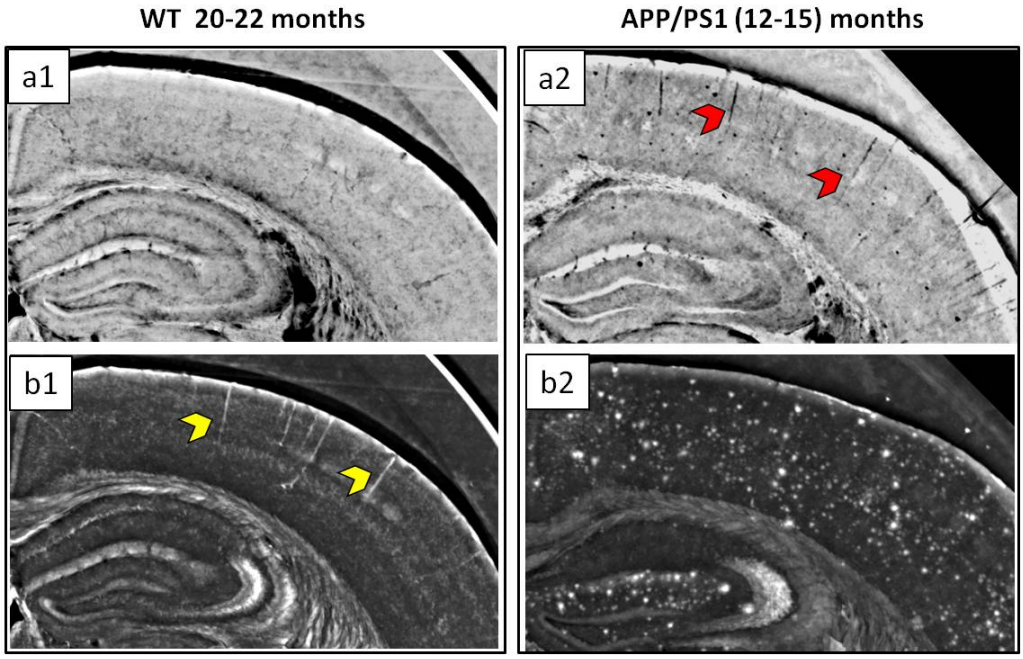

FIGURE 8.9: Maximum (b1-b2) and minimum (a1-a2) intensity projection of XPCT brains corresponding to a thickness of about 100 μm. a1-b1) Wild type brain, a2-b2) AD affected APP/PS1 (12-15) month old. The same gray value scale was used for both images.

8.1.4 Quantitative brain fiber analysis

The 3D reconstruction of the brain allows the visualization of the brain fibers in all the anatomical planes. There are three commonly used anatomical planes: sagittal, coronal and transverse (or axial). The sagittal plane is a longitudinal plane, dividing the body into right and left parts. The coronal plane is a longitudinal plane, dividing

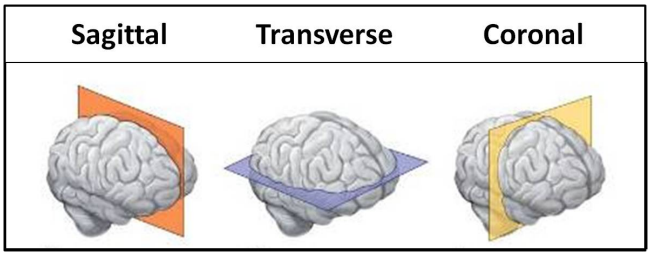

FIGURE 8.10: Description of the three anatomical planes of the brain: sagittal, coronal and transverse (or axial)

the body into anterior (front) and posterior (back) sections. The transverse plane (or axial) is a horizontal plane dividing the body into superior (upper) and inferior (lower) sections. A picture of the anatomical planes is shown in fig.8.10.
One image of the brain in the transverse plane is shown in fig.8.11 a), where the fibers can be seen as white tubular structures in the image. The fiber spatial orientation can

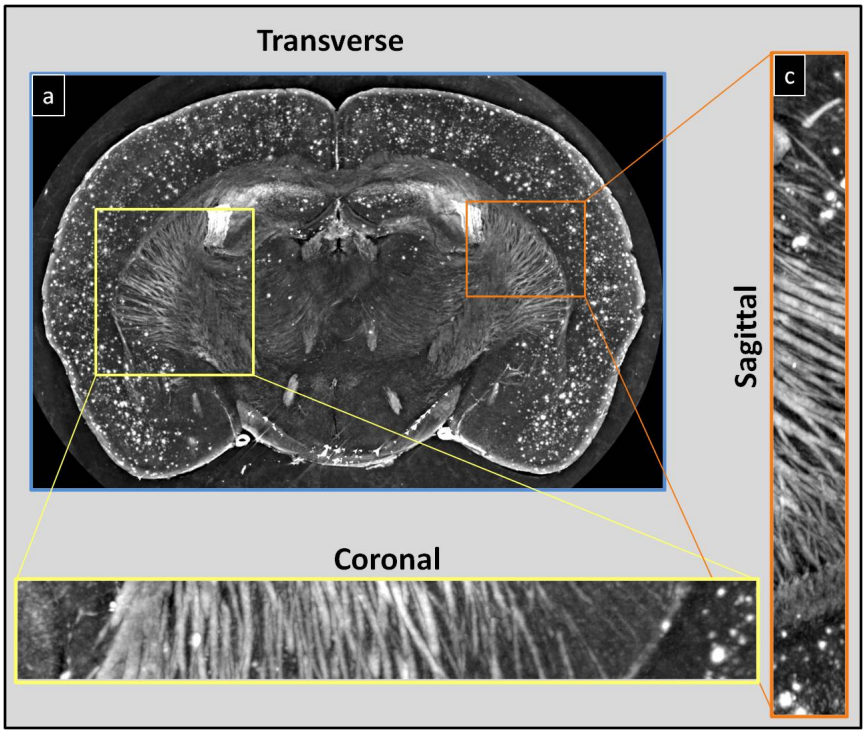

FIGURE 8.11: 3D reconstruction of the brain in all the anatomical planes. a) Brain image in the transverse plane, b) Magnification of the brain fibers in the coronal plane, c) Magnification of the brain fibers in the sagittal plane.

be also observed in the coronal plane (fig.8.11 b) and in the sagittal one fig.8.11 c).

The visualization of the volumetric arrangement of the brain fiber was the first step before performing a quantitative analysis.

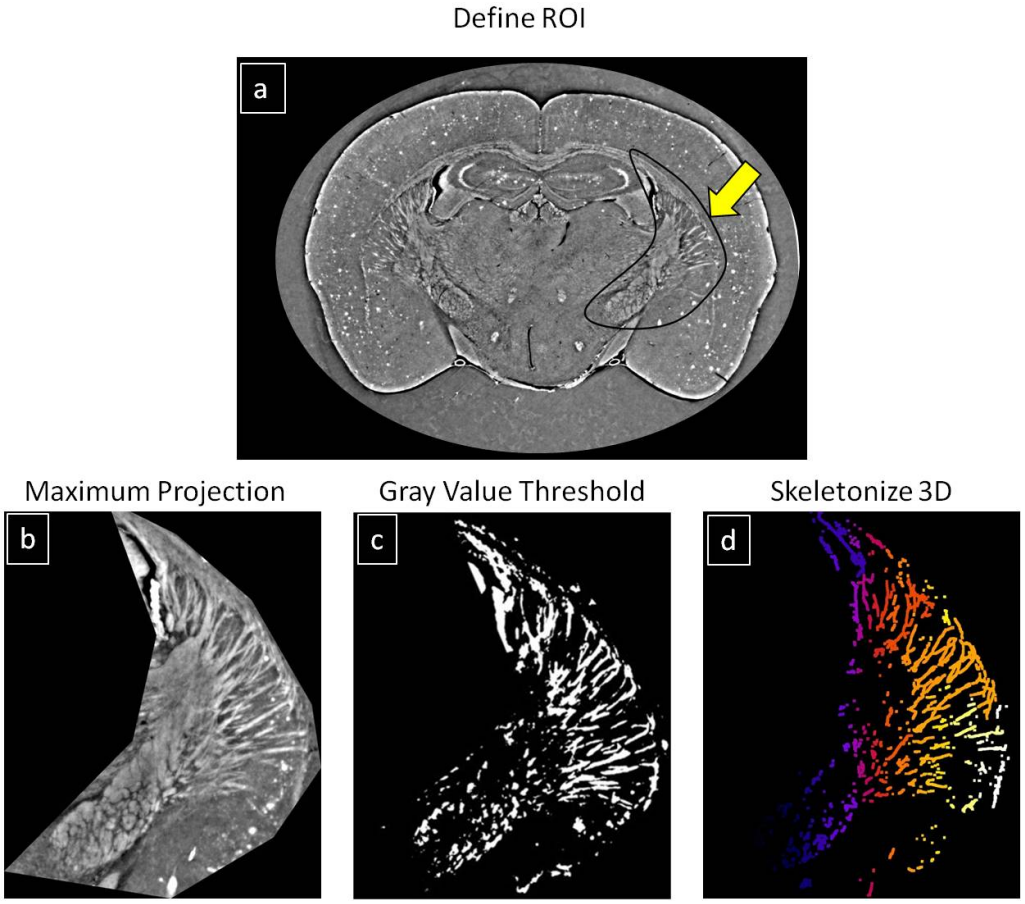

FIGURE 8.12: Description of the data analysis to calculate brain fiber's length. Each of the two volumes corresponding to 12-15 and 20-22 months old APP/PS1 were registered. a) Selection of a region of interest (ROI). b) Maximum intensity projection images every 15 μm. c) Segmentation of the fibers with a gray value threshold. d) Result from the Skeletonize 3D plug-in, available in ImageJ.

In order to characterize the degeneration process of the APP/PS1 model for AD, two time-points of the disease where considered. Mice were sacrificed at 12-15 months and at 20-22 months old. Two samples for each age group were considered and the final result was calculated as their average values. In the following analysis the distribution of fiber length for the two time points will be presented.
The following steps were performed to quantify brain fibers:

- Each of the two volumes corresponding to 12-15 and 20-22 months old APP/PS1 were registered. A volume thickness of 300 μm was considered.
- The same region of interest (ROI) (fig.8.12 a), where the fiber are anatomically located, was chosen in the two volumes.
- Maximum intensity projection images every 15 μm were performed (fig.8.12 b), to make the segmentation more effective and to achieve a better 3D resolution.

- The fibers were segmented with a gray value threshold procedure (fig.8.12 c).
- Finally, the Skeletonize 3D plug-in available in ImageJ was applied (fig.8.12 d), setting 210 μm as a minimum acceptable fiber length, to avoid the analysis of very small objects not compatible with the fiber structure.

First, registration is necessary in order to be able to compare or integrate the data obtained from these different measurements. Essentially, image registration is used to align two or more images of the same scene. Geometric distortions causing differences in angle, orientation, shifting, and distance need to be taken into account. In ImageJ it is possible to estimate the transformation function between two volumes (ie. rigid translation + rotation).
We pre-process a 3D image to extract the relevant morphological information by binarizing and then extracting the skeleton of a binary image with the Skeletonize3D plug-in available in ImageJ (Lee, Kashyap, and Chu, 1994).
The resulting skeletons were analyzed in the 3D image with AnalyzeSkeleton (Arganda-Carreras et al., 2010). This plugin tags all pixel/voxels in a skeleton image and then counts all its junctions, triple and quadruple points and branches, and measures their average and maximum length. The voxels are classified into three different categories depending on their 26 neighbors:

1. End-point voxels: if they have less than 2 neighbors.
2. Junction voxels: if they have more than 2 neighbors.
3. Slab voxels: if they have exactly 2 neighbors.
4. End-point voxels are displayed in blue, slab voxels in orange and junction voxels in purple.

The skeletonize image with the output colour map of the plug-in AnalyzeSkeleton is shown in fig.8.12 d). An histogram of average fiber length for the AD sample APP/PS1 12-15 months old (black bars) and for AD sample APP/PS1 20-22 months old (gray bars) is shown in fig.(8.13). The minimum acceptable fiber length was set at 210 μm, to minimize the contribution from very small fragments segmented in the tissue. The relative frequencies expressed as percentage values can be seen at the top of each column.
It is important to note that for the older time-point (20-22 months old APP/PS1), 38 % of the fibers have a length between 200 and 400 μm; while only 20 % of the fibers is in the same range of lengths for the younger time-point (12-15 months old APP/PS1).
This means that the APP/PS1 model for AD leads to an increase in the number of the shortest fibers in the tissue. The fiber are surrounded by myelin boundles, which main role is to protect the axon, insulate and accelerate the conduction of nerve impulses. Demyelination is the myelin damage, that is characterized by the loss of nerve sheath. Studies have shown that myelin injury may be closely related to neurodegenerative diseases and may be an early diagnostic criteria (Wang et al., 2018). In fact, some researches (Kotter, Stadelmann, and Hartung, 2011) supports that myelin destruction may have a great effect in AD pathology. Decreasing in the average fiber length with disease progression may be explained by myelin damage connected with AD.

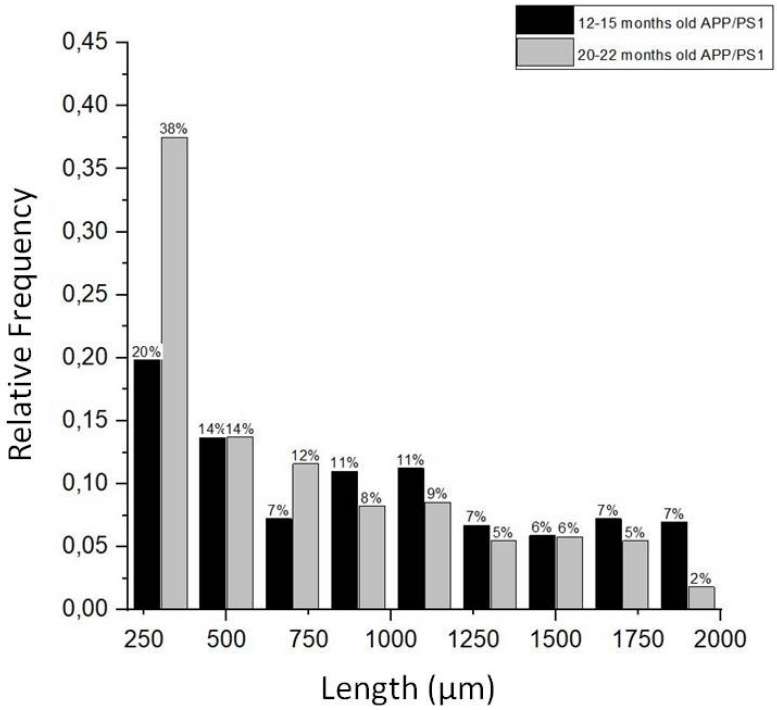

FIGURE 8.13: Histogram of the fiber lenght for the AD sample APP/PS1 12-15 months old (black bars) and for AD sample APP/PS1 20-22 months old (gray bars). For the APP/PS1 20-22 months old sample the number of smaller fiber increases.

8.1.5 Quantitative plaques analysis

An open challenge in diagnostic is the development of methodologies to non-invasively detect and quantify the presence of amyloid agglomerates in AD patients. Phase-contrast X-ray computed tomography (XPCT) can detect Aβ amyloid plaques in three-dimensions with extremely high sensitivity and also enables their quantification and spatial arrangement. Since the amyloid plaques contains heavy metals, they can be specifically detected with phase imaging as high-density aggregates in brain tissue. Numerous bright white spots were observed in the AD affected brains, both at 12-15 and 20-22 months old APP/PS1 mice. A distribution analysis of the number of Aβ amyloid plaques also revealed a characteristic shift toward higher density of plaques when the mouse's age increases. Also, the biggest agglomerates of plaques were observed predominantly in the cerebral cortex and in the hippocampus. We concentrate on these two areas of the brain for the quantitative analysis.
We will now describe the data analysis performed to quantify the number of plaques inside the brain at two time points (2-15 and 20-22months old APP/PS1). First a registration between the two volumes was performed, with the same procedure already presented in section 8.1.4. A volume thickness of 300 μm was considered for both samples, including the brain area where the plaques were more visible. Then, a region of interest (ROI) (fig.8.14 a) was defined corresponding to the brain cortex. Maximum intensity projection images every 15 μm were performed. The plaques were segmented with a gray value threshold procedure on the maximum projection images (fig.8.14 b). Finally, the 3D Object Counter plug-in (BOLTE and

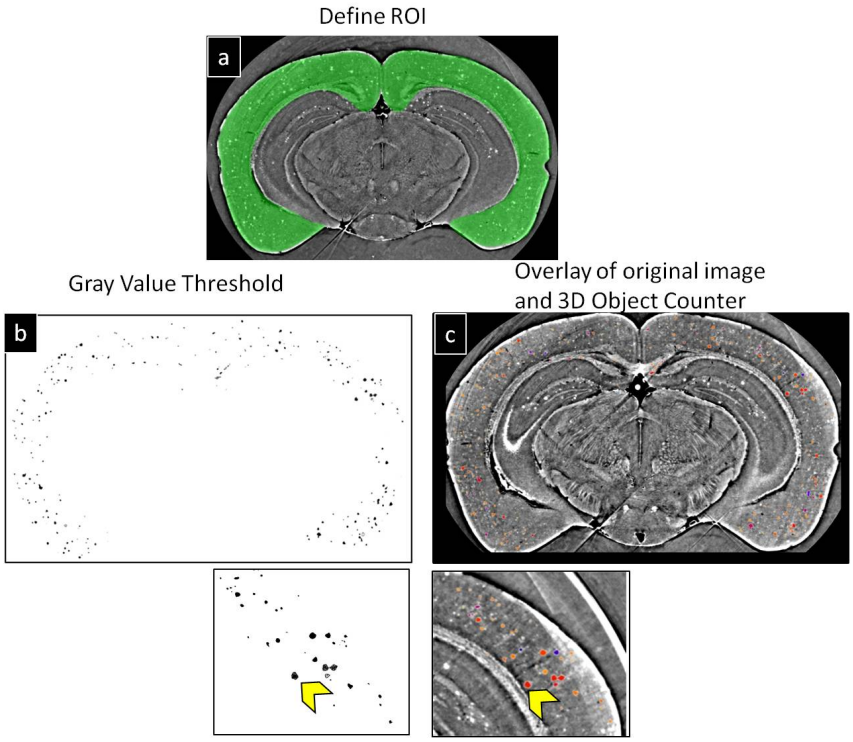

FIGURE 8.14: Description of the data analysis to quantify the brain plaques. Each of the two volumes corresponding to 12-15 and 20-22 months old APP/PS1 were registered. a) Selection of a region of interest (ROI) inside the brain cortex. b) Maximum intensity projection images every 15 μm and segmentation of the plaques with a gray value threshold. c) Overlay of the original image with the result from the 3D Object Counter plugin, available in ImageJ.

CORDELIÈRES, 2006) available in ImageJ was applied to estimate the 3D volume of the plaques. The outcome of the plug-in is overlaid with the original image in fig.8.14 c, where the colors are proportional to the calculated volume of each plaque. In the plug-in options it is possible to exclude from the analysis objects which size is out of the defined range. We consider the following range of acceptable volumes: (4500-27000) μm^3.
The 3D Object Counter plugin starts with a connectivity analysis on a stack of threshold images. First, the stack will be scanned and the first object's pixel is found, the plugin gives it a tag. The tag is a unique number which will be carried by all pixels constitutive of the same object. Each time a new object's pixel is found, its 13 previous neighbors (9 on the upper slice and 4 on the same slice) are checked for an existing tag. The minimum tag found in the surrounding is then attributed to the current pixel. Then, statistic about each objects are then retrieved.
We concentrate on the volume analysis, that returns the number of each object's voxels. First, we will present the results obtain in the cortex region and then we will repeat the same analysis on the hippocampus.
The result of the segmentation of the plaques in the cortex region for the 12-15 and 20-22 months old APP/PS1 mouse is presented in fig.8.15. The volumetric organization of the plaques in the cortex can be observed for the two time-points. Thanks to the 3D reconstruction, it is possible to know the position of each plaque and eventually correlate it with other morphological features inside the brain. Since, from a first

qualitative analysis the number of plaques increases with the sample age, the corresponding volume of each segmented plaque was also quantified. The total number of plaques in the cortex for the APP-PS1 12/15 months old mouse is 1298, while for the APP-PS1 20/22 months old mouse is 1761.

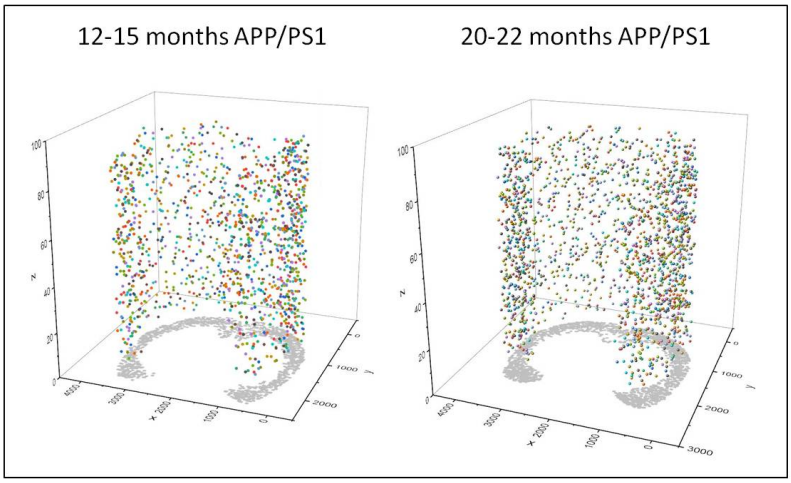

FIGURE 8.15: 3D visualization of the segmentation of the plaques in the cortex region for the 12-15 (left panel) and 20-22 (right panel) months old APP/PS1 mouse.

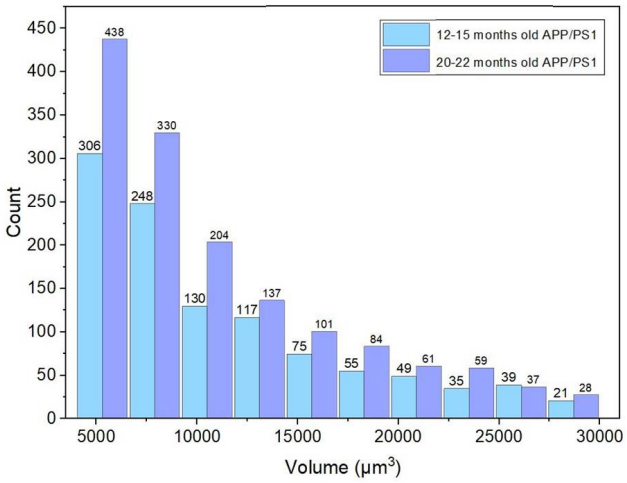

FIGURE 8.16: Histogram of the plaques volume in the cortex in μm^3 for the AD sample APP/PS1 12-15 months old (light blue bars) and for AD sample APP/PS1 20-22 months old (violet bars).

The histogram of the plaque volumes, calculated in μm^3, for the AD sample APP/PS1 12-15 months old (light blue bars) and for AD sample APP/PS1 20-22 months old (violet bars) is shown in fig.8.16. At the top of each bar is reported the relative count for each volume interval. The total number of plaques increases with the sample's age. Also, for APP/PS1 20-22 months old sample, the ratio of smaller plaques augments respect to the APP/PS1 12-15 months old sample, while the number of bigger agglomerates remains quite comparable in the two cases.

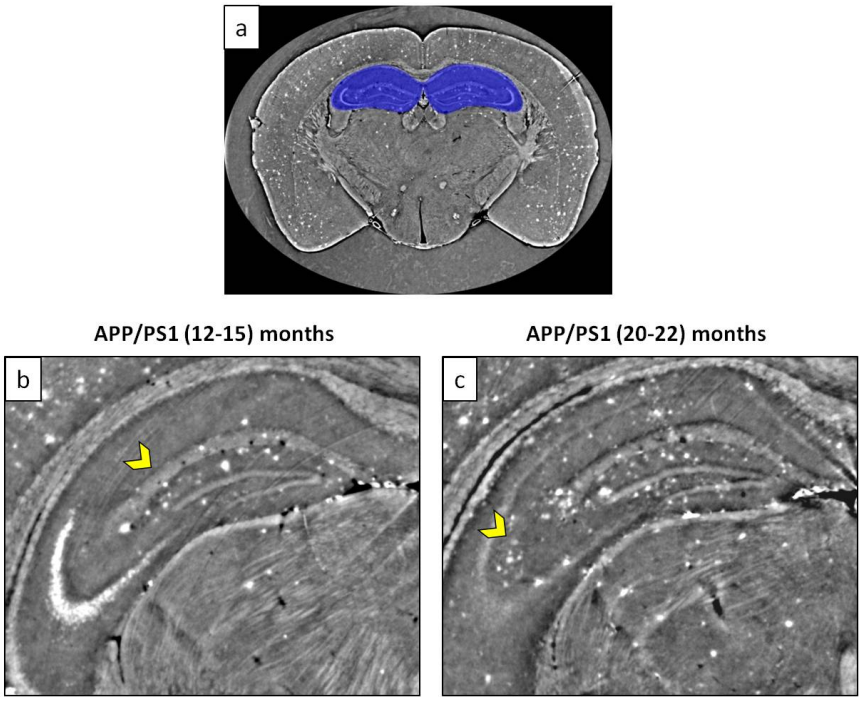

FIGURE 8.17: Quantification of the plaques on the hippocampus. a) the blue ROI indicates the hippocampus region of the brain, b) maximum intensity projection of the left part of the hippocampus for a AD affected APP/PS1 (12-15) months old mouse, c) maximum intensity projection of the left part of the hippocampus for a AD affected APP/PS1 (20-22) months old mouse. Yellow arrows underlines the spreading of plaques in several areas of the hippocampus. Bright cells are more visible in the left part of image a) than in image b), because it depends on the volume part chosen for the two samples.

This result can be interpreted assuming that a certain number of plaques undergo a process of fragmentation with the disease progression. Also, it is possible that, with aging, less space is available for the formation of new plaques, leading to an increase of smaller agglomerates in the brain.
The same analysis was repeated on the brain hippocampus, since, together with the cortex, is the brain area were the highest number of plaques is observed. The hippocampus is part of the limbic system, and plays important roles in the consolidation of information from short-term memory to long-term memory. It is composed of several layers, where different agglomerates of the plaques are present. In fig.8.17 a) the region of the hippocampus is indicated by the blue region of interest. A comparison between the left part of the hippocampus for the two time points of AD affected samples is shown in fig.8.17b-c) with maximum intensity projection images. For the

APP/PS1 (12-15) months old mouse the plaques appears to be concentrated on the inner part of the hippocampus (yellow arrow) and they are less in number than the older time point. Instead, a general spread of the plaques is present in the APP/PS1 20-22 months old in all the hippocampus and they increase in number.
Therefore, plaques seem to present a different spatial organization respect to the degree of progression of AD. We can thus observed that the inner part of the hippocampus is the first involved with the formation of plaques, before they start to appears in the outer part. The same data analysis for plaques quantification, already described in fig.8.14 applied to the cortex, was performed on the hippocampus. The final goal is to quantify the volume of each plaque in the brain hippocampus. The result of the segmentation of the plaques in the hippocampus region for the 12-15 and 20-22 months old APP/PS1 mouse is presented in fig.8.18. From a qualitative point of view, it is clear that the number of plaques increases with the mouse age, as we have already observed in the cortex region. The histogram of the plaque volumes

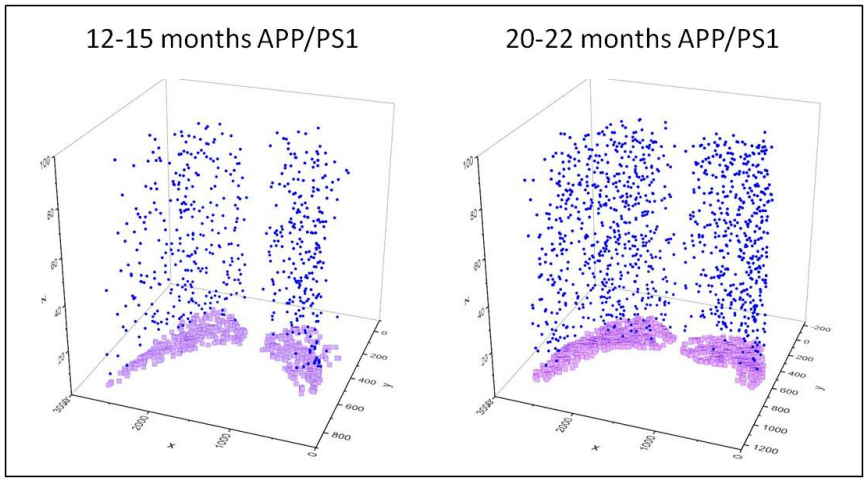

FIGURE 8.18: 3D visualization of the segmentation of the plaques in the hippocampus region for the 12-15 (left panel) and 20-22 (right panel) months old APP/PS1 mouse.

for the AD sample APP/PS1 12-15 months old (light blue bars) and for AD sample APP/PS1 20-22 months old (violet bars) is shown in fig.8.19. At the top of each bar is reported the relative count for each volume interval. As we have already observed in the cortex area, the total number of plaques increases with the sample's age. In the hippocampus we find that the calculated plaques volumes are significantly smaller that in the cortex region. Also, the majority of the plaques have a volume smaller than 2000 μm^3, while larger plaques are not observed for both samples. The volume distribution is comparable for the APP/PS1 20-22 months old sample and the APP/PS1 12-15 months old sample, with a larger number of plaques in the older time-point.
These findings can help to understand the mechanisms of the plaques formation in terms of their spatial organization and volume quantification. Being also able to compare different stages of the disease, can lead to a comprehensive knowledge of AD degeneration processes.

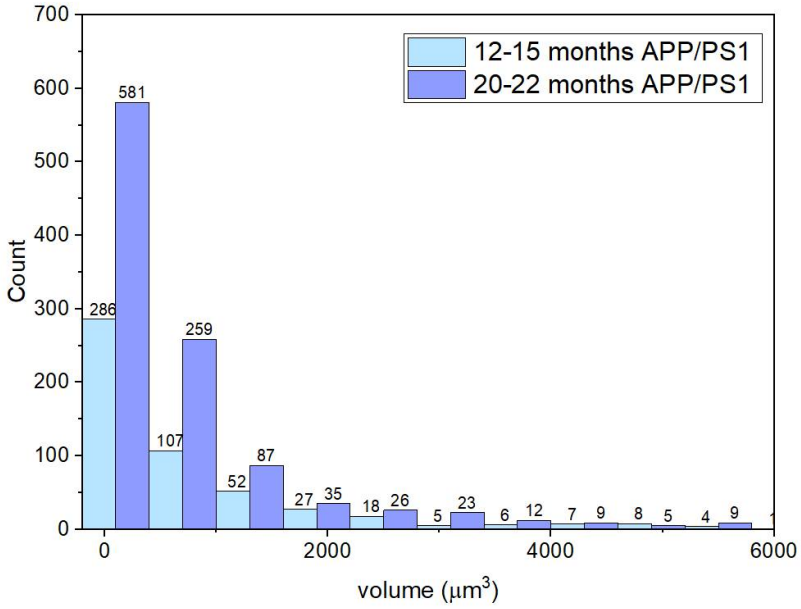

FIGURE 8.19: Histogram of the plaques volume in the hippocampus in μm^3 for the AD sample APP/PS1 12-15 months old (light blue bars) and for AD sample APP/PS1 20-22 months old (violet bars).

8.2 Spinal cord imaging: Amyotrophic lateral sclerosis

We will now present the results from the second experiment performed on mouse spinal cord samples affected by an animal model of Amyotrophic Lateral Sclerosis (ALS). The results were obtained with the free space propagation technique.
ALS is a progressive neurodegenerative disorder affecting motor neurons (Kiernan et al., 2011), nerve cells responsible for carrying signals from the central nervous system towards muscles to cause muscle movement. Typical features in ALS are the loss of upper and lower motor neurons (UMN/LMNs) and their fibers in the primary motor cortex, brainstem and anterior horns of the spinal cord (Saberi et al., 2015).
The development of animal models that well mimic ALS disorder enables both the dissection of disease processes and an early assessment of therapy efficacy.
We use the $SOD1^{G93A}$ animal model for ALS, where the original SOD1-G93A DNA strain, designated G1, expressed approximately 18 copies of human SOD1, randomly inserted into the genome (Gurney et al., 1994). A comprehensive knowledge of neuronal and vascular lesions in the brain and spinal cord is an essential factor to understand the development of the disease.
We applied XPCT to the $SOD1^{G93A}$ ALS mouse to provide a 3D morphological description of the progressive loss of neuronal and vascular network in the spinal cord. The mice were sacrificed at different time points: pre-symptomatic, 60 days old and 90 days old $SOD1^{G93A}$ mouse. With pre-symptomatic we define all the mice that were not presenting any symptom connected with ALS. All the samples were measured at beamline ID17 of ESRF synchrotron, France. The experiment on ALS-affected mice spinal cords was performed with pink beam (spectrum peaked at 44 keV) and 2000 projections were acquired covering a total angle range of 360°. Spinal cord samples were set at 2.3 m from sCMOS detector coupled with optics systems to obtain a final pixel size of 3.06 mm.
Our analysis was focus on the lumbar region of the spinal cord considering a volume thickness of about 1.3 mm.
It is possible to differentiate several bright structures in the XPCT images (Fig. 8.20): meninges and spinal roots that anatomically surround the spinal cord, as well as neuronal cells and veins. Motor neurons (MNs) quantification was performed through

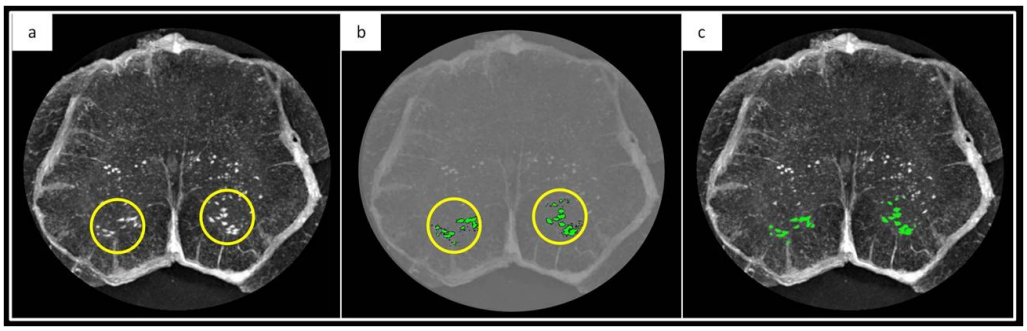

FIGURE 8.20: XPCT images of the lumbar region of the spinal cord. Example of the motor neurons 3D segmentation process. (a) A ROI was selected in the ventral horn of the spinal cord where the MNs are anatomically concentrated. (b) An intensity threshold segmentation was performed to isolate MNs. (c) Superimposed image of (a) and (b) to show the output of the segmentation process.

an automated counting process, using the 3D Objects Counter ImageJ plug-in (fig. 8.20) already described. We selected a region of interest (ROI) in the ventral horn of the spinal cord where the MNs are anatomically concentrated and their size and position were compared with the literature and histological images.
Neuron quantification was carried out in several steps:

- An intensity threshold was performed, since neurons appear as bright objects in XPCT images;
- On the binarized images we applied the 3D object counter plug-in – this plug-in takes as input the volume of the object of interest (in pixels) and counts the number of 3D objects in a stack.

The vascular network was also analyzed inside a selected volume of the lumbar region of the spinal cord. The segmentation of the vascular network was performed through a 3D image segmentation process. Starting from the 3D tomographic reconstruction image, we applied an intensity threshold segmentation to isolate the vascular network (appearing as white tubular objects). On these binarized images, we then applied the Skeletonize ImageJ plug-in to calculate the number of branches per mm^3. This plugin tags all pixel/voxels in a skeleton image. The plug-in was already described in the brain fiber analysis section.
The percentage of MNs loss and vascular density in diseased animals was compared with control samples in the pre-symptomatic and symptomatic stages.

8.2.1 Motoneurons quantification

Neuronal lesions were evaluated at different time-points of the disease through XPCT experiments on mice lumbar spinal cords affected by ALS and were compared with the control samples.

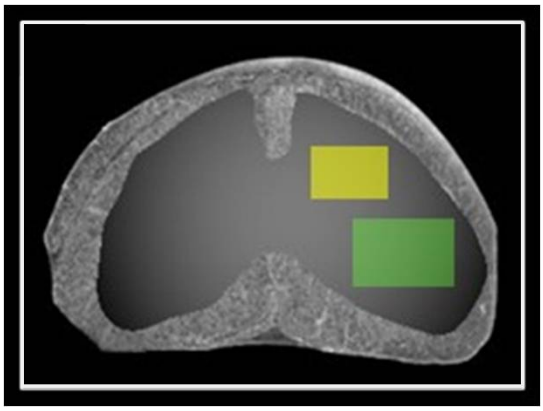

FIGURE 8.21: Schematic representation of the selected ROIs: quantitative analysis was performed in the ventral horn (green) of the spinal cord.

Fig.8.22 summarizes the results. An axial view of the reconstructed tomographic images for the control (fig.8.22 a), pre-symptomatic $SOD1^{G93A}$ 60 days old (fig.8.22 b) and 90 days old $SOD1^{G93A}$ (fig.8.22 c) mice spinal cords are shown.
Images were acquired with a spatial resolution of about 9 μm.
The insets at the top of fig.8.22 represent a magnification of the neuronal cells obtained through maximum intensity projection method.

In order to better visualize the region of interest for our analysis, we provide a sketch (fig.8.21) of the spinal cord with the two analyzed regions depicted in yellow (where the interneurons are present) and in green (where the MNs are located).
As expected, the number of MNs in the ventral horns decreased compared with the control at the time of symptom onset (90 days), as shown in fig.8.22 c) and summarized in the bar chart fig.8.23. Furthermore, at a pre-symptomatic stage (60 days) the loss of motor neurons appears already evident, as appreciated in the bottom inset of fig.8.22 b), compared with the control case.

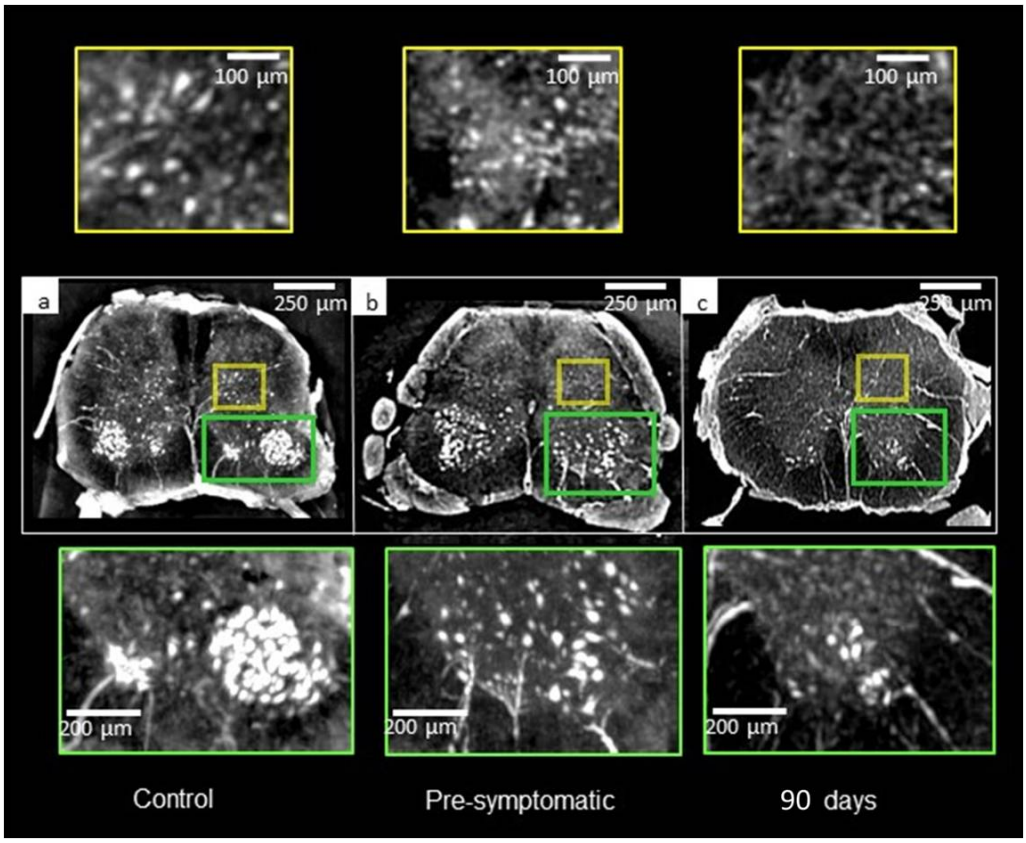

FIGURE 8.22: X-ray phase contrast tomography images of the lumbar region of the spinal cord. Reconstructed volumes (about 1 mm thick) of the lumbar region of the spinal cord. Axial sections of healthy (a), pre-symptomatic (b) and 90 days ALS affected (c) samples. Cell loss induced by ALS progression can be observed in (b) and (c). Lower inset (green): magnification of ROIs in the ventral horn of the spinal cord containing neuronal cells compatible with motor neurons. Upper insets (yellow): magnification of ROIs to show neuronal cells compatible with sensor interneurons. In a pre-symptomatic stage, the number of the sensory neurons remains almost unaltered compared with the control sample, while a decrease in cell number is shown in the 90 days SOD1 mice.

In the pre-symptomatic stage, the number of neurons in the posterior horns of $SOD1^{G93A}$ mice is almost unaltered compared with wild type mice, although their size appears reduced, as shown in the top inset of fig.8.22 b). At 90 days old a reduction in neurons can be appreciated in the ROI of $SOD1^{G93A}$ compared with wild type mice, while small cells compatible with inflammatory cells occupy this region, as reported in the top inset of fig.8.22 c). In fig.8.24, 3D rendering images of 60 days old wild

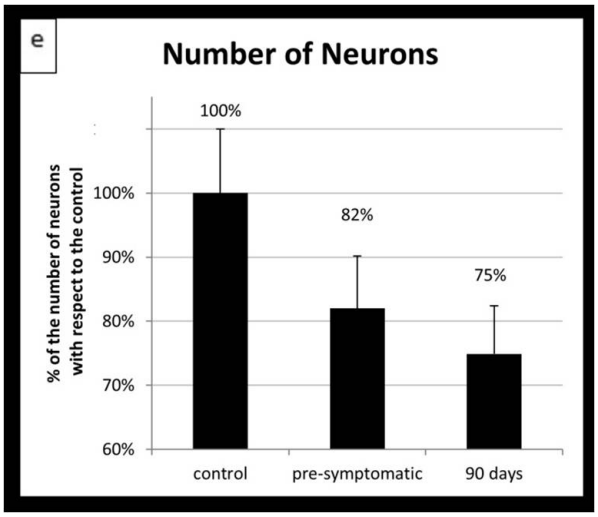

FIGURE 8.23: Percentage of the number of neurons in ALS samples compared with the control samples in the ventral horn at different time-points. Error bars represent standard deviation of data.

type and $SOD1^{G93A}$ mice are shown, offering a more visual proof of the reduction in the distribution and density of neurons (yellow) and blood vessels (red) in the pre-symptomatic stage of $SOD1^{G93A}$ mice compared with controls.

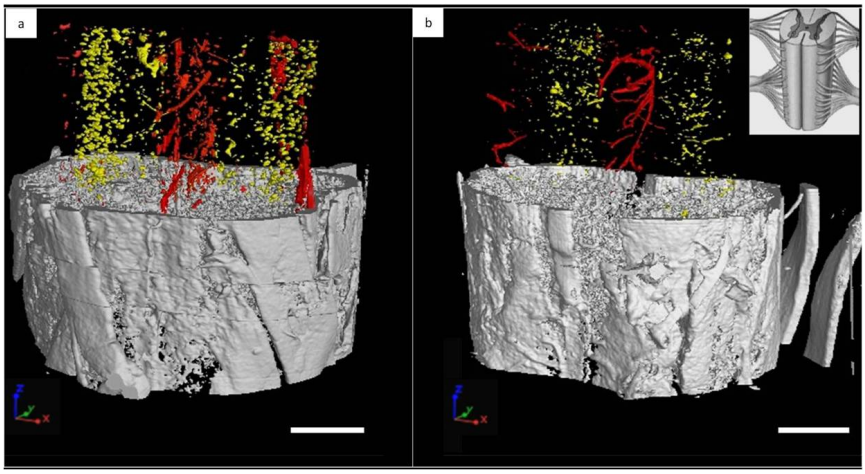

FIGURE 8.24: 3D reconstruction of the vascular network (segmented in red) and the neuronal network (segmented in yellow) of healthy (a) and ALS-affected (b) mice spinal cord. Samples were approximately 60 days old. Inset: Schematic representation of the anatomical orientation of the spinal cord. Scale bar: 400 μm.

8.2.2 Vascular quantification

We performed a segmentation of the same XPCT images already used for the motor neurons quantification in order to isolate the vasculature (fig.8.25, rendered in yellow, blue in the insets) in the ventral (or posterior) and dorsal (or anterior) horn of WT (fig. 8.25 a) and 60 and 90 days old $SOD1^{G93A}$ mice (fig.8.25 b and c respectively). The image of the pre-symptomatic sample is not shown because no apparent vascular alteration was found. However, in the latter case, a slight alteration compared

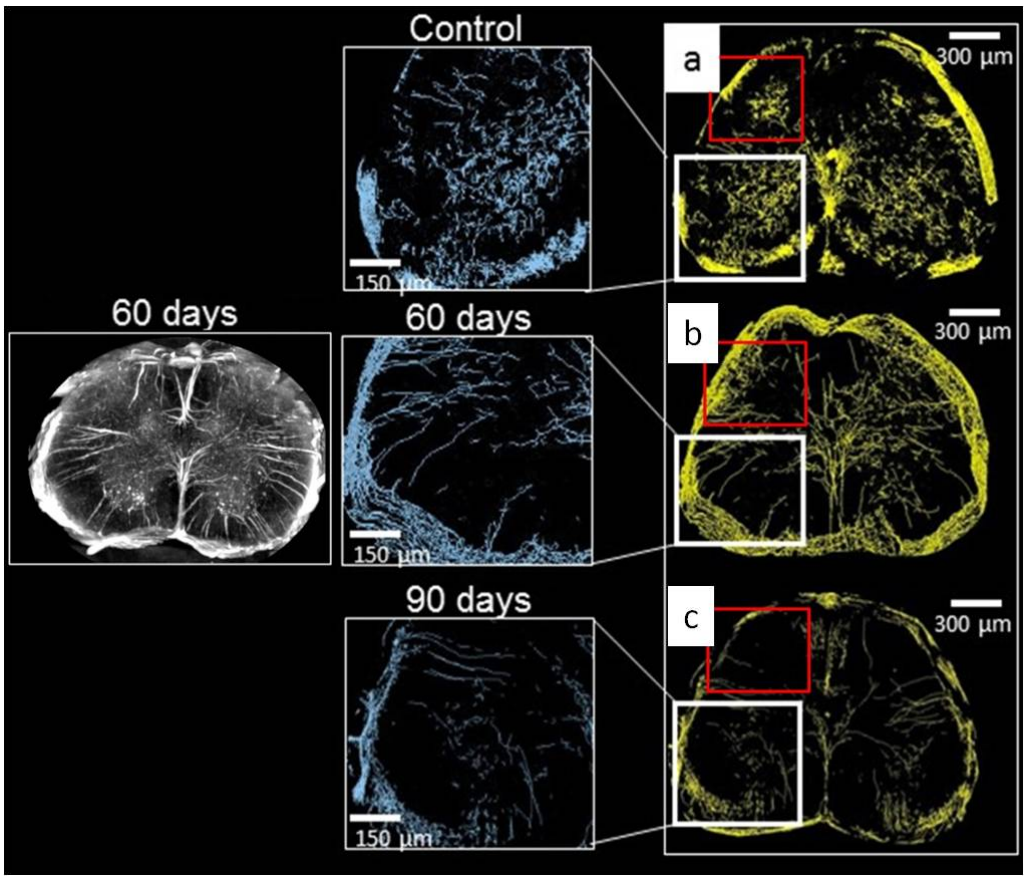

FIGURE 8.25: Vascular segmentation (about 1 mm thick) of the lumbar region of the spinal cord. a) Vascular network segmentation obtained by Skeletonize ImageJ plug-in. White inset: magnification of the selected ROI in the ventral horn of the spinal cord. Red inset: analyzed area in the dorsal horn. A maximum intensity projection image is shown for the 60 days case.

with the control case was found as a result of the quantitative analysis of vascularization in the ventral horn (fig.8.25 b). The images reported in fig.8.25 display the segmented vessels in the XPCT axial reconstructions: insets on the left show a magnification of the ventral horn. We implemented a gray-level segmentation process in order to perform a quantitative analysis that allowed us to make a comparison between the different time-points and the control. The number of branches per mm^3

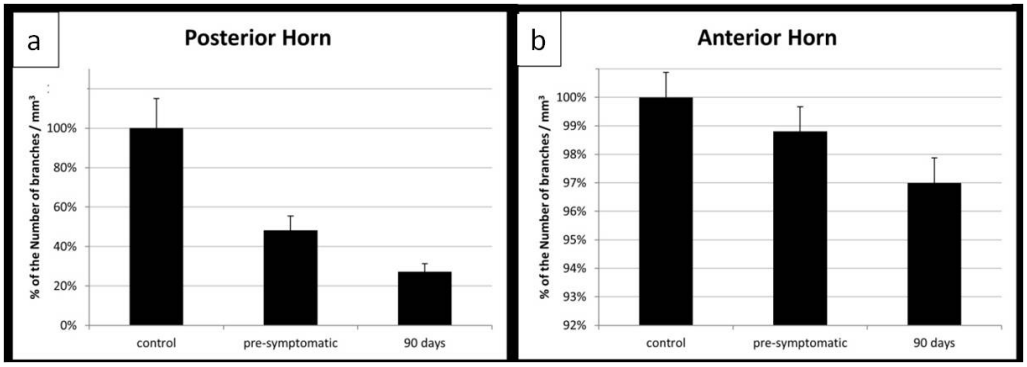

FIGURE 8.26: Quantification of vascular distribution as the percentage of the number of branches per mm^3 in the posterior horn (data normalized to the control sample) and in the anterior horn (data normalized to the control sample).

was calculated, data were normalized with respect to the control sample and expressed as percentage values. A few percentage points of decreasing in the vasculature, compared with the control, are evident in the anterior horn as the time course of the disease progresses (fig.8.26 b). On the other hand, a considerable loss in the vessel branches was found in the posterior horn of $SOD1^{G93A}$ mice compared with wild type samples at the same time points, with a progressive reduction observed also between pre-symptomatic and symptomatic mice (fig.8.26 a).

8.3 Conclusion

In this chapter we have shown the capabilities of the free space propagation technique to image in 3D and with high resolution biological tissues, to better understand the mechanisms underneath neurodegenerative diseases.
A comprehensive analysis was performed on brain samples affected by an animal model of Alzheimer disease. Two time points of the disease were considered, as well as a healthy mouse used as a control. A quantitative analysis was performed on brain fibers, that undergo a demyelination process, meaning a damage of the myelin, a membrane layer that covers axons.
An increase in the number of shorter fibers was observed in the latest time-point of the disease respect to the younger mouse. Also, the volume of plaques deposits both in the brain cortex and hippocampus was quantified, showing a possible decomposition of larger plaques into smaller parts for the oldest time-point.
The second part of the chapter is dedicated to the study of mouse spinal cord affected by an animal model of Amyotrophic lateral sclerosis. Control, pre-symptomatic (60 days old) and 90 days old mice spinal cords were analyzed. We first quantified a specific kind of neurons, called motor neurons, that are responsible for carrying signals from the central nervous system towards muscles to cause muscle movement. The number of motor neurons start decreasing compared with the control already at a pre-symptomatic stage and drop even more at the time of symptom onset (90 days).
We also quantified the alterations in the vasculature of the same samples, finding a different organization of the vessels corresponding to the disease's progression.

Chapter 9

Conclusion and Perspectives

In the present work the capabilities of 3D X-ray phase imaging based on X-ray wavefront sensors were investigated.
A general introduction of X-ray radiation fundamental properties and of X-ray interaction with matter given to help understanding the fundamental interaction mechanisms related with image formation. Particular attention was given to classical coherence theory, a crucial parameter when using a wavefront sensor. The main theoretical principles of X-ray phase-contrast imaging were also given, with particular attention to the wave optic theory applied to free space propagation imaging. The last theoretical section was dedicated to X-ray tomography, considering the mathematical transformations needed to reconstruct an object in 3D.
In order to understand the image formation in a wavefront sensor, we provide a comprehensive description of the wavefront using the Huygens-Fresnel principle, of the wavefront detection algorithms and of the possible wavefront reconstruction methods.
To optimize the design of Hartmann wavefront sensors applied to imaging applications, a chapter was dedicated to the description of a 3D wave propagation simulation tool based on Fresnel propagator. The presented model can manage any degree of spatial coherence of the source. Validation analysis for the modelling of image formation and coherence proprieties are provided. The simulation tool was then applied to understand, first, features connected with the propagation processes and later, parameters connected with the detection algorithms.
Experimental results with the X-ray Hartmann wavefront sensor were shown both for a laboratory set-up and for synchrotron measurements. Three different Hartmann sensors were tested: a compact X-ray Hartmann wavefront sensor and two prototypes with larger fields of view. The results from tomographic scans of biological samples (mouse brain and rat spine) with a laboratory set-up showed the capabilities of the Hartmann wavefront sensor to perform biomedical imaging. Using the Hartmann wavefront sensor, it was also possible to retrieve the density and the chemical composition of test objects composed of known materials. The same samples were analyzed with a polychromatic and monochromatic incident beams.
Biological imaging was also performed with free space propagation technique to image in 3D and with high resolution biological tissues, to better understand the mechanisms underneath neurodegenerative diseases.
The study of X-ray Hartmann wavefront sensor for X-ray phase-imaging was thoroughly explored from theory, modeling and experiments. The thesis demonstrated that this system holds important original capabilities of interest for future end-users. The reconstruction of the object density and of its refraction index components is a

crucial feature that will open new visualisation modalities inside weakly absorbing objects, such as biological tissue or polymeric materials.

As a future prospective for the designed system, it would be advantageous to incorporate a photon counting detector instead of the fluorescent screen followed by a visible detector, as used today on two systems. This type of detector is in fact capable of reducing the bandwidth of incident polychromatic radiation more efficiently and with more versatility than using filters, as shown in Chapter 6, section 7.2. Since the object index of refraction components delta and beta depend on the incident energy, a photon counting detector will increase the accuracy of their determination, and consequently of the object density calculation.
Another important development will be to improve the system benchmarking using an object having different known densities and chemical compositions. A good target sample can be represented by artificial phantoms that mimic the internal structures of biological tissues, such as brain or liver. In particular, artificial structures, doped with gold or gadolinium nanoparticles, capable of mimic real vascularization architectures. More generally speaking, at this step of development, it is important to test the prototypes with as many users as possible.

Chapter 10

Appendix A

10.1 Publications

- High-Sensitivity X-ray Phase Imaging System Based on a Hartmann Wavefront Sensor, Condensed Matter, 2021-12-27 | journal-article , DOI: 10.3390/condmat7010003
- Phase-Contrast Tomography with X-ray Hartmann wavefront sensor , International Conference on X-Ray Lasers 2020, 2021-07-08 | conference-paper, DOI: 10.1117/12.2593107, ISBN: 9781510646186ISBN: 9781510646193
- Corrigendum: X-ray Phase Contrast Tomography Serves Preclinical Investigation of Neurodegenerative Diseases, Frontiers in Neuroscience, 2021-02-17 | journal-article,DOI: 10.3389/fnins.2021.657368, Part of ISSN: 1662-453X
- Modelling of Phase Contrast Imaging with X-ray Wavefront Sensor and Partial Coherence Beams Sensors, 2020-11-12 | journal-article, DOI: 10.3390/s20226469, Part of ISSN: 1424-8220
- X-ray Phase Contrast Tomography Serves Preclinical Investigation of Neurodegenerative Diseases, Frontiers in Neuroscience, 2020-11-09 | journal-article, DOI: 10.3389/fnins.2020.584161,Part of ISSN: 1662-453X
- Investigation of the human pineal gland 3D organization by X-ray phase contrast tomography, Journal of Structural Biology, 2020-10 | journal-article, DOI: 10.1016/j.jsb.2020.107659, Part of ISSN: 1047-8477
- Multiscale pink-beam microCT imaging at the ESRF-ID17 biomedical beamline, Journal of Synchrotron Radiation, 2020-09-01 | journal-article, DOI: 10.1107/s160057752000911x, Part of ISSN: 1600-5775
- X-ray phase contrast tomography for the investigation of amyotrophic lateral sclerosis, Journal of Synchrotron Radiation, 2020-07-01 | journal-article, DOI: 10.1107/s1600577520006785, Part of ISSN: 1600-5775
- X-ray Phase Contrast Tomography for the investigation of ALS disease, Il Nuovo Cimento C, 2020-01-10 | journal-article, DOI: 10.1393/ncc/i2019-19233-4
- Single-shot, high sensitivity X-ray phase contrast imaging system based on a Hartmann mask2020 | conference-paper
- Assessment of the effects of different sample perfusion procedures on phase-contrast tomographic images of mouse spinal cord, Journal of Instrumentation, 2018, DOI:10.1088/1748-0221/13/03/c03027

- Synchrotron Radiation X-ray Phase Contrast Microtomography: What Opportunities More For Regenerative Medicine? in book Advanced High-Resolution Tomography in Regenerative Medicine, 2018, Springer Nature

10.2 Selection of Oral Presentations

- Conference of Condensed Matter for "High Precision X-ray Measurements 2021"
- Joint Meeting (MC+WG+WORKSHOP), COST Action CA16122, BIONECA - Biomaterials and advanced physical techniques for regenerative cardiology and neurology, Vienna , Austria, 2019
- ESRF User Meeting 2020, Grenoble, France
- XVII INTERNATIONAL CONFERENCE ON X-RAY LASERS, International Conference on X-Ray Lasers 2020
- Italian Physical Society National Congress Section 5 - Biophysics and medical physics, 2018
- International worshop on imaging , villa monastero , Varenna (Italia), 2017

10.3 Distinctions

- Condensed Matter for "High Precision X-ray Measurements 2021": Rome, IT, 2021-06-02 | BEST PRESENTATION AWARD
- Best Presentations 2018 at Italian Physical Society National Congress Section 5 - Biophysics and medical physics Second prize, 2018

Bibliography

Ahmed, Syed Naeem (2015). *1 - Properties and sources of radiation*. Ed. by Syed Naeem Ahmed. Second Edition. Elsevier, pp. 1–64. ISBN: 978-0-12-801363-2. DOI: https://doi.org/10.1016/B978-0-12-801363-2.00001-2. URL: https://www.sciencedirect.com/science/article/pii/B9780128013632000012.

Akondi, Vyas, M Roopashree, and Budihal Prasad (Aug. 2009). "Optimization of Existing Centroiding Algorithms for Shack Hartmann Sensor". In:

Anthony S.M.and Granick, S. (2009). "Image Analysis with Rapid and Accurate Two-Dimensional Gaussian Fitting". In: *Langmuir 25(14)*.

Arfelli, F et al. (1998). "Low-dose phase contrast x-ray medical imaging". In: 43.10, pp. 2845–2852. DOI: 10.1088/0031-9155/43/10/013. URL: https://doi.org/10.1088/0031-9155/43/10/013.

Arganda-Carreras, Ignacio et al. (2010). "3D reconstruction of histological sections: Application to mammary gland tissue". In: *Microscopy Research and Technique* 73.11, pp. 1019–1029. DOI: https://doi.org/10.1002/jemt.20829. eprint: https://analyticalsciencejournals.onlinelibrary.wiley.com/doi/pdf/10.1002/jemt.20829. URL: https://analyticalsciencejournals.onlinelibrary.wiley.com/doi/abs/10.1002/jemt.20829.

Attwood, David (1999). *Soft X-Rays and Extreme Ultraviolet Radiation: Principles and Applications*. Cambridge University Press. DOI: 10.1017/CBO9781139164429.

Baker, K. L. (2003). "Curvature wave-front sensors for electron density characterization in plasmas". In: *Review of Scientific Instruments* 74.12, pp. 5070–5075. DOI: 10.1063/1.1628822. eprint: https://doi.org/10.1063/1.1628822. URL: https://doi.org/10.1063/1.1628822.

Baker, K. L. et al. (Feb. 2003). "Electron density characterization by use of a broadband x-ray-compatible wave-front sensor". In: *Opt. Lett.* 28.3, pp. 149–151. DOI: 10.1364/OL.28.000149. URL: http://ol.osa.org/abstract.cfm?URI=ol-28-3-149.

Baker, Kevin L. (2009). "X-ray wavefront analysis and phase reconstruction with a two-dimensional shearing interferometer". In: *Optical Engineering* 48.8, pp. 1 –5. DOI: 10.1117/1.3205036. URL: https://doi.org/10.1117/1.3205036.

Begani Provinciali, Ginevra et al. (2020). "Modelling of Phase Contrast Imaging with X-ray Wavefront Sensor and Partial Coherence Beams". In: *Sensors* 20.22. ISSN: 1424-8220. DOI: 10.3390/s20226469. URL: https://www.mdpi.com/1424-8220/20/22/6469.

Benware, B. R. et al. (1997). "Operation and output pulse characteristics of an extremely compact capillary-discharge tabletop soft-x-ray laser". In: *Opt. Lett.* 22.11, pp. 796–798. DOI: 10.1364/OL.22.000796. URL: http://www.osapublishing.org/ol/abstract.cfm?URI=ol-22-11-796.

Berujon, Sebastien, Hongchang Wang, and Kawal Sawhney (2012). "X-ray multimodal imaging using a random-phase object". In: *Phys. Rev. A* 86 (6), p. 063813. DOI: 10.1103/PhysRevA.86.063813. URL: https://link.aps.org/doi/10.1103/PhysRevA.86.063813.

Biguri, Ander et al. (Sept. 2016). "TIGRE: a MATLAB-GPU toolbox for CBCT image reconstruction". In: *Biomedical Physics & Engineering Express* 2.5, p. 055010. DOI: 10.1088/2057-1976/2/5/055010. URL: https://doi.org/10.1088/2057-1976/2/5/055010.

BOLTE, S. and F. P. CORDELIÈRES (2006). "A guided tour into subcellular colocalization analysis in light microscopy". In: *Journal of Microscopy* 224.3, pp. 213–232. DOI: https://doi.org/10.1111/j.1365-2818.2006.01706.x. eprint: https://onlinelibrary.wiley.com/doi/pdf/10.1111/j.1365-2818.2006.01706.x. URL: https://onlinelibrary.wiley.com/doi/abs/10.1111/j.1365-2818.2006.01706.x.

Bonse, U. and M. Hart (Apr. 1965). "An X-Ray Interferometer". In: *Applied Physics Letters* 6, pp. 155–156. DOI: 10.1063/1.1754212.

Born, Max and Emil Wolf, eds. (1980). Sixth Edition. Pergamon, p. iii. ISBN: 978-0-08-026482-0. DOI: https://doi.org/10.1016/B978-0-08-026482-0.50002-5. URL: https://www.sciencedirect.com/science/article/pii/B9780080264820500025.

Bradski, G. (2000). "The OpenCV Library". In: *Dr. Dobb's Journal of Software Tools*.

Bravin, Alberto, Paola Coan, and Pekka Suortti (2012). "X-ray phase-contrast imaging: from pre-clinical applications towards clinics". In: 58.1, R1–R35. DOI: 10.1088/0031-9155/58/1/r1. URL: https://doi.org/10.1088/0031-9155/58/1/r1.

Burvall, Anna et al. (2011). "Phase retrieval in X-ray phase-contrast imaging suitable for tomography". In: *Opt. Express* 19.11, pp. 10359–10376. DOI: 10.1364/OE.19.010359. URL: http://www.opticsexpress.org/abstract.cfm?URI=oe-19-11-10359.

Cai, Yangjian, Yahong Chen, and Fei Wang (Sept. 2014). "Generation and propagation of partially coherent beams with nonconventional correlation functions: a review". In: *J. Opt. Soc. Am. A* 31.9, pp. 2083–2096. DOI: 10.1364/JOSAA.31.002083. URL: http://josaa.osa.org/abstract.cfm?URI=josaa-31-9-2083.

Colpo, Gabriela D. et al. (2017). "Chapter 42 - Animal Models for the Study of Human Neurodegenerative Diseases". In: *Animal Models for the Study of Human Disease (Second Edition)*. Ed. by P. Michael Conn. Second Edition. Academic Press, pp. 1109–1129. ISBN: 978-0-12-809468-6. DOI: https://doi.org/10.1016/B978-0-12-809468-6.00042-5. URL: https://www.sciencedirect.com/science/article/pii/B9780128094686000425.

Couprie, M.E. et al. (2004). "Control of the electron beam vertical instability using the super-ACO free electron laser". In: ed. by E.J. Minehara, R. Hajima, and M. Sawamura, pp. 287–290. DOI: https://doi.org/10.1016/B978-0-444-51727-2.50067-5. URL: https://www.sciencedirect.com/science/article/pii/B9780444517272500675.

Daniel R. Neal James Copland, David A. Neal (2002). "Shack-Hartmann wavefront sensor precision and accuracy". In: *Advanced Characterization Techniques for Optical, Semiconductor, and Data Storage Components*. Ed. by Angela Duparré and Bhanwar Singh. Vol. 4779. International Society for Optics and Photonics. SPIE, pp. 148 – 160. URL: https://doi.org/10.1117/12.450850.

Davis, Timothy J. et al. (1995). "Phase-contrast imaging of weakly absorbing materials using hard X-rays". In: *Nature* 373, pp. 595–598.

Diagnostic Radiology Physics (2014). Non-serial Publications. Vienna: INTERNATIONAL ATOMIC ENERGY AGENCY. ISBN: 978-92-0-131010-1. URL: https://www.iaea.org/publications/8841/diagnostic-radiology-physics.

Duguay, MA and PM Rentzepis (1967). "Some approaches to vacuum UV and X-ray lasers". In: *Applied Physics Letters* 10.12, pp. 350–352.

Eisett, S et al. (Apr. 2005). "Lensless imaging of magnetic nanostructures by X-ray spectro-holography". In: *Nature 432:885-888,2004*. URL: https://www.osti.gov/biblio/890897.

Emma, P. et al. (Aug. 2010). "First lasing and operation of an Ångstrom-wavelength free-electron laser". In: *Nature Photonics* 4, pp. 641–647. DOI: 10.1038/nphoton.2010.176.

Ferstl, Roman (2016). "Master thesis: Optimised Centroiding of Stars for Space Applications". In: *Vienna University*.

Filevich, Jorge et al. (July 2004). "Picosecond-resolution soft-x-ray laser plasma interferometry". In: *Appl. Opt.* 43.19, pp. 3938–3946. DOI: 10.1364/AO.43.003938. URL: http://www.osapublishing.org/ao/abstract.cfm?URI=ao-43-19-3938.

Flower, M.A. (2012). *Webb's Physics of Medical Imaging, Second Edition*. Series in Medical Physics and Biomedical Engineering. Taylor & Francis. ISBN: 9780750305730. URL: https://books.google.it/books?id=qkFljemf7y0C.

Förster, Eckhart, K. Goetz, and P. Zaumseil (1980). "Double crystal diffractometry for the characterization of targets for laser fusion experiments". In: *Crystal Research and Technology* 15, pp. 937–945.

Francesco, Silvia De and Augusto Silva (2004). "Efficient NUFFT-based direct Fourier algorithm for fan beam CT reconstruction". In: *Medical Imaging: Image Processing*.

Fried, David L. (Mar. 1977). "Least-square fitting a wave-front distortion estimate to an array of phase-difference measurements". In: *J. Opt. Soc. Am.* 67.3, pp. 370–375. DOI: 10.1364/JOSA.67.000370. URL: http://www.osapublishing.org/abstract.cfm?URI=josa-67-3-370.

Gbur, G. and T.D. Visser (2010). "Chapter 5 - The Structure of Partially Coherent Fields". In: ed. by Emil Wolf. Vol. 55. Progress in Optics. Elsevier, pp. 285–341. DOI: https://doi.org/10.1016/B978-0-444-53705-8.00005-9. URL: https://www.sciencedirect.com/science/article/pii/B9780444537058000059.

Gilbert, Peter (1972). "Iterative methods for the three-dimensional reconstruction of an object from projections". In: *Journal of Theoretical Biology* 36.1, pp. 105–117. ISSN: 0022-5193. DOI: https://doi.org/10.1016/0022-5193(72)90180-4. URL: https://www.sciencedirect.com/science/article/pii/0022519372901804.

Goodman, J.W. (2005). *Introduction to Fourier Optics*. McGraw-Hill physical and quantum electronics series. W. H. Freeman. ISBN: 9780974707723. URL: https://books.google.it/books?id=ow5xs_Rtt9AC.

Gori, Franco (1997). *Diffractive Optics: An Introduction*.

Graafsma, H. and T. Martin (Mar. 2008). "DETECTORS FOR SYNCHROTRON TOMOGRAPHY". In: *Advanced Tomographic Methods in Materials Research and Engineering* 10.

Griffiths, Harry J. (1989). "Tissue Substitutes in Radiation Dosimetry and Measurement. No. 4". In: *Radiology* 173.1, pp. 202–202. DOI: 10.1148/radiology.173.1.202. eprint: https://doi.org/10.1148/radiology.173.1.202. URL: https://doi.org/10.1148/radiology.173.1.202.

Gurney, Mark et al. (July 1994). "Motor Neuron Degeneration in Mice that Express a Human Cu,Zn Superoxide Dismutase Mutation". In: *Science (New York, N.Y.)* 264, pp. 1772–5. DOI: 10.1126/science.8209258.

Gustafsson, M. G. L. (2000). "Surpassing the lateral resolution limit by a factor of two using structured illumination microscopy". In: *Journal of Microscopy* 198.2, pp. 82–87. DOI: https://doi.org/10.1046/j.1365-2818.2000.00710.x. eprint: https://onlinelibrary.wiley.com/doi/pdf/10.1046/j.1365-2818.2000.00710.x. URL: https://onlinelibrary.wiley.com/doi/abs/10.1046/j.1365-2818.2000.00710.x.

Hansen, Per Christian and Jakob Sauer Jørgensen (2017). "AIR Tools II: algebraic iterative reconstruction methods, improved implementation". English. In: *Numerical Algorithms*, pp. 1–31. ISSN: 1017-1398. DOI: 10.1007/s11075-017-0430-x.

Hartmann, J. (1900). "Bemerkungen über den Bau und die Justierung von Spektrographen". In: *Z. Instrumentenkd.* 20, pp. 47–58.

Hecht, E. (1998). *Optics*. 4th. Addison-Wesley.

Henke, B.L., E.M. Gullikson, and J.C. Davis. (1993). "X-ray interactions: photoabsorption, scattering, transmission, and reflection at E=50-30000 eV, Z=1-92". In: *Atomic Data and Nuclear Data Tables* 54 (2), pp. 181–342.

Hounsfield, Godfrey Newbold (1995). "Computerized transverse axial scanning (tomography): Part I. Description of system. 1973." In: *The British journal of radiology* 68 815, H166–72.

Hsieh, J. (2003). *Computed Tomography: Principles, Design, Artifacts, and Recent Advances*. SPIE Press monograph. SPIE Press. ISBN: 9780819444257. URL: https://books.google.it/books?id=JX__lLLXFHkC.

Hubbell, J.H. and S.M. Seltzer (2004). "Tables of X-Ray Mass Attenuation Coefficients and Mass Energy-Absorption Coefficients (version 1.4)." In: DOI: https://dx.doi.org/10.18434/T4D01F.

Hudgin, Richard H. (Mar. 1977). "Wave-front reconstruction for compensated imaging". In: *J. Opt. Soc. Am.* 67.3, pp. 375–378. DOI: 10.1364/JOSA.67.000375. URL: http://www.osapublishing.org/abstract.cfm?URI=josa-67-3-375.

Idir, Mourad et al. (Sept. 2011). "X-ray optics simulation using Gaussian superposition technique". In: *Opt. Express* 19.20, pp. 19050–19060. DOI: 10.1364/OE.19.019050. URL: http://www.opticsexpress.org/abstract.cfm?URI=oe-19-20-19050.

Jack, C (2010). "The vascular hypothesis of Alzheimer's disease: bench to bedside and beyond". In: *Neurodegenerative Diseases* 7.1-3, pp. 116–121.

Jiang, Ming and Ge Wang (2001). "Convergence of the simultaneous algebraic reconstruction technique (SART)". In: *Conference Record of Thirty-Fifth Asilomar Conference on Signals, Systems and Computers (Cat.No.01CH37256)*. Vol. 1, 360–364 vol.1. DOI: 10.1109/ACSSC.2001.986951.

Kak, A C and M Slaney (Jan. 1988). "Principles of computerized tomographic imaging". In: URL: https://www.osti.gov/biblio/5813672.

Kiernan, Matthew C et al. (2011). "Amyotrophic lateral sclerosis". In: *The lancet* 377.9769, pp. 942–955.

Kotter, Mark R, Christine Stadelmann, and Hans-Peter Hartung (2011). "Enhancing remyelination in disease—can we wrap it up?" In: *Brain* 134.7, pp. 1882–1900.

La Rochefoucauld, Ombeline de et al. (2020). "Single-shot, high sensitivity X-ray phase contrast imaging system based on a Hartmann mask". In:

La Rochefoucauld, Ombeline de et al. (2021). "EUV and Hard X-ray Hartmann Wavefront Sensing for Optical Metrology, Alignment and Phase Imaging". In: *Sensors* 21.3. ISSN: 1424-8220. DOI: 10.3390/s21030874. URL: https://www.mdpi.com/1424-8220/21/3/874.

Le Pape, S. et al. (Apr. 2002). "Electromagnetic-Field Distribution Measurements in the Soft X-Ray Range: Full Characterization of a Soft X-Ray Laser Beam". In: *Phys. Rev. Lett.* 88 (18), p. 183901. DOI: 10.1103/PhysRevLett.88.183901. URL: https://link.aps.org/doi/10.1103/PhysRevLett.88.183901.

Lee, Ta-Chih, Rangasami L. Kashyap, and Chong-Nam Chu (1994). "Building Skeleton Models via 3-D Medial Surface/Axis Thinning Algorithms". In: *CVGIP: Graph. Models Image Process.* 56.6, 462–478. ISSN: 1049-9652. DOI: 10.1006/cgip.1994.1042. URL: https://doi.org/10.1006/cgip.1994.1042.

Li, Lu et al. (Aug. 2020). "High numerical aperture Hartmann wave front sensor for extreme ultraviolet spectral range". In: *Opt. Lett.* 45.15, pp. 4248–4251. DOI: 10.1364/OL.396356. URL: http://ol.osa.org/abstract.cfm?URI=ol-45-15-4248.

Lok, Kenghoe et al. (2013). "Characterization of the APP/PS1 mouse model of Alzheimer's disease in senescence accelerated background". In: *Neuroscience Letters* 557, pp. 84–89. ISSN: 0304-3940. DOI: https://doi.org/10.1016/j.neulet.2013.10.051. URL: https://www.sciencedirect.com/science/article/pii/S0304394013009555.

Mahajan, V.N. (1998). *Optical Imaging and Aberrations :: Part II : Wave Diffraction Optics*. SPIE Optical Engineering Press. URL: https://books.google.fr/books?id=02wazAEACAAJ.

Massimi, Lorenzo et al. (2018). "An improved ring removal procedure for in-line x-ray phase contrast tomography". In: *Physics in Medicine & Biology* 63.4, p. 045007.

Mayo, Sheridan C. and Brett Sexton (Apr. 2004). "Refractive microlens array for wave-front analysis in the medium to hard x-ray range". In: *Opt. Lett.* 29.8, pp. 866–868. DOI: 10.1364/OL.29.000866. URL: http://ol.osa.org/abstract.cfm?URI=ol-29-8-866.

Mercère, Pascal et al. (Sept. 2003). "Hartmann wave-front measurement at 13.4 nm with λEUV/120 accuracy". In: *Opt. Lett.* 28.17, pp. 1534–1536. DOI: 10.1364/OL.28.001534. URL: http://ol.osa.org/abstract.cfm?URI=ol-28-17-1534.

Michette, A.G. and S. Pfauntsch (1996). *X-rays: The First Hundred Years*. John Wiley & Sons. ISBN: 9780471965022. URL: https://books.google.it/books?id=1rrvAAAAMAAJ.

Momose, Atsushi et al. (1996). "Phase–contrast X–ray computed tomography for observing biological soft tissues". In: *Nature Medicine* 2, pp. 473–475.

Morlens, Anne-Sophie et al. (2006). "Submicrometer digital in-line holographic microscopy at 32 nm with high-order harmonics". In: *Opt. Lett.* 31.21, pp. 3095–3097. DOI: 10.1364/OL.31.003095. URL: http://opg.optica.org/ol/abstract.cfm?URI=ol-31-21-3095.

Nave, Klaus-Armin (2010). "Myelination and the trophic support of long axons". In: *Nature Reviews Neuroscience* 11.4, pp. 275–283.

Nightingale, Alice and Stanislav Gordeyev (July 2013). "Shack-Hartmann wavefront sensor image analysis: a comparison of centroiding methods and image-processing techniques". In: *Optical Engineering* 52, p. 071413. DOI: 10.1117/1.OE.52.7.071413.

O'brien, Richard J and Philip C Wong (2011). "Amyloid precursor protein processing and Alzheimer's disease". In: *Annual review of neuroscience* 34, pp. 185–204.

Olivo, A. et al. (Aug. 2001). "An innovative digital imaging set-up allowing a low-dose approach to phase contrast applications in the medical field". In: *Medical Physics* 28.8, pp. 1610–1619. DOI: 10.1118/1.1388219.

Olivo, Alessandro and Robert Speller (2007). "A coded-aperture technique allowing x-ray phase contrast imaging with conventional sources". In: *Applied Physics Letters* 91.7, p. 074106. DOI: 10.1063/1.2772193. eprint: https://doi.org/10.1063/1.2772193. URL: https://doi.org/10.1063/1.2772193.

Oppenheim Alan V., Schafer Ronald W. (2009). *Discrete-Time Signal Processing, 3rd edition*. Pearson.

Optic, Imagine. *Imagine Optic*. URL: https://www.imagine-optic.com/product/haso-hxr/.

Paganin, D. et al. (2002). "Simultaneous phase and amplitude extraction from a single defocused image of a homogeneous object". In: *Journal of Microscopy* 206.1,

pp. 33–40. ISSN: 1365-2818. DOI: 10.1046/j.1365-2818.2002.01010.x. URL: http://dx.doi.org/10.1046/j.1365-2818.2002.01010.x.

Peatross, Justin and Michael Ware (2010). "Physics of Light and Optics: A Free Online Textbook". In: *Frontiers in Optics 2010/Laser Science XXVI*, JWA64. URL: http://www.osapublishing.org/abstract.cfm?URI=LS-2010-JWA64.

Pogany, Andrew, Da Chao Gao, and Stephen W. Wilkins (1997). "Contrast and resolution in imaging with a microfocus x-ray source". In: *Review of Scientific Instruments* 68, pp. 2774–2782.

Radon, Johann (1986). "On the determination of functions from their integral values along certain manifolds". In: *IEEE Transactions on Medical Imaging* 5, pp. 170–176.

Raparia, D, J Alessi, and A Kponou (July 1997). "The Algebraic Reconstruction Technique (ART)". In: URL: https://www.osti.gov/biblio/491450.

Rasmussen, Jay et al. (2017). "Amyloid polymorphisms constitute distinct clouds of conformational variants in different etiological subtypes of Alzheimer's disease". In: *Proceedings of the National Academy of Sciences* 114.49, pp. 13018–13023. ISSN: 0027-8424. DOI: 10.1073/pnas.1713215114. eprint: https://www.pnas.org/content/114/49/13018.full.pdf. URL: https://www.pnas.org/content/114/49/13018.

Reynolds, George O. et al. (1989). *Physical optics notebook: Tutorials in Fourier optics*.

Robert M. Gray, Joseph Goodman (1995). *Fourier Transforms: An Introduction for Engineers*. Springer US.

Rohringer, Nina and Richard London (2009). "Atomic inner-shell x-ray laser pumped by an x-ray free-electron laser". In: *Phys. Rev. A* 80 (1), p. 013809. DOI: 10.1103/PhysRevA.80.013809. URL: https://link.aps.org/doi/10.1103/PhysRevA.80.013809.

Rueden, Curtis T. et al. (2017). "ImageJ2: ImageJ for the next generation of scientific image data". In: *BMC Bioinformatics* 18.

Ruiz-Lopez, Mabel et al. (Jan. 2017). "Coherent X-ray beam metrology using 2D high-resolution Fresnel-diffraction analysis". In: *Journal of Synchrotron Radiation* 24, p. 196. DOI: 10.1107/S1600577516016568.

Saberi, Shahram et al. (2015). "Neuropathology of amyotrophic lateral sclerosis and its variants". In: *Neurologic clinics* 33.4, pp. 855–876.

Schreiber, S. et al. (2010). "FEL User Facility FLASH". In: *Proc. 1st Int. Particle Accelerator Conf. (IPAC'10)* (Kyoto, Japan). JACoW Publishing, pp. 2149–2151. URL: http://accelconf.web.cern.ch/IPAC10/papers/TUPE004.pdf.

Shechtman, Yoav et al. (2015). "Phase Retrieval with Application to Optical Imaging: A contemporary overview". In: *IEEE Signal Processing Magazine* 32.3, pp. 87–109. DOI: 10.1109/MSP.2014.2352673.

Shi, Xianbo et al. (2014). "A hybrid method for X-ray optics simulation: combining geometric ray-tracing and wavefront propagation". In: *Journal of Synchrotron Radiation* 21, pp. 669–678. DOI: 10.1107/S160057751400650X. URL: https://hal.archives-ouvertes.fr/hal-01573008.

Shiryayev, A. N. (1992). "Interpolation and Extrapolation of Stationary Random Sequences". In: *Selected Works of A. N. Kolmogorov: Volume II Probability Theory and Mathematical Statistics*. Ed. by A. N. Shiryayev. Dordrecht: Springer Netherlands, pp. 272–280. ISBN: 978-94-011-2260-3. DOI: 10.1007/978-94-011-2260-3_28. URL: https://doi.org/10.1007/978-94-011-2260-3_28.

Simon, R. and N. Mukunda (Jan. 1993). "Twisted Gaussian Schell-model beams". In: *J. Opt. Soc. Am. A* 10.1, pp. 95–109. DOI: 10.1364/JOSAA.10.000095. URL: http://josaa.osa.org/abstract.cfm?URI=josaa-10-1-95.

Smith, Raymond et al. (Nov. 2003a). "Longitudinal coherence measurements of a transient collisional x-ray laser". In: *Optics letters* 28, pp. 2261–3. DOI: 10.1364/OL.28.002261.

Smith, Raymond F. et al. (Nov. 2003b). "Longitudinal coherence measurements of a transient collisional x-ray laser". In: *Opt. Lett.* 28.22, pp. 2261–2263. DOI: 10.1364/OL.28.002261. URL: http://ol.osa.org/abstract.cfm?URI=ol-28-22-2261.

Snigirev, A. et al. (1995). "On the possibilities of x-ray phase contrast microimaging by coherent high-energy synchrotron radiation". In: *Review of Scientific Instruments* 66.12, pp. 5486–5492. DOI: 10.1063/1.1146073. eprint: https://doi.org/10.1063/1.1146073. URL: https://doi.org/10.1063/1.1146073.

Sólyom, J. (2010). *Fundamentals of the Physics of Solids: Volume 3 - Normal, Broken-Symmetry, and Correlated Systems*. Theoretical Solid State Physics: Interaction Among Electrons. Springer Berlin Heidelberg. ISBN: 9783642045189. URL: https://books.google.it/books?id=rL5eGGiY1WUC.

Southwell, W.H. (Aug. 1980). "Wave-front estimation from wave-front slope measurements". In: *J. Opt. Soc. Am.* 70.8, pp. 998–1006. DOI: 10.1364/JOSA.70.000998. URL: http://www.osapublishing.org/abstract.cfm?URI=josa-70-8-998.

Spiricon (2004). "BHartmann Wavefront Analyzer Tutorial". In: *Spiricon, Inc.*

Starikov, A. and E. Wolf (July 1982). "Coherent-mode representation of Gaussian Schell-model sources and of their radiation fields". In: *J. Opt. Soc. Am.* 72.7, pp. 923–928. DOI: 10.1364/JOSA.72.000923. URL: http://www.osapublishing.org/abstract.cfm?URI=josa-72-7-923.

Suetens, P. (2009). *Fundamentals of Medical Imaging*. Cambridge medicine. Cambridge University Press. ISBN: 9780521519151. URL: https://books.google.it/books?id=iUHgx5E4zLMC.

Tejnil, Edita et al. (1997). "At-wavelength interferometry for extreme ultraviolet lithography". In: *Journal of Vacuum Science & Technology B: Microelectronics and Nanometer Structures Processing, Measurement, and Phenomena* 15.6, pp. 2455–2461. DOI: 10.1116/1.589666. eprint: https://avs.scitation.org/doi/pdf/10.1116/1.589666. URL: https://avs.scitation.org/doi/abs/10.1116/1.589666.

Tessa, Van et al. (Jan. 2007). "ITERATIVE RECONSTRUCTION ALGORITHMS The implementation of iterative reconstruction algorithms in MATLAB". In:

Thibault, Pierre (Jan. 2007). "Algorithmic methods in diffraction microscopy". PhD thesis. Cornell University.

Tremsin, A. S. et al. (2003). "Centroiding algorithms and spatial resolution of photon counting detectors with cross strip anodes". In: *Proc. SPIE.* 5164.

Tyler, G. A. and D. L. Fried (1982). "A wave optics propagation algorithm". In:

Vahimaa, Pasi and Jari Turunen (Feb. 2006). "Finite-elementary-source model for partially coherent radiation". In: *Opt. Express* 14.4, pp. 1376–1381. DOI: 10.1364/OE.14.001376. URL: http://www.opticsexpress.org/abstract.cfm?URI=oe-14-4-1376.

Valasek, Joseph (1950). "Introduction to Theoretical and Experimental Optics". In: *American Journal of Physics* 18.4, pp. 230–231. DOI: 10.1119/1.1932545. eprint: https://doi.org/10.1119/1.1932545. URL: https://doi.org/10.1119/1.1932545.

Vasquez, Sergio X. et al. (Apr. 2011). "Optimization of MicroCT Imaging and Blood Vessel Diameter Quantitation of Preclinical Specimen Vasculature with Radiopaque Polymer Injection Medium". In: *PLOS ONE* 6.4, pp. 1–6. DOI: 10.1371/journal.pone.0019099. URL: https://doi.org/10.1371/journal.pone.0019099.

Voelz, D.G. (2011). *Computational Fourier Optics: A MATLAB Tutorial*. SPIE Press. URL: https://books.google.fr/books?id=fd9ZnQAACAAJ.

Vogt, Ulrich et al. (Aug. 2005). "Single-optical-element soft-x-ray interferometry with a laser-plasma x-ray source". In: *Opt. Lett.* 30.16, pp. 2167–2169. DOI: 10.1364/OL.30.002167. URL: http://www.osapublishing.org/ol/abstract.cfm?URI=ol-30-16-2167.

Walker, Espen J et al. (2011). "Cerebrovascular casting of the adult mouse for 3D imaging and morphological analysis". In: *Journal of visualized experiments: JoVE* 57.

Wang, Sha-Sha et al. (2018). "Myelin injury in the central nervous system and Alzheimer's disease". In: *Brain Research Bulletin* 140, pp. 162–168. ISSN: 0361-9230. DOI: https://doi.org/10.1016/j.brainresbull.2018.05.003. URL: https://www.sciencedirect.com/science/article/pii/S0361923018302016.

Wansleben, Malte et al. (2019). "Photon flux determination of a liquid-metal jet X-ray source by means of photon scattering". In: *J. Anal. At. Spectrom.* 34 (7), pp. 1497–1502. DOI: 10.1039/C9JA00127A. URL: http://dx.doi.org/10.1039/C9JA00127A.

Weissleder, Ralph et al., eds. (2011). *Chapter 1 - Chest Imaging*. Fifth Edition. Philadelphia: Mosby, pp. 1–71. ISBN: 978-0-323-06538-2. DOI: https://doi.org/10.1016/B978-0-323-06538-2.00001-9. URL: https://www.sciencedirect.com/science/article/pii/B9780323065382000019.

Weitkamp, Timm et al. (2005). "X-ray phase imaging with a grating interferometer". In: *Opt. Express* 13.16, pp. 6296–6304. DOI: 10.1364/OPEX.13.006296. URL: http://www.osapublishing.org/oe/abstract.cfm?URI=oe-13-16-6296.

White, Lon R. et al. (2002). "Cerebrovascular Pathology and Dementia in Autopsied Honolulu-Asia Aging Study Participants". In: *Annals of the New York Academy of Sciences* 977.

Wiener, Norbert (1930). "Generalized harmonic analysis". In: *Acta Mathematica* 55.none, pp. 117 –258. DOI: 10.1007/BF02546511. URL: https://doi.org/10.1007/BF02546511.

Yoneda, Hitoki et al. (Aug. 2015). "Atomic inner-shell laser at 1.5-ångström wavelength pumped by an X-ray free-electron laser". In: *Nature* 524, pp. 446–449. DOI: 10.1038/nature14894.

Zabler, S. et al. (2005). "Optimization of phase contrast imaging using hard x rays". In: *Review of Scientific Instruments* 76.7, p. 073705. DOI: 10.1063/1.1960797. eprint: https://doi.org/10.1063/1.1960797. URL: https://doi.org/10.1063/1.1960797.

Zamir, Anna et al. (2017). "Recent advances in edge illumination x-ray phase-contrast tomography". In: *Journal of Medical Imaging* 4.4, pp. 1 –8. DOI: 10.1117/1.JMI.4.4.040901. URL: https://doi.org/10.1117/1.JMI.4.4.040901.

Zeitoun, Philippe et al. (Sept. 2004). "A high-intensity highly coherent soft X-ray femtosecond laser seeded by a high harmonic beam". In: *Nature* 431, pp. 426–429. DOI: 10.1038/nature02883. URL: https://hal-polytechnique.archives-ouvertes.fr/hal-00522630.

ECOLE DOCTORALE

Titre : Imagerie X de phase basée sur le capteur de front d'onde de Hartmann pour application sur l'étude des maladies neurodégénératives

Mots clés : Capteur de front d'onde, Contraste de phase, Tomographie, Rayon X, Imagerie biologique

Résumé : L'objectif de cette thèse consiste en le développement d'une technique d'imagerie X de phase basée sur l'utilisation d'un senseur de front d'onde de type Hartmann pour être exploité sur différentes applications et de comparer ce nouveau système avec des techniques bien connues d'imagerie en contraste de phase. L'imagerie de phase sera principalement réalisée en 3D par tomographie. L'application principale inclue l'étude d'altérations du système nerveux central induites par des maladies neurodégénératives. La première section d'introduction décrit les aspects de base de l'interaction rayons X-matière et de la théorie de la cohérence avec des application spécifiques à la conception de senseur de front d'onde de Hartmann. Dans le deuxième chapitre, une introduction à l'imagerie par contraste de phase est donnée, avec une attention particulière sur la technique en propagation libre. Le troisième chapitre examine les principes de la tomographie et des logiciels de reconstruction disponibles. Un chapitre séparé, numéroté 4, est dédié à la théorie des senseurs de front d'onde de Hartmann. Un modèle de propagation en 3D basé sur le propagateur de Fresnel a été développé pour optimiser l'architecture du senseur complet incluant la plaque de Hartmann, les distances entre les différents éléments du montage et enfin les propriétés de la source X. Le modèle peut gérer n'importe quel degré de cohérence spatiale, permettant de réaliser des modélisation précises d'une grande variété de source X. Différentes simulations de situation expérimentales sont décrites pour valider le programme. Puis, les programmes principaux de reconstruction du front d'onde ont été analysés. Dans le chapitre 5, nous allons présenter des résultats expérimentaux obtenus avec le senseur de font d'onde X en géométries de faisceau parallèle (synchrotron) ou conique (mesure en laboratoire). Différentes plaques de Hartmann ont été utilisé sur le montage de laboratoire pour visualiser une série d'échantillons tes et biologiques. De plus, sur synchrotron, nous avons testé le senseur de Hartmann pour retrouver la composition chimique d'objets composés de matériaux connus. La composition chimique peut être estimée à partir de mesures directes et indépendantes de la partie réelle (proportionnelle à la phase) et la partie imaginaire (proportionnelle à l'absorption) de l'indice de réfraction de l'échantillon. Dans le chapitre 6, les résultats expérimentaux obtenus en tomographie X par contraste de phase en propagation libre seront discutés. Nous avons exploité la capacité de l'imagerie X par contraste de phase pour étudier les effets des maladies neurodégénératives du système nerveux central.

Title : X-ray phase imaging based on Hartmann Wavefront Sensor for applications on the study of neurodegenerative diseases

Keywords : Wavefront sensor, Phase Contrast, Tomography, X-rays, Biological imaging

Abstract : The aim of this PhD thesis is to develop the technic of X-ray phase imaging with Hartmann wavefront sensor for various applications and to compare this new system against well-established phase-contrast techniques. The X-ray phase imaging will be mainly performed in 3D using tomographic setup. The main application includes the study of alterations in the central nervous system induced by neurodegenerative diseases. The first introductory section describes the basic aspects of X-ray interaction with matter and of the coherence theory with specific application to the Hartmann wavefront sensor design. In the second chapter, an introduction to phase-contrast imaging is given, with particular attention to the free-space propagation technique. The third chapter examines the principles of tomography acquisitions and the available reconstruction algorithms. A separate chapter, labeled 4, is dedicated to the theory of Hartmann wavefront sensor. A 3D wave propagation model based on Fresnel propagator was developed to optimize the architecture of the full wavefront sensor including the Hartmann plate, the distances between the different elements of the set-up as well as the X-ray source properties. The model can manage any degree of spatial coherence, enabling the accurate simulation of a wide range of X-ray sources. Several simulations of standard experimental situations are described to valid the program. Then, the main wavefront reconstruction algorithms have been analyzed. In chapter 5, we will present experimental results obtained with the X-ray Hartmann wavefront sensor using both a parallel beam geometry (synchrotron measurements) and a cone beam geometry (laboratory measurements). Different Hartmann plates were used with the laboratory set-up to visualize a series of test and biological samples. Also, using synchrotron, we tested the Hartmann sensor to retrieve the chemical composition of objects composed of known materials. The chemical composition could be inferred starting from direct and independent measurements of the real part (proportional to the phase) and the imaginary part (proportional to the absorption) of the sample refractive index. In chapter 6, the experimental results obtained with free space propagation X-ray phase contrast tomography will be discussed. We exploited the capability of X-ray phase contrast imaging to investigate the effects of neurodegenerative diseases on the central nervous system.

Institut Polytechnique de Paris
91120 Palaiseau, France